On Nucleation and Droplet Growth
in Condensing Nozzle Flows

by Grazia Lamanna

On Nucleation and Droplet Growth
in Condensing Nozzle Flows

PROEFSCHRIFT

door

GRAZIA LAMANNA

geboren te Napoli, Italia

Dit proefschrift is goedgekeurd door de promotoren:

prof.dr.ir. M.E.H. van Dongen
en
prof.dr.ir. H.W.M. Hoeijmakers

FOM

*Experience is the name
everyone gives to his own errors.*

Oscar Wilde (1856-1900)

*Ai miei cari,
ed in particolare a Bipidi.*

Contents

List of symbols

Latin symbols and abbreviations:

symbol	definition
a_0	molecular surface area
a_f	thermally frozen speed of sound
A	interface area
A	light beam cross section
$A_0 - A_{11}$	constants
B_0, B_1	constants
c_p	isobaric specific heat capacity
c_v	isochoric specific heat capacity
C_0	constant
C_{abs}	absorption cross section
C_{ext}	extinction cross section
C_{sca}	scattering cross section
CNT	Classical Nucleation Theory
J	nucleation rate
d	distance between two successive scattering events
$D_0 - D_3$	constants
$\mathcal{D}$	diffusion coefficient
$\mathcal{D}_{mod}$	modified diffusion coefficient
e	specific internal energy
$\mathbf{e}$	unit vector
E	total specific energy
$\dot{E}$	energy flow rate from droplet
$E(x, y)$	complex amplitude of the electric field
f	focal length
f	frequency
f_x	spatial frequency along x-axis
f_y	spatial frequency along y-axis
f_{co}	cut-off frequency
$f(r)$	droplet size distribution
$f(r, \mathbf{p})$	zeroth-order log-normal size distribution

F	convective flux vector in the x-direction
$\mathcal{F}(\theta,\varphi)$	scattering function
g	condensate mass fraction
$g(\alpha)$	spectral turbidity
G	geometric cross section of a scatterer
G	Gibbs' potential
G	convective flux vector in the y-direction
gya63	Gyarmathy droplet growth model [48]
gya82	Gyarmathy droplet growth model [49]
h	specific enthalpy
h^*	nozzle throat height in $[cm]$
$\dot{H}$	conduction heat flow from droplet
HK	Hertz-Knudsen droplet growth model [57, 68]
$i_1,\ i_2$	irradiance components of the scattering matrix $\underline{\underline{S}}$
I	irradiance
I_0	irradiance of incident light
I_s	irradiance of scattered light
ICCT	Internally Consistent Classical Theory
J	nucleation rate
$J_m,\ J_{qc}$	mass and heat conduction fluxes from the droplet
k	thermal conductivity of vapour-gas mixture
$\vec{k}$	wave number vector
k_x	wave vector component along x-axis
k_y	wave vector component along y-axis
k_B	Boltzmann constant
K	Gladstone-Dale constant
Ke	Kelvin factor
Kn	Knudsen number, $l/2\,r_d$
l	mean free path, $2\mu\sqrt{RT}/p$
l	slab width; geometrical pathlength
l_{coher}	coherence length of the laser
L	latent heat of condensation
L	width of the test section
$L_{mm},\ L_{mq},\ L_{qm},\ L_{qq}$	phenomenological coefficients
m	mass of a vapour molecule
m	refractive index
M	Mach number
$\dot{M}$	mass flow rate from droplet
M	mass
M	magnification of the imaging system
M_a	axial magnification
M_t	transverse magnification

n	number of molecules in a cluster
n	number of wavelengths employed in the extinction measurements
n_d	droplet number density
$n(x(s), y(s), z(s))$	refractive index distribution
N	total number of molecules
$Nu_{\dot{E}}$	Nusselt number for energy transfer
$Nu_{\dot{H}}$	Nusselt number for conduction heat transfer
$Nu_{\dot{M}}$	Nusselt number for mass transfer
$\mathbf{p}$	parameter vector (r_m, ε)
p	pressure
p	micrometer position
p_{vr}	vapour pressure at the droplet surface
p_{sr}	saturation pressure at T_d and r_d
P_e	attenuated beam power
P_s	scattered beam power
$p(d)$	probability density function
$p(\theta)$	θ-angle probability density function
Pr	Prandtl number of the vapour-gas mixture $\mu\,c_p/k$
$q_c,\ q_e$	condensation and evaporation coefficient
Q_{abs}	absorption efficiency
Q_{ext}	extinction efficiency
Q_{sca}	scattering efficiency
$\mathcal{Q}_n$	n-th moment of the droplet size distribution
r	radius
r_m	modal radius
r_{32}	Sauter mean radius
R	specific gas constant
R_{max}	maximum modal radius
R_{0-}^*	radius of curvature upstream of the nozzle throat in $[cm]$
R_{0+}^*	radius of curvature downstream of the nozzle throat in $[cm]$
R_{i1}	Rayleigh parameter $\frac{\beta_i \lambda_i^4}{\beta_1 \lambda_1^4}$
$\mathcal{R}$	residue $\sum_{i=1}^{n}(\beta_{theo,i} - \beta_{exp,i})^2$
$\mathcal{R}_{perfect}$	optimal minimum value for the residue $\mathcal{R}$
s	coordinate along the ray path
S	supersaturation $p_v/p_{s\infty}(T)$
S	entropy
S	source term
$\dot{S}$	rate of entropy production
$\underline{\underline{S}}$	amplitude scattering matrix
Sc	Schmidt number $\mu/\varrho\,\mathcal{D}$
SN	signal-to-noise ratio
t	time; exposure time

t	temperature (in degree Celsius)
T	temperature (in degree Kelvin)
u	cartesian speed component in the x-direction
U	internal energy
U	vector of unknowns
$U(x, y)$	complex amplitude of an optical wave
v	cartesian speed component in the y-direction
v_l	liquid molecular volume
V	volume
$\underline{V}$	velocity vector
$\vec{X}$	vector scattering amplitude
$<x>$	photon mean free path
x, y, z	cartesian coordinates
ZOL	zeroth-order log-normal

Greek symbols:

symbol	definition
α	size parameter $2\pi r_d/\lambda$
β	extinction coefficient
β	constant defining Knudsen-continuum interface
β	slope of the amplitude transmittance
δ	optical thickness
δ	parameter for determining T_d
Δ	difference
ΔG_n	formation energy of a cluster with n molecules
Δl_{min}	smallest resolvable separation in an image
Δl_{path}	pathlength mismatch between interfering beams
ΔT	thermodynamic force $\Delta T = T_d - T_\infty$
Δp_v	thermodynamic force $\Delta p_v = p_v - p_{sr}$
$\Delta \beta_{exp}$	inaccuracy in the experimental determination of β
$\Delta \phi$	phase delay
$\Delta \Phi$	optical pathlength difference
$\Delta \varphi$	phase difference
ε	relative variance of the size distribution
η	dimensionless parameter
θ	scattering angle
θ_{max}	maximum detection angle
Θ	dimensionless surface tension
λ	parameter in transition correction formula
$\lambda, \lambda`$	wavelength
μ	chemical potential per unit mass

μ	dynamic viscosity of vapour-gas mixture
$\mu(\beta)$	expectation value for the extinction coefficient
$\mu(\mathcal{R}_{perfect})$	expectation value for the residue $\mathcal{R}_{perfect}$
ξ	constant multiplicative factor
ξ_r, ξ_0	spatial frequencies
ϱ	density
σ	surface tension of liquid
σ	standard deviation
τ_0	constant background transmittance
τ_i	relaxation time internal rate processes
τ^*	characteristic time for reaching steady-state nucleation
$\tau(x,y)$	film transmittance
v	voltage reading at the detector in $[mV]$
v_d	dark value reading at the detector in $[mV]$
φ	azimuthal angle
Ψ_0	unwrapped phase
ω	solid angle

Subscripts:

symbol	pertains to
a	carrier gas (air/nitrogen)
abs	absorption
ad	adiabatic
avr	averaged value
ct	continuum
d	droplet
exp	experimentally determined value
ext	extinction
f	frozen state
g	inert gas; gaseous phase
h	hologram
i	Knudsen-continuum interface
i	image
inc	incident
ini	supply (initial) conditions
$inlet$	nozzle inlet
I	irradiance
k	kinetic
l	liquid
m	evaluated at the intermediate temperature T_m
max	maximum
min	minimum

Mie	derived from Mie scattering theory
mod	modified version
o	object
p	position reconstruction beam
$perfect$	optimal value
r	reference
rec	reconstruction
ref	reference
Ray	derived from Rayleigh scattering theory
s	saturated value
sca	scattering
sr	curvature corrected saturated value
t	transmitted
$theo$	theoretical value
tot	total value
v	vapour
vr	vapour component at droplet surface
x, y, z	x-, y-, z-coordinate axis
0	stagnation condition; initial value
32	relative to Sauter mean radius
∞	value at a flat surface
∞	value far from droplet (far field)
β	extinction coefficient

Superscripts:

symbol	pertains to
ct	continuum
fm	free molecular
l	bulk liquid
s	interface layer
tr	transition
v	bulk vapour
1	one particle
$*$	complex conjugate
$*$	value of the critical cluster
$*$	value at $M = 1$
$-$	averaged properties

Otherwise explicitly indicated, all properties are expressed in SI-units. All symbols not listed here are directly defined in the sections where they are employed.

Chapter 1

Introduction

1.1 Background

Dropwise condensation from a gaseous supersaturated state is of relevance to many environmental and technological processes. With reference to environmental applications, for example, the formulation of quantitative models for weather predictions requires the numerical solution of condensing flows. The prediction of fall-out phenomena, following nuclear explosions, has also acquired dramatic relevance due to nuclear weapons testing or nuclear accidents. In these cases, condensation occurs primarily on foreign particles (ions, dust or salt crystals) and is normally termed heterogeneous condensation. In industry, heterogeneous condensation is important, for example, for condensation on substrates in metallurgical applications, or for the production of sprays in the pharmacological industry.

There exist also examples in which condensation nuclei are produced spontaneously within the vapour phase. In these cases, the actual phase transition is preceded by homogeneous nucleation, which involves the formation of metastable clusters due to molecular fluctuations, and then proceeds as droplet growth due to condensation on the nuclei. Phase transition through homogeneous nucleation plays a key role in many natural and industrial processes, as well. For example, the formation of aerosols is associated with many catalytic reactions influencing, amongst others, the atmospheric ozone concentration. The formation of plumes by condensation of hot exhaust gasses or the venting of a tank into vacuum are examples of interests for the aerospace industry. In steam turbines applications, homogeneous condensation may lead to an increased loss of efficiency (thermodynamic wetness loss) and/or to the erosion of turbine blades. In the petrochemical industry, nucleation of water and higher hydrocarbons may lead to advanced methods for condensate separation, thereby reducing significantly the costs for the exploitation and handling of oil and natural gases. In all these industrial applications, a key element for their success is related to the possibility of predicting and, therefore, controlling the homogeneous/heterogeneous nucleation rate processes. Obviously, a fundamental prerequisite for controlling any process relies on the understanding of its physical mechanism.

From this standpoint, expansion flows in supersonic nozzles are extremely useful and provide excellent test cases for condensation studies. The study of homogeneous condensation in supersonic nozzle flows presents many advantages over test cases involving cloud chambers or wave tube methods. The accurate modelling of nozzle flows is, in fact, extremely sensitive to the quality and accuracy of nucleation and droplet growth theories. Consider, for example, that a typical inaccuracy in determining nucleation rates in expansion wave tubes experiments is 1 to 2 orders of magnitude. The same inaccuracy, when testing nucleation models in nozzle flows, would lead to significant discrepancies. Pressure distributions, frequency data, and droplet sizes are, in fact, very sensitive parameters to test the quality of nucleation rates. Furthermore, thanks to the large subcoolings that can be achieved in nozzle flows, experiments of condensing nozzle flows may convey information on some unknown physical properties, such as surface tension. It is, therefore, the aim of this thesis to gain more physical insight on the modelling of nucleation and droplet growth processes by a systematic and thorough study of homogeneously condensing nozzle flows.

1.2   Phenomenology

The general problem of non-equilibrium condensing flows can be incorporated in the framework of relaxation gas dynamics. Therefore, its physical understanding rests largely on the role played by the relaxation times of the internal rate processes. From an heuristic viewpoint, the effects of nonequilibrium condensation can be summarised as follows. During the expansion of a condensable vapour in a supersonic nozzle, the thermodynamic state in the flow may approach the coexistence region between the vapour and liquid phase. Nevertheless, due to the high cooling rates $[O(10^6)\,K s^{-1}]$, the gaseous phase may depart radically from the equilibrium phase distributions. A state of high supersaturation is therefore achieved, indicative of a metastable non-equilibrium state of the vapour phase. In absence of foreign particles, the actual phase transition is preceded by homogeneous nucleation, involving the formation of small clusters of molecules due to statistical fluctuations. As these metastable clusters exceed some critical size, the process of droplet growth sets in, leading to the formation of a stable liquid phase.

The accompanying release of latent heat to the flow has a strong impact on the flow pattern. Depending on the initial stagnation conditions, different flow regimes may result. If the amount of heat, released at a certain axial location in the nozzle, is below some critical amount, then only a local increase in temperature, pressure, and density is observed over a relatively small distance (subcritical flow), as shown in Fig. 1.1-top. If the amount of heat released exceeds this critical value, the flow becomes thermally choked and a steady shock appears embedded in the nucleation zone, as shown in Fig.1.1-bottom.

The details of the condensation process are immediately inferable from Fig. 1.2. First nucleation sets in just upstream of the nozzle throat ($x = 0$) and no perturbation of the flow properties is observed. As soon as the droplet growth process starts and significant heat is released to the flow, a shock appears due to the compressive effects from excessive heat release, thus interrupting the nucleation process.

Subcritical Flow

Supercritical Flow
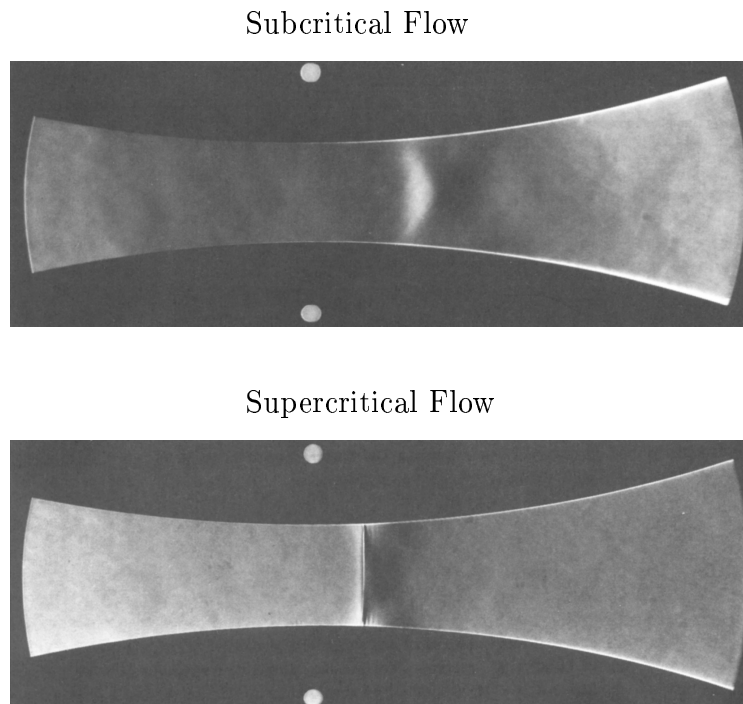
Figure 1.1: *Schlieren pictures of steady flow experiments. Nozzle: S2. Flow direction: from left to right. Courtesy of G.H. Schnerr & S. Adam (S. Adam, PhD thesis, Universität Karlsruhe, 1996).*
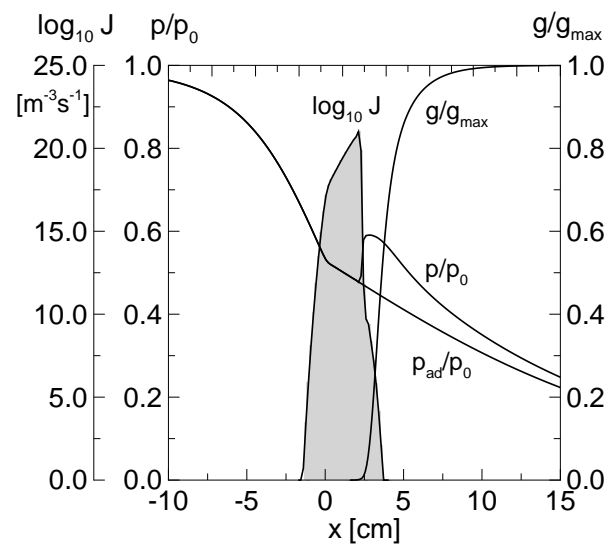
Figure 1.2: *Example of a supercritical flow prediction. Axial distributions of pressure p/p_0, condensate mass fraction g/g_{max}, and nucleation rate J. The pressure profile p_{ad}/p_0 for dry nozzle flow is also included. Nozzle: G2.*

As a result, the nucleation rate becomes a sharply peaked function of x. If the amount of heat released increases further, a steady flow solution cannot be obtained and self-sustained oscillations appear due to the non-linear coupling between the flow and the nucleation process. Schnerr & Adam [3] presented a detailed discussion on the modality of these oscillations and their dependence on the nozzle geometry. There exist different types of oscillating regimes. Figure 1.3 shows the schlieren streak recording of the different oscillations modes [2,3].

<div align="center">

Mode I   *Mode II*   *Mode III*

</div>
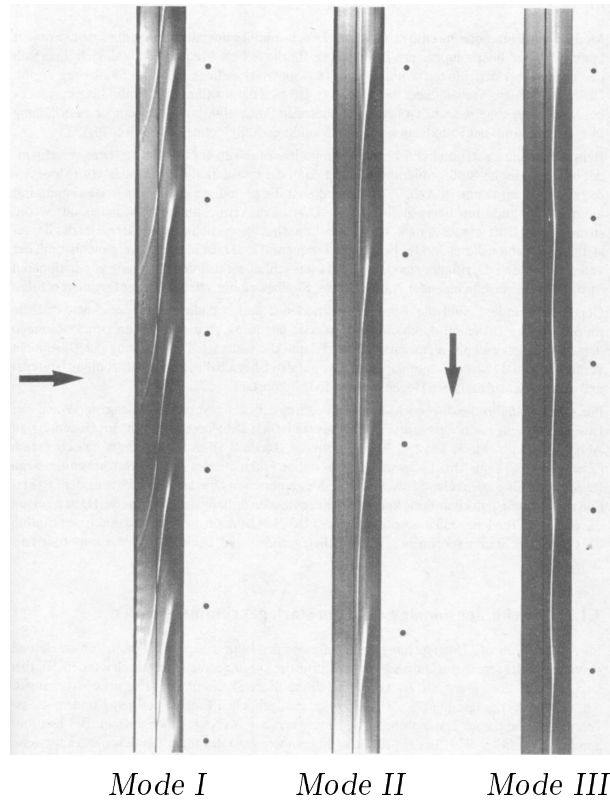
Figure 1.3: *Schlieren streak recording of the different modes of oscillation in nozzle S2. Flow direction: from left to right. Time scale: from top to bottom. Courtesy of S. Adam and G.H. Schnerr (JFM, Vol. 348, pp. 1-28, 1997).*

The thin vertical line in middle of each recording indicates the nozzle throat. Proceeding from left to right, first Mode I is depicted. This oscillation mode is characterised by upstream propagating disturbances crossing the nozzle throat. Then, Mode II is presented where the disturbances die out before reaching the throat. The last mode, denoted as Mode III, is characterised by very rapid, small-amplitude oscillations. Schnerr and Adam [2,3] also reported the first example of bifurcations in these types of flows with the occurrence of asymmetric flow regimes. An example of the flow structure is shown in Fig. 1.4.
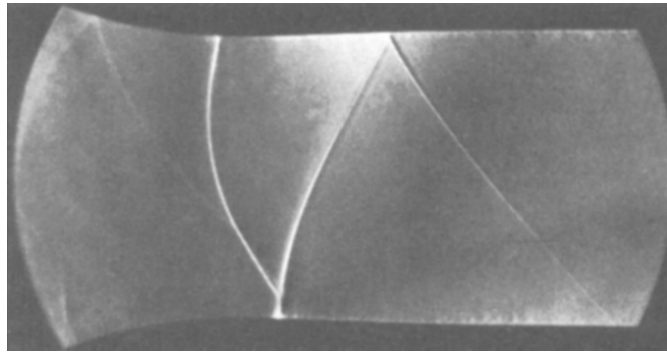
Figure 1.4: *Example of a schlieren recording of an asymmetric periodic oscillating flow. Nozzle: A1. Flow direction: from left to right. Courtesy of G.H. Schnerr & S. Adam (S. Adam, PhD thesis, Universität Karlsruhe, 1996).*

The occurrence of these self-sustained oscillations (either symmetric or asymmetric) has a strong impact on the droplet formation and size. On a time-averaged basis, the condensation zone is spread over a much greater distance in the flow direction than a simple steady-flow analysis would indicate. Further, the predicted droplet size spectra vary in time, ranging from an almost monodispersed distribution with larger mean diameters to broad distributions with much smaller mean diameters. Unfortunately to date, an experimental confirmation of this trend has not been provided yet. In fact, progress in the experimental determination of droplet spectra via optical techniques has been scarce and much less satisfactory, mostly due to the difficulties of both resolving the details of the spectrum and inverting optical transmission data. Furthermore, most of the efforts concentrated on the experimental study of wet-steam in nozzle flows or steam turbines due to the importance of these types of flows for technological applications. Despite the noteworthy progress, there is still the inability of any theory to provide a truly satisfying physical explanation of the observed facts. In particular, the effect of unsteadiness on nucleation and droplet growth is not fully understood, and reliable unsteady droplet size measurements are not yet available to corroborate the theoretical models. This work aims to contribute to a better understanding of these complicated phenomena.

1.3 Literature overview

An extensive body of literature exists on the modelling of non-equilibrium flows with condensation, especially with reference to wet-steam condensation. Although it is very difficult to draw a line (due to the many common features), this section focuses mainly on the directly relevant investigations for this thesis: namely, previous works on homogeneous condensation in water vapour/carrier gas mixtures. The literature overview with respect to the employed experimental techniques is deferred to chapters 4 and 5.

Early investigators of air flow in supersonic wind tunnels were surprised by the observation of two shock-like disturbances in the flow. The first visualisation of such disturbances

was presented at the Volta Congress in Roma, in 1935, by Prandtl [148] and is reproduced below in Fig. 1.5. In the ensuing discussion, Wieselberger suggested that a possible cause could be attributed to the presence of water vapour in the air flow.
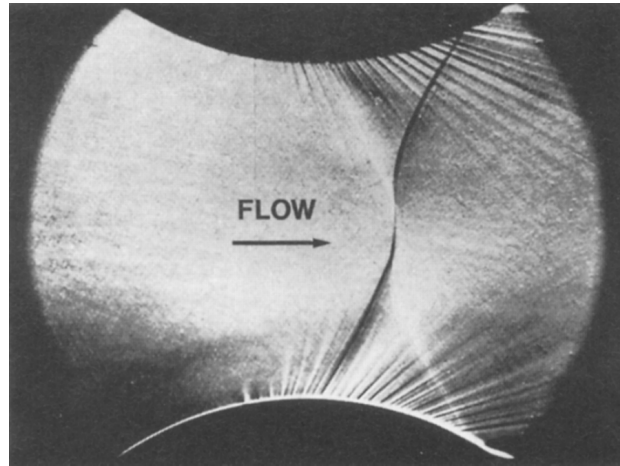
Figure 1.5: *Schlieren photograph of an X-shock, presented by Prandtl at the Volta congress [148], in Roma.*

Hermann [56] investigated systematically this phenomenon and demonstrated that these disturbances were indeed caused by condensation of water vapour in air. A unified kinetic and thermodynamic analysis of moist air and steam condensation was proposed by Oswatitsch [94–96] in 1942. He was the first to suggest that the modelling of nonequilibrium condensation should be separated in two distinct processes, namely homogeneous nucleation and droplet growth. Oswatitsch [95], Head [52], Lukaiewicz and Royle [78], and Wegener [155] performed early experiments aimed to establish empirical correlations between supply relative humidity, nozzle geometry and size, and onset of condensation. Important contributions to an understanding and analysis of condensation phenomena were also provided by Daum and Gyarmathy [24], Willmarth and Nagamatsu [161], and Wegener and Mack [156]. In 1966, Hill [58] re-examined the existing data on condensation of steam and moist air in supersonic nozzles and compared them with the prediction based on nucleation and droplet growth theory. The theoretical predictions were obtained with a 1-D numerical code for steady flows. Hill was among the first to stress the importance of an adequate droplet growth calculation, before theory and experiment can be compared. In more recent years, Schnerr [116, 118] visualised by means of schlieren techniques complex two-dimensional structures, for steady flows, in strongly curved nozzles due to the non-linear interactions of pressure waves and nucleation fronts.

The phenomenon of self-sustained oscillations in slender nozzle flows was first discovered and visualised by Schmidt [113]. Barschdorff [7] obtained, both for moist air and pure steam, the first quantitative results for the frequency of oscillations and established how the latter depends on the supply relative humidity. Zierep and Lin [166] derived the first similarity law for the dimensionless frequency as a function of nozzle throat height,

expansion rates, and supply conditions. Further quantitative data for pure steam nozzle flows were provided by Barschdorff and Filippov [8] and by Deych *et al.* [32], who were amongst the first to measure droplet sizes in pure steam nozzle flows. The first droplet size measurements in nozzle flows of moist air were proposed by Conrad [23] in 1977. Wegener and Cagliostro [157] and Matsuo *et al.* [82, 83] conducted further experiments using either supersonic wind tunnels or a Ludwieg tube, for mixtures of water vapour and carrier gas. Here, very high frequencies were reached ($\approx 6\,KHz$) due to the fact that, in the Ludwieg tube facility, supersaturated stagnation conditions could be easily reached. The influence on the variation of inert gas concentration was experimentally investigated by Wegener and Mosnier [158], using water vapour either in helium or in argon. Early investigations of homogeneous condensation of moist air in a Prandlt-Meyer expansion flow were performed by Smith [129] for steady flow regimes. The occurrence of self-sustained oscillations, in supersonic expansion flows around sharp corners, was first visualised by Frank [37, 38].

A study of theoretical solutions for steady nozzle flows with heat addition was presented by Zierep [167]. Sichel [126] studied analytically unsteady nozzle flows with heat addition. Barschdorff and Filippov [8] provided, under the assumption of one-dimensional unsteady flow with condensation, a semianalytical solution and derived a simplified formula for the frequency of the oscillations. Blythe and Shih [11] introduced the use of asymptotic methods for the description of the condensation shock structure in nozzle flows. Further studies on the detailed structure of the condensation zones, for both subcritical and supercritical flows, have been conducted by Delale *et al.* [28–30], using the asymptotic prediction method proposed by Blythe and Shih. More recently, Delale *et al.* [31] investigated the stability limit of stationary shock waves where bifurcations to unsteady periodic flow occur.

The first numerical calculations of unsteady two-phase nozzle flows with non-equilibrium condensation of pure steam were obtained, with a 1-D code, by Saltanov and Thalenko [110]. They were also able to capture the characteristics of the two oscillations modes (I and II). Skillings and Jackson [127] adopted a Lagrangian framework and tracked the evolution of 25 different droplet classes, in their 1-D code for pure steam. Numerical simulations of the two different oscillation modes were also provided by Guha and Young [46]. Collignan [22] first determined, numerically, the frequency minimum in wet steam nozzle flow with a 1-D Euler code.

The first 2-D calculations of wet steam flow were presented by White and Young [159]. They clarified the effects of the periodic quenching of the nucleation rate on the droplet size distribution and predicted the instantaneous formation of a bimodal distribution within the oscillation period. A 2-D Euler solver has also been developed by Walpot *et al.* [84, 150] by blending together modelling elements from Hill [58], Young [162], and Schnerr and Dohrmann [117]. Mundinger [91] developed a 2-D numerical scheme of high accuracy for the calculation of unsteady flows of water vapour/carrier gas mixtures. Utilising this code, Schnerr and Mundinger [119] and Schnerr *et al.* [121] performed a systematic investigation of the frequency dependence on the stagnation conditions and nozzle geometry. Here, for slender nozzles and in agreement with the experiments of Adam [2], three modes of oscillations were determined and a sharp frequency minimum determined. Furthermore, they proved that strongly two-dimensional flow fields have a stabilising effect on the flow. More

recently, Adam [2] and Adam and Schnerr [3] discovered a new instability phenomenon in homogeneously condensing flows which has been also experimentally confirmed. Here, in a perfectly symmetric nozzle, a systems of upstream propagating oblique shocks suddenly develops, with strong effects on the frequency and droplet size distribution. The influence of possible heterogeneous effects in nozzle flows of water vapour/carrier gas mixtures has been numerically investigated by Heiler [54, 55]. He concluded that, with increasing number of foreign particles, the frequency of oscillation decreases till the flow stabilises due to subsonic heat addition.

1.4   Thesis overview

The aim of this thesis is to provide an experimental database which is subsequently used to validate several condensation models. Due to the fact that a complete model check can only be done when both droplet sizes and frequency data (or pressure distributions) are available, special emphasis is given to the accurate experimental determination of droplet sizes, frequencies, and density fields The structure of this thesis is, therefore, a modular one. Chapter 3, 4, and 5 concentrate on the experimental methods and techniques, whereas in chapters 2 and 6 several condensation models are discussed and validated.

Specifically, chapter 2 focuses on the modelling of homogenous nucleation and droplet growth processes. Efforts are made to highlight the key features and critical aspects in the modelling process. Particularly, the extrapolation of surface tension data to low temperatures is analysed in light of equilibrium thermodynamics. Surface tension plays, in fact, an essential role in the performance of nucleation models, especially for nozzle flows nucleating at very high subcoolings.

Chapter 3 concentrates on the practical and operational aspects of the experimental equipments. Here, detailed specifications on the various set-ups can be found. Chapter 4 discusses some important features of holographic imaging, which are of particular relevance for interferometric study of transparent media. It is shown that the quality of the interferograms depends mostly on the properties and quality of the adopted hologram type.

Chapter 5 contains a review on methods for the measurement of droplet sizes. Emphasis is given on the accuracy of the measurements with respect to noise level, number of signals recorded, scattering effects, and distance from the regime of Rayleigh scattering. Particularly, the validity of the single scattering assumption is verified by means of a Monte Carlo numerical simulation. The results are, then, compared with the theoretical predictions from single scattering theory. This comparison shows clearly that, despite the high droplet number densities, the measurements are not jeopardised by multi-scattering effects.

Chapter 6 compares different condensation models on the basis of a large selection of experimental results for water vapour/carrier gas mixtures. Starting from the droplet size measurements, which allow a thorough validation of the condensation models, an optimised model is derived which best correlates all experimental data. Chapter 7 contains the conclusions of the present investigation.

Chapter 2

Physical model and computational method

2.1 Introduction

In section 1.2, the qualitative effects of nonequilibrium condensation in transonic nozzle flows have been illustrated. Macroscopically, they result in two major products, namely the release of latent heat to the flow and the spontaneous generation of a liquid droplet cloud, whose properties strongly depend on the coupling between the flow and the condensation process itself. In addition, it is also pointed out that the modelling of nonequilibrium condensation can be separated in two distinct processes, namely: homogeneous nucleation and droplet growth. Homogeneous nucleation refers to the spontaneous formation, within the vapour phase, of stable clusters by the kinetic process of evaporation and impingement of molecules; droplet growth refers to the process in which stable droplets increase in size by gaining more and more molecules.

In this chapter, the modelling of condensing flows is discussed in more detail, in the hypothesis of a gaseous mixture of condensable vapour (water vapour) and an inert gas (nitrogen and/or air). The topic is tackled in a very broad manner, ranging from thermodynamic to numerical issues. An extensive body of literature already exists on this subject [3, 48, 49, 54, 58, 162, 165], and these works are referred to as much as possible. Despite the noteworthy progress, there are still a few open questions regarding the modelling of liquid droplet condensation in presence of an inert gas. It is, thus, on these unresolved issues that the present analysis is mainly focused. One of the major difficulties is the correct prediction of the nucleation rate J as function of the thermodynamic state at very large supercoolings, i.e. for temperatures in the range of $[220 \div 235\ K]$. At these low temperatures, in fact, significant uncertainty exists with regard to the surface tension of subcooled liquid water. This uncertainty makes the assessment of nucleation models extremely critical, since it strongly depends on the extrapolation of surface tension data to low temperatures. This is discussed in subsection 2.3.2, where a new fit for the surface tension is introduced on the basis of experimental results and thermodynamic considera-

tions. A second relevant issue concerns the modelling of the droplet growth process in the presence of an inert gas. For practical and computational purposes, it is often assumed that the condition of thermal equilibrium between the droplet and the vapour is approximately maintained throughout the growth process. In other words, the droplet and gas temperature are considered equal $T_d = T_g$. This assumption relies on the surmise that, due to the high concentration of inert gas molecules, the droplet is promptly and effectively cooled down. In sections 2.4.1.1 and 2.4.2, it is shown that this supposition is incorrect and that significant errors are introduced in the evaluation of the droplet growth rate. By comparing different formulations of the growth law, the appropriate driving potentials are identified and the importance of accounting correctly for the energy flux between the droplet and its environment is ascertained. Further, it is shown that the temperature difference has a strong influence on the condensation process, particularly in the initial stage of droplet growth, where the quenching of the nucleation rate occurs.

This chapter consists of two distinct parts. The first part describes the physical modelling of the two-phase vapour-liquid mixture. In particular, section 2.2 summarises the thermo-fluid-dynamic model, while sections 2.3 and 2.4 illustrate various condensation models and discuss their underlying assumptions. The second part of this chapter describes concisely the numerical method. For a more detailed description, the reader is referred to Prast [104].

2.2   Thermodynamic properties and conservation laws

Consider a mixture of a carrier inert gas (nitrogen and/or air) and a condensable vapour (water vapour), both initially in the gaseous phase. Objective of this section is to characterise the thermo-fluid-dynamic state of this mixture, while it expands from a dry to a wet state. The issue is not trivial since, unless the condition of local thermodynamic equilibrium is satisfied, it is theoretically impossible to describe the state of the mixture by means of simple thermodynamic relations, such as equation of state, internal specific energy e, specific heats, speed of sound, etc. It should be recalled, in fact, from Callen [18], that these properties are defined and have physical meaning only if the condition of local thermodynamic equilibrium is satisfied everywhere in the flow field.

The general behaviour of non-equilibrium condensing flows was examined by Marble [79] (1969) from the viewpoint of relaxation gas dynamics and later (1982) revised and extended to more general conditions by Young and Guha [163]. Summarising the most relevant issues, the approach of the above mentioned authors is closely followed. First, it is observed that, until the moment homogeneous nucleation sets in, the flowing mixture is in a state of *metastable* thermodynamic equilibrium. Thus, the standard thermo-fluid-dynamic relations can be applied to each of the gas components. Upon the occurrence of homogeneous nucleation, the system changes to a liquid-vapour mixture consisting of a large number of droplets, which are assumed for simplicity to be spherical, immersed in a homogeneous gaseous background. Since the total mixture is not in thermodynamic equilibrium (i.e. the droplet growth process is active), there will be in general an interface exchange of mass,

momentum, and energy. Each of these processes is characterised by its own relaxation time τ_i and the physical understanding of the complex flow field rests largely on the role played by these relaxation times.

This problem was studied in detail by Young and Guha [163] for the flow of a wet vapour. However, the analysis is valid and can be reformulated to include also an inert diluter. Young and Guha identified essentially three different relaxation processes: thermal equilibrium of the droplets, interface velocity slip, and thermal equilibrium of the whole medium. Each of them is associated to one of the above mentioned internal rate processes. Their analysis led to the following: the relaxation process for the droplet thermal equilibrium is the fastest one, which implies that the droplet temperature approaches relatively fast its equilibrium value T_s[1]. If the droplets are small ($r_d \ll 10^{-6}$ m), then also the interface momentum transfer reaches fast its equilibrium state, and there is no velocity difference between the two phases. The third relaxation process, i.e. where the gas phase temperature relaxes to its equilibrium value, develops relatively slowly and can, therefore, be considered as *frozen*. In other words, due to the high cooling rates, typically being $(-dT/dt)$ of the order of 0.3 $K/\mu s$, the variations driven by the flow field are faster than the thermal variations due to condensation. Thus, the mechanics and thermodynamics of the gas and liquid phase are uncoupled and the gas phase flow behaves like that of a simple single phase gas.

Based on the foregoing discussion, the fluid dynamic behaviour of the two-phase mixture can be described by the system of conservation laws, corresponding to the conservation of the total mass, momentum, and energy, combined with the equation of state for the mixture gas phase, plus an additional equation describing the formation of the condensate mass. For completeness, the most relevant relations are summarised below.

The total mass of mixture M, present in a control volume, is given by

$$M = M_a + M_v + M_l, \tag{2.1}$$

where the subscripts a, v, l indicate the inert carrier gas, the vapour, and the liquid phase, respectively. The liquid mass fraction g is simply

$$g = \frac{M_l}{M} = \frac{M_l}{M_a + M_v + M_l}; \tag{2.2}$$

and the maximum condensate mass is

$$g_{max} = \frac{M_{v0}}{M}, \tag{2.3}$$

where the subscript (0) refers to the stagnation conditions. For small wetness fractions ($g \leq 0.1$), the volume occupied by the liquid phase can be neglected, since it is of 4 to 5 orders of magnitude smaller than the volume occupied by the gas phase. Under this assumption, the density of the mixture is equal to:

$$\varrho = \frac{\varrho_a + \varrho_v}{1 - g}, \tag{2.4}$$

---

[1]where the notation T_s stands for saturation temperature.

where ϱ_a and ϱ_v are the density of the carrier and vapour components, which can be expressed as

$$
\begin{align}
\varrho_a &= (1 - g_{max})\, \varrho, \tag{2.5}\\
\varrho_v &= (g_{max} - g)\, \varrho. \tag{2.6}
\end{align}
$$

The isochoric and isobaric specific heats c_{v0} and c_{p0}, and the specific gas constant R_0 of the mixture, calculated with respect to the reservoir conditions, are defined as:

$$
\begin{align}
c_{v0} &= (1 - g_{max})\, c_{va} + g_{max}\, c_{vv}, \tag{2.7}\\
c_{p0} &= (1 - g_{max})\, c_{pa} + g_{max}\, c_{pv}, \tag{2.8}\\
R_0 &= (1 - g_{max})R_a + g_{max}R_v. \tag{2.9}
\end{align}
$$

The static pressure of the mixture, under the hypothesis of an incompressible liquid phase, is simply the sum of the partial pressure of the gas components:

$$
p = p_a + p_v. \tag{2.10}
$$

Under the hypothesis of perfect gases, which is a reasonable assumption for the vapour and inert gas pressures considered in this thesis, it results:

$$
\begin{align}
p_a &= \varrho_a\, R_a\, T, \tag{2.11}\\
p_v &= \varrho_v\, R_v\, T. \tag{2.12}
\end{align}
$$

Thus, the equation of state for the whole mixture becomes:

$$
\begin{align}
p &= \varrho\, T \left[(1 - g_{max})R_a + (g_{max} - g)R_v \right], \\
&= \varrho\, T (R_0 - g R_v). \tag{2.13}
\end{align}
$$

The specific internal energy and enthalpy of the mixture can be expressed as:

$$
\begin{align}
e &= (1 - g_{max})e_a + (g_{max} - g)e_v + g e_l, \\
&= c_{v0}\, T + g\, (R_v T - L); \tag{2.14}\\
h &= (1 - g_{max})h_a + (g_{max} - g)h_v + g h_l, \\
&= c_{p0}\, T - gL; \tag{2.15}
\end{align}
$$

where L denotes the latent heat of condensation. Its expression in terms of the temperature T, together with all gas physical properties, is provided in Appendix A.

The condition $T_d = T_s$ automatically yields for the droplet temperature the equality $p_d = p_{sr}(T_d, r_d)$, since at equilibrium these two are related by the Clausius-Clapeyron equation. The notation p_{sr} represents the phase equilibrium pressure at a curved liquid-vapour interface:

$$
p_{sr}(T_d, r_d) = p_{s\infty} \exp Ke(T_d, r_d), \tag{2.16}
$$

where the subscript "∞" refers to a phase equilibrium at a flat interface and the Kelvin factor Ke is defined as

$$Ke(T_d, r_d) = \frac{2\sigma}{\varrho_l \, R_v \, T_d \, r_d}. \tag{2.17}$$

The relevant speed of sound for the non-equilibrium condensing mixture is, on the basis of our introductory discussion, the thermally frozen speed of sound, calculated at constant entropy s and condensate mass g. In other words, this is the propagation speed of a sound wave in a medium where a) the droplets and the vapour move together without slip, b) the droplets are locally in thermal equilibrium ($T_d = T_s$), and c) the droplet and vapour temperatures are uncoupled $T_d \neq T$, as are their pressures $p_v \neq p_{sr}$. Following Mundinger [91], this results into:

$$a_f^2 = \left(\frac{\partial p}{\partial \varrho} \right)_{s,g} = \left(\frac{\partial p}{\partial \varrho} \right)_{e,g} + \frac{p}{\varrho^2} \left(\frac{\partial p}{\partial e} \right)_{\varrho,g}. \tag{2.18}$$

The droplet temperature T_d is calculated explicitly by means of an energy balance at the droplet surface, as shown in section 2.4.1.

To conclude this section, the whole set of equations is reported hereafter. Because of its importance, it is stressed again that this single phase formulation holds only if the condition of mechanical equilibrium (i.e. no slip between droplets and gas/vapour) is identically satisfied throughout the flow field. Further, assuming the flow to be inviscid and thermally non-conducting, for each control volume the system of equations in conservative form reduces to the balance equations for mass, momentum and energy supplemented with an equation for the rate of change of the liquid mass fraction:

Conservation of mass:

$$\frac{\partial \varrho}{\partial t} + \frac{\partial (\varrho u)}{\partial x} + \frac{\partial (\varrho v)}{\partial y} = 0, \tag{2.19}$$

Momentum balance:

$$\frac{\partial (\varrho u)}{\partial t} + \frac{\partial (\varrho u^2 + p)}{\partial x} + \frac{\partial (\varrho u v)}{\partial y} = 0, \tag{2.20}$$

$$\frac{\partial (\varrho v)}{\partial t} + \frac{\partial (\varrho v u)}{\partial x} + \frac{\partial (\varrho v^2 + p)}{\partial y} = 0, \tag{2.21}$$

Conservation of energy:

$$\frac{\partial (\varrho E)}{\partial t} + \frac{\partial ((\varrho E + p)u)}{\partial x} + \frac{\partial ((\varrho E + p)v)}{\partial y} = 0, \tag{2.22}$$

Condensate mass formation:

$$\frac{Dg}{Dt} = \left[\frac{4\pi}{3} \, \varrho_l \, r^{*3}(t) \cdot \frac{J(t)}{\varrho(t)} + \int_{-\infty}^{t} 4\pi \, \varrho_l \, \frac{J(\tau)}{\varrho(\tau)} \, \frac{\partial r(t,\tau)}{\partial t} \, r^2(t,\tau) \, d\tau \right], \tag{2.23}$$

where u and v are the cartesian velocity components in the x- and y- direction, respectively, and E is the total energy ($E = e + 1/2[u^2 + v^2]$). The symbolism Dg/Dt denotes the

"substantial derivative" of g and represents the change of condensate mass in a Lagrangian frame of reference:

$$\frac{Dg}{Dt} = \frac{\partial g}{\partial t} + \underline{V} \cdot \nabla g. \tag{2.24}$$

Equation (2.23) expresses the variation of condensate mass along a pathline as the sum of two terms. The first term represents changes in g due to the production, by homogeneous nucleation, of new droplets; the second term represents the growth of droplets, born at the time τ. Equation (2.23) is a complicated integro-differential equation. There exists several different ways to integrate this equation [54, 58, 159], one of these is briefly discussed in Appendix C. The system of equations is formally closed once a specific relation is provided for the nucleation rate process J and for the droplet growth rate dr/dt as a function of the thermo-fluid-dynamic state. In the subsequent sections, several nucleation and droplet growth models are reviewed, especially with regard to the still existing uncertainties in the models.

2.3   Homogeneous nucleation

Homogeneous nucleation involves the formation of metastable clusters from a population of vapour molecules in a supersaturated state, which are big enough to act as condensation nuclei. The notion of "sufficiently big" is specified more precisely later in this section. During this process, embryos of all sizes are continuously agglomerating and evaporating, due to molecular fluctuations within the vapour phase. It should be noted that the formation of molecular clusters is not an exclusive prerogative of a supersaturated vapour. However, the probability that they may lead to irreversible droplet growth is directly related to the occurrence of a supersaturated vapour state. As a first step, thus, the notion of supersaturation has to be established. The latter can be defined as follow:

$$S = \frac{p_v}{p_{s\infty}(T)}, \tag{2.25}$$

where $p_{s,\infty}(T)$ is the saturation vapour pressure of a vapour in equilibrium with a flat liquid surface, at the temperature T. Obviously, in saturated equilibrium it holds $p_v = p_s(T)$ and $S = 1$. Thus, the notion of supersaturation is directly connected to that of thermodynamic non-equilibrium. Once supersaturated, the system searches its way back to equilibrium by condensing either onto an eventually available surface (such as liquid bulk surface, foreign particles or wettable walls) or by spontaneously forming clusters in the gas phase, that are large enough to act as condensation nuclei. With regard to nozzle flow applications, Heiler [54, 55] proved that heterogeneous effects can be neglected due to the comparatively low concentrations of foreign particles present in laboratory experiments, such as those performed in our department. Therefore, this section concentrates solely on the process of *homogeneous nucleation*.

The free energy of formation of a cluster containing n molecules can be expressed, on thermodynamics grounds [75, 85], as the sum of two terms:

$$\Delta G_n = -n \, k_B \, T \, \ln S + \sigma \, a_0 \, n^{2/3}, \tag{2.26}$$

where k_B is the Boltzmann constant, σ is the surface tension of liquid water, and a_0 is a molecular surface area, defined as $a_0 = (36\pi)^{1/3}(v_l)^{2/3}$, v_l is the liquid molecular volume. The first term represents the decrease in free-energy due to the formation of the liquid bulk phase, the second term, instead, represents the increase in free-energy due to the formation of the interface between the two phases. If $S < 1$, then ΔG_n increases monotonically with n and, thus, the probability of phase transition tends to zero; if, instead, $S > 1$ there exists always a critical value of n^* such that it becomes energetically favourable to initiate the phase transition. The critical value n^*, or equivalently the critical radius r^*, can be found by setting the derivative of Eq. (2.26) with respect to r equal to zero, leading to

$$r^* = \frac{2\sigma(T)}{\varrho_l \, R_v \, T \, \ln(S)}.$$

(2.27)

This critical cluster of radius r^* is in metastable equilibrium with its vapour. It should be noted that increasing the degree of supersaturation results in decreasing both the activation barrier ΔG_n and the critical embryo size r^*. In other words, by increasing S, the probability that a certain cluster exceeds fortuitously the critical sizes increases. At this point, homogeneous nucleation effectively starts, and phase transition can finally begin.

It is not the purpose of this thesis to review the status of nucleation theory. Excellent reviews on the state-of-art for nucleation research and its derivation can be found in [1, 75, 76, 97]. Suffice here to say that basically all nucleation theories assume the nucleation rate J - that is the rate of formation of metastable clusters per unit time and volume - to be proportional to the *equilibrium* number density of critical embryos. That is

$$J = K \exp(\Delta G_{n^*}/k_B \, T).$$

(2.28)

The explicit form for the factors K and ΔG_{n^*} depends on the specific models adopted for the kinetic process of clusters agglomeration and for the free-energy, respectively. It should be stressed that in this formulation of the nucleation rate, thermodynamic equilibrium parameters are used to characterise a non-equilibrium process (essentially because of a lack of a better alternative). In light of this remark, huge discrepancies have to be expected between theoretical predictions and experimentally measured nucleation rates, in particular for nucleation models that strongly rely on the capillarity approximation. In the next section, two of these models are briefly reviewed.

2.3.1 Classical nucleation theory

By blending together elementary thermodynamics and kinetics considerations, a closed expression for the nucleation J can be derived, expressing the latter as a function of the thermodynamic state of the nucleating vapour. The resulting formula represents the *Classical Nucleation Theory* (CNT), which has been, aside from slightly different variants, widely applied to the study of transonic condensing flows. In this section, two different variants are considered, namely the above mentioned (CNT) model and the *Internally*

Consistent Classical Theory (ICCT) version. Their formulation is reported below:

$$J_{CNT} = \frac{\rho_v^2}{\rho_l}\sqrt{\frac{2\sigma}{\pi m^3}} \exp\left[-\frac{4}{27}\frac{\Theta^3}{(\ln S)^2}\right];\qquad(2.29)$$

$$J_{ICCT} = \frac{1}{S}\,J_{CNT}\,\exp\Theta;\qquad\Theta = \frac{\sigma a_0}{k_B T};\qquad(2.30)$$

where m is the mass of a vapour molecule, and Θ is a dimensionless surface tension, measuring the relative importance of surface to thermal energy. The two models, thus, differ essentially from each other for the presence of the factor $1/S$, which is somehow connected to the detail of the applied cluster model, and for the presence of the exponential factor $\exp\Theta$. The latter is directly connected to issues of self-consistency in modelling the formation energy ΔG_n [75]. On this issue, no general agreement can be found in the literature. Therefore, the comparison between experimental and theoretical values is employed as a pragmatic base for preferring one model to the other. Following this approach, Luijten [75] suggested, on the basis of wave tube experiments, that for water-nitrogen systems the best agreement is found using the (ICCT) formulation. In Luijten's work [77, 98], "best agreement" means that the ICCT theory overestimates the actual nucleation rate by two orders of magnitude, as opposed to the CNT theory which underestimates it by 3-4 orders of magnitude.

Unfortunately, the extrapolation of Luijten's results to homogeneously nucleating nozzle flows is not straightforward, essentially for three reasons. First, Luijten's conclusions are derived for a vapour nucleating in a range of temperatures and supersaturations different from those encountered in condensing nozzle flows. Second, the performance of a certain nucleation model depends strongly on the substance and temperature range at which nucleation actually takes place. Enlightening is in this respect the article of Girshick and Chiu [43]. Third, the ambiguities on the surface tension of subcooled water - typically at temperatures of the order of 230 K - make the assessment of the quality of nucleation models highly questionable. In section 2.3.2, the approach employed in this work to overcome these uncertainties is briefly illustrated. A detailed description can be found in chapter 6.

On the basis of these considerations, there is no sound justification for preferring the ICCT to the CNT model, in the sense that both theories require a correction. Given the uncertainties, it seems a good course of action to simply introduce an empirical factor ξ in the nucleation expression; while it is relatively irrelevant if this correction is applied to the ICCT or to the CNT model. The experimental validation of nucleation theory will then indicate the correct value for the parameter ξ. In the forthcoming sections, the ICCT model is retained. The CNT model is maintained only for reference. In chapter 6, in fact, our theoretical predictions are compared with those of other condensation models, based on the CNT formulation. Here, one of the results is anticipated: the validation of nucleation theory, in the range $(218 < T < 275\,K)$ and $(3 < S < 50)$, confirmed Luijten's findings $J_{ICCT}/J_{exp} = 10^2$. Summarising, thus, the implemented nucleation rate is $J_{ICCT}^{\xi} = \xi\,J_{ICCT}$, where $\xi = 0.01$. The expressions for the vapour pressure and surface tension are provided in Appendix A.

As concluding remarks, it should be mentioned that both nucleation models are based on macroscopic properties (i.e. capillarity approximation) and assume a cluster to be spherical and smooth, with an interface of zero thickness. Second, this value of J represents the steady-state solution. This means that the *flux* J, at which the number density of clusters varies in time, is constant and independent of cluster size. The question now is whether this formulation of the nucleation rate can still be applied to nozzle flows where the flow field may vary in time faster than the characteristic time required to reach the state-state nucleation solution. According to Abraham [1], a steady-state solution for the nucleation rate is reached within a characteristic time τ^* of $10^{-7} - 10^{-6}$ s. For the nozzles considered in this study, typical cooling rates are within a range of $[0.2 - 0.8]$ $K/\mu s$, thus, implying a temperature variation of less than 1 K in one microsecond. For a periodically oscillating flow, a typical value of the period is of the order of $\tau = O(10^{-3})$ s, which is three to four orders of magnitude higher than τ^*. In conclusion, the steady-state nucleation formulation can in good approximation be applied both to steady and unsteady condensing nozzle flows.

2.3.2 Extrapolation of surface tension data to low temperatures

In section 1.1, it is observed that nozzle experiments of condensing flows may constitute a precise tool for validating condensation models. In fact, as pointed out by Young [162]: "when both pressure measurements and droplet size data are available, the accuracy of nucleation and droplet growth theory can be tested to a certain extent independently". Unfortunately, in the case of water vapour/carrier gas mixtures, this validation process is strongly hampered by the significant uncertainty with regard to the surface tension of subcooled liquid water. This uncertainty makes the assessment of nucleation models extremely critical, since it strongly depends on the extrapolation of surface tension data to low temperatures of the order of 230 K. Despite its importance, this problem has been only marginally addressed in the literature. Typically, most authors dealing with nucleation studies have bypassed the issue and simply adopted a linear fit to extrapolate the surface data to even lower temperatures. This approach is, in fact, undertaken by Luijten [75] for his high pressure nucleation study, and maintained by Prast [104] for his simulations of condensing nozzle flows. The fit is based on the experimental data of Hacker [50], who managed, by means of a simple and reliable method, to achieve the largest subcoolings so far reported in literature. His data go down to roughly 250 K and are plotted in Fig. 2.1. The fit proposed by Luijten and Prast σ^{LP} is reported hereafter and shown graphically in the same figure.

Luijten - Prast surface tension fit

$$\sigma^{LP}(T) = 0.127245 - 1.89845 \cdot 10^{-4} T \quad [N/m]; \qquad \text{for} \quad T < 268.0 \ K \tag{2.31}$$

Since for some of the experiments considered in chapter 6, nucleation occurs at temperatures well above 265 K, a different correlation is chosen by the present author, which is

presented later in this section. A second surface tension fit, which has been extensively applied to condensing flows, was proposed by Schnerr and Dohrmann [117]. The Schnerr and Dohrmann fit is also included in Fig. 2.1.

Schnerr - Dohrmann surface tension fit

$$\sigma^{SD}(T) = \begin{cases} (76.1 + 0.155 \cdot (273.15 - T)) \cdot 10^{-3} & [N/m] \\ \quad \text{for} \quad T \geq 249.39K \\ ((1.1313 - 3.7091 \cdot 10^{-3}\,T)\,T^4 \cdot 10^{-4} - 5.6464) \cdot 10^{-6} & [N/m] \\ \quad \text{for} \quad T < 249.39K \end{cases} \tag{2.32}$$

The first branch of this curve $(T > 249.39\,K)$ follows Pruppacher and Klett [105]; the second branch represents the authors' extrapolation of surface tension data to lower temperatures. As it can be inferred immediately from Fig. 2.1, considerable differences appear only in the extrapolated range. Schnerr and Dohrmann [117] argue that their extrapolation is in agreement with the experimental results of Peters and Paikert [100]. However, in this article the surface tension is not directly measured, but derived under the assumption that the CNT theory is correct[2].
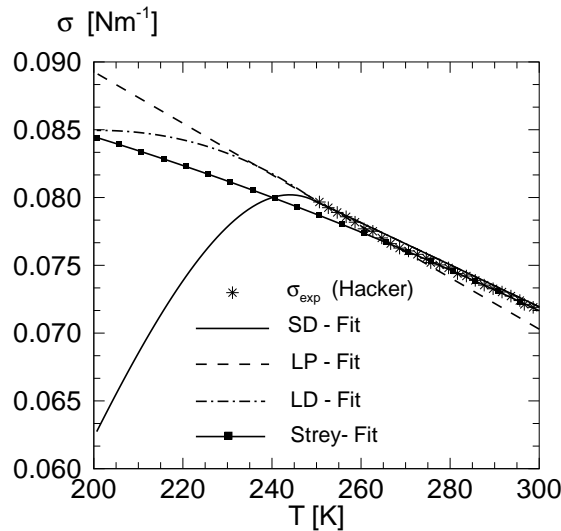
Figure 2.1: *Surface tension σ of liquid water and its extrapolation to low temperatures according to various authors.*

In the present section a new fit is presented, which is also shown in Fig. 2.1. For $T > 250\,K$, the LD-fit follows Pruppacher and Klett. In this range of temperatures, Hacker's

---

[2]Schnerr [122] correctly points out that the agreement between experiment and numerical simulation, based on the CNT (or ICCT) model, cannot lead to conclusions about the thermodynamic state of small clusters, because of the simplifications in the classical theory in describing the homogeneous nucleation process. In particular, when the clusters are very small, it is to be expected that the surface energy of these clusters will be strongly size dependent, so that the capillarity approximation will not hold.

and Pruppacher's data do not differ appreciably. However, the Pruppacher and Klett formula provides slightly better results for the frequency dependence with supersaturation and therefore their fit has been preferred. It should be noted that, for $T \approx 248\,K$, Hacker's and Pruppacher's data coincide both in value and slope. Thus, Hacker's experimentally determined trend is assumed as base to start the surface tension data extrapolation.

New surface tension fit: LD fit

$$\sigma^{LD}(T) = \begin{cases} 8.52000 \cdot 10^{-2} - 3.54236 \cdot 10^{-4}\,T + 3.50835 \cdot 10^{-6}\,T^2 \\ -8.71691 \cdot 10^{-9}\,T^3 \quad [N/m] \quad \text{for} \quad T < 250.0\,K \\ (76.1 + 0.155 \cdot (273.15 - T)) \cdot 10^{-3} \quad [N/m] \\ \quad \text{for} \quad T \geq 250.0\,K \end{cases} \qquad (2.33)$$

In deriving this extrapolation, a different approach is adopted, based on thermodynamic and experimental considerations. Experimentally, the available and well-documented published data on vapour/carrier gas condensation have been collected and compared with the theoretical predictions. In order to avoid the simple "fitting" of theory to experiments, a well-defined strategy has been undertaken in this work. First, the quality of nucleation and droplet growth theory has been assessed separately, in a range of temperatures where no arbitrariness exists on surface tension data ($T > 260\,K$). Then, the optimised and **validated** condensation model has been used to gain more insight on the surface tension dependence on temperature for subcooled liquid water. The details of this approach can be found in sections 6.1 and 6.6.

Thermodynamically, the issue is more complex and requires familiarity with the postulatory approach to thermodynamics conceived by Tisza and excellently developed and divulged by Callen [18]. In this section, the most important issues which led to the formulation of the thermodynamic constraint are summarised. For an understanding of its physical meaning and implications, the reader is referred to the book of Callen [18]. The analysis proceeds from the recognition that σ is, by definition, the surface tension of liquid water in *equilibrium* with its own vapour. As pointed out in section 2.3, the expression for the nucleation rate J contains solely parameters defined for the corresponding thermodynamic equilibrium state. This is not surprising since σ is defined, solely at equilibrium, as the superficial intensive parameter associated with the presence of an interface between the vapour and the bulk liquid phase.

Since one is referring to equilibrium parameters, all the properties and postulates of equilibrium thermodynamics must hold, in particular, the so-called *Nernst postulate or third law of thermodynamics*. It states that the entropy of any system vanishes at zero temperature. As a consequence of this postulate, a number of the cross partial derivatives in the fundamental relations must also vanish, such as the specific heats. To illustrate the implications of the *Nernst postulate* on the surface tension, consider as thermodynamic system a vapour in equilibrium with its own liquid at a flat interface. This composite system is closed, i.e. is surrounded by walls which are restrictive with respect to the total energy, total volume and total number of molecules. The internal energy of the total system

may be written as

$$U = U^v + U^l + U^s, \tag{2.34}$$

where U^v and U^l are the internal energies of the bulk vapour and liquid phases and U^s is the contribution of the interface layer to the actual internal energy U. At equilibrium [1, 18], the fundamental relation for the Gibbs potential is $G = U + pV - TS$ and its complete differential dG is

$$dG = -S\,dT + V\,dp + \sigma\,dA + \mu\,dN, \tag{2.35}$$

where S, V, N are the total entropy, volume, and number of molecules, respectively, A is the area of the interface, and μ is the chemical potential. The condition of thermodynamic equilibrium implies that temperature T, pressure p, and chemical potential μ are uniform throughout the system. According to the Nernst postulate, the change in entropy corresponding to an isothermal stretching of the interface vanishes at zero temperature, hence

$$\left(\frac{\partial S}{\partial A}\right)_{T,p,N} \to 0 \qquad \text{as} \qquad T \to 0, \tag{2.36}$$

and, by applying the appropriate Maxwell relation, which follows directly from (2.35):

$$\left(\frac{\partial S}{\partial A}\right)_{T,p,N} = -\left(\frac{\partial \sigma}{\partial T}\right)_{A,p,N} \to 0 \qquad \text{as} \qquad T \to 0. \tag{2.37}$$

Relations such as (2.37) are valid for all intensive parameters, which can be derived from the fundamental relation. Particularly, it holds for the intensive variable σ. In conclusion, any plausible extrapolation of surface tension data to lower temperatures must satisfy this condition. Of course, Eq. (2.37) establishes only a trend for the surface tension fit, and it does not guarantee that the σ^{LD} fit reproduces correctly the dependence of surface tension with temperature. The quality of the fit has to be proven by a careful comparison with a variety of experimental data, as shown in chapter 6.

Figure 2.1 illustrates also the surface tension fit proposed more recently by Strey *et al.* [134]. Although this fit satisfies the thermodynamic constraint, it differs considerably from the experimentally determined surface tension values already for temperatures $T < 260\,K$. On the basis of this observation, the proposed fit was not taken into consideration.

Strey *et al.* surface tension fit

$$\sigma^{Strey}(T) = (93.6635 + 0.009133\,T - 0.000275\,T^2)\cdot 10^{-3} \quad [N/m]. \tag{2.38}$$

2.3.3   Nucleation: a summary

In the previous sections, two different nucleation models have been presented. In elucidating these models, the importance of surface tension fits has been extensively discussed. This section elaborates further on the difference among the various models. Basically three combinations are considered. The first one $J_{ICCT}^{\xi-LD}$ is proposed by the present author: it combines the ICCT model, corrected by a factor $\xi = 0.01$, with a new fit for surface

tension σ^{LD}. The second combination $J_{ICCT}^{\xi-LP}$ differs from the first one only for the expression of the surface tension: here the Luijten-Prast fit is employed. The third combination J_{CNT}^{SD} was proposed by Schnerr and Dohrmann [117]. It employs the CNT model and the surface tension fit proposed by the same authors. In order to get some insight on the differences between these models, their ratio has been plotted in Fig. 2.2 for three values of the supersaturation S. In Fig. 2.2(a), the J_{CNT}^{SD} and the $J_{ICCT}^{\xi-LP}$ models are compared. For
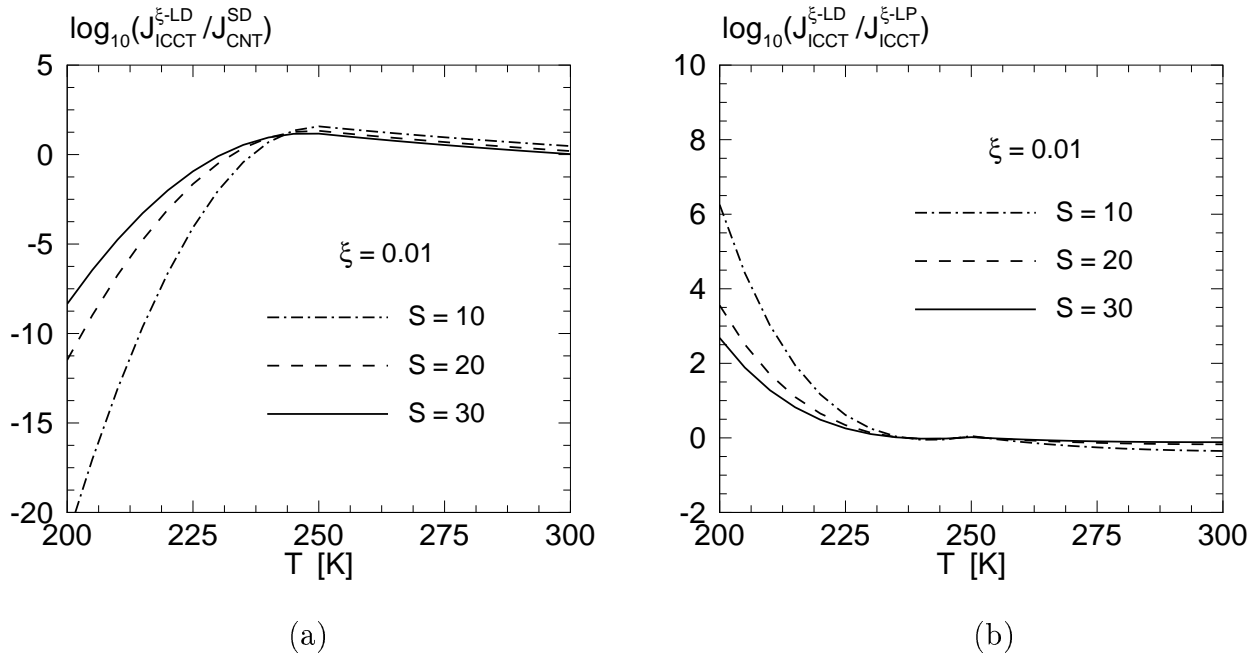
Figure 2.2: *Comparison of nucleation models: (a) $J_{ICCT}^{\xi-LD}$ over J_{CNT}^{SD}; (b) $J_{ICCT}^{\xi-LD}$ over $J_{ICCT}^{\xi-LP}$.*

temperatures $T > 240\ K$ they do not differ considerably: the $J_{ICCT}^{\xi-LD}$ values are roughly one order of magnitude higher than the J_{CNT}^{SD} ones. Nevertheless, this discrepancy may still induce significant differences in the frequency, as shown in chapter 6. For temperatures $T < 240\ K$, instead, the difference between the two models may amount to almost ten orders of magnitude depending on the supersaturation, the J_{CNT}^{SD} producing in this range the highest nucleation rates. This difference is imputable mainly to the surface tension fit. Figure 2.2(b) compares, instead, the $J_{ICCT}^{\xi-LD}$ model with the $J_{ICCT}^{\xi-LP}$ one. Here considerations similar to the previous case apply. For temperatures $T > 240\ K$, no appreciably difference is observed. For temperatures $T < 230\ K$, the $J_{ICCT}^{\xi-LP}$ values become too low and the model is not able to reproduce correctly all features of the condensation process. Figure 2.2 shows clearly that huge differences in the predicted nucleation rates appear at increasingly lower temperatures, essentially because of the different extrapolations chosen by the various authors. One of the objectives of chapter 6 is to individuate a "reasonable" extrapolation (within the experimental accuracy) by combining a critical and rigorous examination of nozzle experiments with theoretical considerations.

2.4   Droplet growth

The process of droplet growth involves the net flux of mass (vapour molecules) towards the droplet, and the simultaneous net flux of energy (latent heat) away from the droplet. The mechanism of these transfers depends to a large extent on the Knudsen number Kn. The latter is defined as the ratio of the mean free path of vapour molecules to the diameter of the droplet ($Kn = l/2r_d$), where $l = 2\mu\sqrt{RT}/p$ and μ is the dynamic viscosity of the mixture. For small Kn, the transfer is governed by diffusion; for large Kn, growth is controlled by the kinetic process of impingement of vapour molecules onto the droplet (gas-kinetic regime). Thus, a generally applicable growth model requires a set of equations valid for all Knudsen numbers. Unfortunately, an accurate solution of this problem at intermediate Kn numbers is to date not yet available. A copious literature exists, addressing this problem at various level of complexity [39, 48, 49, 58, 101, 165]. The large variety of models proposed in the literature can be classified into two main categories. One category is based on the inclusion of rarefied gas effects even when modelling the transitional or diffusion controlled growth regimes. The Langmuir model represents, in this respect, an elegant method to encompass in a single model both continuum and rarefied gas effects. In this model, the flow field around a droplet is divided into an outer zone, where the equations of continuum mechanics apply, and an inner region (Knudsen layer) where the transfer processes are kinetically controlled, as shown in Fig. 2.3.
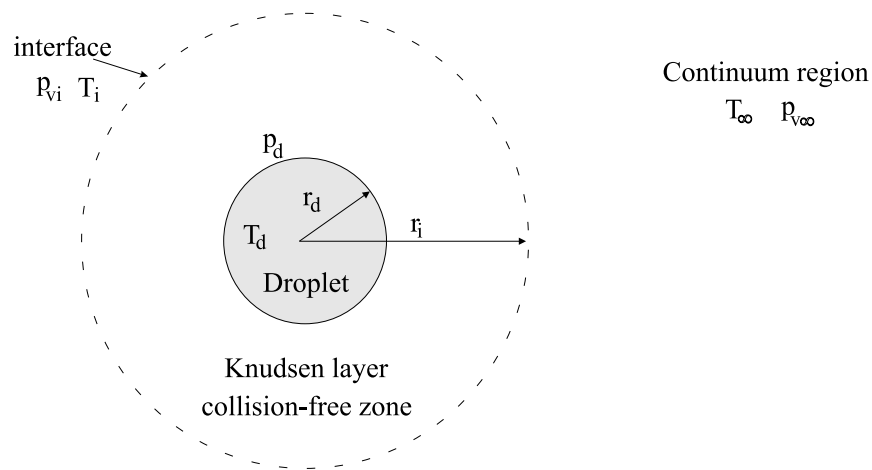
Figure 2.3: *The Langmuir model.*

The work of Young [165] represents, within this framework, the current state-of-art in dropwise condensation at arbitrary Knudsen numbers and in the presence of an inert gas. It provides clear physical insights into the growth mechanism. First, Young examines the transport processes in light of linear irreversible thermodynamics and is able to clarify all the appropriate driving potentials (thermodynamic forces) for the droplet growth process, namely the temperature ($\Delta T = T_d - T$) and vapour pressure difference ($\Delta p_v = p_{sr} - p_v$). Second, by accurately modelling the molecular velocity distributions in the Knudsen

layer, the model is able to predict many features of the kinetics of condensation which are normally only revealed by a direct solution of the Boltzmann equation. In Young's model, the energy and mass fluxes are evaluated both in the Knudsen layer and in the continuum region. Next, the flux matching occurs on a sphere of radius $r_i = r_d + \beta l$ (i.e. the interface i), where β is a constant of order unity. Thus, the description of the transition regime depends, to a certain extent, on the choice of β.

In the second approach, the droplet growth rate is calculated in the gas kinetic and/or continuum regime - where an accurate description of the process is possible - and then multiplied by a correction factor $f(Kn)$ to obtain the growth at intermediate Kn. The general form of the growth rate is, therefore, of the type:

$$\frac{dr}{dt} = f(Kn)\frac{dr}{dt}\bigg|_{ct} = f_1(Kn)\frac{dr}{dt}\bigg|_{k},\qquad(2.39)$$

where the subscripts ct and k denote the continuum and kinetic regime, respectively. There exist several methods to derive the correction factor $f(Kn)$. An exhaustive and unifying review on the subject has been presented by Fuchs and Sutugin [39]. Here, the main findings from their review are briefly summarised. Following from the general theory of transfer processes, $f(Kn)$ can be expressed as

$$f(Kn) = \frac{1}{1 + \lambda\,Kn},\qquad(2.40)$$

where different values have been proposed in literature for the parameter λ. Fuchs and Sutugin argue that a promising solution is the one proposed by Sahni [111]. Within this framework, Gyarmathy proposed a droplet growth model, hereafter denoted as gya63, and described in section 2.4.3. From a computational standpoint, the gya63 model is very attractive and has been widely applied. It is this consideration that motivated the present author to validate the gya63 model. Another way of determining the correction factor $f(Kn)$ is by conjugating the free molecular and diffusive fluxes. In this approach, first the energy and mass fluxes are calculated independently both for the continuum and kinetic regime. Then, an expression for these fluxes in the intermediate situations is simply found by means of an interpolating fit between these two limits. The interpolation fit is derived by way of a flux-matching technique similar to those used by Young. The flux-matching can occur either at an intermediate interface or at the droplet surface. Following the latter approach, Gyarmathy proposed a second growth model, indicated hereafter as gya82, and described in section 2.4.1.

For a variety of binary mixtures, Peeters *et al.* [99] compared the results of the transitional Young and gya82 models with their experimental growth trajectories. From their experiments, which have been carried out in a range of Kn numbers from 0.5 down to the continuum limit, they concluded that the gya82 model predicts a broader transition regime in terms of Knudsen number Kn and gives a good description of the droplet growth for the near free molecular regime.

In the present work, the gya82 model is used. However, this particular choice is not fundamental. For the experiments considered here, the growth process occurs always at Kn

numbers in the range $2-50$. For this range, droplet growth can be accurately described with the Hertz-Knudsen (HK) formula, subject to the condition that the appropriate driving potentials and boundary conditions are implemented. This is shown in section 2.4.2 where Young's analysis is employed to select the proper boundary values.

2.4.1   The Gyarmathy model (gya82)

The gya82 model has been extensively described in literature [49, 75], therefore a detailed derivation of the model is not presented here. Instead, this section focuses on the most important relations, which characterise the model, and discusses their underlying assumptions from the standpoint of the Langmuir model. As stated in section 2.4, the key feature of the gya82 model consists in expressing the growth rate, occurring at intermediate Kn numbers, in terms of the growth rates occurring in the two limiting cases of $Kn = 0$ and $Kn \to \infty$. Therefore, the first necessary step is to derive an expression for the mass and energy fluxes in these limiting cases.

Continuum limit

$$\dot{M}^{ct} = 4\pi r_d \left(\frac{\mathcal{D}_m}{R_v T_m} \right) (p_{sr} - p_{v\infty}),$$

$$\dot{E}^{ct} = \frac{1}{2}(T_d + T_\infty)\dot{M}^{ct}c_{pv} + 4\pi k_m r_d(T_d - T_\infty),$$

(2.41)

where the subscript "∞" refers to the far field region. The thermal conductivity k_m, the binary diffusion coefficient $\mathcal{D}_m$, and the density of the mixture ρ_m are evaluated at the intermediate temperature T_m, defined, according to Hubbard et al. [62], as

$$T_m = \frac{1}{3}(2T_d + T_\infty).$$

(2.42)

The expressions for the binary diffusion coefficient and for the thermal conductivity of the gas-vapour mixture can be found in Appendix A. The underlying assumptions of Eqs. (2.41) are: $p_{vi} = p_{sr}$ and $T_i = T_d$. The first assumption is quite reasonable in the continuum limit; the second one $T_i = T_d$ may lead to erroneous predictions for pure vapours or low concentration of inert gas, as extensively discussed by Young [165] and Onishi [92]. For dilute mixtures, as those considered in the present study, the assumption $T_i = T_d$ is reasonable.

Free molecular limit

$$\dot{M}^{fm} = 4\pi r_d^2 \left(\frac{p_{sr}}{\sqrt{2\pi R_v T_d}} - \frac{p_{v\infty}}{\sqrt{2\pi R_v T_\infty}} \right),$$

(2.43)

$$\dot{E}^{fm} = 4\pi r_d^2 \left[\frac{p_{v\infty}\left(c_{pv} - \frac{R_v}{2}\right)}{\sqrt{2\pi R_v T_\infty}} + \frac{p_{g\infty}\left(c_{pg} - \frac{R_g}{2}\right)}{\sqrt{2\pi R_g T_\infty}} \right] (T_d - T_\infty) + \dot{M}^{fm}\left(c_{pv} - \frac{R_v}{2}\right)T_d.$$

Contrary to the continuum limit, here the assumptions at the interface become: $p_{vi} = p_{v\infty}$ and $T_i = T_\infty$. In section 2.4.2.1, it is investigated for which Knudsen number range these assumptions can be retained.

Transition regime

As a first step, Gyarmathy introduced a non-dimensional expression for the mass and energy transfer. The definition of these Nusselt numbers is the following:

$$Nu_{\dot{M}} = \frac{\dot{M}}{2\pi r_d \mathcal{D}_{mod}(p_{sr} - p_{v\infty})/p_{g\infty}};$$

$$Nu_{\dot{E}} = \frac{\dot{E}}{2\pi r_d k_m (T_d - T_\infty)};$$

$$(2.44)$$

where $p_{g\infty}$ is the inert gas pressure in the far field and $\mathcal{D}_{mod}$ is defined as

$$\mathcal{D}_{mod} = \frac{\mathcal{D}_m \, p_{g\infty}}{R_v T_m}. \qquad (2.45)$$

Both k_m and $\mathcal{D}_{mod}$ have to be evaluated at the intermediate temperature T_m, given by Eq. (2.42). Then, the Nusselt number Nu^{tr}, at intermediate Knudsen numbers, can be expressed as:

$$Nu^{tr} = \frac{Nu^{ct}}{1 + Nu^{ct}/Nu^{fm} + f(Kn)}. \qquad (2.46)$$

Gyarmathy attributed relation (2.46) to Kang [65] and Fukuta and Walter [40], who obtained it from flux matching methods, for both energy and mass transfers, based on the Langmuir model. Next, Gyarmathy extensively argues, on the basis of experimental data, that it is appropriate to omit the function $f(Kn)$. Therefore, the remaining expression, also known as Sherman interpolation formula [124], can be written as

$$Nu^{tr} = \frac{Nu^{ct} Nu^{fm}}{Nu^{ct} + Nu^{fm}}, \qquad (2.47)$$

which shows the correct asymptotic behaviour for both small and large Kn numbers. That is: $Nu^{tr} \to Nu^{fm}$ as $Kn \to \infty$, and $Nu^{tr} \to Nu^{ct}$ as $Kn \to 0$.

In this formulation, the droplet temperature T_d is treated as an input variable. However, in practical situations, the latter is unknown and has to be calculated from the energy balance at the droplet surface, which effectively provides, in the gya82 model, the coupling between the mass and energy flux:

$$\dot{E} = \frac{\mathrm{d}}{\mathrm{d}t}(M_d h_d) = \dot{M} h_d + M_d \dot{h}_d, \qquad (2.48)$$

where h_d and M_d represent the droplet enthalpy and total mass, respectively. Now, if the far field conditions T_∞ and $p_{v\infty}$ vary slowly with respect to the thermal relaxation

time of the droplet, which, as clarified in section 2.2, is always the case for nozzle flow applications [163], the internal energy flux of the droplet can be neglected. Then, the above equation can be rewritten as:

$$\dot{E} \quad = \quad -\dot{M}\left(h_{vs} - h_d\right) + \dot{M}h_{vs} = -\dot{M}L + \dot{M}h_{vs}, \tag{2.49}$$

where L is the latent heat of condensation and h_{vs} is the vapour enthalpy at equilibrium. The above assumption of quasi-equilibrium between mass and energy transfer is known as the "wet-bulb approximation".

Equation (2.49), combined with the appropriate expression for $\dot{E}$, provides an implicit formula from which the droplet temperature T_d can be calculated via an iterative procedure. Unfortunately, this evaluation is computationally quite time consuming, therefore explicit approximate expressions have been proposed by several authors [6,48,80,90,149]. They are all based on a Taylor expansion of $p_{vr} = p_{sr}(T_d)$ around of $p_{s\infty}(T_\infty)$. Thus, it is implicitly assumed that the vapour pressure at the droplet surface p_{vr} is approximately equal to the curvature corrected saturation pressure. As explained earlier (see section 2.2), this is a reasonable assumption for the problem considered here. Smolders [130] evaluated a number of explicit models and concluded that the best results were obtained with the formulation due to Gyarmathy [48]. In evaluating the first order coefficient for the Taylor expansion, Gyarmathy used a simplified version of the wet-bulb equation, specifically:

$$\dot{H} = -\dot{M}L, \tag{2.50}$$

where $\dot{H}$ represents the heat transfer. In this formulation, $\dot{H}$ can be calculated without major difficulties in the continuum limit, where it results: $\dot{H}^{ct} = 4\pi r_d k_m (T_d - T_\infty)$. Problems, though, arise in the free molecular regime, where no clear distinction can be made between convective and diffusive energy fluxes. The issue has been clarified by Prast [104]. By comparing the full wet-bulb expression (Eq. 2.49) with its simplified version (Eq. 2.50), both evaluated in the free molecular limit, he showed that Gyarmathy's approximation consists in neglecting the term $\dot{M}^{fm}T_d R_v/2$ in Eq. (2.43), which is, for water vapour/carrier gas mixtures, much smaller ($< 5\%$) than $\dot{M}^{fm}L$. Therefore, Eq. (2.50) can be employed without introducing a significant error.

Following then Eq. (2.50), the explicit formulation for the droplet temperature can be cast in the general form:

$$\left(\frac{T_d}{T_\infty} - 1\right) = f(S_\infty, Ke_\infty)\left[C_1 + C_2\right]^{-1}. \tag{2.51}$$

Here Ke_∞ is the Kelvin factor, defined as $Ke_\infty = 2\sigma/(\rho_l R_v T_\infty r_d)$. The terms C_1, C_2, θ_∞, and $f(S_\infty, Ke_\infty)$ are all functions of the far field conditions:

$$
\begin{aligned}
f(S_\infty, Ke_\infty) \quad &= \quad \ln S_\infty - Ke_\infty; \\
C_1 \quad &= \quad \frac{T_\infty}{\theta_\infty S_\infty}\left(\frac{p_\infty}{p_{s\infty}} - S_\infty\right); \quad \theta = \frac{\mathcal{D}_{mod}L}{k}\frac{Nu_M^{tr}}{Nu_E^{tr}}; \\
C_2 \quad &= \quad \frac{L_\infty}{R_v T_\infty};
\end{aligned}
\tag{2.52}
$$

where p_∞ is the pressure of the mixture in the far field. In deriving this explicit relation (Eq. 2.51), Gyarmathy further assumed: $\frac{T}{T_d} \approx 1$, and $\frac{p_{vr}}{p_{v\infty}} \approx 1$. It should be noticed that these approximation are solely due to mathematical rather than physical constraints. Smolders [130] formulated a second order correction to the Gyarmathy explicit formula:

$$\left(\frac{T_d}{T_\infty} - 1 \right) = f(S_\infty, Ke_\infty)[C_1 + C_2]^{-1}(1 - \delta_1); \qquad (2.53)$$

where

$$\delta_1 \approx \frac{\frac{1}{2}C_1^2 - C_2}{(C_1 + C_2)^2} (\ln S_\infty - Ke_\infty). \qquad (2.54)$$

Prast [104] evaluated in detail the accuracy of Eq. (2.53) with respect to the implicit solution. He concluded that in the whole range of relevant growth, the error remains always confined to $\pm 5\%$. More details on the derivation of Smolders' explicit formula can be found in Appendix B.

Once the droplet temperature has been calculated, the droplet growth rate can be computed either via the energy or via the mass conservation law, which in terms of Nusselt numbers reads as follow:

$$\frac{dr_d^2}{dt} = \frac{Nu_E^{tr}}{\rho_l L} (T_d - T) = -\frac{Nu_M^{tr} \mathcal{D}_{mod}}{\rho_l} \frac{p_{v\infty} - p_{sr}}{p_{g\infty}}. \qquad (2.55)$$

2.4.1.1 The driving potentials

This section illustrates in more detail to what extent the inclusion of temperature differences between the gas phase and the liquid droplets is relevant for modelling the growth process. Specifically, our objective is to prove that the droplet growth rate is controlled by two thermodynamic forces, namely the vapour pressure difference $\Delta p_v = p_{sr} - p_{v\infty}$ and the temperature difference $\Delta T = T_d - T_\infty$, combined with the assumption of local phase equilibrium at the droplet surface.

The analysis presented here is not new: these considerations, at different degree of complexity and generality, can be traced down to the works of many authors throughout the last century [18, 49, 164, 165]. However, for reasons of completeness and clarity, the theoretical framework within which the interpretation of the droplet growth process should be viewed is summarised here. To this aim, the growth process is first analysed from the standpoint of linear irreversible thermodynamics. Then, the gya82 model is re-interpreted in light of these findings. It is shown that, despite the many simplifications, Gyarmathy was able to incorporate, in a simple manner, the key features of the growth process, in full agreement with the thermodynamic findings.

The correct description of an irreversible process (such as droplet growth) relies on the identification of all thermodynamic "forces" (or affinities), which drive the process, and the system's response to these forces, the so-called associated fluxes [18]. A convenient way to identify all the relevant affinities, which characterise a given irreversible process, is

to determine the rate of entropy production. Young [164, 165] derived this relation for the case of dropwise condensation:

$$\frac{\dot{S}}{R_v} = 4\pi r_d^2 \left\{ J_m \left(\frac{\Delta p_v}{p_{v\infty}} \right) + J_{qc} \left(\frac{\Delta T}{T_\infty} \right) \right\},\tag{2.56}$$

where J_m and J_{qc} represent the mass and heat conduction fluxes from the droplet, respectively. For small departures from equilibrium ($|\Delta T|/T_\infty \ll 1$ and $|\Delta p_v|/p_{v\infty} \ll 1$), the phenomenological relations for mass and heat transfer take the form:

$$
\begin{aligned}
J_m &= \left\{ L_{mm} \left(\frac{\Delta p_v}{p_{v\infty}} \right) + L_{mq} \left(\frac{\Delta T}{T_\infty} \right) \right\}, \\[2ex]
J_{qc} &= \left\{ L_{qm} \left(\frac{\Delta p_v}{p_{v\infty}} \right) + L_{qq} \left(\frac{\Delta T}{T_\infty} \right) \right\},
\end{aligned}
\tag{2.57}
$$

where the coefficients L_{mm}, L_{mq}, L_{qm}, and L_{qq} are often called kinetic coefficients and are functions of the local intensive parameters. Algebraic expressions for these coefficients have been derived by Young [165].

Here, the implications of Eqs. (2.56) and (2.57) are briefly discussed. Particularly, Eq. (2.56) states that the growth process is governed by two thermodynamic forces: the partial vapour pressure difference and the temperature difference. Relations (2.57) show that the mass and heat transfers are functions of both driving forces and, therefore, are mutually interdependent. In some specific problems, one of the two driving forces may become zero, thus simplifying considerably the treatment (see, for example, Peters [101]).

With reference to the gya82 model, its underlying assumptions are now reviewed in light of the proper thermodynamic framework. In his work on "The spherical droplet in gaseous carrier streams", Gyarmathy ([49], pp. 114) clearly identifies two driving forces for the heat and vapour mass fluxes, namely the above mentioned temperature and vapour pressure differences. However, his main assumption (pp. 135) is to regard the heat and mass transfers as decoupled. In other words, Gyarmathy assumes that these transfer processes, although occurring simultaneously, are not influenced by each other, or more accurately their mutual influence is weak. As a consequence of this main assumption, he adopts the following simplifications (Table 4, pp. 136):

    1) $\dot{M}$ is only a function of Δp_v;
    2) $\dot{H}$ is only a function of ΔT.

Note that Gyarmathy provides also correction factors to take into account the cross-influence of heat and mass transfer. Thus, the fully correct model could eventually be implemented as well. In this simplified version, the coupling between heat and mass transfer is re-introduced via the wet-bulb equation. The latter, thus, not only serves to formally

close the system of equations, but also expresses the mutual influence and interdependence between the rate of heat and mass transfer.

To prove that these arguments are not arbitrary speculations, consider Fig. 2.4(a) and (b). Here the following two combinations are considered: $J_{ICCT}^{LD-\xi}$ for the nucleation rate, and the gya82 model for the droplet growth process, with and without wet-bulb correction. As it can be inferred immediately from Fig. 2.4(a), the wet-bulb model predicts large temperature differences in the initial phase of the growth process. This can be understood because while the gas temperature decreases rapidly due to the expansion, the droplet temperature stays constant due to the release of latent heat at the droplet surface.

(a)   (b)
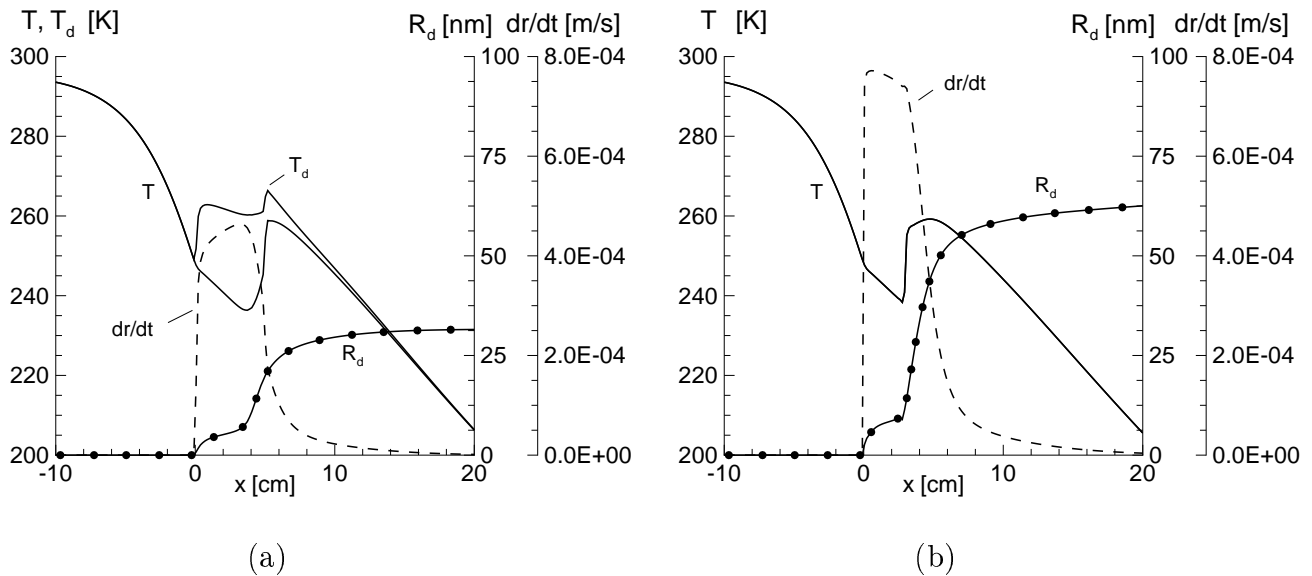
Figure 2.4: *Axial distribution of temperatures T, T_d, modal radius R_d, and droplet growth rate dr/dt. Models: (a) $J_{ICCT}^{LD-\xi}$ and gya82 with wet-bulb equation ($T_d \neq T$); (b) $J_{ICCT}^{LD-\xi}$ and gya82 with the assumption $T_d = T$. Nozzle: G2. Stagnation conditions: $P_0 = 8.67 \cdot 10^4 \, Pa$, $T_0 = 296.6 \, K$, $S_0 = 0.50$.*

The macroscopic consequence of this is twofold. First, the temperature difference effectively damps the growth process: $(dr/dt)_{wet-bulb}$ is roughly two times smaller than $(dr/dt)_{T_d=T}$. That is, because of the high latent heat of water, the growth rate is limited by the rate at which heat can be conducted away from the droplet. Second, smaller modal radii R_d are predicted by the wet-bulb law: since the rate of heat addition is considerably lower in this model, the nucleation rate is quenched somewhat farther downstream, as shown in Fig. 2.5. As a consequence, more critical clusters are produced while the total amount of liquid mass stays the same. In chapter 6, the correctness of this theoretical analysis is verified by comparing the theoretical droplet sizes with the experimental results for a number of droplet growth models.
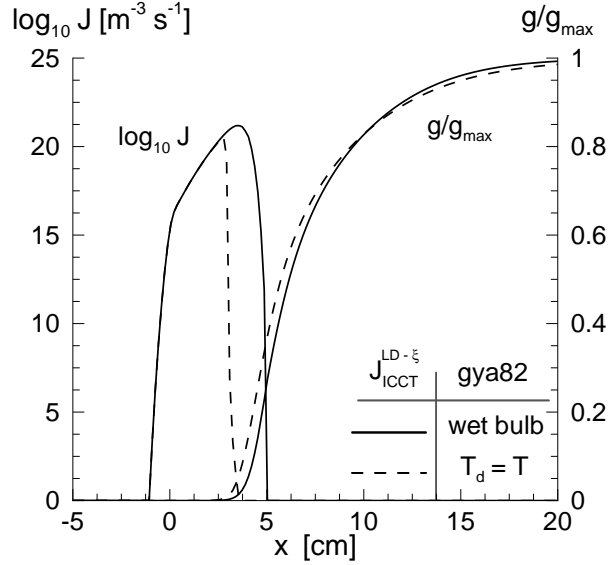
Figure 2.5: *Comparison of nucleation rates as derived by the following condensation models: $J_{ICCT}^{LD-\xi}$ and gya82 with and without wet-bulb. Nozzle: G2. Stagnation conditions: $P_0 = 8.67 \cdot 10^4 \, Pa$, $T_0 = 296.6 \, K$, $S_0 = 0.50$.*

2.4.2   Validity of the Hertz-Knudsen model

In section 2.4.1.1, the existence of two driving potentials, which control the growth process, has been ascertained. Objective of this section is to understand whether the good performance of the gya82 model is due solely to the inclusion of all relevant thermodynamic forces or to a combination of the latter and transitional growth effects. To this aim, the droplet growth law is reduced to the more simple and direct Hertz-Knudsen (HK) formula [57,68]. Incidentally, it should be observed that this simplification is less restrictive than it appears at first sight. In fact, recalling the Langmuir model depicted in Fig. 2.3, the HK formula can always be applied, provided the interfacial values T_i and p_{vi} are known. Young [162,165] provided two explicit formulas for calculating these interfacial values. These formulas are used in the following subsections to select the proper boundary conditions for the HK formulation. Then, by comparing the gya82 and HK models, the validity of the proposed simplification is proved.

2.4.2.1   Near free-molecular growth regime

A modified expression for the droplet growth in the near free-molecular flow regime can be cast, following Young [165], in the form:

$$\left(1 - \frac{r_d^2}{2r_i^2}\right) \frac{dr}{dt} = \frac{1}{\rho_l} \left[\frac{q_c p_{vi}}{\sqrt{2\pi R_v T_i}} - \frac{q_e p_{vr}}{\sqrt{2\pi R_v T_d}} \right], \tag{2.58}$$

where the bracketed term on the left hand side represents Schrage's correction, p_{vi}, T_i, r_i are the interfacial values as defined in Fig. 2.3, and T_d, p_{vr} are the temperature and vapour pressure at the droplet surface, respectively. Recalling the definition of the interface radius $r_i = r_d + \beta l$, the Schrage's correction can be re-written as follow:

$$\left(1 - \frac{r_d^2}{2r_i^2}\right) = \left[1 - \frac{1}{2(1 + 2\beta Kn)^2}\right]. \tag{2.59}$$

Assuming for β a value of 0.75^3 and a Kn number of about $1.5 - 2$, the Schrage factor corresponds to a correction of about $3 - 5\%$. Since for the experiments considered in this study, the Kn number is always larger than two, the Schrage factor can be neglected without introducing an appreciable error. Further, as clarified in the previous sections 2.2 and 2.4.1, the droplet temperature T_d has to be explicitly calculated using Eq. (2.53); while the surface vapour pressure p_{vr} is equal to the curvature corrected saturation pressure $p_{vr} = p_{sr}(T_d, r_d)$. The only unresolved issue is, thus, the value to choose for p_{vi} and T_i. In the free molecular limit ($Kn \gg 1$), a very good approximation for the interfacial variables is: $p_{vi} = p_{v\infty}$ and $T_i = T_\infty$.
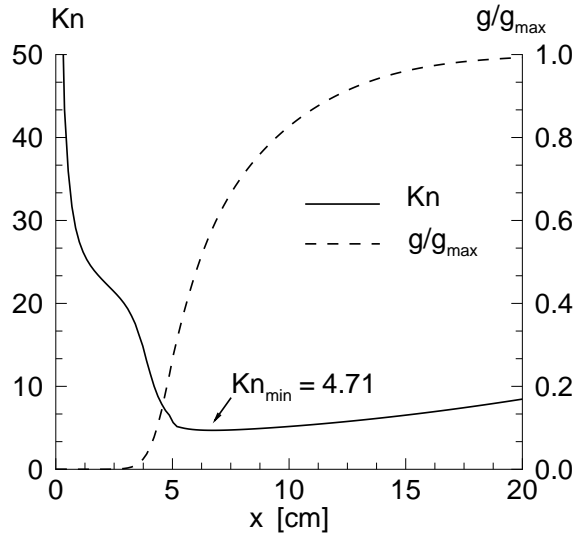
Figure 2.6: *Axial distributions of the Knudsen number Kn and condensate mass fraction g/g_{max}, downstream of throat. Nozzle: G2. Case: S50 - Stagnation conditions: $P_0 = 8.67 \cdot 10^4$ Pa, $T_0 = 296.6$ K, $S_0 = 0.50$.*

Unfortunately, for the experiments considered in this work, this assumption is not adhered to straightforwardly. As an example, the axial distributions of the Knudsen number and condensate mass fraction along the nozzle axis are plotted in Fig. 2.6, for the representative case S50. As it can be inferred from this plot, the relevant growth occurs at values of the Knudsen number of $O(1)$. To identify the proper conditions for the applicability of the HK formula, some results from Young's analysis are considered. As a starting point, it

---

^{3}This value of β seems to yield the best results [99, 165].

should be recalled that from conservation of momentum, the pressure is uniform along any ray emanating from the droplet centre, provided the radial bulk velocity of the gaseous phase is much smaller than the local speed of sound. Thus, for a pure vapour, it always results $p_{vi} = p_{v\infty} \neq p_{sr}$ at any Knudsen number. In presence of an inert gas, though, this inequality does not hold anymore. In fact, conservation of momentum simply implies $p_i = p_{gi} + p_{vi} = p_\infty = p_{g\infty} + p_{v\infty}$, thus no a priori relation exists between p_{vi}, $p_{v\infty}$, and p_{sr}. Young [165] derived, in the continuum limit, an explicit relation for the ratio between the (Knudsen layer) vapour pressure jump $(p_{sr} - p_{vi})$ and the overall pressure difference $(p_{sr} - p_{v\infty})$. The graphic representation of this is plotted in Fig. 2.7 for a set of Knudsen numbers Kn representing the approach to the continuum limit.
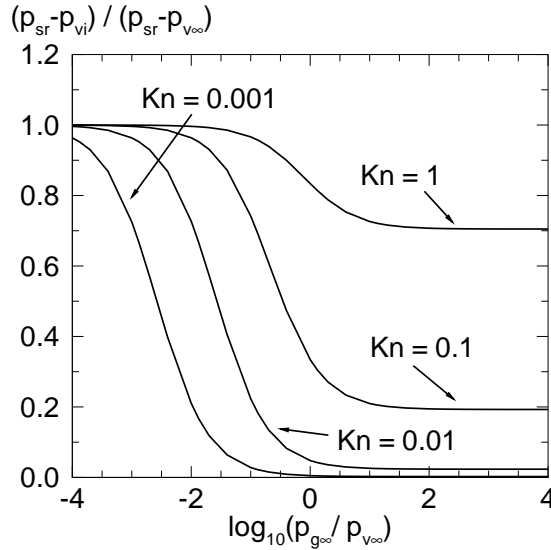
Figure 2.7: *The Knudsen layer vapour pressure jump for water in air, as derived from Young [165].*

Figure 2.7 is very interesting: it shows that for a pure vapour $[\log_{10}(p_{g\infty}/p_{v\infty}) \to -\infty]$, the equality $p_{vi} = p_{v\infty}$ is always identically satisfied. As soon as the concentration of inert gas is increased, the proper value for the interfacial vapour pressure is somewhere in between the two limiting conditions p_{sr} and $p_{v\infty}$. Further, the transition from one limit to the other depends upon the Kn number and inert gas concentration $\log_{10}(p_{g\infty}/p_{v\infty})$ values.

In the present application, inert gas concentrations of $1.5 < \log_{10}(p_{g\infty}/p_{v\infty}) < 2$ are considered at Kn numbers of $O(1)$. Therefore, a relation expressing the ratios T_i/T_∞ and $p_{vi}/p_{v\infty}$ valid for this range of Kn numbers and inert gas concentration is required. These relations are also provided by Young [165], [Eq. (47) and (53) (pp. 2949-2950)]. Here, the vapour pressure jump is expressed in terms of the fluid dynamic field variables and interfacial temperature T_i, where the latter has to be determined via a flux-matching technique. To avoid this complicated calculation, a simplified expression for the interfacial temperature T_i is used. This expression was also proposed by Young in an earlier paper [162]. It

reads[4]:

$$T_i = T_d - \delta(T_d - T_\infty), \tag{2.60}$$

where

$$\delta = \frac{3.78\frac{Kn}{Pr}}{\frac{1}{(1+2\beta Kn)} + 3.78\frac{Kn}{Pr}}. \tag{2.61}$$

The Prandtl number is defined by

$$Pr = \frac{\mu c_p}{k}, \tag{2.62}$$

where μ and k are the dynamic viscosity and thermal conductivity of the vapour-gas mixture, respectively. Their definition can be found in Appendix A. For the nozzle experiments considered in the present study, the relevant part of the growth occurs typically at the following conditions: $T_\infty = 259\,K$ and $p_\infty = 0.48\,bar$. Figure 2.8 shows the variation of the parameter δ as function of the Kn number. Clearly, the condition $T_i = T_\infty$ can be retained basically down to $Kn = 2$ without introducing a significant error.
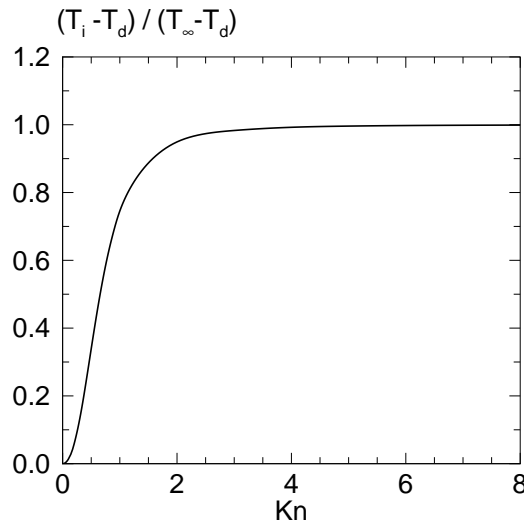
Figure 2.8: *Parameter δ versus the Knudsen number. The evaluation is conducted at the following representative conditions: $p_\infty = 0.48\ bar$, $T_\infty = 259\ K$, $T_d = 267\ K$, $r_d = 20\,nm$, and $\beta = 0.75$.*

Once the interfacial temperature T_i is known, the corresponding value of the vapour pressure at the interface p_{vi} can be evaluated from Young's relation [165] [Eq. (53), pp. 2950], which, assuming the evaporation q_e and condensation q_c coefficient equal to 1.0, has been re-arranged as follows:

$$(\eta + 1)\frac{p_{vi}}{p_{v\infty}} = \eta + \frac{p_{sr}}{p_{v\infty}} - \frac{(T_d - T_i)}{2T_\infty}, \tag{2.63}$$

---

[4]Equation (2.60) is not able to predict the Knudsen layer temperature jump, since $T_i \to T_d$ as $Kn \to 0$. However, this simplified approach is of no relevance in the near free-molecular regime where T_i should results approximately equal to T_∞.

where

$$\eta = (1 - \frac{r_d^2}{2r_i^2})\frac{r_i}{r_d}\frac{4Kn}{Sc}\left(\frac{R}{R_v}\right)^{1/2}\frac{p_\infty}{p_{v\infty}}. \tag{2.64}$$

The Schmidt number is defined by

$$Sc = \frac{\mu}{\rho\mathcal{D}}. \tag{2.65}$$

Here μ, ρ, and $\mathcal{D}$ are the dynamic viscosity, density, and binary diffusion coefficient of the vapour-gas mixture, respectively. Equations (2.60) and (2.63) can now be used to calculate the interfacial properties for a representative nozzle simulation (case S50). In fact, the thermo-fluid-dynamic flow field is solved using the $ICCT^{LD-\xi}$ model for the nucleation rate, and the gya82 model for the droplet growth law. Then, the flow variables are used as inputs to calculate the interfacial properties by means of Eqs. (2.60) and (2.63). The results are plotted in Fig. 2.9.
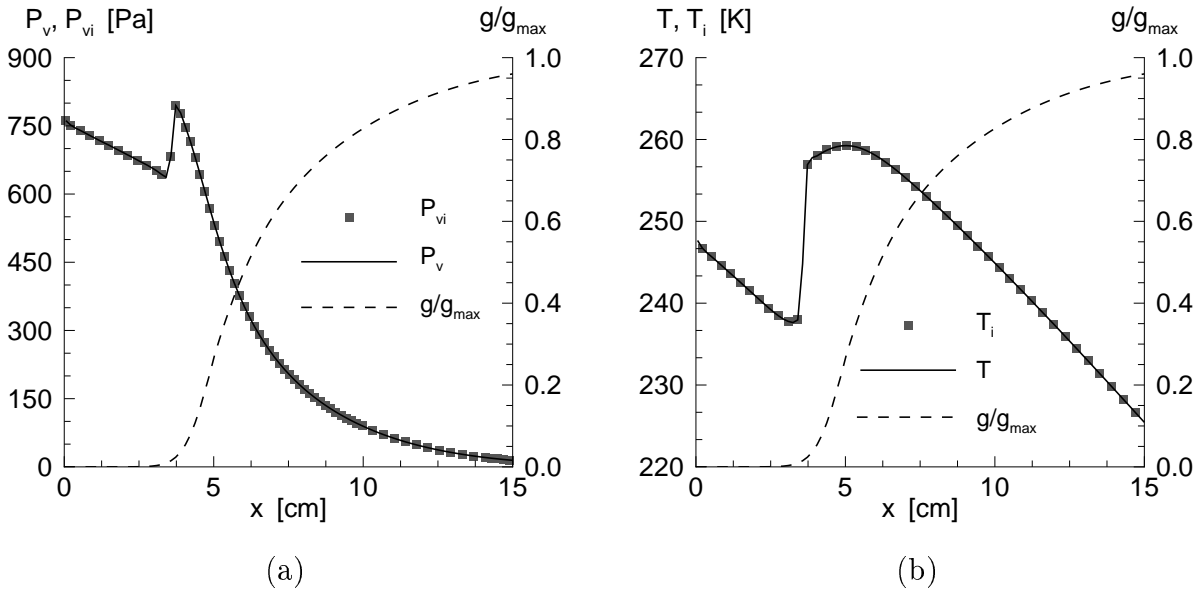
Figure 2.9: *Axial distribution, downstream of throat, of the interfacial and far field conditions, for a typical nozzle flow. Nozzle: G2. Case: S50 - Stagnation conditions:* $P_0 = 8.67 \cdot 10^4\, Pa$, $T_0 = 296.6\, K$, $S_0 = 0.50$.

From the equality of p_{vi} and T_i with their corresponding far field values, the applicability of the gas kinetic equations is proven. Concluding, thus, the droplet growth rate reduces simply to:

$$\frac{dr}{dt} = \frac{1}{\rho_l}\left[\frac{p_v}{\sqrt{2\pi R_v T}} - \frac{p_{sr}}{\sqrt{2\pi R_v T_d}}\right]. \tag{2.66}$$

As an additional proof of our assertion, the same case (S50) is re-calculated several times, using the models presented in Table 2.1. The results of this comparison are plotted in Fig. 2.10 where a remarkably good agreement is found between the HK and gya82

model. This indicates again that, for the water vapour/carrier gas systems and the range of Kn numbers considered here, no appreciable difference exists between the predictions of the gya82 and HK formulations. This holds even when the wet-bulb approximation is not implemented.

Case	Nucleation rate	Droplet growth model
S50	$ICCT^{LD-\xi}$	gya82 & wet-bulb
		gya82 & $T_d = T$
		HK & wet-bulb
		HK & $T_d = T$

Table 2.1: *A synoptic sketch of different condensation models. All models are applied to case S50.*
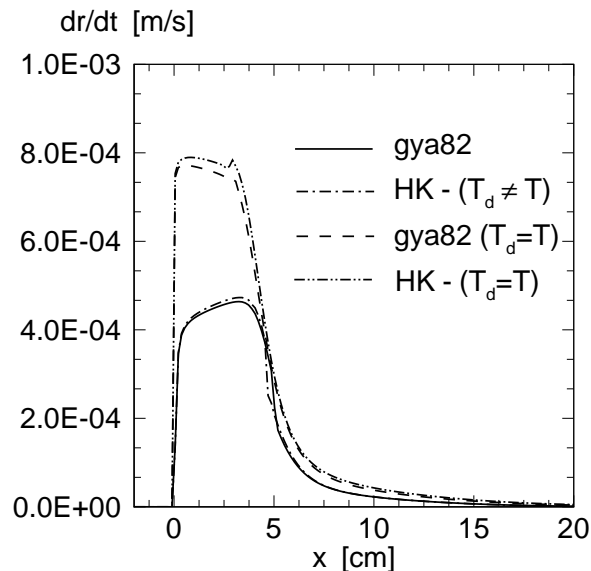
Figure 2.10: *Comparison of growth rate dr/dt, as predicted by the different droplet growth laws presented in Table 2.1. Nozzle: G2. Case: S50 - Stagnation conditions: $P_0 = 8.67 \cdot 10^4 \, Pa$, $T_0 = 296.6 \, K$, $S_0 = 0.50$.*

The same trend is also confirmed by the fluid dynamic variables, which match very well for the gya82 and HK formulations, provided all proper driving potentials are included, as shown in Fig. 2.11(a), (b). However, with respect to the fluid dynamic field, the omission of the wet-bulb correction reveals some effects on the axial distributions of the modal radius and temperature. The observed discrepancies can be explained as follows: the implementation of the gya82 growth law differs from the (HK) one by the inclusion of transitional effects. For the present range of Knudsen numbers, this difference is totally

negligible when compared to the effects due to the thermodynamic force (ΔT), which strongly dominates the growth process. Therefore, when this thermodynamic potential is omitted, the tiny differences between the two models become relatively important, thus producing the observed differences.

(a)

(b)
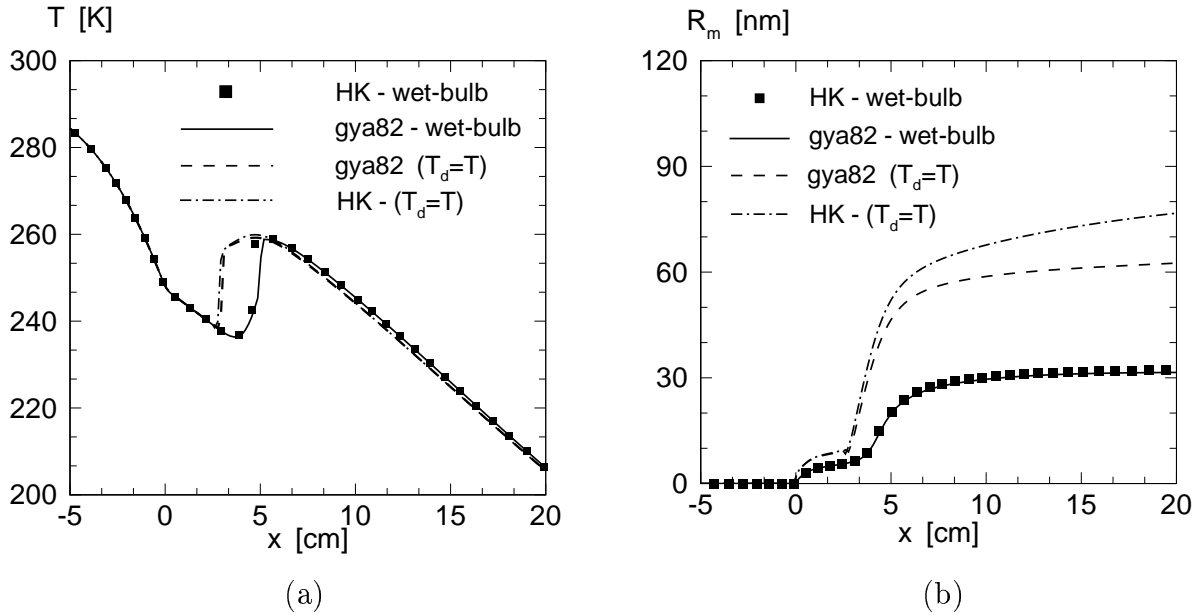
Figure 2.11: *Comparison of the thermo-fluid-dynamic field, as predicted by the condensation models of Table 2.1. (a) Temperature distribution. (b) Maximum droplet radius. Nozzle: G2. Case: S50 - Stagnation conditions: $P_0 = 8.67 \cdot 10^4 \, Pa$, $T_0 = 296.6 \, K$, $S_0 = 0.50$.*

(a)

(b)
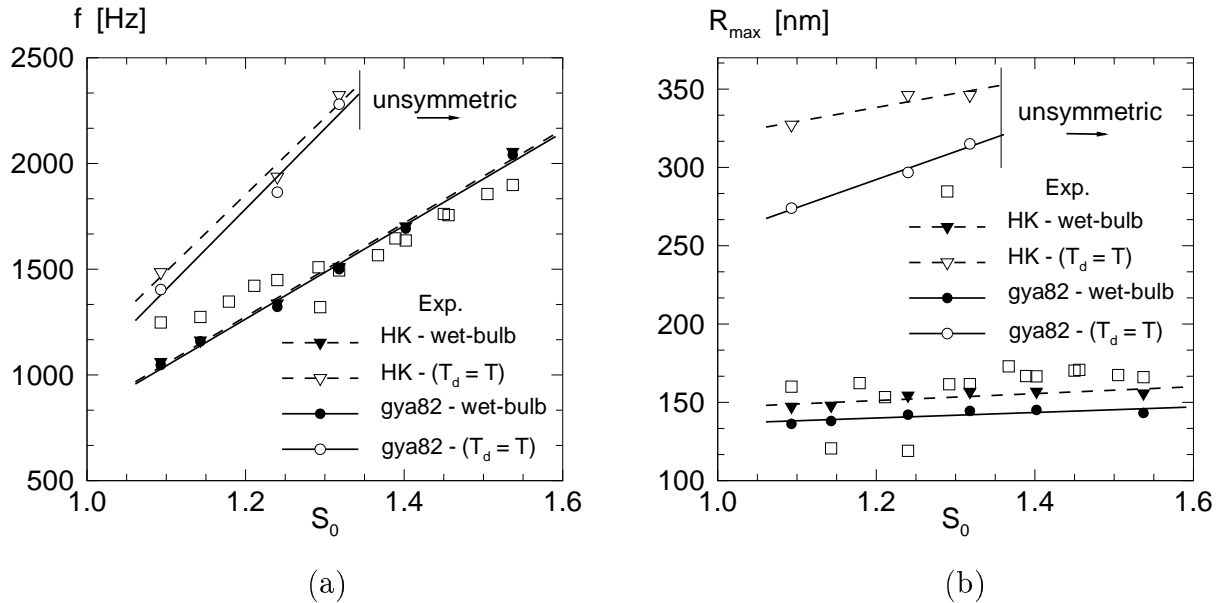
Figure 2.12: *Comparison of frequency of oscillations (a) and maximum droplet radius (b), as predicted by the condensation models of Table 2.1. Nozzle: G2. Stagnation conditions: $P_0 = (8.67 \pm 0.015) \cdot 10^4 \, Pa$, $T_0 = 296.6 \pm 0.4 \, K$.*

Case	S_0	Frequency Data [Hz]				
		Experiment	**HK & wet-bulb**	**HK & $T_d = T$**	**gya82 & wet-bulb**	**gya82 & $T_d = T$**
J41	1.102	1248	1061	1485	1047	1404
J55	1.249	1449	1338	1937	1322	1864
J58	1.327	1494	1511	2343	1500	2301
J53	1.411	1636	1702	asymmetric	1692	asymmetric
J46	1.546	1898	2055	asymmetric	2041	asymmetric

(a)

Case	S_0	Maximum Droplet Radius Data [nm]				
		Experiment	**HK & wet-bulb**	**HK & $T_d = T$**	**gya82 & wet-bulb**	**gya82 & $T_d = T$**
J41	1.102	160	147	327	136	274
J55	1.249	119	154	346	142	297
J58	1.327	162	157	321	145	315
J53	1.411	167	157	asymmetric	145	asymmetric
J46	1.546	166	156	asymmetric	143	asymmetric

(b)

Table 2.2: *Frequency data (a) and maximum droplet radius (b) as predicted by the condensation models of Table 2.1. Nozzle: G2. Stagnation conditions: $P_0 = (8.67 \pm 0.015) \cdot 10^4\ Pa$, $T_0 = 296.6 \pm 0.4\ K$.*

The same conclusions hold also for the unsteady flow regimes, where the experimentally determined droplet size and frequency of oscillations are compared with the theoretical predictions from the models listed in Table 2.1. The results of this comparison are reported in Fig. 2.12 and in Table 2.2(a) and (b). Again no significant difference is observed between the HK – wet-bulb and gya82 – wet-bulb models. From these results, the following can be concluded:

1)   for the Kn range of our experiments $[2-50]$, the growth process is dominated by gas kinetic effects. Thus, the choice of the HK formula to describe the growth process is a proper one. Transitional effects play a marginal role;

2)   for the Kn range of our experiments $[2-50]$, the correct modelling of the growth process is obtained solely by the inclusion of all relevant driving potentials;

3)   the transitional formulation of the gya82 model describes satisfactorily the passage from free molecular to transitional regime down to Kn numbers of roughly 2. Note that Young's model stays longer ($\approx$ till $Kn = 1$) in the free molecular regime than the gya82 model. Therefore Young's model performs also correctly in the Knudsen range considered here $[2-50]$.

2.4.3   The Gyarmathy 63 model

In 1963, Gyarmathy [48] proposed a simplified droplet growth model for the whole range of Knudsen numbers, which, to date, has been widely applied. Following Gyarmathy, the droplet growth rate can be expressed as:

$$\frac{dr}{dt} = \frac{1}{r_d\,\varrho_l}\,f(Kn)\left[\frac{L^2}{k\,R_v\,T_\infty^2} + \frac{p_\infty - p_{v\infty}}{p_\infty}\,\frac{R_v\,T_\infty)}{p_{v\infty}\,D}\right]^{-1}\left(1 - \frac{r^*}{r_d}\right)\ln(S_\infty), \qquad (2.67)$$

where k is the thermal conductivity, r_d is the droplet radius, p_∞ the pressure of the mixture in the far field, and r^* the critical radius corresponding to the thermodynamic state $(T_\infty,\,p_\infty,\,S_\infty)$. As correction factor, Gyarmathy suggested the following[5]:

$$f_{Gy}(Kn) = \frac{1}{1 + 3.18Kn}. \qquad (2.68)$$

According to Fuchs and Sutugin [39], the value 3.18 is too high and the correction formula does not show the correct asymptotic behaviour for the free-molecular regime. Therefore, the gya63 model, can possibly lead to wrong predictions in the limit $Kn \gg 1$. In deriving Eq. (2.67), Gyarmathy implicitly used some linearisation in the expression for the droplet temperature, which he approximated as follows:

$$T_d = T_s(p_{vr}) - \frac{r^*}{r_d}\,\Delta T_{sub}, \qquad (2.69)$$

---

[5]For reasons of consistency with the gya82 model, the same mean free path $l = 2\mu\sqrt{RT}/p$ is adopted. In the original article, Gyarmathy used the following definition $l = 1.5\mu\sqrt{RT}/p$.

where $[\Delta T_{sub} = T_s(p_{v\infty}) - T_\infty]$ is the subcooling. Note that the droplet calculation provided by Smolders (see section 2.4.1) is an extension of Eq. (2.69). Summarising, thus, the gya63 and gya82 model differ from each other essentially with respect to the choice of the correction factor $f(Kn)$ as well as the calculation of the droplet temperature.

2.5 Computational method

This section describes briefly the main features of the computational method employed in the simulations presented in this thesis. The method is based on the work of Mundinger [91] and has been further extended by Prast. For a detailed description of the numerical scheme and its accuracy, the reader is referred to Prast [104].

In order to solve numerically the system of Eqs. (2.19) - (2.23), first the integro-differential Eq. (2.23) is transformed from a Lagrangian to an Eulerian frame of reference. This is achieved by adopting Hill's approach [58]. Hill's method consists of tracking the evolution in time and space of the low-order moments of the size distribution and is described in Appendix C. The major advantage of Hill's method is that many physical properties of the droplet cloud can be estimated, without any *a priori* knowledge of the size distribution itself, as explained in Appendix C as well. However, as pointed out by McGraw [86], the parameterisation of a distribution in terms of its lower-order moments does not define the size distribution univocally. That is, two size distributions can exhibit the same set of low-order moments, despite substantial qualitative differences, such as multimodal versus monomodal. This poses serious limitations to the ability of the numerical method in predicting the actual form of the droplet spectra in unsteady flow conditions, where a slight bimodality has already been theoretically predicted [159]. For a detailed derivation of the equations for the moments, the reader is referred to Prast [104]. Here, only the final result is reported, expressing the rate of condensate mass production in terms of a set of four coupled equations. The complete system then reduces to

$$\frac{\partial U}{\partial t} + \frac{\partial F}{\partial x} + \frac{\partial G}{\partial y} = S, \tag{2.70}$$

where U is the vector of unknowns, F and G represent the convective fluxes in the $x-$ and $y-$ direction respectively, and S is the source term:

$$U = \begin{pmatrix} \varrho \\ \varrho u \\ \varrho v \\ \varrho E \\ \varrho g \\ \varrho \mathcal{Q}_2 \\ \varrho \mathcal{Q}_1 \\ \varrho \mathcal{Q}_0 \end{pmatrix} , \quad F = \begin{pmatrix} \varrho u \\ \varrho u^2 + p \\ \varrho v u \\ (\varrho E + p)u \\ \varrho g u \\ \varrho \mathcal{Q}_2 u \\ \varrho \mathcal{Q}_1 u \\ \varrho \mathcal{Q}_0 u \end{pmatrix} , \quad G = \begin{pmatrix} \varrho v \\ \varrho u v \\ \varrho v^2 + p \\ (\varrho E + p)v \\ \varrho g v \\ \varrho \mathcal{Q}_2 v \\ \varrho \mathcal{Q}_1 v \\ \varrho \mathcal{Q}_0 v \end{pmatrix} ,$$

$$S = \begin{pmatrix} 0 \\ 0 \\ 0 \\ 0 \\ \frac{4}{3}\pi\varrho_l \left(Jr^{*3} + 3\varrho\mathcal{Q}_2 \frac{d\bar{r}}{dt} \right) \\ Jr^{*2} + 2\varrho\mathcal{Q}_1 \frac{d\bar{r}}{dt} \\ Jr^* + \varrho\mathcal{Q}_0 \frac{d\bar{r}}{dt} \\ J \end{pmatrix}. \tag{2.71}$$

This hyperbolic system of partial differential equations is first divided into a homogeneous and inhomogeneous part, according to the Fractional-Step-Method of Oran and Boris [93], yielding:

$$\frac{\partial U^{hom}}{\partial t} + \frac{\partial F}{\partial x} + \frac{\partial G}{\partial y} = 0, \tag{2.72}$$

$$\frac{\partial U}{\partial t} = S\left(U^{hom} \right). \tag{2.73}$$

Both systems of Eqs. (2.72) and (2.73) are then discretised with a cell-centered Finite-Volume-Method on a body fitted structured mesh. Following the MUSCL approach, the convective fluxes are calculated at the cell interfaces with the flux vector splitting of van Leer in the version for real gases, according to Shuen *et al.* [125]. The extrapolation of the latter to the cell interface is performed using the k-scheme of Anderson, Thomas, and van Leer [4] with the van Albada limiter. This technique provides a spatial accuracy of the third order, except near shocks where the limiter reduces it to first order spatial accuracy to prevent oscillations. The time integration is explicit and second-order accurate, using the scheme of Bölcs *et al.* [13]. At the nozzle inlet, non-reflecting boundary conditions are implemented, following Poinsot and Kele [102]. All experiments considered here have a supersonic outflow. At such nozzle outlets, all flow variables are obtained by extrapolation from the interior. At a solid wall, according to the assumption of inviscid flow, the velocity component normal to the wall is zero. The pressure at the wall is obtained using the method of Deconinck and Struys [25] which assures a low numerical entropy production.

The influence of the computational grid density on the numerical solution has been investigated by Mundinger [91] and Adam [2], both for steady and unsteady flow regimes. Following their conclusions, similar mesh densities have been adopted for the nozzle flow calculations presented in this thesis. Details can be found in Appendix D.

2.6   Conclusions

In this chapter, a review is presented of the modelling of non-equilibrium condensation for a mixture of water vapour and carrier gas. The fundamental idea of splitting the condensation process into a nucleation and droplet growth process dates back to Oswatitsch [94]. The numerical method relies on the scheme developed by Schnerr *et al.* [91, 117]. Their

scheme is chosen because of its capability in accurately resolving complex shock structures, for both steady and unsteady cases. Several physical models have been considered. Starting from the Schnerr and Dohrmann model [33], which guarantees an accurate determination of pressure distributions and frequencies of oscillations, two essential modifications have been made, specifically: the surface tension fit and the droplet growth model. By blending together thermodynamic considerations (i.e. the Nernst Postulate), measured surface tension data and experimental validation, a new surface tension fit is proposed. The new fit not only gives good results for condensing flows in a wide temperature range $(215 < T < 270 \ K)$, as shown in chapter 6, but also satisfies the thermodynamic constraint $\partial \sigma / \partial T \to 0$ as $T \to 0$.

For the droplet growth process, the Gyarmathy model [49] is implemented, which is valid in the whole range of Knudsen numbers. However, as extensively discussed in section 2.4.1, the fundamental difference with the Schnerr/Dohrmann model lies in the inclusion of the temperature difference $\Delta T = T_d - T$ as additional thermodynamic driving potential; while transitional effects play a negligible role. The existence of $\Delta T = T_d - T$ as thermodynamic force that controls the growth process is substantiated on the basis of:

a) linear irreversible thermodynamic theory, which has been applied to dropwise condensation by Young [165];

b) theoretical considerations of Young [165] and Gyarmathy [49];

c) comparison of numerical results for droplet size with experimental data.

Chapter 3

Wave tube experiments

This chapter describes the experimental methods and procedures adopted to characterise condensing flow fields, both in steady and periodic oscillating flow regimes, and to measure some of its relevant parameters, such as density fields, droplet sizes, frequencies of oscillations, just to name a few. These topics are tackled mostly from an operational and practical point of view, while all the relevant theoretical issues are deferred to chapters 4 and 5. The experiments are performed in a so-called *Ludwieg tube*. This facility is a simple and effective device to produce steady initial conditions of short duration, without employing pressure regulators or similar accessories. A detailed description of the TUE Ludwieg tube and its operating principles can be found in section 3.1. Two diagnostic techniques have been utilised to obtain qualitative and quantitative information on the flow field. Double exposure holographic interferometry is an excellent tool to determine both visually and quantitatively the density field. The technique is mostly applicable to steady flow situations. Nevertheless, by a careful optimisation of the experimental procedure and the use of an accurate trigger unit, it is possible to obtain snapshots of periodic oscillating flows as well. Section 3.2 describes the interferometer, its operation, and the reconstruction procedure. A white light extinction method has been employed to optically characterise the droplet cloud at the nozzle exit. From this characterisation, both the time-resolved droplet modal radius $r_m(t)$ and number density $n_d(t)$ can be deduced. The optical set-up, its operation and calibration procedures are examined in section 3.3.

3.1   The Ludwieg tube

In this section, a particular example of expansion wave tube is discussed, namely the *Ludwieg tube*. This facility was conceived and first introduced by Ludwieg [73] in 1955. Its design and operating principles have been extensively described in literature [35, 74]. The Ludwieg tube was initially developed for testing of vehicles flying at high transonic speeds. Its application to condensing nozzle flows was first proposed and successfully applied by Wegener at Yale University [64, 89, 157]. The TUE Ludwieg tube, depicted schematically in Fig. 3.1, consists of a long tube of square cross section, with a nozzle mounted in

its test section.   Downstream of the nozzle, a diaphragm is situated, which separates the Ludwieg tube from a vacuum vessel.   Initially, the supply section (upstream of the diaphragm) is filled with the condensable mixture at high pressure (typically $P_{ini} = 1\ bar$), while the dump section (downstream of the diaphragm) is evacuated.   Upon rupture of the membrane, an expansion fan travels through the nozzle into the supply section.   A flow is thereby initiated from the supply to the dump section.   As the flow in the nozzle throat becomes choked, expansion waves cannot travel upstream anymore and only a finite expansion fan goes past the throat.   This results in a steady supply condition for the nozzle flow.   This situation persists for about 50 ms and terminates when the reflected expansion fan returns to the nozzle inlet, where it is reflected again.   This mechanism is schematically illustrated in Fig. 3.1, together with the variation of the inlet pressure P_{inlet} as a function of time. P_{inlet} is measured by a dynamic pressure transducer, indicated in the figure as Pk_1 and located at 1 m from the nozzle throat.
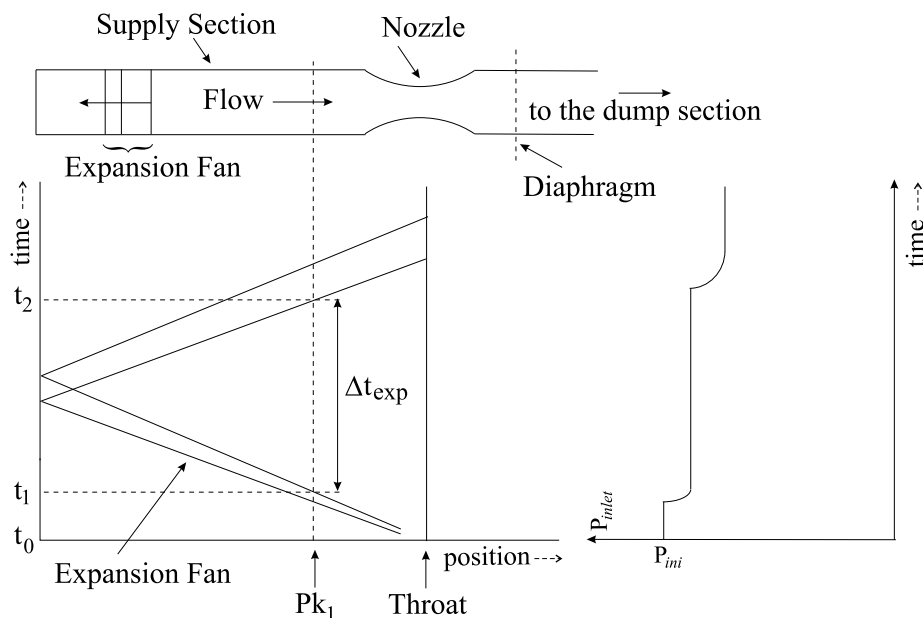
Figure 3.1: *Sketch of Ludwieg tube, expansion wave, and inlet pressure diagram (not in scale).*

This type of wind tunnel presents several advantages.   Due to the small size of the supply tube, initial mixtures may be prepared at well-defined conditions and relatively low cost.   It is also easily possible to vary the initial conditions, specifically supply pressure, temperature, and saturation ratio $[S_{ini} = p_v/p_{s\infty}(T)]$.   The pressure range is limited mostly by the strength of the glass windows (used for optical access) and diaphragm material.   The temperature range essentially depends upon the power of the electrical heating system and quality of the insulation.   In the present investigation, the supply pressure is always kept constant at atmospheric value; while two different supply temperatures are applied 21 and 37 °C, respectively.   The supply saturation ratio is varied within a wide range, from

dry to saturated conditions ($0 < S_{ini} < 1$). It is noteworthy mentioning that, because of the unsteady expansion fan, a supersaturated stagnation condition can be readily achieved with this device ($0 < S_0 < 1.8$). Further, various cooling rates can be readily obtained by inserting nozzle blocks of different expansion rates in the test section. Because the testing time is very short, special instrumentation is required. A detailed description of the set-up and its peripherals is presented in the next subsection.

3.1.1 The experimental equipment

A schematic description of the experimental set-up is shown in Fig. 3.2. The supply section is 12 m long and consists of a Ni-coated steel tube with an internal square cross-section of 10×10 cm^2. The tube is also thermally controlled and an initial temperature as high as $40°C$ can be achieved. A polyester membrane (Melinex polyester film) of 20 μm thickness separates the test section from the vacuum vessel. The membrane rests against cross-shaped supports with resistance wires mounted on them (Kanthal wires, $\phi = 0.1$ mm, $R = 150$ Ω/m). The membrane can be opened by electrically heating the wires. The volume of the vacuum vessel is 0.4 m^3. A re-circulation system is also connected to the supply tube by valves (V_1 and V_3): it comprises a circulation pump CP (Verder VDE 0530) with a capacity of 50 ltr/min, a water vapour H_2O and gas N_2 injectors, a pressure gauge P, and a transducer RH (Vaisala HMP 234). The transducer HMP-234 incorporates a Pt100 temperature sensor and the so-called Humicap sensor, whose operating principle is based on changes in the capacitance of the sensor as its polymer film absorbs water molecules.

PS	pressurised section	RH	Humicap sensor
TS	test section	$Pk_{1,2}$	pressure transducers
VT	vacuum tank	$VP_{1,2}$	vacuum pumps
CP	circulation pump	$V_{1,2,3}$	valves
P	pressure gauge	P_d	Barocel (600A)
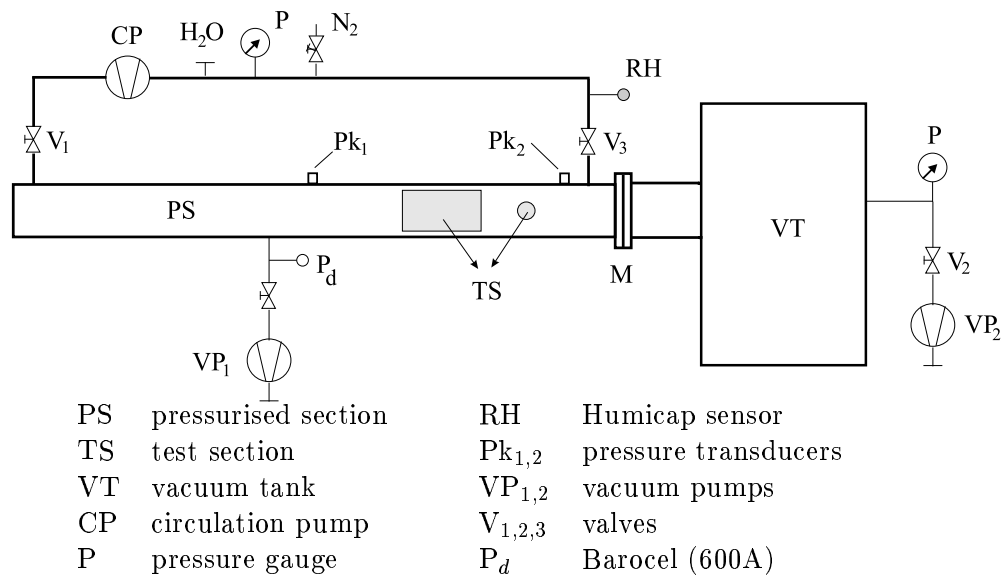
Figure 3.2: *Sketch of Ludwieg tube and its peripherals.*

Static pressure measurements are performed in the supply tube at two different locations upstream (Pk_1) and downstream (Pk_2) of the test section, as indicated in Fig. 3.2. Two

piezoelectric calibrated transducers (Kistler 5011A-10 and Kistler 5001SN) are employed for this purpose. The sensitive membrane of the transducers is coated with epoxy resin in order to prevent erroneous reading due to temperature gradients. The thickness of the coating is approximately 0.2 mm. All data (e.g. pressure and extinction signals) are recorded by means of a LeCroy transient recorder (Model 8013A - module 6810).
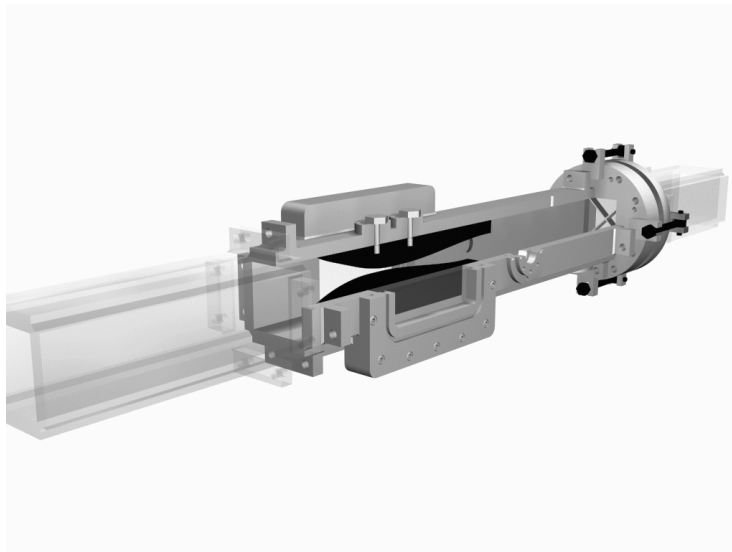
Figure 3.3: *View of the test-section and nozzle G2.*

Nozzle Data

Nozzle	Type	l [cm]	h^* [cm]	$R_{0^-}^*$ [cm]	$R_{0^+}^*$ [cm]	$(-dT/dx)_{1-D}^*$ [K/cm]	$(-dT/dt)_{1-D}^*$ [K/μs]
G1	Parallel outflow	20	2	8	6	25.74	0.820
G2	Parallel outflow	50	2	30	400	3.15	0.100
S1	Circular arc	-	12	10	10	8.14	0.237
S2	Circular arc	-	3	40	40	8.14	0.237

Table 3.1: *Geometric characteristics, temperature gradients, and cooling rates for the investigated nozzles. All values are evaluated at the representative stagnation temperature $T_0 = 293$ K. Nozzles G1 and G2 from this work. Nozzles S1 and S2 from Schnerr and co-workers [119, 120, 168].*

The nozzle is placed at a distance of 1 m from the diaphragm at a windowed position along the tube, as shown in Fig. 3.3. As windows, two Perspex plates are used. Two

nozzles, designated as G1 and G2, are utilised in this study. Their exit isentropic Mach numbers are $M = 2.5$ and 2.0, respectively. Their pertinent specifications are tabulated in Table 3.1 together with those from nozzles employed in previous studies. In this table, the symbols R_{0-}^* and R_{0+}^* indicate the radii of curvature to the left and to the right of the nozzle throat, respectively; while h^* denotes the throat height.

Nozzle G1 has a strong two-dimensional character and has been mostly employed for visualisation purposes. Nozzle G2, instead, is very slender. Due to its low cooling rate, it is possible to produce optically detectable droplets, and therefore it has been extensively employed to measure droplet sizes. To this aim, quartz windows have been placed at 24 cm from the nozzle throat, as shown in Fig. 3.3. The contour profiles for both nozzles (G1 and G2) are given in Appendix D.

3.1.2   Experimental procedure

A "series" of experiments is defined as a sequence of wave tube runs with constant stagnation pressure P_0 and temperature T_0, and varying vapour fraction or supersaturation S_0. In the experiments considered in this work, the stagnation pressure is always equal to $P_0 = (8.7 \pm 0.015) \cdot 10^4 \ Pa$, while two different stagnation temperatures are considered, specifically $T_0 = 280$ and $296 \pm 0.4 \ K$. The possible error in the determination of the supply saturation ratio S_{ini} is of the order of $\pm 1 \%$ for S_{ini} values in the range $[0 \dots 0.9]$ and of the order $\pm 2 \%$ for S_{ini} in the range $[0.9 \dots 1.0]$. A typical inaccuracy for the supply temperature T_{ini} is of $\pm 0.1 \ ^\circ$C for the Humicap electronics at $+20 \ ^\circ$C. Prior to each experiment, the supply pressure P_{ini}, temperature T_{ini}, and saturation ratio S_{ini} are obtained. The supply pressure is, then, used as a reference value to deduce the pressure P_{inlet}, at the nozzle inlet, from the time pressure profile, measured by the LeCroy transient recorder. Then, by applying standard gas dynamic relations, the stagnation conditions can be derived. The relations between supply and stagnation conditions are reported in Appendix E.

The preparation procedure is the following. First, upon mounting a new membrane, both the supply section and the re-circulation system are evacuated with pump VP$_1$ (Pfeiffer duo 016B) in order to eliminate any impurities in the tube. Typically, the evacuation proceeds down to a pressure of 10 Pa. The vacuum vessel is also evacuated with pump VP$_2$ (Speedivac ISC 450B) to prevent premature self-destruction of the membrane due to pressure differences. Subsequently, distilled water is injected into the system, where it vaporises instantaneously due to the extreme low pressure. Then, the carrier gas (typically nitrogen) is injected. To secure the preparation of a homogeneous mixture and prevent local condensation effects, the circulation pump CP is active during the whole filling procedure. The filling is interrupted as soon as atmospheric conditions are reached in the tube. The mixture is circulated until the Humicap reading reaches a stationary value, which is assumed as the supply value for the mixture temperature and saturation ratio humidity.

Upon reaching this condition, the vacuum vessel is evacuated again and the experiment can be started.

## 3.2   Holographic interferometer

In compressible flows, the line integral of the density along the light path can be measured by means of holographic interferometry. The adjective "holographic" indicates that at least one of the interfering wavefronts is generated holographically. The theoretical aspects of holographic interferometry are illustrated in chapter 4. This section describes comprehensively the holographic interferometer and its operation. A preliminary design of the interferometer was developed by Theeuwes [138], who performed a feasibility study for the application of holographic methods to the study of compressible flows. From the original set-up, only the structural elements and a number of optical components have been retained; while both the layout and the optical system have been radically modified by the present author. A detailed discussion on the differences between the two optical systems, essentially Fresnel or Image holography, can be found in sections 4.2 and 4.3. Figure 3.4(a) shows a three dimensional view of the interferometer and its location with respect to the Ludwieg tube. A first important requirement to fulfil is the stability requirement: mechanical vibrations from the surroundings or temperatures fluctuations should not affect the interferometric recording significantly. To assure the damping of unwanted vibrations, concrete blocks of about 500 kg, positioned on rubber mats have been adopted as optical base. Theeuwes [138] performed several stability tests and estimated a resonance frequency lower than 25 Hz for the whole system. On the basis of his tests, the same optical base is adopted for the present interferometer. Most of the optical components are mounted on stiff aluminium rail profiles with riders (Spindler & Hoyer - X95 system), as shown in Fig. 3.4(a). To minimise temperature fluctuations, the interferometer is placed in a temperature-controlled and isolated environment, where the ambient temperature is kept at the constant value of $T_{amb} = 22 \pm 0.5\,°C$.

Figure 3.4(b) shows a schematic top view of the interferometer, where an outline of the optical configuration is presented. The light source of the interferometer consists of a *ruby pulse laser/continuous wave HeNe laser* combination. The pulse laser (HLS2 - Lumonics Ltd.) generates a 30 ns pulse at a wavelength of $\lambda = 694.3\ nm$ and at an energy level adjustable in the range of $[0.01 \div 1]\ Joule$. The adjustment of the energy output is achieved by varying the laser amplifier delay in the range $[300 \div 500]$, at a constant capacitor voltage of 190 V. The continuous wave CW-HeNe laser (Uniphase - Mod. 1136P) has a wavelength equal to $\lambda' = 632.8\ nm$ and an output power of $20\,mW$. The pulsed ruby laser is used to expose the holographic plates, whereas the CW-HeNe laser serves to reconstruct the holograms. The CW laser is incorporated in the laser head of the pulsed laser in such a way that the optical axes of the two laser sources coincide, as schematically shown in Fig. 3.4(b). Inside the pulsed laser head, both beams are spatially filtered by a pinhole, located in the focal plane of a positive lens. Due to this construction, both beams diverge with an angle of 0.01 *steradians*. To correct for this divergence, a

positive lens (L$_1$, $f = 1000$ mm) is placed outside the laser head, at a distance f from the pinhole. Aside from reconstruction purposes, the CW-HeNe laser is also employed to align the optical components of the interferometer, prior to each experimental run. Upon entering the set-up, the light beam is divided into a reference and scene beam, where the term *scene beam* refers to the one passing through the test section. This is achieved by means of a $\frac{1}{2}\lambda$-retardation plate (HLP) and a polarising beam splitter (PBS). This optical configuration offers also the possibility of varying the intensity ratio between the scene and reference beam, as needed.

For the recording of a hologram, an optimal intensity ratio of $6 \div 5$ between object and reference beam is required. After the polarising beam splitter, a $\frac{1}{4}\lambda$-plate (QLP) is placed, whose function is to polarise circularly the beams. This guarantees that the requirement for observing interference is always automatically met, as explained in section 4.2.1. Because of its importance, the scene beam is described first. Mirrors M$_1$ and M$_2$ serve simply to re-direct the scene beam, which is then expanded by the negative lens (L$_2$, $f = -63.5$ mm) and collimated by the spherical mirror (SM$_1$, $f = 1500$ mm). The parallelism of the beam is accurate up to a maximum divergence angle of 0.005 rad. This precision is achieved by requiring the simultaneous crossing of four channels, $10\,cm$ long and $1\,mm$ wide. It is worth mentioning explicitly the following: first, in order not to deteriorate the scene beam, a high quality elliptical plane mirror (with a dielectric-coating) is chosen for M$_1$ (Spindler & Hoyer - ϕ x $L = 22.4$ x $31.5\,mm$, No. 340483). This mirror is especially designed for high-energy laser applications at an angle of 45° of incidence. Second, a negative lens is used to expand the beam in order to avoid focusing of the latter by a positive lens, which might cause ionisation of the surrounding air, when the pulsed laser is fired. After traversing the test section, the scene beam is imaged onto the holographic plate (HP) by the optical system SM$_2$ ($f = 1600$ mm), M$_3$ (Spindler & Hoyer - $\phi = 50\,mm$, No. 340016, ARB2 coated), and L$_3$ ($f = 1000$ mm). The optical properties and advantages of this configuration are discussed in section 4.3.

The reference beam path is somewhat easier to describe. A succession of mirrors (M$_4$, M$_5$, M$_6$, M$_7$) is employed, which reflect the unexpanded reference beam several times, in order to secure the equality of paths between the two interfering beams. In fact, the difference in paths should not exceed the coherence length of the laser. In the present application, it resulted $l_{coher} = 1$ m and $\Delta l_{paths} \approx 1$ cm. For mirror M$_7$, the same considerations and hence characteristics hold as for mirror M$_2$ (i.e. M$_7$ = M$_2$). Finally a combination of lenses (L$_4$ and L$_5$), identical to L$_1$ and L$_4$ respectively, is used to image the collimated reference beam onto the holographic plate. Mirror TM is a tilting mirror which, by means of a mechanical device, is canted in between the two exposures in order to create a set of reference horizontal fringes, as explained in section 4.4.
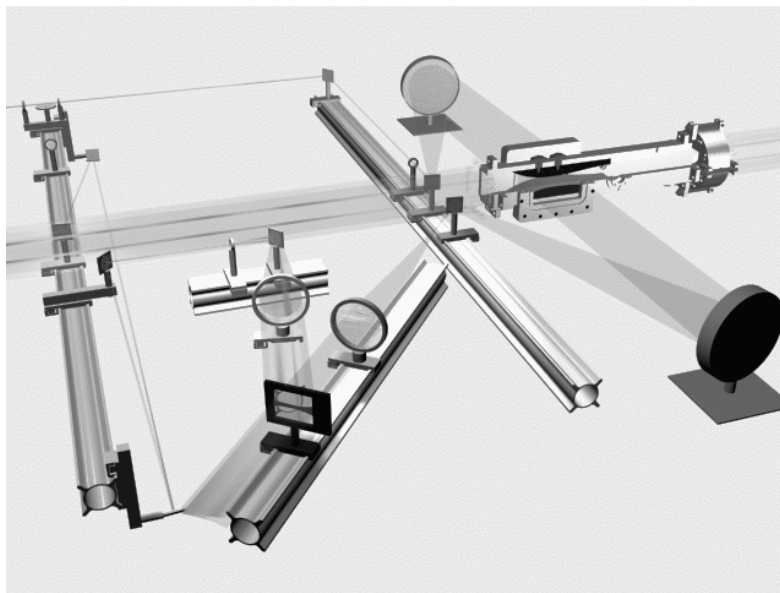
(a)
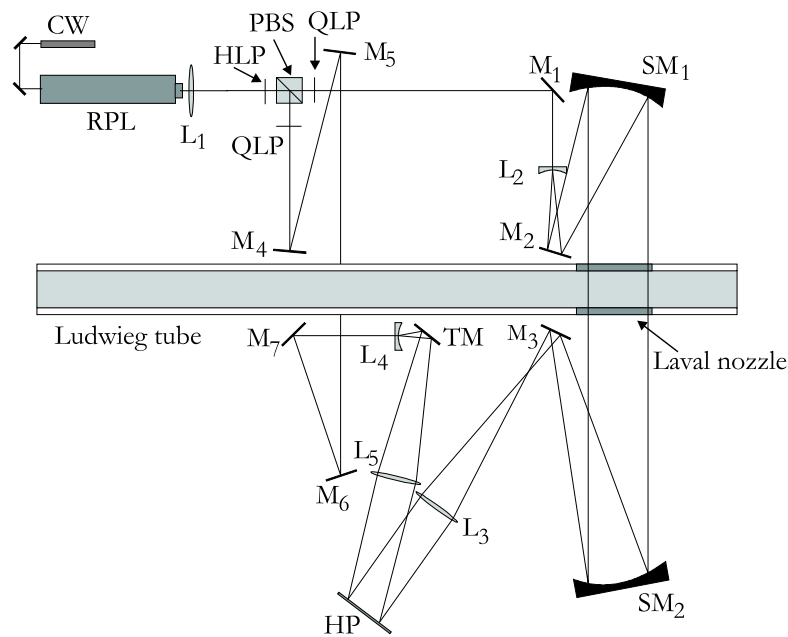
(b)

RPL	Ruby pulse laser	PBS	Polarising beam splitter
QLP	$\frac{1}{4} - \lambda$ plate	TM	Tilting mirror
HLP	$\frac{1}{2} - \lambda$ plate	HP	Holographic plate
$M_{1,...,7}$	Mirror	$L_{1,3,5}$	Convex lens
$SM_{1,2}$	Spherical mirror	$L_{2,4}$	Concave lens
CW	Continuous laser HeNe		

Figure 3.4: *Schematic representation of the holographic interferometer: (a) three-dimensional view; (b) outline of the interferometer, top view.*

3.2.1 Reconstruction set-up

After chemical processing, the hologram is placed back in the interferometer in its original position. The reconstruction of the original wavefront takes place by simply re-illuminating the hologram with the reference beam. As light source, the CW-HeNe laser is employed; as reconstruction set-up, the reference path of the interferometer is adopted, as shown in Fig. 3.5. The only difference is the interposition between lens L_4 and L_5 of an additional lens (L_6, $f = -100\ mm$), whose function is of expanding further the reference beam.
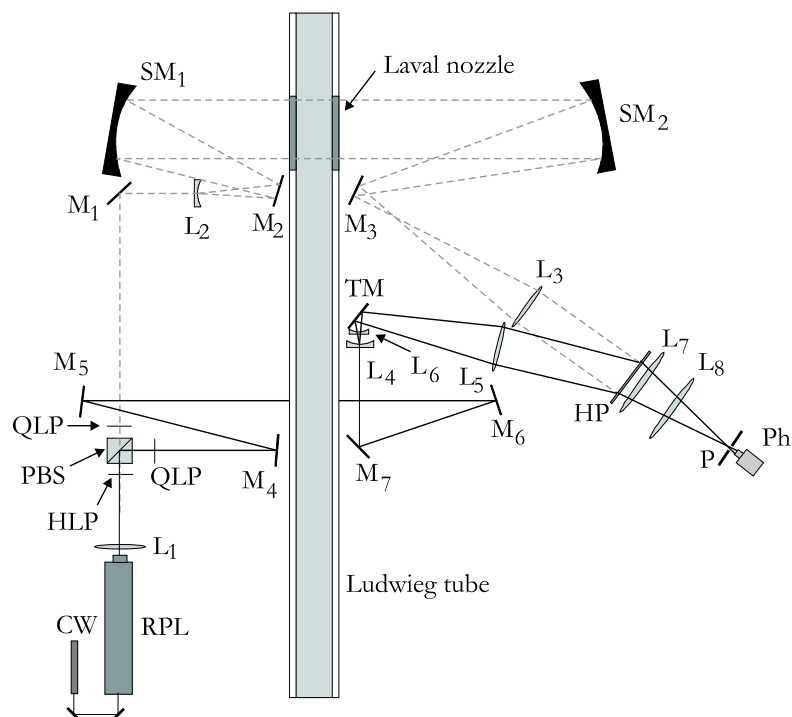
RPL	Ruby pulse laser		PBS	Polarising beam splitter
QLP	$\frac{1}{4} - \lambda$ plate		TM	Tilting mirror
HLP	$\frac{1}{2} - \lambda$ plate		HP	Holographic plate
$M_{1,...,7}$	Mirror		$L_{1,3,5,7,8}$	Convex lens
$SM_{1,2}$	Spherical mirror		$L_{2,4,6}$	Concave lens
P	Pinhole		Ph	Photographic camera
CW	Continuous laser HeNe			

Figure 3.5: *Schematic representation of the reconstruction set-up. The only active beam is the reference one, indicated in the picture with a solid black line.*

As a matter of fact, the quality and uniformity of the reconstruction beam influences greatly the quality of the reconstructed image. Since the CW-HeNe laser shows significant irregularities in its intensity distribution, only its central core is used and, therefore, a stronger beam expansion is required. The light diffracted by the hologram is imaged by

lenses L_7 and L_8 ($L_7 = L_8$, $f = 800\ mm$, ARB2 coated) onto a photographic camera (Nikon, F-801s). To select the correct order of the image and to improve the quality of the photograph, the residual background light is spatially filtered by the pinhole (P). In taking a photograph of the interferogram, the camera lens is focused onto the hologram to assure that a sharp image of the test section is recorded onto the photograph. Further, a long exposure time is selected in order to average out possible non-uniformities or noise of the light source.

As pointed out in section 4.2.2, if the wavefront is reconstructed with a different laser beam ($\lambda_{rec} \neq \lambda_{ref}$), then a shift in the location of the reconstructed image is produced. To counteract this effect, the hologram is rotated until the reconstructed image is coaxial with the optical axis of lenses L_7 and L_8. After developing the photographic film, the negatives are scanned with a high resolution scanner (Minolta, F-2800) at a resolution of [3000 x 3000] pixels. The photographic processing is preferred to direct digital acquisition due to the higher resolution of photographic materials and their higher signal-to-noise ratio with respect to standard CCD cameras.

3.3   Multi-wavelength light extinction set-up

A sketch of the multi-wavelength light extinction set-up (MWLS) is provided in Fig. 3.6, together with all the relevant geometric properties of the optical system. The design of the MWLS is, in its essence, inspired by the work of Walters [151]. For the present application, a high spatial and temporal resolution are additionally required. How these requirements are met in practice is elucidated next.
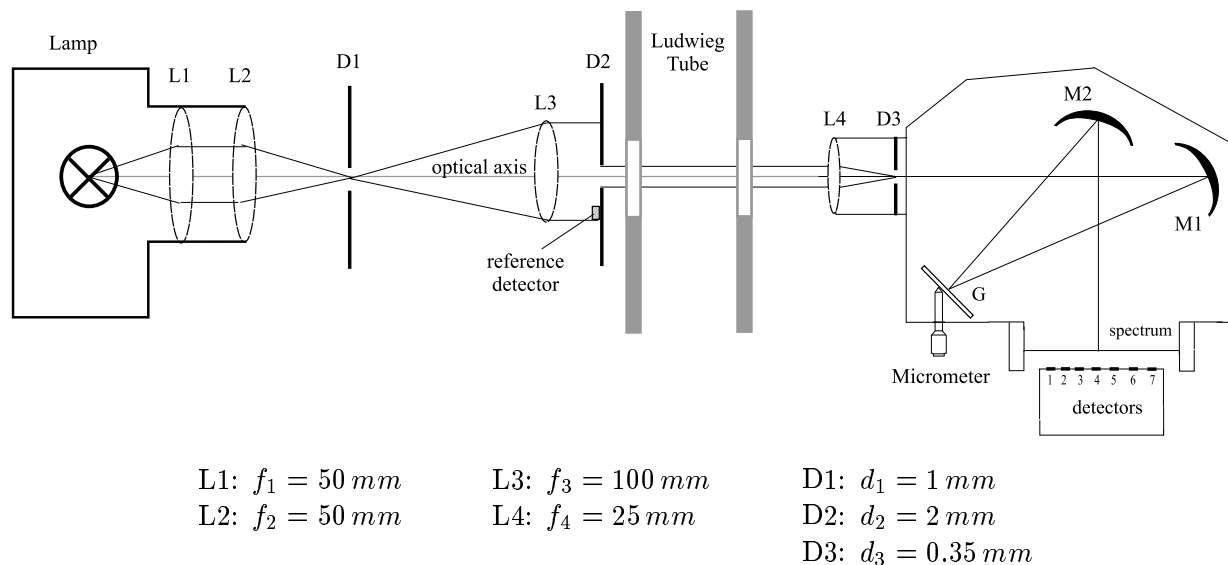

L1: $f_1 = 50\ mm$	L3: $f_3 = 100\ mm$	D1: $d_1 = 1\ mm$
L2: $f_2 = 50\ mm$	L4: $f_4 = 25\ mm$	D2: $d_2 = 2\ mm$
		D3: $d_3 = 0.35\ mm$

Figure 3.6: *Multi-wavelength light extinction set-up (not in scale).*

A Xenon lamp (Oriel 6221, $P = 450~W$) is employed as light source. The lamp is mounted in a metal box together with the two lenses L1 and L2, that image the light source onto the diaphragm D1, situated in the back focal plane of lens L3. The divergence of the beam is characterised by an angle $\alpha = d_1/2f_3$. In principle, the smaller the angle α, the higher the spatial resolution of the set-up, at the expense of beam power. As a compromise, the beam diameter is chosen equal to 2.0 mm and is determined by the size of diaphragm D2. Lens L3 collimates the beam, which then crosses the Laval nozzle on its symmetry axis at 24 cm from the nozzle throat. After traversing the test section, the light beam is focused by lens L4 onto the entrance slit (D3) of the spectrograph. The latter is described in detail in subsection 3.3.1.

3.3.1   Spectrograph and detection system

An enlarged view of the spectrograph and detection system is provided in Fig. 3.7. The main function performed by the spectrograph is to resolve the white light beam into its spectral components. The entering beam is focused by lens L4 onto the entrance slit D3. The ratio between the beam diameter at D1 and at D3 depends solely on the ratio of the focal distances of lenses L3 and L4, which is equal to $f_3/f_4 = 100/25 = 4$. Thus, at D3, a beam diameter of 250 μm is obtained.
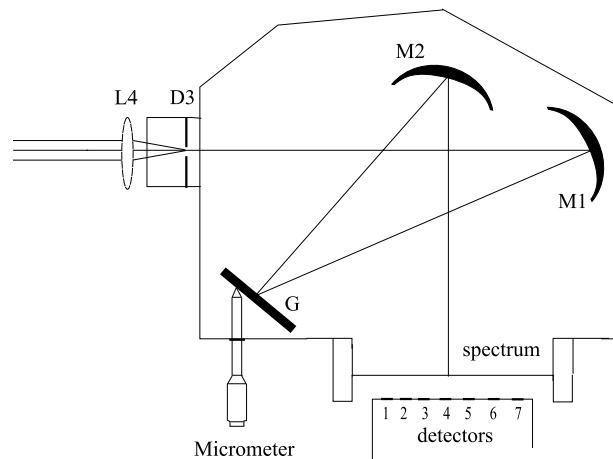
Spectrograph: Oriel Multispec 77400
Grating: Oriel 77417
                - spectral range: 400-1100 nm
                - resolution: 1.0 nm

Figure 3.7: *The spectrograph.*

The entrance slit D3 is situated in the focal plane of mirror M1, which has the function of collimating the beam. The parallel beam is then re-directed towards the grating G. This grating, suitable for wavelengths in the range $[400 \div 1100]~nm$, resolves the white light beam into its spectral components. Mirror M2, then, images this spectrum at the exit

plane of the spectrograph. For each wavelength, constructive interference is accomplished in a separate direction. Therefore, each wavelength will correspond with a unique position at this exit plane. The angular position of the grating can be adjusted by changing the position of the micrometer, thus producing a shift of the spectrum at the exit plane. By placing a detector at a certain location of this plane, the light intensity corresponding with a certain wavelength can be measured. By mounting a CCD array at the exit plane, it is possible to measure the whole extinction spectrum. However, since the response time of the available CCD array was roughly 1 ms, and therefore too slow for detecting frequencies of 1 kHz or higher, it was necessary to develop a different detection system, capable of acquiring data at a higher rate. A schematic drawing of the new detection system is shown in Fig. 3.8. The latter has been developed, at our laboratory, by Holten. It consists of a plane support, allocating seven equidistant slits. Behind each slit, a photodiode (Siemens BPW 34) is placed, able to detect frequencies up to 100 kHz. The distance between two consecutive slits is 3.0 mm and their width amounts to only 400 μm. The response of the photodiodes is given in Appendix F. With this system, it is then possible to measure simultaneously extinction signals at seven different wavelengths.
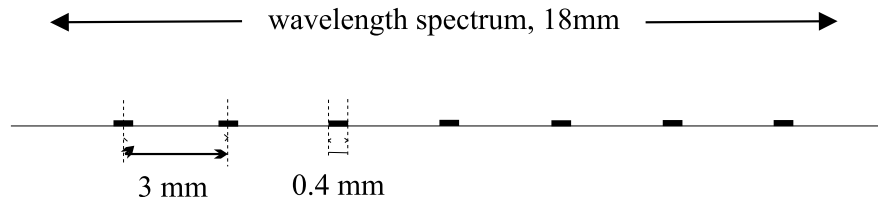

Figure 3.8: *Detail of the detection system. Data acquisition takes place at seven equidistant locations in the spectrum.*

Chapter 4

Holographic interferometry

4.1   Introduction

Flow visualisation techniques are important diagnostic tools for the experimental investigation of transparent media since they provide instantaneous qualitative information through two/three-dimensional images of the flow field. Further, they may also provide information on the spatial variation of some field properties, by measuring the distortions undergone by the wavefront which traverses the flow field. These distortions are produced every time a light beam passes through a medium where gradients in the refractive index are present. The refractive index of an optical medium is defined as the ratio between the speed of light in vacuum and the speed of light in that particular medium. Therefore, gradients in the refractive index cause the different parts of the wavefront to propagate at different speeds and, thus, introduce phase distortions. By means of interferometry this phase delay is measured, which is proportional to a line integral of the density along the light path through the flow field. In this respect, it provides not only a means to visualise these distortions, but it can be also used for obtaining quantitative information on the density field. This chapter deals with a particular application of interferometry and specifically holographic interferometry. This means that at least one of the interfering wavefronts is generated holographically.

Holography is a unique imaging technique since, contrary to traditional photographic or digital methods, it assures that both the amplitude and phase of the wavefront can be retrieved, thus providing an exact replica of the original wave. The first experiments in holography were conducted by Dennis Gabor in 1948 [41, 42]. In spite of the fact that recording media respond only to irradiance, Gabor first recognised that both the amplitude and phase of a wave scattered by an object could still be stored. This can be achieved by recording on a transparency the interference pattern due to this scattered wave and a mutually coherent reference wave. Second, he demonstrated that, upon chemically processing the photographic film, a kind of grating was obtained by way of a fringe configuration, which he called *hologram*. Then, upon re-illuminating the hologram with a collimated beam, a replica of the original wave was produced by diffraction from this grating. Two

remarks stem immediately from this brief description: first the phenomena of interference and diffraction are central to an understanding of the process of holographic imaging. These phenomena are, therefore, tackled in a concise manner in subsection 4.2.1. Second, the properties of the hologram and the quality of the reconstructed image strongly depend on the diffraction or imaging conditions that exist between the object and the photographic plate. Thus, one refers to a *Fresnel* hologram when the recording plane lies in the region of Fresnel diffraction, whereas it is a *Fraunhofer* hologram when the transformation from object to the hologram plane is best described by the Fraunhofer diffraction equation. It is beyond the scope of this chapter to provide a detailed classification and analysis of the different types of holograms and related properties. For more information, the reader is referred to the many existing textbooks, such as those of Vest [147], Caulfield [19], Collier *et al.* [21]. A recent review on the most recent developments in the technique of holographic imaging can be found in Hariharan [51].

This chapter focuses on a particular type of hologram: the *image* hologram and its application to the technique of double exposure interferometry. The *image* hologram possesses a series of properties which make it particularly attractive for the study of two-dimensional flow fields, and is therefore described in some detail in section 4.3. Section 4.4 describes the technique of double exposure interferometry, while in section 4.5 the specific method employed to analyse the interferograms is discussed.

4.2 Principles of holographic imaging

The fundamental problem addressed by holography is that of recording and later reconstructing both the amplitude and phase of an optical wave scattered by a coherently illuminated object. The formation of a hologram is an interferometric process, while the reconstruction of holographically recorded optical waves involves diffraction. To this purpose, this section starts with a concise summary of interference and diffraction phenomena. Then, the processes of wavefront reconstruction and image formation are explained for the case of an off-axis Fresnel hologram. This choice is dictated by two main reasons. First, the optical system required to generate Fresnel holograms is one of the simplest and, thus, it is the most suitable one to introduce the basic concepts of holographic imaging. Second, the importance of the imaging conditions and the advantages of image holography are best appreciated when comparing different optical systems.

4.2.1 Interference and diffraction

Interference
A standard technique to convert phase information into intensity variations, for recording purposes, is interferometry. It consists of adding to the unknown wavefront a second one, mutually coherent with the first and of known amplitude and phase. Then, the irradiance of the sum of the two complex fields depends on both the amplitude and phase of the

unknown wavefront. Thus if

$$E_1(x, y) = |E_{01}(x, y)| e^{-i\phi_1(x,y)}, \tag{4.1}$$

represents the complex amplitude of the unknown wavefront and if

$$E_2(x, y) = |E_{02}(x, y)| e^{-i\phi_2(x,y)}, \tag{4.2}$$

represents the reference wave, the irradiance of the sum of the two beams: $E = E_1 + E_2$, is given by:

$$\begin{aligned}
I &= |E|^2 = |E_1|^2 + |E_2|^2 + 2\,|E_1|\,|E_2|\,\cos(\phi_1 - \phi_2), \\
&= \underbrace{I_1 + I_2}_{bias} + \underbrace{2\,(I_1 I_2)^{1/2}\cos(\phi_1 - \phi_2)}_{modulation},
\end{aligned} \tag{4.3}$$

where I_1, I_2 are the irradiances of two waves and $\Delta\phi = (\phi_1 - \phi_2)$ represents the phase difference between the two waves at the considered location. In the above formula, one can distinguish a bias irradiance (*background*), and a modulation term (*contrast*). In the latter term, the phase ϕ_1 of the unknown wavefront is, then, encoded by way of a fringe pattern. Note that if the two vectors are perpendicularly polarised, the total irradiance is simply the sum of the two irradiances, and no interference is observed. In all other cases, some degree of interference is present. The total irradiance varies from a minimum value $I_{min} = I_1 + I_2 - 2(I_1 I_2)^{1/2}$ at points where $\Delta\phi = (2m+1)\pi$ (m is an integer), to a maximum $I_{max} = I_1 + I_2 + 2(I_1 I_2)^{1/2}$ where $\Delta\phi = 2m\pi$. The visibility (*contrast*) of the fringes is defined as:

$$\frac{I_{max} - I_{min}}{I_{max} + I_{min}}. \tag{4.4}$$

To obtain the phase delay from an interferogram, the contrast of the fringes should be as high as possible. For the best visibility, the intensity of the beams should be equal as well as their polarisation.

The above analysis is strictly valid under the assumption of monochromatic light sources. However, real sources are always radiating within a well-defined range of wavelengths $\Delta\lambda$ to which corresponds a set of frequencies $\Delta\nu$. The coherence length is then defined as $c/\Delta\nu \approx \lambda_0^2/\Delta\lambda$, where c is the speed of light and λ_0 is the average wavelength of the light source. If the mismatch between the pathlengths of the interfering beams exceeds the coherence length of the light source, then the fringe visibility decays to zero.

Diffraction

Diffraction relates simply to the fact that if a portion of a wavefront is obstructed by some obstacles, the remaining unobstructed part gives rise to a very complicated interference pattern whose characteristics depend on the geometry of the obstacles, and on the reciprocal distance between the light source and the plane of observation. Recalling the Huygens-Fresnel principle [53], one can envision the unobstructed wavefront as an array of in-phase coherent oscillators, which act as sources of secondary spherical wavelets. Then,

the difference in phase among each contribution is crucial to the determination of the field at P, as shown in Fig. 4.1.
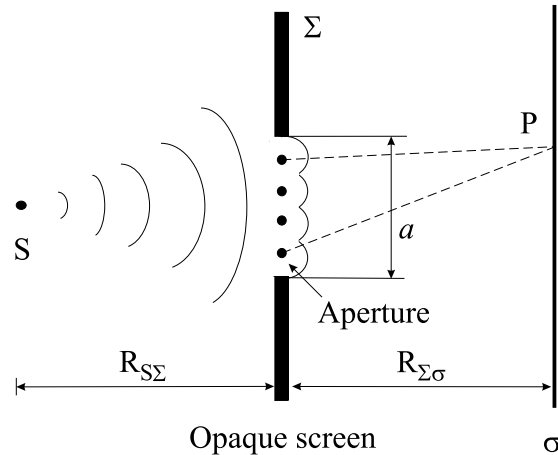

Figure 4.1: *Schematic representation of diffraction from an aperture.*

For a detailed treatment of diffraction, the reader is referred to the book of Hecht [53]. Here only a few basic notions are recalled, which are fundamental for an understanding of the reconstruction process. Essentially the characteristics of the diffracted field depend on the relative distance of the light source and/or the plane of observation from the aperture. If this relative distance is small, then the phenomenon known as Fresnel or near-field diffraction appears. In this case, the curvature of the incoming and outgoing wavefronts cannot be neglected. If the plane of observation is moved to a greater distance (infinity), the Fraunhofer or far-field diffraction is obtained. In practice, as long as both the incoming and outgoing wave can be approximated to being planar over the extent of the diffracting aperture (i.e. differing therefrom by a small fraction of the wavelength), Fraunhofer diffraction prevails. As a practical rule of thumb, Fraunhofer diffraction occurs when $R > a^2/\lambda$ where a is the width of the aperture and R is the smaller of the two distances from the source (S) to the aperture (Σ) and from the latter to the screen (σ), i.e. $R = min\{R_{S\Sigma}, R_{\Sigma\sigma}\}$.

Because of its importance in understanding the functioning of gratings and its relevance for the *image* hologram, a short description of Fraunhofer diffraction is presented. A practical realisation of the Fraunhofer condition, where both (σ) and (S) are effectively at infinity, is achieved by using the arrangement depicted in Fig. 4.2(a). The effect of lens L_2 placed behind the object is that of shifting the image plane (σ) from infinity to its back focal plane. Recalling a few notions of Fourier analysis [44], the field distribution of the Fraunhofer diffraction pattern can be expressed as the Fourier transform of the field distribution across the aperture. Bearing in mind this interpretation, the function performed by the lens in Fig. 4.2(a) becomes clear. The object scatters plane waves (its Fourier components), which are collected by the lens, and parallel bundles of rays are brought to convergence at its back focal plane. If a screen is placed there, the so-called
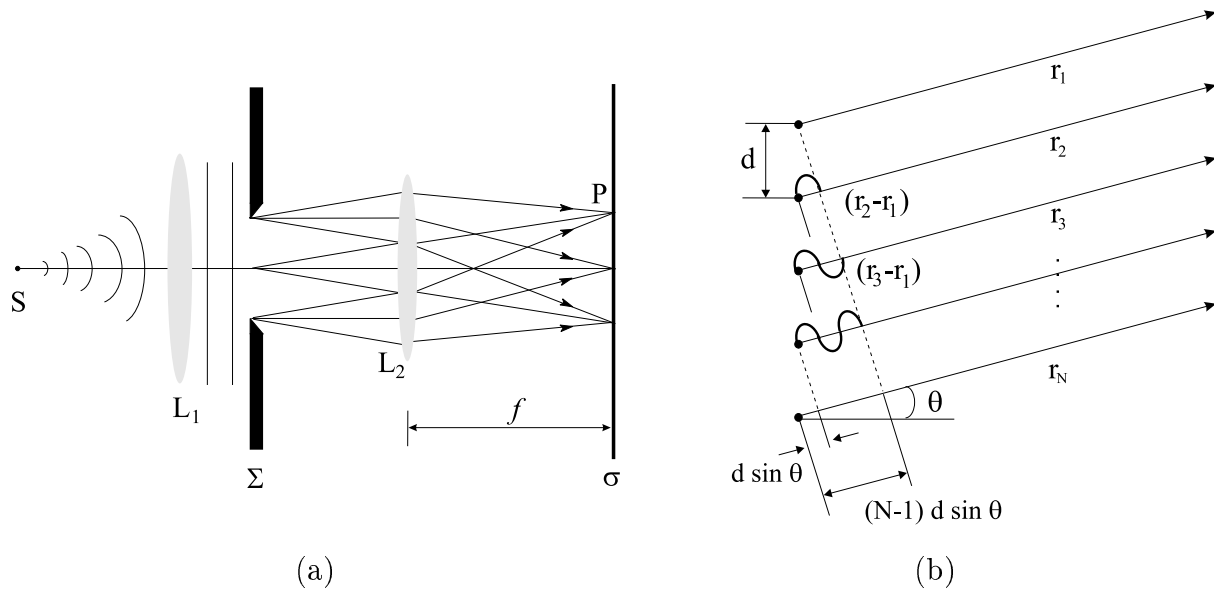
Figure 4.2: *Fraunhofer diffraction. (a) Typical set-up to visualise Fraunhofer diffraction. (b) One of the many sets of wavefronts emitted from a line of coherent point sources.*

transform plane, the far field diffraction pattern of the object would be seen, or in other words the spatial frequency spectrum of the diffracting object. Incidentally, it is important to realise that in case the aperture of the lens is not large enough to collect all diffracted light, the higher spatial frequencies are rejected and effectively the lens acts as a low-pass filter. This effect is known as *vignetting* and represents the limiting factor which ultimately defines, for a given imaging system, the sharpness and resolution of the image.

The irradiance distribution within the diffraction pattern due to N coherent and identical point sources, shown in Fig. 4.2(b), is given by [53]:

$$I = I_0 \frac{\sin^2[N(kd/2)\sin\theta]}{\sin^2[(kd/2)\sin\theta]}, \tag{4.5}$$

where N is the number of oscillators, d is the distance between two consecutive oscillators, and k is the wave number. The quantity $\delta = kd\sin\theta$ represents the phase difference between adjacent sources. This expression produces to a series of sharp principal peaks, separated by small subsidiary maxima. The principal maxima occur in directions θ_m, such that $\delta = 2m\pi$, where $m = 0, \pm 1, \pm 2, \ldots$. Then it follows that:

$$d\sin\theta_m = m\lambda. \tag{4.6}$$

Equation (4.6) is known as the *grating equation* for normal incidence. The values of m specify the order of the various principal maxima. The $m = 0$, or zeroth-order, peak corresponds to the undeflected light ($\theta = 0$), different values of m correspond to higher orders and are obtained at larger angles θ. The smaller the distance (d), the lower will be the number of visible orders. A repetitive array of diffracting elements, either apertures

or obstacles, that has the effect of producing periodic alterations in the phase and/or amplitude of an emergent wave is said to be a diffraction grating. In the case of a sinusoidal grating, Eq. (4.6) still holds, however only few orders are observable: the zero-frequency central peak and the first orders ($m = \pm 1$) on either side of the centre.

4.2.2 Holographic imaging and magnification

Objective of this section is to introduce the principles of wavefront reconstruction and image formation by means of holographic techniques. The characteristics of the reconstructed image strongly depend on the location and type of optical waves used in the recording and reconstruction process. To illustrate this dependence, the analysis of Goodman [44] is briefly summarised hereafter.

Consider, therefore, two point sources representative of the reference and object wave, respectively, and situated at the positions (x_r, y_r, z_r) and (x_o, y_o, z_o), as shown in Fig. 4.3(a). Further, it is assumed for generality that during the reconstruction process, the hologram is illuminated by a point source situated at the coordinates (x_p, y_p, z_p), as indicated in Fig. 4.3(b). The recording wavelength is λ_1, the reconstruction one is λ_2.
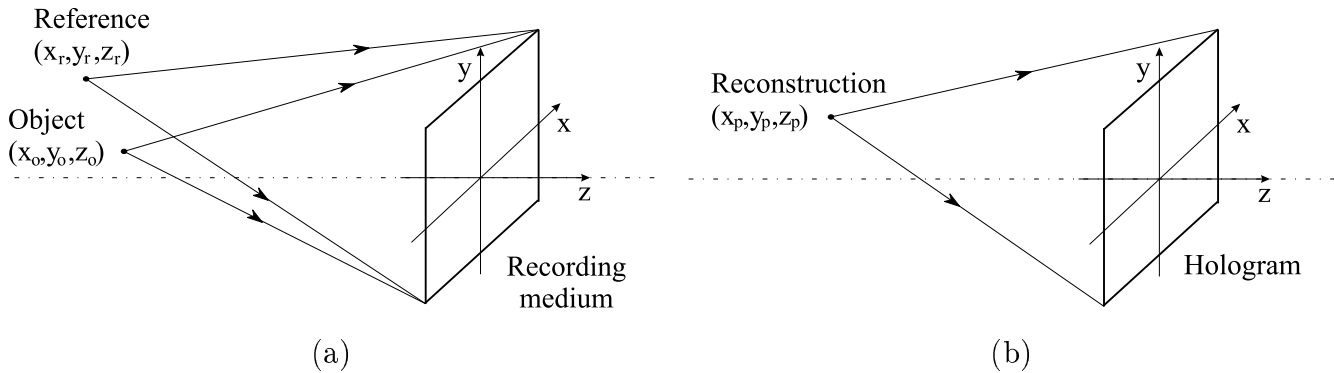
Figure 4.3: *Generalised recording (a) and reconstruction (b) systems.*

Since only spherical waves are considered, the complex amplitude of the total field, due to the interference of reference and object beams, is:

$$
\begin{aligned}
U_{tot}(x, y) &= U_r \exp \left\{ -i \frac{\pi}{\lambda_1 z_r} [(x - x_r)^2 + (y - y_r)^2] \right\} + \\
&\quad + U_o \exp \left\{ -i \frac{\pi}{\lambda_1 z_o} [(x - x_o)^2 + (y - y_o)^2] \right\},
\end{aligned}
\tag{4.7}
$$

where the subscripts (r,s) denote reference and object wave. U_r and U_o represent the amplitude and relatives phases of the two spherical waves, i.e. U_r and U_o are both complex.

The resultant intensity at the photographic plate is:

$$I(x, y) = |U_r|^2 + |U_o|^2 \tag{4.8}$$

$$+ \underbrace{U_r U_o^* \exp\left\{ -i\frac{\pi}{\lambda_1 z_r}[(x - x_r)^2 + (y - y_r)^2] + i\frac{\pi}{\lambda_1 z_o}[(x - x_o)^2 + (y - y_o)^2] \right\}}_{t_3}$$

$$+ \underbrace{U_r^* U_o \exp\left\{ i\frac{\pi}{\lambda_1 z_r}[(x - x_r)^2 + (y - y_r)^2] - i\frac{\pi}{\lambda_1 z_o}[(x - x_o)^2 + (y - y_o)^2] \right\}}_{t_4}.$$

Assuming that, after chemical processing, the transparency has an amplitude transmittance proportional to exposure, the film transmittance can be written as

$$\tau(x, y) = \tau_0 + \beta t\, I(x, y), \tag{4.9}$$

where β is the slope (a negative number for a negative transparency) of the amplitude transmittance versus exposure characteristic of the photographic material, t is the exposure time, and τ_0 is a constant background transmittance. To regenerate the image, the hologram is illuminated with a reconstruction beam, which may (or may not) coincide with the reference beam of the recording phase. To keep the analysis as general as possible, a spherical wave of wavelength λ_2 is chosen as reconstruction beam:

$$U_{rec}(x, y) = A_{rec} \exp\left\{ -i\frac{\pi}{\lambda_2 z_p}[(x - x_p)^2 + (y - y_p)^2] \right\}. \tag{4.10}$$

The complex amplitude $U_t(x, y)$ of the transmitted wave can be obtained by multiplying the film transmittance (Eq. 4.9) by the reconstruction wave U_{rec}. After some algebra, the two wavefronts of interest behind the transparency can be expressed as

$$\begin{aligned} U_3(x, y) &= \beta t\, t_3\, U_{rec}(x, y), \\ U_4(x, y) &= \beta t\, t_4\, U_{rec}(x, y). \end{aligned} \tag{4.11}$$

Goodman [44] showed that these two waves emerging from the hologram can be expressed as a product of quadratic-phase exponentials and, thus, can be cast in the form

$$U_i(x, y) = A_i \exp\left\{ -i\frac{\pi}{\lambda_2 z_i}[(x - x_i)^2 + (y - y_i)^2] \right\}, \tag{4.12}$$

where the subscript "i" stands for image wavefront. By equating the corresponding phase terms expressing the (x, y, z) dependence, the coordinates of the image of the point source can be found. These are:

$$\begin{aligned} z_i &= \left(\frac{1}{z_p} \pm \frac{\lambda_2}{\lambda_1 z_r} \mp \frac{\lambda_2}{\lambda_1 z_o} \right)^{-1}, \\ x_i &= \mp \frac{\lambda_2 z_i}{\lambda_1 z_o} x_o \pm \frac{\lambda_2 z_i}{\lambda_1 z_o} x_r + \frac{z_i}{z_p} x_p, \\ y_i &= \mp \frac{\lambda_2 z_i}{\lambda_1 z_o} y_o \pm \frac{\lambda_2 z_i}{\lambda_1 z_o} y_r + \frac{z_i}{z_p} y_p. \end{aligned} \tag{4.13}$$

Equations (4.13) provide the fundamental relations that allow to predict the location of the images created by the holographic process. These results can be generalised to an extended object by regarding the latter as a collection of mutually coherent point sources. As can be deduced from these relations, the location of the image strongly depends on the positions of the reference and object wave and on the wavelengths used. Depending on the optical configurations, these images can be one real and the other virtual or both real. The last-named case occurs, for example, when both the reference and object waves originate from infinity (i.e. parallel waves). Then, relations (4.13) indicate clearly that both conjugate images are also at infinity ($z_i \Rightarrow \infty$) and, thus, only real images are produced.

From equations (4.13), it is also possible to derive the transverse and axial magnification of the holographic process. These magnifications are given by:

$$
\begin{aligned}
M_t &= \left| \frac{\partial x_i}{\partial x_o} \right| = \left| \frac{\partial y_i}{\partial y_o} \right| = \left| 1 - \frac{z_o}{z_r} \mp \frac{\lambda_1 z_o}{\lambda_2 z_p} \right|^{-1} , \\
M_a &= \left| \frac{\partial z_i}{\partial z_o} \right| = \left| \frac{\partial}{\partial z_o} \left(\frac{1}{z_p} \pm \frac{\lambda_2}{\lambda_1 z_r} \mp \frac{\lambda_2}{\lambda_1 z_o} \right)^{-1} \right| = \frac{\lambda_1}{\lambda_2} M_t^2 .
\end{aligned}
\tag{4.14}
$$

It is worth noticing that, in general, these two magnifications will not be identical. Considering Eqs. (4.13) and (4.14), it can be deduced that the use of reference beams of different wavelengths for the recording and reconstruction process introduces a shift in the image location and is responsible for additional axial and transverse distortions in the final image. Further, even if the wavelength is not changed, the holographic imaging process is not able to reconstruct the wavefront without introducing some degree of distortion in the image, as inferable from Eq. (4.14). Fortunately, this conclusion does not hold for the image hologram, which holds a privileged status among most holograms types. In fact, if all wavefronts are at infinity (i.e. parallel waves), then both magnifications tend to the limiting value of one: that is, the hologram is able to transform plane waves into plane waves, without introducing distortions, and is insensitive to the reconstruction wavelength.

4.2.3   Fresnel holography

This section illustrates how the principles of holographic imaging, introduced in the previous section, can be applied to an extended object. The analysis is conducted for one of the simplest configurations of the imaging system, shown in Fig. 4.4(a) and under the following assumptions:

(i)   *both the object and reference beam originate from the same light source;*

(ii)   *the reference wave is a collimated beam of uniform intensity, impinging on the hologram at an offset angle θ;*

(iii)   *the photographic plate is located in the region of Fresnel diffraction from the object.*

Under these hypotheses, the complex amplitude of the object beam at any point (x,y), on the recording plane z_0, can be written as:

$$U_o(x, y, z_0) = u_o(x, y, z_0) \exp\left[-i\varphi(x, y, z_0)\right], \tag{4.15}$$

while that due to the reference beam is:

$$U_r(x, y, z_0) = u_r(x, y, z_0) \exp\left(-i2\pi\xi_r x\right), \tag{4.16}$$

where $\xi_r = \sin\theta/\lambda$ is the spatial frequency at which the reference beam crosses the photographic plane along the x axis. The resultant intensity at the photographic plate is, omitting the z coordinate:

$$
\begin{aligned}
I(x, y) &= \left|U_r(x, y) + U_o(x, y)\right|^2, \\
&= \left|U_r(x, y)\right|^2 + \left|U_o(x, y)\right|^2 + u_r u_o e^{-i\varphi(x,y)} e^{i2\pi\xi_r x} + u_r u_o e^{i\varphi(x,y)} e^{-i2\pi\xi_r x}.
\end{aligned}
\tag{4.17}
$$

To reconstruct the image, the hologram is illuminated once again with the same reference beam used to record it, as shown in Fig. 4.4(b).
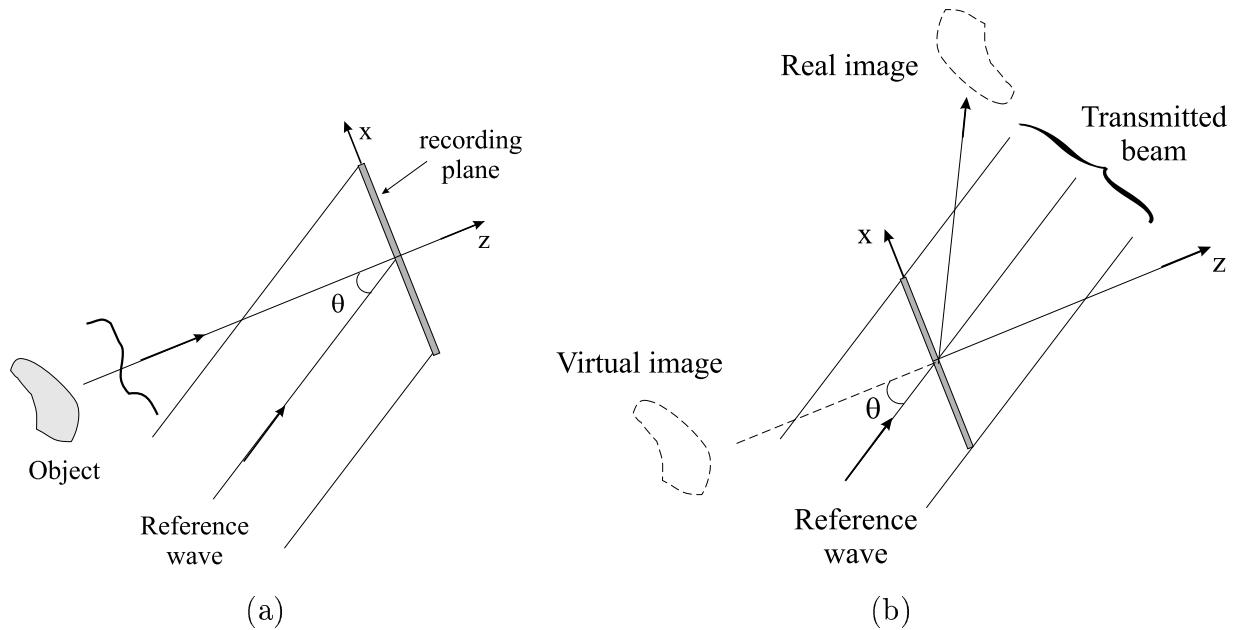

Figure 4.4: *Fresnel hologram: off-axis configuration. (a) Recording process. (b) Reconstruction process.*

In the usual fashion, Eq. (4.9) yields for the complex amplitude $U_t(x, y)$ of the transmitted wave:

$$
\begin{aligned}
U_t(x, y) &= U_r(x, y)\,\tau(x, y), \\
&= U_1(x, y) + U_2(x, y) + U_3(x, y) + U_4(x, y),
\end{aligned}
\tag{4.18}
$$

where

$$
\begin{aligned}
U_1(x,y) &= (\tau_0 + \beta t u_r^2)u_r \exp\left(-i2\pi\xi_r x\right), \\
U_2(x,y) &= \beta t u_r \left|U_o(x,y)\right|^2 \exp\left(-i2\pi\xi_r x\right), \\
U_3(x,y) &= \beta t u_r^2 U_o(x,y), \\
U_4(x,y) &= \beta t u_r^2 U_o^*(x,y) \exp\left(-i4\pi\xi_r x\right).
\end{aligned}
\tag{4.19}
$$

The transmitted wave $U_t(x,y)$ results in the sum of four terms, each corresponding to one of the terms of Eq. (4.17). The first term on the right-hand side $U_1(x,y)$ is merely the attenuated reference beam, which is a plane wave directly transmitted through the hologram. The second term $U_2(x,y)$ creates a halo around $U_1(x,y)$, whose angular spread is determined by the extent of the object boundaries $\left|U_o(x,y)\right|^2$. The third term $U_3(x,y)$ is, aside from a constant factor, identical to the original object wave. Thus, it must appear to an observer to be caused by the original object, in spite of the fact that the latter has been removed. In other words, $U_3(x,y)$ generates a virtual image of the object in its original position. This image is at an angle θ with respect to the directly transmitted wave. Similarly, the fourth term $U_4(x,y)$ gives rise to the conjugate image. This corresponds to a real image as a result of an actual focusing of light in space. The factor $[\exp\left(-i4\pi\xi_r x\right)]$ indicates that the conjugate image is deflected from the z axis at an angle θ_1, approximately twice the angle at which the reference beam intersected the z axis: $\theta_1 \approx 2\sin^{-1}(\xi_r\lambda)$. From these considerations, it is clear that the two images reconstructed with this configuration are angularly separated and, thus, do not overlap. The minimum angle θ (or similarly minimum spatial frequency ξ_r) for which no overlapping of images occurs can be derived from Fourier analysis and results in the condition: $\xi_r > 3\,\xi_{max}$, where ξ_{max} is the highest spatial frequency in the object beam spectrum.

4.3   The image hologram

This section deals with a particular application of holographic imaging, which is especially attractive for transparent media and two-dimensional fields. The idea for adopting such optical configuration is essentially inspired by the work of Takayama, Onodera *et al.* [60, 81, 135], who combined a schlieren system with a holographic interferometer. A schematic representation of the set-up is plotted in Fig. 4.5. To understand the properties of a hologram produced with this configuration, first an heuristic description of the optical properties of this set-up is provided.

The object beam is collimated by the lens L_1 and the spherical mirror PM_1. Upon traversing the test section, the beam is diffracted and/or distorted by any obstacle or non-homogeneity present in the test chamber. This distorted wavefront can be resolved into a new set of plane waves (its Fourier components), each corresponding to a specific order (i.e. spatial frequency) and travelling in a specific direction. As an example, one of these components is also depicted in Fig. 4.5. The objective mirror PM_2 serves as a transform lens producing the Fraunhofer diffraction pattern of the object on the transform

plane Σ_t (which is located in the front focal plane of L_2). In other words, it produces on Σ_t a two-dimensional Fourier transform of the object beam. That is, the spatial frequency spectrum of the object is spread across this plane. Lens L_2 projects this diffraction pattern, distributed over Σ_t on the image plane. Therefore, the combined effects of PM_2 and L_2 is to image the test section (i.e. plane Σ_o) onto the holographic plate Σ_h.
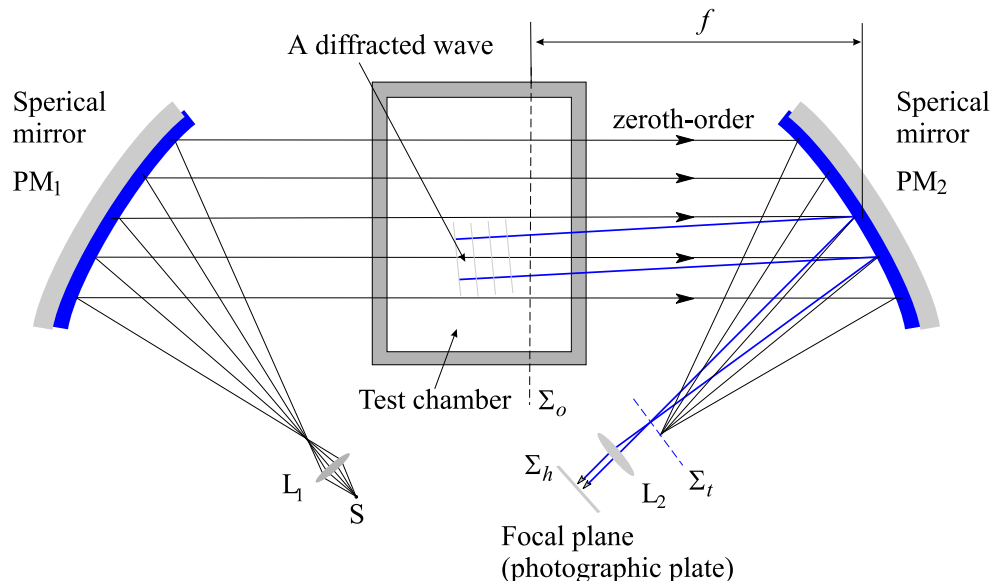
Figure 4.5: *Schematic representation of the optical system used to generate the image hologram.*

Note that the specific location of the plane Σ_o does not affect the quality of the image, but only the phase of the complex amplitude distribution. This property is very important and useful when dealing with interferometric studies of transparent media, where in presence of strong refractive fields, it may be necessary to shift the plane of focus in order to minimise refraction errors [72, 147]. The reference beam passes outside the test section and is collimated by a combination of lenses analogous to L_1 and L_2. Then, it impinges at an angle θ on the hologram, where interferes with the object beam. A more detailed description of the holographic interferometer can be found in section 3.2. This section focuses primarily on the characteristics and properties of the generated hologram.

The optical configuration described above produces a special type of hologram, which can be defined as an off-axis *image* hologram, using collimated beams. Image holograms are characterised by the fact that a real image of the object is recorded, instead of the object itself. As mentioned before, this is, in fact, the function exploited by mirror PM_2 and lens L_2. The main advantage of the image hologram is that a sharp image of the test section can be obtained. The diffraction efficiency of the set-up is, in fact, determined by the aperture of the objective mirror PM_2. If this is large enough to collect all diffracted light, then a sharp image can be produced. This is not true in the case of Fresnel holograms, where the high spatial frequencies are inevitably lost. A second important feature of this

optical configuration is the use of collimated beams both for recording and reconstruction purposes. As explained in section 4.2.2, this assures the generation, in the reconstruction phase, of two real images, completely free of distortions. A few properties of the *image* hologram are discussed in more detail in subsection 4.3.1 and compared to those of classical Fresnel holography.

Denoting with $U_o(\xi, \eta) = u_o(\xi, \eta) \exp[-i\varphi(\xi, \eta)]$ the complex amplitude of the object wave in the plane of focus Σ_o, the first step is to determine the complex amplitude of the object wave $U_h(x, y)$, in the recording plane Σ_h. The optical system (depicted in Fig. 4.5) projects an image of the object wave on this plane. According to geometrical optics (i.e. the effects of diffraction are neglected), the complex amplitudes of image and object are related by

$$U_h(x, y) = \frac{1}{|M|} U_o(\xi, \eta), \tag{4.20}$$

where x, y denote the coordinates in the recording plane and the factor $M = -f_2/f_1$ represents the magnification of the imaging system.

Assuming that the reference beam is a simple collimated wave, impinging on the hologram at angle θ_0 to the object beam, it can be expressed as $U_r(x, y) = u_r(x, y) \exp[-i2\pi\xi_0 x]$. The intensity pattern recorded on the photographic plate is:

$$\begin{aligned} I(x, y) &= |U_r(x, y) + U_h(x, y)|^2; \\ &= |U_r(x, y)|^2 + |U_h(x, y)|^2 + U_r^* U_h + U_r U_h^*. \end{aligned} \tag{4.21}$$

After chemical processing the transparency, the transmitted wave $U_t(x, y)$ can be obtained by multiplying the reconstruction beam $U_r(x, y)$ by the amplitude transmittance $\tau(x, y)$ (Eq. 4.9). As for Fresnel holography, $U_t(x, y)$ results in the sum of four terms. The two wavefronts of interest, denoted with $U_3(x, y)$ and $U_4(x, y)$ are

$$\begin{aligned} U_3(x, y) &= \beta t u_r^2 U_h(x, y), \\ U_4(x, y) &= \beta t u_r^2 U_h^*(x, y) \exp\left(-i4\pi\xi_o x\right). \end{aligned} \tag{4.22}$$

Contrary to the case of Fresnel holography, both U_3 and U_4 are, in this case, plane waves. As demonstrated in section 4.2.2, if plane wavefronts are used in the recording and reconstruction procedure, only plane waves are transmitted by the hologram. U_3 propagates along the original direction of the object wave; U_4 is deflected by an angle $\theta_0 \approx 2 \sin(\xi_0\lambda)$. The reconstruction process is, then, accomplished by placing the hologram in a beam of coherent light and using a lens to take the Fourier transform of the complex wavefront emerging from the hologram. This operation can be achieved by placing a lens right after the hologram, to minimise the vignetting effect, and observing the Fraunhofer diffraction pattern in the back focal plane of this lens. This configuration is shown in Fig. 4.6.
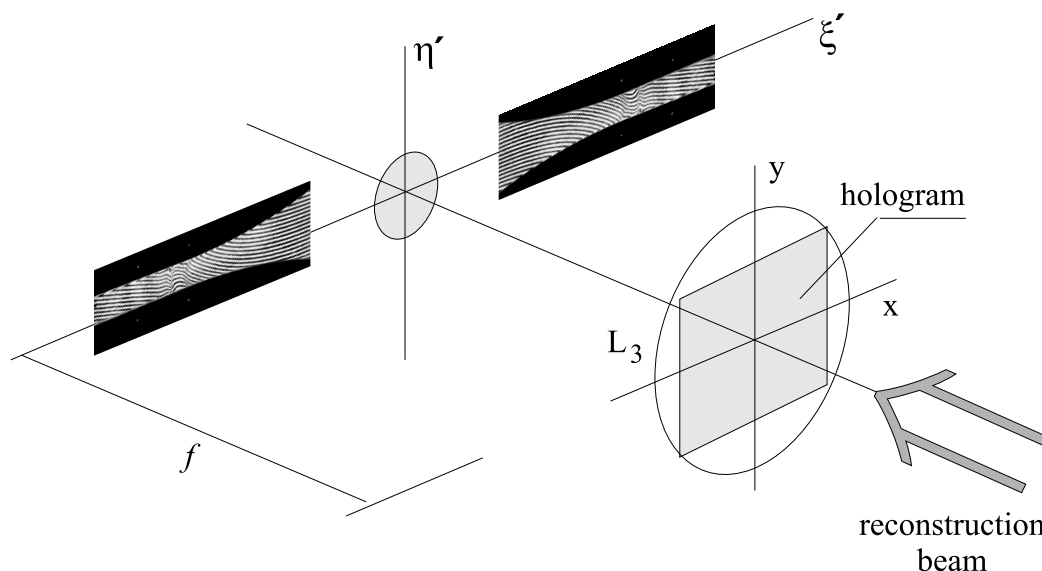
Figure 4.6: *Reconstruction of real images from an image hologram. Real images are obtained only if collimated beams are employed both in the recording and reconstruction process.*

Since the Fourier transform operation may be regarded as a decomposition of a complicated wavefront into a collection of plane waves propagating in different directions, two conjugate plane wavefronts, corresponding to two real images, will appear in the back focal plane of lens L_3, as shown in Fig. 4.6. Due to the presence of the exponential term $\exp\left(-i4\pi\xi_o x\right)$, the image U_{4i} is shifted with respect to U_{3i} by an amount $(2\,\xi_0)$. These two conjugate images can only be distinguished by the fact that they are inverted. To obtain a photographic and/or digital recording of the interferogram, one of these images has to be selected. Since in the plane ξ', η', no sharp image can be obtained, the actual reconstruction system is in practice more complicated than the one depicted in Fig. 4.6. A detailed description of the reconstruction set-up can be found in section 3.2.1. Here only its main components are briefly listed. First, a system of lenses is required to obtain a sharp image of the hologram on the desired plane. Second, the quality of the reconstructed image is greatly improved by spatially filtering the chosen wavefront from any undesired background light.

4.3.1   Properties of the image hologram

This subsection focuses on some of the advantages offered by the collimated image hologram relative to traditional Fresnel holography. This review is certainly not exhaustive. For more detailed information, the reader is referred to the book of Caulfield [19] and Hariharan [51].

Image aberration

In general, the quality of the image obtained with holographic imaging techniques is strongly limited by all sorts of aberrations introduced during the reconstruction process. In this context, the collimated image hologram offers a major advantage. Since in this type of hologram both the object and the reference wave are effectively at infinity in the recording step, this assures that practically aberration free images may be always reconstructed, even when the reconstruction beam is not coinciding with the recording reference beam. The reason for this is that if a hologram must change the curvature of an incident wave, aberrations are inevitably introduced. However, whenever the object and the reference source are projected to infinity, all the waves incident on the holograms in the recording step are plane waves. If the hologram is then reconstructed with any plane wave, an aberration-free image results, because a hologram can transform an incident plane wave into another plane wave without introducing aberrations.

Image sharpness and Resolution limit

As pointed out in section 4.2.1, the sharpness of an image is strongly dependent on the aperture of the objective lens. If this is not large enough to collect all diffracted light from the object, this results in a loss of image sharpness and resolution. Goodman [44] showed that if the diameter of the lens is at least twice the diameter of the object field, then a space-invariant Fourier transform of the object may be obtained, provided that no spatial frequency greater than $R/2\lambda d$ is present in the object frequency spectrum, where R is the radius of the objective lens and d is the distance from the object to the lens. This frequency takes the name of cut-off frequency of the imaging system and, in this specific application, it is equal to $f_{co} = 7.20 \cdot 10^4 \ m^{-1}$. In case of an off-axis Fresnel hologram, the cut-off frequency is much lower due to the smaller aperture of the holographic film. To increase its value, the distance d between object and lens is often reduced. However, this results in a decrease of the resolving power of the imaging system. The latter is, in fact, defined as $1/(\Delta l)_{min}$, where $(\Delta l)_{min} = 1.22 f\lambda/d$ is the smallest resolvable separation in the image and f is the focal distance of the imaging lens. This optical configuration, thus, guarantees the best compromise between image resolution and sharpness.

4.4   Double exposure holographic interferometry

Holographic interferometry represents one of the most important scientific applications of holographic imaging. There exist several different modalities of performing holographic interferometry, a detailed treatment on this topic can be found in the books of Vest [147] and Schumann [123]. Despite this large variety, they all rely on the ability of a hologram to store two or more complex wave fields on the same recording medium. Then, due to the linearity of the recording process, these wavefronts are all reconstructed independently. The subsequent interference pattern is generated upon reconstruction and is only visible in the imaging plane of the camera lens. Holographic recording introduces, thus, a third dimension, namely *time*, in that it is now possible to compare, interferometrically, wavefronts generated at different time instants.

   This section focuses specifically on the technique of double exposure interferometry. In this process, two recordings are made on the hologram: one serves as reference state, the other serves to measure the spatial variation of the quantity of interest. For this particular application, the two exposures correspond to the following states: a reference state with the mixture at rest (no flow) and a second recording with the flow activated in the test section. The major advantage of such technique is that all imperfections due to the optical components (lenses, mirrors etc.) cancel out reciprocally, thus improving the quality of the measurements. To appreciate fully this property of double exposure interferometry, the resultant intensity on the photographic plate is calculated explicitly. Irrespective of the specific imaging conditions (Fresnel, Fourier, ... hologram types), the wavefronts impinging on the recording plate can be cast in the form:

$$
\begin{aligned}
U_h(x,y) &= u_h(x,y)e^{-i\varphi_0(x,y)}, \\
U_h^{'}(x,y) &= u_h(x,y)e^{-i[\varphi_0(x,y)+\Delta\varphi(x,y)]}, \\
U_r(x,y) &= u_r(x,y)e^{-ikx},
\end{aligned}
\tag{4.23}
$$

where $U_h(x,y)$ and $U_h^{'}(x,y)$ represent the object waves and $U_r(x,y)$ is the reference wave, which is assumed to be same in the two recordings. The underlying assumption in Eq. (4.23) is that small disturbances or deformations influence primarily the phase of the object wave and not its amplitude, which, as first approximation, can be considered constant between the two exposures. Indicated with $U_1 = U_r + U_h$ and $U_2 = U_r + U_h^{'}$ the total complex amplitude at each recording, the total irradiance is given by:

$$
\begin{aligned}
I(x,y) &= |U_1(x,y)|^2 + |U_2(x,y)|^2 \\
&= (U_r + U_h)(U_r + U_h)^* + (U_r + U_h^{'})(U_r + U_h^{'})^*, \\
&= u_r^2 + \underbrace{U_h U_r^*}_{a} + U_r U_h^* + u_h^2 + u_r^2 + \underbrace{U_h^{'} U_r^*}_{b} + U_r U_h^{'*} + u_h^{'2}.
\end{aligned}
\tag{4.24}
$$

It is important to realise that this equation provides an intensity distribution, which does not correspond to the desired interferogram, but is simply an encoding of the desired information. After chemically processing the hologram, this intensity pattern is then translated into a certain transmission, according to Eq. (4.9). Supposing that the hologram is reconstructed with the same reference beam used during the recording, the two imaging terms (a, b), which give rise to the desired interference pattern, can be expressed as:

$$
\begin{aligned}
U_3(x,y) &= \beta t u_r^2 U_h(x,y), \\
U_4(x,y) &= \beta t u_r^2 U_h^{'}(x,y).
\end{aligned}
\tag{4.25}
$$

These two waves are generated during the reconstruction procedure. As they interfere with each other, the desired interferogram is produced which carries the information on the changes in the flow field. This interferogram, thus, is visible only in the plane of focus of a camera lens looking through the hologram. Apart from a constant attenuating factor,

the two waves U_3 and U_4 are identical to the original object waves, and the final interference pattern is given by:

$$I_F(x, y) = |U_3(x, y) + U_4(x, y)|^2 = 2C_1 u_h^2 [1 + \cos \Delta\varphi(x, y)]. \qquad (4.26)$$

This intensity distribution provides the information on the changes occurred in the test section between the two exposures. The interferogram is also referred to as *infinite fringe* interferogram and the fringe pattern is directly proportional to variations in density.

If the reference beam is tilted in between the two exposures, then an additional set of fringes is produced and the interferogram is called a *finite fringe* interferogram. To understand how this set of carrier fringes can be introduced, consider Fig. 4.7(a) showing the tilting of the reference beam between the two recordings. In the hypothesis that both reference beams U_r and U_r' are situated in the y-z plane, follows that:

$$U_r(x, y) = u_r e^{-i\vec{k}\cdot\vec{r}}, \qquad (4.27)$$

where $\vec{k} = k_y \vec{e}_y + k_z \vec{e}_z$ is the wave number vector. Since the wavelength of the reference beam does not change during the two exposures, its modulus is simply $k = 2\pi\lambda^{-1}$ and its components along the coordinates axis are $k_y = \cos\alpha_y$ and $k_z = \cos\alpha_z$, respectively.
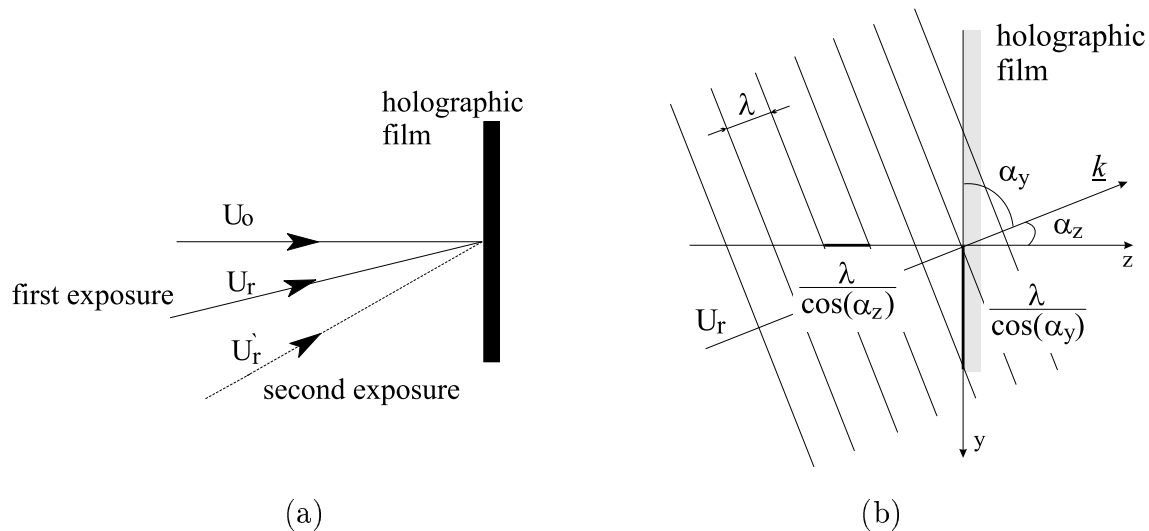

Figure 4.7: *Schematic representation of the recording process in the finite fringe interferogram. (a) Tilting of the reference beam. (b) Spatial angular frequency $\underline{k}$ of the reference beam $U_r(x, y)$.*

Denoted with f_y and f_z the spatial frequencies ($f_i = \cos\alpha_i \lambda^{-1}$, $i = y, z$), the four

wavefronts impinging on the hologram during the two exposures are given by:

$$
\begin{aligned}
U_r(x, y) &= u_r e^{-i2\pi[f_y y + f_z z]}; \\
U_h(x, y) &= u_h(x, y) e^{-i\varphi_0(x,y)}; \\
U_r'(x, y) &= u_r e^{-i2\pi[f_y' y + f_z' z]}; \\
U_h'(x, y) &= u_h(x, y) e^{-i[\varphi_0(x,y) + \Delta\varphi(x,y)]};
\end{aligned}
\tag{4.28}
$$

where the primes denote the wavefronts in the second exposure. Further, it is implicitly assumed that the amplitude of the object wave does not change appreciably, and the reference beam is simply a plane wave of uniform intensity. Then the irradiance I recorded on the hologram is given by:

$$
I(x, y) = (U_r + U_h)(U_r + U_h)^* + (U_r' + U_h')(U_r' + U_h')^*.
\tag{4.29}
$$

After some algebra and recalling the expression for the amplitude transmittance Eq. (4.9), the following two interfering waves emerge from the hologram:

$$
\begin{aligned}
U_3(x, y) &= \beta t u_r^2 U_h(x, y); \\
U_4(x, y) &= \beta t u_r^2 U_h'(x, y) e^{-i\varsigma} e^{-i2\pi(f_y - f_y')y};
\end{aligned}
\tag{4.30}
$$

where the quantity $\varsigma = 2\pi(f_z - f_z')z_0$ is constant along the photographic plate. Following exactly the same procedure as in the previous case, it can be shown that the intensity distribution of the interferogram is given by

$$
\begin{aligned}
I_F(x, y) &= (U_3 + U_4)(U_3 + U_4)^*, \\
&= 2C_1 u_h^2 [1 + \cos(\Delta\varphi(x, y) + 2\pi(f_y - f_y')y + \varsigma)].
\end{aligned}
\tag{4.31}
$$

Since the phase term ς is constant on the film plate, the set of carrier fringes is only dependent on the y-coordinate and results in a horizontal fringe pattern. The orientation of the lines (vertical or horizontal) depends simply on the way the reference beam is tilted in between the two recordings. If the tilting, instead of occurring in the yz-plane, as supposed here, is made in the xz-plane, then a series of vertical lines will appear. The resulting interference pattern, thus, shows carrier fringes modulated by the phase difference $\Delta\varphi$ due to density variations in the flow field. As an example, a typical interferogram is shown in Fig. 4.8. The flow proceeds from left to right. At inflow, the density of the mixture is almost constant and thus the fringe pattern stays basically horizontal. As the expansion proceeds along the nozzle, the density decreases and correspondingly the fringe pattern bends downward. This process continues until significant latent heat is released to the flow due to condensation effects. At this point the fringe pattern bends upwards indicating the local increase in the mixture density. This qualitative explanation is translated into quantitative information in section 4.5, where the extraction of density data from interferometric images is discussed.
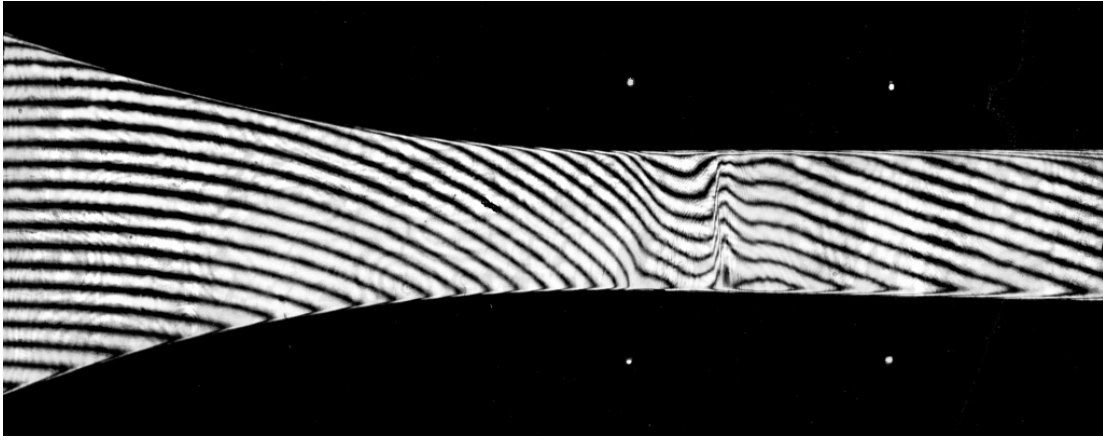
Figure 4.8: *Finite fringe interferogram. Nozzle: G2. Exp. H61 - Stagnation conditions:*
$P_0 = 9.13 \cdot 10^4 \ Pa$, $T_0 = 283.1 \ K$, $S_0 = 0.613$.

4.5   The interferogram

As discussed in the previous section, upon reconstruction of a hologram the two waves
scattered by the object at different times are simultaneously reconstructed. Their instan-
taneous interference pattern represents a contour map of the changes experienced by the
object between the two exposures. In the case of transparent media, the quantity actually
measured by interferometric studies is the change in refractive index due to some changes
in the object volume. Assuming that the refractive index is uniform during the first expo-
sure n_0, the optical pathlength difference $\Delta\Phi$ between the distorted and undistorted beam
can be written as [147]:

$$\Delta\Phi = \int [n(x(s), y(s), z(s)) - n_0]ds, \tag{4.32}$$

which results in a phase delay of

$$\Delta\phi = \frac{2\pi}{\lambda} \int [n(x(s), y(s), z(s)) - n_0]ds, \tag{4.33}$$

where $n(x, y, z)$ is the refractive index distribution during the second exposure, λ is the
wavelength of light, and s is the coordinate along the ray path. When refraction is negli-
gible, then the rays remain straight lines and the path integral becomes a line integral

$$\Delta\phi = \frac{2\pi}{\lambda} \int_0^L [n(x, y, z) - n_0]dz, \tag{4.34}$$

where L is the width of the test section and x, y are the coordinates perpendicular to the
light propagation direction z. Equation (4.34) provides the *actual* phase delay, which is
sought. It is, in fact, the phase delay due to changes in the refractive index $[n(x, y, z) - n_0]$

the quantity of interest, and not the delay due to integration along different paths. For 2-D fields it was shown that, in order to minimise refraction errors [61, 72], a plane at 2/3 of the width of the test section (measured from the entrance plane) should be imaged onto the hologram.

For humid nitrogen, the density may be derived from the refractive index using the Gladstone-Dale relation:

$$(n - 1) = K\rho, \tag{4.35}$$

where the Gladstone-Dale constant K for the mixture is given by

$$K = (1 - g) K_{N_2} + g K_{H_2O}. \tag{4.36}$$

Here, g is the specific humidity and the Gladstone-Dale constants [129, 138] for nitrogen and water vapour are $K_{N_2} = 0.236 \cdot 10^{-3} \ m^3/kg$ and $K_{H_2O} = 0.316 \cdot 10^{-3} \ m^3/kg$, at a wavelength of $\lambda = 694.3 \ nm$. Because of the low specific humidity encountered in the experiments, K is evaluated using the nozzle supply specific humidity. Thus, in determining K, the presence of the condensate is neglected. Since the condensate mass fraction cannot exceed the supply specific humidity ($g_{max} \approx 0.007$), the resulting error in density measurements is small. As can be inferred from the above discussion, the phase delay determined by interferometry is a direct measure for the density integrated along the light path.

4.5.1 Interferogram analysis

There exist a large number of techniques for extracting density data from an interferogram. They can be essentially classified in two main categories: (semi-automated) fringe counting and bias phase modulation. An exhaustive review on these two classes can be found in [109, 140]. An additional method is provided by Fourier transform analysis, which lends itself quite efficiently to the self-extraction of the phase information. Furthermore, it possesses the additional advantage of being suitable to remove a significant amount of experimental noise. Two-dimensional Fourier transform analysis is most successful when an appropriate heterodyning process is implemented in the interferometry technique, provided that the spatial frequency of the heterodyning is sufficiently large. The method has been extensively described by Bone *et al.* [14], Bone [15], and Babinsky and Takayama [5]. More recently Houwing and Takayama [60] improved this technique for automated interactive data analysis and demonstrated its application to a wide range of flow configurations.

The selection of a suitable algorithm relies strongly on the subject under study and the environmental recording conditions. For our specific application, a semi-automatic fringe counting method is adopted. The technique relies on the fact that the difference between the maxima (or minima) of two neighbouring fringes is 2π. By ordering all maxima in a consecutive manner, the phase values in the whole field can then be determined by interpolation. Fringe counting methods have two major disadvantages. First, they require additional information to establish whether a phase shift represents an increase or a decrease in density. This problem is usually bypassed on the base of knowledge of the physics of the phenomenon studied. The second disadvantage refers to its low spatial

resolution, which is strongly dependent on the fringe density in a certain area, and thus varies over the image. Further, for weakly refractive fields with small gradients, only broad fringes are obtained, so that only a few widely separated maxima are present. To overcome this problem, heterodyning frequencies are introduced by tilting one of the mirrors in the reference beam path. At any rate, because of the sinusoidal variation of the intensity with the phase difference, the accuracy with which the maxima (or minima) can be located is usually not better than 0.1 of the fringe spacing. Despite these drawbacks, the method has been adopted due to its simplicity and commercial availability (TimWin application package).

The analysis proceeds as follows. First, the image is analysed for noise and shade removal. A high noise level in the digitised picture can seriously hamper the quality and accuracy of the phase extraction process. Second, the grey value image is reduced to one containing only fringe maxima and minima. This operation is called binarisation of the fringe pattern and is performed by thresholding the picture. The threshold range has to be determined separately for each interferogram. Based on this segmentation of the image, the skeleton is determined. This is achieved by thinning the region of fringe maxima to a line structure, which then constitutes the fringe skeleton. Whenever needed, the skeleton is completed (manually) by linking interrupted lines, removing line crossings, and adding missing points. As an example, the skeleton of the interferogram shown in Fig. 4.8 is plotted below.
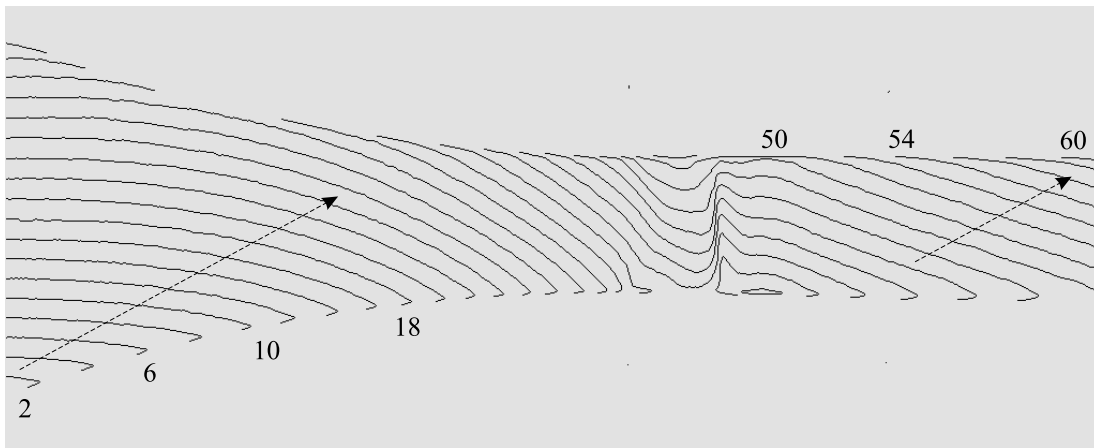
Figure 4.9: *Skeleton and semi-automatic fringe ordering. Nozzle: G2. Exp. H61 - Stagnation conditions: $P_0 = 9.13 \cdot 10^4$ Pa, $T_0 = 283.1$ K, $S_0 = 0.613$.*

The accuracy of the skeletonising process is strongly affected by the noise level in the image. The presence of irregularities, in fact, may drastically jeopardise the automatic detection of the fringe skeleton. Ideally the fringe pattern in an interferogram should be described by a simple sinusoidal intensity distribution, in practice this is not the case due to imperfections in the optical components, non-uniformities, and noise of the light source. To minimise the noise level, the reconstruction procedure is optimised with respect to quality

of the reconstruction beam and exposure time. Details on the reconstruction procedure can be found in section 3.2.1. In this way, no intervention on the photo histogram is required (i.e. the intensity distribution on the photo was almost sinusoidal), and the skeleton can be derived in a straightforward manner.

Once the skeleton is obtained, the fringes are interactively ordered. The phase difference between successive fringes is ambiguous, since it is only known modulo 2π. The process of determining the number of 2π steps to be added to these raw values is called phase unwrapping. Thus, phase unwrapping requires a knowledge of the sign as well as the magnitude of the raw phase. This information has to be provided by the user. This is done by drawing an imaginary vector (Fig. 4.9) on the fringe skeleton, which indicates the direction of increase and/or decrease of the phase. As a starting point, where the phase difference is equalled to zero (reference point), the bottom left of the nozzle is chosen. A grey value is then assigned to each fringe according to the order indicated by the vector.

The phase map for the whole field is subsequently calculated by interpolation. A built-in procedure in TimWin performs the required interpolation using a second order algorithm. The resulting image is a grey value image, in which the grey value represents the height of the point in question. A mask, derived in the pre-processing stage, helps to keep the image clean by removing parts outside the nozzle. Figure 4.10 shows the interpolated unwrapped phase map corresponding to the interferogram of Fig. 4.8.
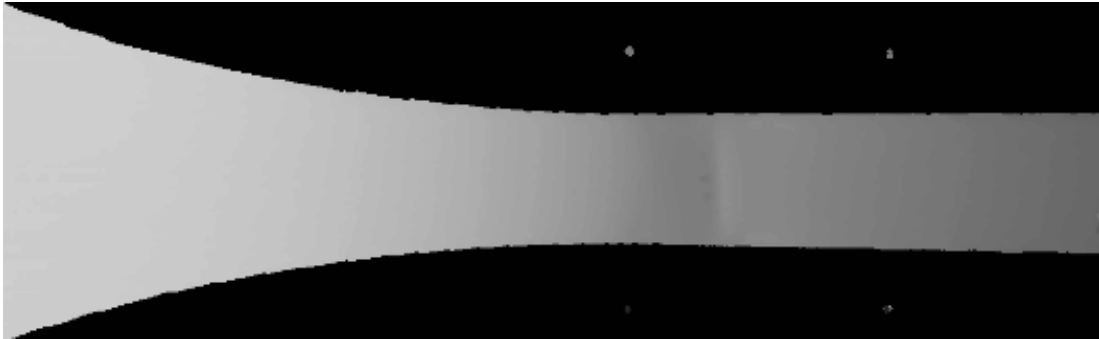
Figure 4.10: *Unwrapped phase map. Nozzle: G2. Exp. H61 - Stagnation conditions: $P_0 = 9.13 \cdot 10^4$ Pa, $T_0 = 283.1$ K, $S_0 = 0.613$.*

The density difference $\Delta\rho$ between a point in the flow field and the reference point is:

$$\Delta\rho = \rho_{ref} - \frac{\lambda}{KL}\left[\Psi_0 - (\vec{r} \cdot \vec{s})\right], \tag{4.37}$$

where Ψ_0 is the computed phase, $\rho_{ref} = 1.1$ kg/m^3 is the density assigned to the reference point, $\vec{r}$ is the distance vector between field point and reference point, $\vec{s}$ is the wave vector of the fringes corresponding to the superimposed linear phase distribution, $\lambda = 694.3$ nm is the wavelength of the light source, K is the Gladstone-Dale constant for the mixture (given by Eq. 4.36), and $L = 10$ cm is the optical path length. The axial density distribution,

determined with this procedure, is presented in Fig. 4.11. It should be noted that this density distribution is characterised by a quite low noise level, thus confirming the good quality of the recording and reconstruction process. The comparison between theoretical and experimental density fields can be found in chapter 6, where the validation of various condensation models is performed.

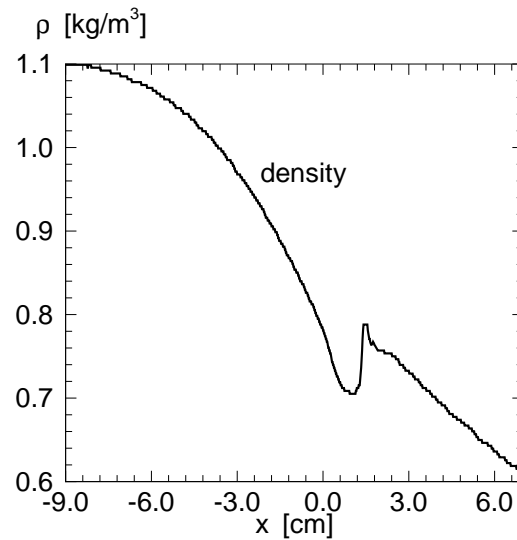**Figure 4.11:** *Density distribution measured along the nozzle midline. Nozzle: G2. Exp. H61 - Stagnation conditions:* $P_0 = 9.13 \cdot 10^4$ *Pa,* $T_0 = 283.1$ *K,* $S_0 = 0.613$.

Chapter 5

Droplet sizing by light extinction

5.1   Introduction

The development of instrumentation for accurate measurements of droplet size distributions is important for a diversity of applications: fuel spray combustion, nuclear reactor safety, meteorology, and a variety of industrial processes. In this chapter the optical characterisation of a droplet cloud, generated by homogeneous nucleation in supersonic expanding flows, is the subject of interest. In this context, characterisation of the cloud implies that the time dependent droplet modal radius, number density, and (if possible) the variance in droplet size are determined, at the nozzle exit, as accurately as possible. The relevance of such measurements is twofold. First, droplet size is a key parameter in assessing the quality of the proposed condensation models, as discussed in chapter 6. Second, in light of the industrial application which motivated this study, the droplet size distribution affects drastically the efficiency of the separator. Ideally one would like to obtain, constantly in time, a maximum modal radius with an almost monodispersed size distribution. Whether this is at all attainable and at which conditions is one of the questions to be addressed in the following chapters.

A large variety of experimental methods for optical fog characterisation has been proposed in the past years. A comprehensive review of the theoretical issues pertinent to optical characterisation of disperse systems can be found in [69]. A survey of recent developments was edited by Gouesbet and Gréhan [45], and a more general overview of techniques for droplet sizing was given by Tayali and Bates [137]. More recently two novel techniques for droplet sizing have been proposed. The so-called "rainbow" technique, developed at the von Kármán Institute, was successfully applied to droplet sizing by van Beeck [9]. Sorensen *et al.* [133] combined fractal and light scattering theory and were able, by means of scattering-extinction measurements, to describe the random chainlike structure of combustion generated soot aerosols. Despite the noteworthy progress, the experimental determination of droplet spectra via optical techniques in condensing nozzle or turbine flows has been less satisfactory. This is due to the difficulties of both resolving accurately in time the details of the spectrum and inverting the optical transmission data

for dense clouds of nanometre droplets with a high degree of polydispersion. As a matter of fact, most of the above mentioned techniques were developed for the characterisation of clouds originated in less extreme conditions than those normally encountered in condensing flows, namely: lower degree of polydispersion, larger droplet sizes, lower optical densities, and steady or slowly varying flow regimes. Therefore, their application to the study of condensing flows is, by far, not straightforward.

To the author's knowledge, in the past years only few groups have been actively working in this field. The works of Conrad [23] in 1977 and of Moses and Stein [88] in 1978 represent the first attempts to validate nucleation and droplet growth models. They both used light scattering techniques to determine the mean droplet size in steady nozzle flow for moist air and wet-steam, respectively. Unfortunately, due to the large experimental uncertainties, their studies cannot be considered conclusive in assessing the quality of the various condensation models. In 1980, Walters [153] determined, for the first time and fully, the droplet size distribution in the case of condensing steam and in a variety of experimental configurations. His method consists of recording the attenuated white-light flux at eighteen different wavelengths by using a sequence of special optical filters. The technique is mainly applicable to steady flow situations and its description and validation are presented in an earlier paper [151]. Walters' method proved to be extremely successful in experimentally determining the spectral turbidities and inverting those data to obtain accurate information on the size distribution function. Due to its accuracy and to the availability of a detailed technical documentation, it has been widely employed to perform wetness measurements in the low-pressure (LP) stages of steam turbines. Among these, one can mention the work of Skillings et $al.$ [128], Kantola [66], Walters [154], and White et $al.$ [160]. In the last-named case, it was possible to measure droplet sizes, with "reasonable" accuracy, down to $50\,nm$, which is at the very limit of optical detection. In 1986, Tatsuno and Nagao [136] developed an optical fiber sizer, based on the forward scattering method. The performance of the sizer was accurately verified in the $[0.1 \div 5.0\,\mu m]$ diameter range. They also measured average droplet sizes in LP turbines, obtaining results very similar to those of Walters and Skingley [152]. Although very promising, their method can only be applied to measure droplets larger than $0.2\,\mu m$ in diameter and, therefore, cannot be employed to typify droplet clouds in nozzle flows where the droplet sizes are in the range of $[30 \div 200\,nm]$ in modal radius. More recently (1997), Cinar et $al.$ [20] investigated the nucleation process of steam flowing through a nozzle at high pressures and temperatures. To this aim, they performed extinction measurements (employing only one wavelength) using a mercury lamp as a light source. The scarcity of data on the experimental procedure makes it very difficult to verify the reliability of the performed measurements.

Based on this review, the method of Walters is chosen: it proved to be the most successful and reliable one for measuring droplet sizes in the range of $[30 \div 200\,nm]$, which is the expected range in our experimental environment. In order to be able to follow the time evolution of the droplet size distribution in unsteady flow regimes, a few modifications have been introduced, which increased its temporal resolution up to values of the order of $1\,\mu s$ and made it particularly appealing for measuring rapidly changing phenomena with a satisfactory accuracy. A detailed description of the set-up can be found in chapter 3.

Hereafter some theoretical issues and limitations are discussed which are pertinent to the reliability and accuracy of the experimentally determined droplet sizes. A first difficulty arises from the fact that almost all existing techniques for retrieving size information from the spectral data are based on the assumption of single scattering. However, droplet clouds generated by homogeneous nucleation are, optically, extremely dense media. In such cases, multiscattering effects may play a major role and hamper, therefore, the interpretation of the transmission data. An additional complication stems from the high degree of polydispersion of the size distribution, which makes the inversion of the optical transmission data more cumbersome. Finally an additional problem is represented by the fact that, in many applications, one is dealing with droplet clouds of nanometre size. Due to the theoretical impossibility of obtaining the size information in the Rayleigh regime, it is necessary to develop a criterion in order to assess whether the Rayleigh limit is reached and, consequently, exclude these points from the analysis.

These issues are discussed in a detailed manner in the following sub-sections. Specifically section 5.2 deals with some basic scattering theory. This theory has been described in several textbooks, such as those of Bohren and Huffman [12], Kerker [67], and van der Hulst [63], and therefore its mathematical derivation is not repeated here. Instead, it is preferred to recall, whenever necessary, some basic theoretical notions and stress immediately their implications for the interpretation and analysis of the experimental results. In section 5.3 the specific inversion method is discussed and some results are presented. Here, the term "inversion" refers to the method used to derive the size distribution from the measured spectrum. The chapter ends with a detailed analysis of the influence of forward scattered radiation on the extinction measurements. The study encompasses both single and multiple-scattering effects and is discussed in section 5.4. Although this section is not essential for an understanding of the droplet sizing procedure, it plays a major role in assessing the reliability of the latter both from an experimental and theoretical perspective. The most important outcome of this analysis is the verification of the applicability of the Lambert & Beer law for a variety of experimental conditions and optical thickness as high as eight.

5.2 Basic scattering theory

In this section, the interaction of light of arbitrary wavelength with a single particle (or a collection of particles), embedded in a homogeneous medium, is considered. If a particle is illuminated by an electromagnetic wave, as shown in Fig. 5.1, the electric charges in the particles are set into oscillatory motion by the electric field of the incident wave. As a result of this, part of this electromagnetic energy is re-emitted as secondary radiation, the so-called scattered wave, part is, instead, transformed into other forms. The latter process is called absorption. With the expression *light extinction*, one means that energy is removed from the forward direction, i.e. the direction of propagation of the incident light wave. This attenuation of the light beam is the result of the combined effect of scattering and absorption of electromagnetic energy by the droplet(s). The magnitude of
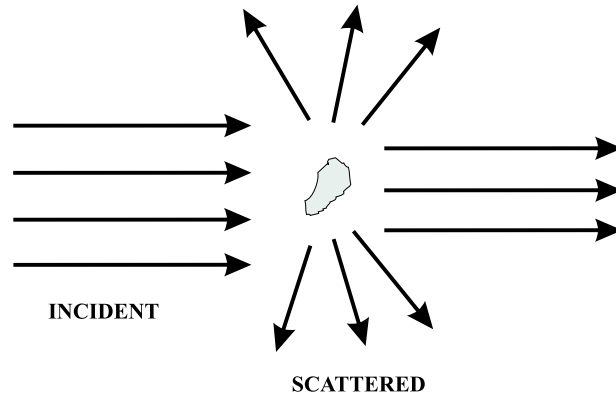
Figure 5.1: *Scattering by an obstacle.*

the extinction depends on the ratio between the droplet size and the wavelength of the light used. It is now clear that scattering, absorption, and extinction are not mutually independent processes and that the solution of the scattering problem must be derived from the equation of conservation of electromagnetic energy (Maxwell equations) with the appropriate boundary and initial conditions.

The problem of scattering of the electromagnetic field by an arbitrarily shaped body has not yet been solved in general form. However, the specifics of the propagation of radiation can be analysed in the case of elementary shapes, such as a sphere. This problem was rigorously solved by Gustav Mie, in 1907. Here, it suffices to note that solving the scattering problem implies determining the properties of the scattered light at any given position in space, namely its irradiance, polarisation, and phase. For many practical purposes, the most important property is the irradiance, i.e. the energy flux per unit area, so the following treatment is restricted essentially to the last-named parameter.

With reference to Fig. 5.2, consider a point P at a large distance r from the particle ($kr \gg 1$), where k is the wave number of the light, defined as $k = 2\pi/\lambda$, and λ is the wavelength in the surrounding medium. The direction of scattering, i.e. the direction from the particle to the point of observation, is characterised by the scattering angle θ and the azimuthal angle φ. At the observation point (P), the following relation holds between the irradiances of the incident and scattered wave, I_0 and I_s, respectively:

$$I_s = \frac{I_0}{k^2 r^2}\, \mathcal{F}(\theta, \varphi), \tag{5.1}$$

where $\mathcal{F}(\theta, \varphi)$ depends on the polarisation of the incident wave and the orientation of the particle with respect to the former. For the case of a spherical particle and unpolarised incident light, the exact expression for $\mathcal{F}(\theta, \varphi)$ can be found in Appendix G.

An alternative quantitative description of the scattering process is represented by the notion of a scattering cross-section C_{sca}. The scattering cross-section is defined as the ratio of total scattered-energy flux to that incident per unit area. In other words, the total energy scattered in all directions can, by definition, be put equal to the energy of the
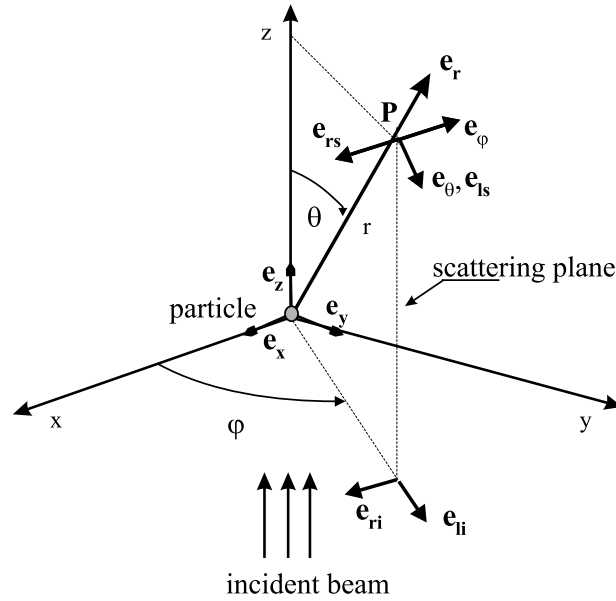
Figure 5.2: *Scattering by an arbitrary particle.*

incident wave falling on an area C_{sca}, yielding:

$$\frac{\iint_A I_s \, dA}{I_0} = C_{sca} = \frac{1}{k^2} \int F(\theta, \varphi) \, d\omega, \qquad (5.2)$$

where $d\omega = \sin\theta d\theta d\varphi$ is the element of solid angle in a droplet-centred coordinate system and the integral is taken over all directions.

In an analogous way, the energy absorbed inside the particle can, by definition, be put equal to the energy incident on the area C_{abs} and the energy removed from the original beam can be put equal to the energy incident on the area C_{ext}. Application of the conservation law of energy yields:

$$C_{ext} = C_{sca} + C_{abs}. \qquad (5.3)$$

The quantities $C_{ext}, C_{sca}, C_{abs}$ are called the extinction, scattering, and absorption cross sections, respectively.

The efficiency factors can be derived directly from the corresponding cross sections. These factors are dimensionless quantities and are defined as the ratios of the scattering, absorption, and extinction cross sections to the characteristic geometric cross section G.

$$\begin{aligned}
Q_{ext} &= \frac{C_{ext}}{G} \\
Q_{sca} &= \frac{C_{sca}}{G} \\
Q_{abs} &= \frac{C_{abs}}{G}.
\end{aligned} \qquad (5.4)$$

Obviously the efficiency factors obey also the relation:

$$Q_{ext} = Q_{sca} + Q_{abs}. \tag{5.5}$$

Indicating the size parameter by $\alpha = 2\pi r_d/\lambda$ (r_d represents the droplet radius), the refractive index of the light beam in the surrounding medium by m, and the scattering angle by θ, it is worth emphasizing that Q_{ext} is solely a function of α and m, since $\theta = 0°$ (forward direction).

5.2.1   The fundamental extinction formula

In this subsection, the theoretical dependence of the extinction efficiency on the size parameter (α) is presented for the case of a spherical water droplet in nitrogen. In such situations, absorption can be neglected and the solution of the extinction problem reduces to solving the scattering one. With reference to Fig. 5.2, the relation between scattered and incident wave can be cast, in the most general case, in the form:

$$
\begin{aligned}
\vec{E}_{sca} &= \frac{e^{ik(r-z)}}{-ikr} \, \underline{\underline{S}} \, \vec{E}_{inc}, \\[2mm]
\begin{pmatrix} E_{ls} \\ E_{rs} \end{pmatrix} &= \frac{e^{ik(r-z)}}{-ikr} \begin{pmatrix} S_2 & S_3 \\ S_4 & S_1 \end{pmatrix} \begin{pmatrix} E_{li} \\ E_{ri} \end{pmatrix},
\end{aligned}
\tag{5.6}
$$

where $\underline{\underline{S}}$ is the *amplitude scattering matrix*. Its elements S_j (j = 1, 2, 3, 4) depend, in general, on the scattering angle θ and the azimuthal angle φ. This matrix assumes a very simple form in the hypothesis of an incident plane electromagnetic wave, scattered by a spherical homogeneous droplet. Now Mie theory can be applied and results into $S_3 = S_4 = 0$. Mie theory provides also a rigorous determination of the efficiency factors in terms of the orthogonal components of the scattered light, which are polarised perpendicularly and parallel to the scattering plane, respectively. These components are shown in Fig. 5.2. Their detailed analytical expressions can be found in Appendix G. Assuming, for convenience, the incident electric field $\vec{E}_{inc} = E_0 \, \mathbf{e_x}$ to be x-polarised, the fundamental extinction formula reduces to the following relation:

$$Q_{ext} = \frac{4}{k^2 r_d^2} \, Re[(\vec{X} \cdot \mathbf{e_x})_{\theta=0}], \tag{5.7}$$

where r_d is the droplet radius and $\vec{X}$ is the *vector scattering amplitude*. The latter is related to the elements S_j of the amplitude scattering matrix as follows:

$$\vec{X} = S_2 \cos \varphi \, \mathbf{e_{ls}} + S_1 \sin \varphi \, \mathbf{e_{rs}}. \tag{5.8}$$

Equation (5.7) is a particular form of the *optical theorem*. This theorem expresses the fact that, although extinction is the combined effect of absorption and scattering in all directions, it depends only on the scattering amplitude in the forward direction. For

a complete understanding of the derivation and implications of the *optical theorem*, the reader is referred to the book of Bohren and Huffman [12] (pp. 69-77). Here only its most important consequence is reported: extinction is effectively the manifestation of interference between incident and forward scattered light. However, conservation of energy requires that the light removed from the incident beam by interference is accounted for by scattering in all other directions. This equivalent description of the extinction mechanism is applied in the next section to calculate the total extinction by a collection of particles.

Theoretical curves of attenuated light flux versus the size parameter, according to Mie theory, show corresponding series of extrema (extinction peaks), as depicted in Fig. 5.3. This illustrates clearly that extinction is, indeed, the result of interference between incident and forward scattered light, which results in a decrease of energy flux in the forward direction. Rigorously speaking, this plot expresses the variation of the extinction efficiency versus α, for a fixed value of the refractive index (m). In this particular case, this approximation can be retained since the refractive index of water in nitrogen does not change appreciably in the range of wavelengths considered here $[400 - 800\,nm]$. The validity of this assumption is confirmed by the work of Thormählen *et al.* [139], who investigated the dependence of the refractive index on wavelength, temperature, and density for subcooled water and steam.
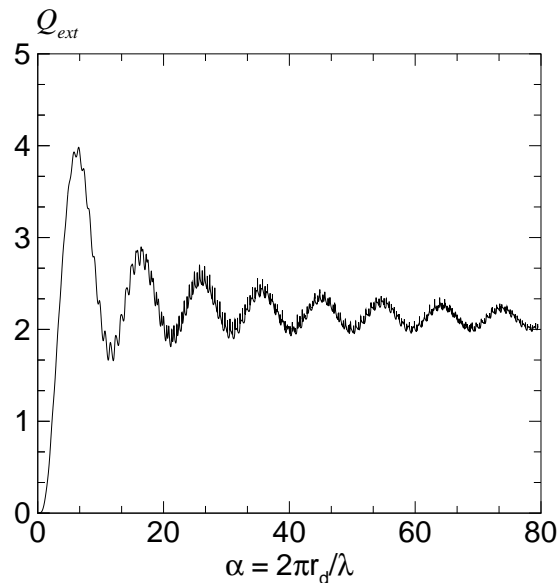

Figure 5.3: *The extinction efficiency Q_{ext} for a homogeneous spherical water droplet as a function of the size parameter α ($m = 1.33$).*

In Fig. 5.3, it is possible to distinguish two limits. For $\alpha \ll 1$ scattering occurs in the Rayleigh regime. In this limit, it can be shown that

$$Q_{ext} \propto \frac{1}{\lambda^4}, \tag{5.9}$$

Due to this inverse proportionality, it is impossible in the Rayleigh limit to retrieve information on the droplet size distribution, as explained in the next section (5.2.2). For $\alpha \gg 1$, the scattering process is described by Fraunhofer diffraction theory and Q_{ext} tends, in this limit, to the value of two.

5.2.2   Extinction by a slab filled with particles

The results presented in the previous section hold for a single spherical droplet embedded in a homogeneous medium. Aim of this section is to generalise the fundamental extinction formula to a collection of spherical droplets. Let us consider such a collection confined to a finite volume bounded by two semi-infinite planes, as shown in Fig. 5.4(a). The present treatment is restricted to the following assumptions:

   (i)   *elastic scattering: the scattered light has the same frequency as the incident light. This implies that all quantum mechanical effects are excluded;*

   (ii) *incoherent scattering: the irradiances of the waves scattered by the various particles can be added without regard to their respective phase;*

   (iii) *single scattering: the number of particles is sufficiently small and their separation sufficiently large that, in the neighbourhood of any particle, the total field scattered by all the particles is small compared with the incident field.*
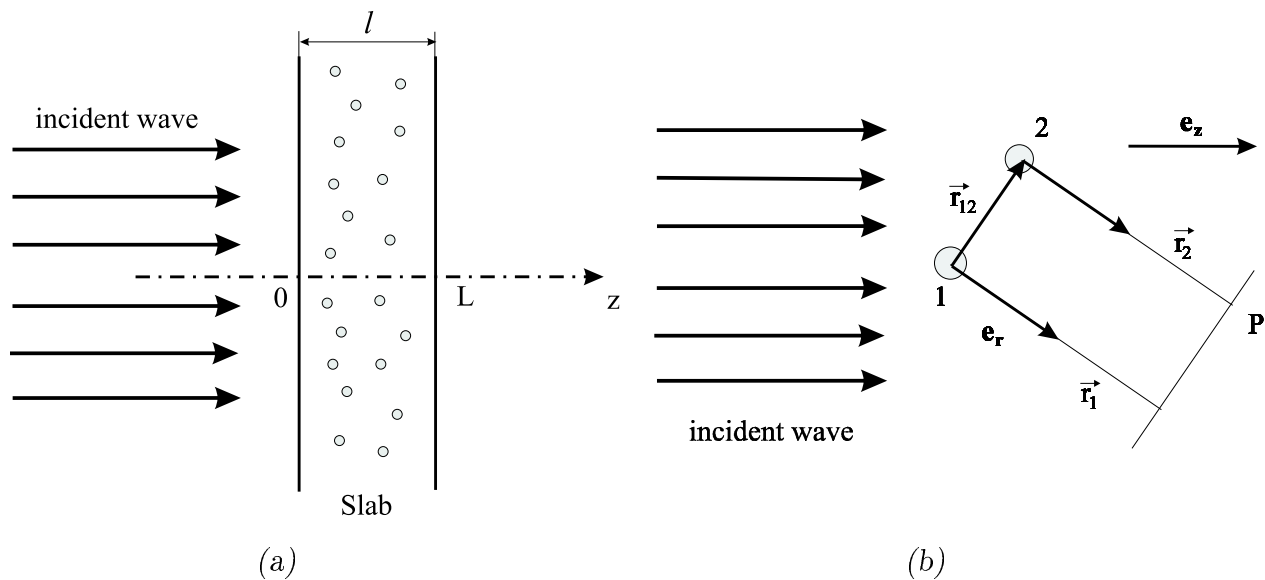

Figure 5.4: *Extinction by a slab filled with droplets. (a) Schematic representation of the slab. (b) Phase relation between two identical droplets.*

It is important to realise that, even in the hypothesis of *incoherent scattering*, light scattered in the forward direction ($\mathbf{e_r} = \mathbf{e_z}$) is always coherent. This can be understood immediately from Fig. 5.4(b): in fact the phase difference $\Delta\varphi$ at a point (P) in the far field is given by

$$\Delta\varphi = k\,[\vec{r}_{12} \cdot (\mathbf{e_z} - \mathbf{e_r})]. \tag{5.10}$$

Therefore when ($\mathbf{e_r} = \mathbf{e_z}$), $\Delta\varphi$ is identically zero regardless of the droplet separation. On the basis of Eq. (5.10), the calculation of the total extinction coefficient should take into account the phase relations among the scattered waves. However, recalling the equivalence principle stated by the *optical theorem*, the computation of the total extinction can be related to that of total scattering, which is, under the present assumptions, incoherent.

Under these hypotheses, if a plane light wave impinges on an infinitesimal slab filled with particles, the attenuation of the light beam (dI) can be calculated as:

$$dI = -\beta I_0\, dz, \tag{5.11}$$

where

$$\beta(\lambda, m) = \int_0^\infty Q_{ext}(\frac{2\pi r_d}{\lambda}, m)\, f(r_d)\, \pi\, r_d^2\, dr_d. \tag{5.12}$$

Equation (5.12) follows directly from the assumption of incoherent scattering. It states that the attenuation coefficient of the cloud is simply the sum of the extinction coefficients of all droplets. Since they are not necessarily identical, their size dispersion is described by the function $f(r_d)$.

Generalisation to a slab of finite thickness is straightforward since the latter can be seen as a sequence of infinitesimal slabs. Then, if $f(r_d)$ is the same everywhere on the path of the original light beam, integration of Eq. (5.11) yields

$$I = I_0\, e^{-\beta l}. \tag{5.13}$$

Equation (5.13) is the so-called Lambert-Beer law. In this formula, l represents the geometrical path length, i.e. the distance that the attenuated light beam travels through the droplet cloud. Underlying equation (5.13), and hence the exponential attenuation of irradiance in particulate media, is the requirement that the product $\beta l \ll 1$, i.e. multiple scattering effects are negligibly small. This condition is justified more rigorously in section 5.4. Here the following heuristic explanation suffices: when multiple scattering effects are strong, it must be realised that light that is scattered and taken away from the original beam can be brought back in the original beam by a second scattering event and no distinction can be made between this scattered light and the attenuated light of the incident beam. Clearly, the greater the scattering cross-section, particle number densities, and slab thickness l, the greater will be the multiple scattering contribution to the irradiance. Since all these effects can be encompassed in the optical thickness $\delta = \beta l$, if the latter is sufficiently small, one may ignore multiple scattering effects and still make use of the Lambert-Beer law. This condition may be somewhat relaxed if the scattering contribution to the total attenuation is small, as shown in subsection 5.4.3.2.

In view of the functional relationship between extinction coefficients and size distribution function (see Eq. 5.12), by measuring these coefficients at n different wavelengths, a set of n linearly independent equations is obtained. By solving this system of equations, the desired information about the droplet cloud can be acquired. The number of extinction signals to be recorded depends on the number of parameters identifying the size distribution function and the specific inversion technique used. The only drawback is encountered when the droplets are considerably smaller than the wavelengths used ($\alpha < 1$). In this case (near-Rayleigh regime), the functional dependence of the extinction coefficients upon wavelength is such that the rank of the system coefficient matrix tends to two and thus is lower than the number of unknowns n. Therefore, there exist infinitely many solutions all of which are obtained by determining two suitable unknowns, in terms of the remaining *n-2*, to which arbitrary values can be assigned.

Since in condensing nozzle flows one may be often working in the near-Rayleigh regime, special care must be paid to ascertain the reliability of the inversion analysis in this limit. This is achieved by defining an *ad hoc* parameter (Rayleigh parameter), as a measure of the deviation of the experimental data from the Rayleigh limit. The Rayleigh parameters are introduced in the next subsection 5.2.3.

5.2.3   The Rayleigh parameters

The possibility of retrieving, with the desired accuracy, size information from the extinction spectrum relies on the condition of being far away from the Rayleigh regime. In fact, in the limit of Rayleigh scattering, the following relation holds:

$$\beta \propto \left(n_d \, r_d^6 \, \lambda^{-4} \right) , \tag{5.14}$$

and no distinction can be made between droplet size and number density. In order to evaluate how distant the experimental data are from this limiting condition, the following ratios have been defined:

$$R_{i1} = \frac{\beta_i \, \lambda_i^4}{\beta_1 \, \lambda_1^4} ; \qquad \qquad i = 2, \ldots, n \tag{5.15}$$

where λ_1 is the largest wavelength used in the experiments, specifically $772.3 \; nm$. This definition is based on the following simple reasoning: in the Rayleigh limit Eq. (5.14) holds, thus by eliminating the wavelength dependence, all the extinction coefficients tend to the same limiting value ($n_d \, r_d^6$). Their ratio, then, will tend to one, individuating in this way the regime of Rayleigh scattering.

The great advantage of the Rayleigh parameters is that they offer indirectly an immediate indication on the droplet size, without any complex analysis or complicated calculations. Figure 5.5 shows the theoretical dependence of the R_{i1} on the droplet size, for the wavelength range adopted in the experiments $[400 \div 800] \; nm$. The calculations are conducted according to Mie theory and for a monodispersed distribution.
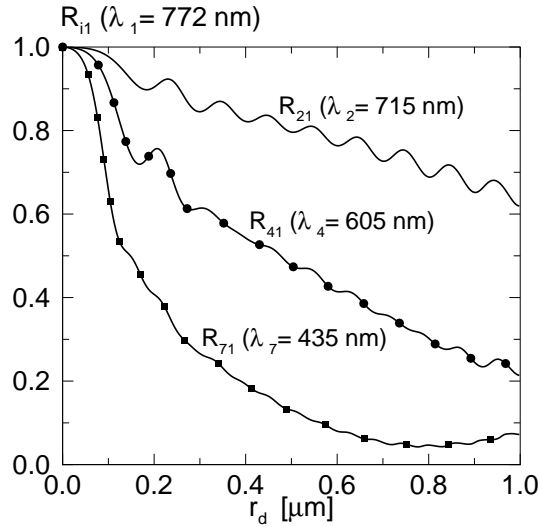
Figure 5.5: *Theoretical curves of the Rayleigh parameter R_{i1} versus droplet modal radius (r_d) and for a monodispersed distribution $(\varepsilon = 0)$.*

This plot demonstrates unequivocally the ability of the Rayleigh parameters in predicting whether the analysis is meaningful or not. In the Rayleigh regime, they all tend to the limiting value of one, independently of the specific wavelength considered. In other words, only for values of the parameter R significantly smaller than unity, it is theoretically possible to extract accurate information from the experimental data. Furthermore, for a given modal radius, the longer the wavelength, the higher is the value of the corresponding Rayleigh parameter: that is, the longest wavelengths are the first to enter the Rayleigh limit.

5.3 Droplet sizing

As mentioned in the previous sections, the relation between the wavelength dependent extinction coefficient $\beta(\lambda, m)$ and the size distribution function $f(r)$ can be written as a Fredholm integral equation of the first kind:

$$\beta(\lambda, m) = n_d \int\limits_{0}^{\infty} \pi\, r^2\, f(r)\, Q_{ext}(\frac{2\pi r}{\lambda}, m)\, dr, \qquad (5.16)$$

where Q_{ext} is the kernel function provided by Mie theory and n_d is the droplet number density. The inverse problem of reconstructing the function $f(r)$ from the spectral extinction involves the inversion of Eq. (5.16). Because the information content in a set of extinction measurements is limited, inverse problems are usually ill-posed and do not possess a unique solution.

There are several ways to tackle the inversion problem: Twomey [144] gave a detailed account of the mathematics of inversion and described many of the schemes used to solve inverse problems. More recently, Bertero *et al.* [10] discussed the general formulation of this class of problems and reviewed more solution methods. Unfortunately no "universal" method could be found in literature which provides, for any sort of applications, satisfactory results: in fact, the solution of the inverse problem depends strongly on the appropriate combined choice of the measurement and inversion technique. In general, techniques for solving the inverse problem are classified as either analytical or empirical. Analytical techniques involve formal solutions of Eq. (5.16). Because of their ill-posed nature, they require the use of *a priori* information regarding the distribution function or a careful optimisation of the inputs. Empirical inversion techniques generally require that a proper discretization model of the extinction process be developed. Walters [153] reviewed two of these empirical methods for application to spectral turbidities in steam flow. Those methods consist of:

(a)   finding an empirical distribution that satisfies (5.16);

(b)   the direct inversion of (5.16), expressed as a quadrature in matrix form, and subjecting solutions to a smoothing constraint.

Method (b), known as the matrix inversion method of Philips and Twomey [142,143], has the advantage that the unknown size distribution may be generated directly from the data without making any *a priori* assumption. Although this method did yield good results for condensing flows, it has two major disadvantages. First, the choice of the smoothing parameter affects strongly the final results. Second, the acquired solution very often oscillates. Method (a), instead, makes use of trial functions which depend on a parameter vector **p**. A parametric model of the extinction process is accordingly developed. The parameters are, then, adjusted within physically realistic bounds so that a least squares fit of the measured data is obtained. This method by trial function has been heavily criticised in its premises by Twomey [142,143]. Nevertheless, it was widely applied yielding often satisfactory results. Walters applied this method to condensing nozzle flow and the final results in determining realistic monomodal distributions were of very accurate. Walters argues that although the mathematical principle of this method is questionable, its apparent success must be justified by the smoothness of the size distribution function compared to the kernel Q_{ext}. For the case of turbine flows, where a distribution with a large dispersion or even a bimodal distribution can be readily expected, method (b) seems to be more accurate than method (a) in predicting all the features of the size distribution function. In a later paper [154], Walters improved further the Twomey matrix method by devising a new procedure for the detection of bimodality in the spectral data.

By careful assessment of the physics of the condensation process in nozzle flows and by a particular choice of the Laval nozzle, it is reasonable to expect, for the specific cases considered, a smooth monomodal size distribution function. Based on this consideration, the *trial function* method was, then, chosen due to its simplicity and direct applicability. An additional consideration which led to prefer the *trial function* method is due to the particular functional dependence exhibited by the extinction coefficients with wavelength in the near-Rayleigh regime. In this limit, as explained in the section 5.2.2, the relative

variance cannot be determined accurately and, thus, the ability of method (b) in better characterising size distribution with a larger dispersion is no longer valid.

5.3.1   The inversion technique

The trial function method employed here is based on the previous work of Snoeijs [131] and van Dongen *et al.* [34]. It was originally developed to study droplet size distributions due to heterogeneous condensation in adiabatically expanding vapours. Although its conceptual base remains unaltered, a few modifications were necessary to adapt it to the conditions encountered in homogeneously condensing nozzle flows. These modifications were implemented by van Poppel [103] and are summarised below for completeness. First, following van Dongen *et al.* [34], the particle distribution function is specified as:

$$f(r, \mathbf{p}) = \frac{1}{\sqrt{2\pi}\varepsilon r_m} exp\left[\frac{-(y^2 + \varepsilon^4)}{2\varepsilon^2}\right], \qquad y = \ln\left(\frac{r}{r_m}\right), \qquad (5.17)$$

where $\mathbf{p}$ is the parameter vector (r_m, ε), r_m is the modal radius, and ε is the relative variance. This function is the well-known zeroth-order log-normal (ZOL) distribution; it has the advantage of being defined in the domain $r_m > 0$, in agreement with the physical reality. Some examples of ZOL functions are shown in Fig. 5.6.
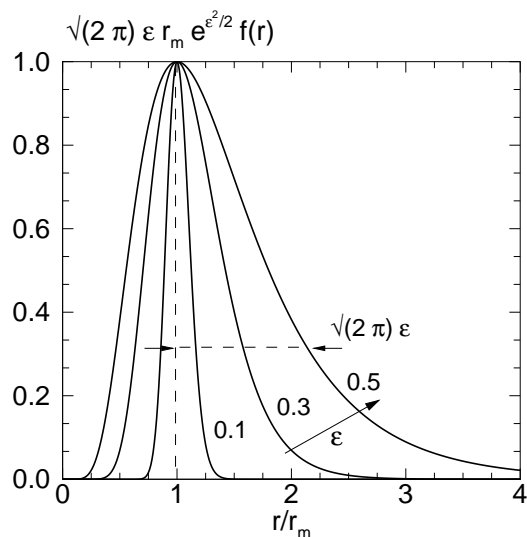

Figure 5.6: *Normalised zeroth-order log-normal distributions. Distribution parameters: r_m = modal radius, ε = relative width.*

By measuring the extinction coefficients β_i at a set of n equidistant wavelengths λ_i, a corresponding set of theoretical β's can be defined at the same wavelengths. Those are

given by the following expression:

$$\beta_{theo}(\lambda_i, m, \mathbf{p}) = n_d \int_0^\infty \pi r_d^2 \, Q_{ext}(\frac{2\pi r_d}{\lambda_i}, m) \, f(r_d, \mathbf{p}) \, dr_d, \qquad i = 1, \ldots, n. \qquad (5.18)$$

In order to find the best choice of parameters to describe the unknown size distribution, the sum of squares of the theoretical β_{theo}'s and corresponding experimental β_{exp}'s is minimised. The latter is defined as:

$$\mathcal{R}(\mathbf{p}) = \sum_{i=1}^n (\beta_{theo,i} - \beta_{exp,i})^2, \qquad (5.19)$$

where n is the number of extinction coefficients measured at the n different wavelengths. In this way the combination of parameter values of the trial function is found for which the set of theoretical extinction coefficients is closest to the experimental ones. The parameters of the ZOL distribution function can vary in the specified range:

	lower bound	upper bound
n_d:	$10^9 \ m^{-3}$	$10^{19} \ m^{-3}$
r_m:	$5 \ nm$	$1 \ \mu m$
ε:	0	0.5

Standard numerical methods are used to determine the minimum value of the residue $\mathcal{R}(\mathbf{p})$ and the corresponding optimum values of the parameters involved. The least squares procedure requires the numerical evaluation of the integrals (5.18) for a large number of parameter values, which is not attractive. To simplify this numerical evaluation, several steps are adopted. First, the dependence of Q_{ext} on the refractive index m is ignored. Based on the measurements of Thormählen *et al.* [139], at a pressure of 0.5 bar and in a temperature range of $[0 \div 20]$ °C, the relative error in refractive index $\Delta m/m_0$ is of order 1%, when neglecting its dependence on the wavelength. Second, the extinction efficiency Q_{ext} is evaluated and tabulated for a large number of discrete values α_j, at a representative value of the refractive index $m_0 = 1.33$. Therefore, in the following sections, the dependence of β and Q_{ext} on the refractive index m is not explicitly indicated anymore.

Despite these simplifications, the minimisation procedure is in some cases still cumbersome. This complication is caused by the insensitivity of the β's, in the near-Rayleigh regime, to the relative variance ε, so that it is difficult to determine this parameter accurately in the presence of noise. This insensitivity is the crucial factor responsible for the difficulties in inverting the data. To overcome such difficulties, Van Poppel [103] introduced the ε-discrete method. It consists in applying subsequently constant-ε fits where, at each successive fit, the relative width is varied in the range $[0 \div 0.5]$, with steps of $\Delta \varepsilon = 0.05$. From these constant-$\varepsilon$ fits, it is possible to reconstruct the time dependence of the relative variance, with now ε not as a continuous parameter, but as a parameter that can attain only certain discrete values. The reconstruction is done by determining, for each measuring point, the value of ε corresponding with the smallest residue $\mathcal{R}_{min}$ and storing the related ZOL parameters.

Van Poppel [103] compared in detail the ε-discrete method to the ε-continuous fit. He showed that both methods yield almost identical results with respect to the ZOL parameters. Further, the qualities of the fits are comparable in magnitude and the quality is slightly better for the ε-discrete method. This is because in the discrete method the whole range of ε's is analysed. Consequently, contrary to the continuous method, where local minima may be intercepted, it is more likely that a global minimum is found.

5.3.2 Accuracy & reliability of the inversion method

This subsection focuses on a number of issues which are crucial in assessing the accuracy and reliability of the inversion technique. In general, the quality of the inversion depends upon the number of wavelengths recorded and the relative importance of the noise in the measured irradiances. First, it is necessary to individuate an adequate criterion for evaluating whether a set of parameters, that minimise the residue $\mathcal{R}(\mathbf{p})$, is indeed a good approximation of the real droplet size distribution. To this purpose, it must be realised that a minimum value of zero for $\mathcal{R}(\mathbf{p})$ can almost never be obtained as a direct result of noise in the measurements. The most dominant noise source is detector noise. Therefore, the quality of the fit has been related to the latter, since it provides a lower bound for the minimisation of the residue. This issue is tackled in subsection 5.3.2.1, where a direct indication of the accuracy of the analysis is given. However, it should be noted that this information is in itself sterile if not combined with the corresponding value of the Rayleigh parameters, which indicate whether the analysis is also physically meaningful.

Finally, the convergence of the inversion technique with respect to the number of signals employed has to be checked. Recalling that the *trial function* method consists of parameterising a model and adjusting these parameters to obtain a least squares fit to the data, it is well known that a large number of data points is necessary for an accurate fit. Typically it was found that, for small size parameters ($\alpha \leq 3$), one requires about ten data points. This number increases drastically with the size parameter: for $\alpha \geq 20$ hundreds of data points may be required for a fit of much lower quality [106]. In this specific case, seven wavelengths are used; thus the sensitivity and reliability of the solution has to be examined also with respect to the number of wavelengths employed. This issue is discussed in subsection 5.3.2.2.

5.3.2.1 Detector noise

In this section, the quality of the least squares fit is related to the detector noise level. To this purpose, it should be recalled that the Lambert-Beer law (Eq. 5.13) provides a functional relation between variations in the attenuated beam irradiance and the extinction coefficients. Since these irradiances are affected by detector noise, so are the corresponding extinction coefficients. Indicating with $\mu(\beta)$ the expectation value for the extinction coefficient (i.e. the value the latter would assume upon averaging over several periods), it results:

$$\beta_{exp,i} = \mu(\beta_{exp,i}) + \Delta\beta_{exp,i} \tag{5.20}$$

where $\Delta\beta_{exp,i}$ represents the inaccuracy in the determination of β due to detector noise. It is noted here that, in general, $\Delta\beta_{exp,i}$ will depend on the value of β itself, because detector noise is not strongly dependent on the absolute value of the transmitted irradiance. If the trial function matches the *unknown* size distribution perfectly, the minimisation is optimal when

$$\beta_{theo,i} = \mu(\beta_{exp,i}). \tag{5.21}$$

Unfortunately, the actual value for $\mu(\beta_{exp,i})$ is not known *a priori*, and thus an alternative procedure must be devised to estimate the noise level in the detectors. Recalling Eq. (5.19), the corresponding value of the residue $\mathcal{R}(\mathbf{p})$ in the ideal case of a perfect fit is:

$$\mathcal{R}_{perfect} = \sum_{i=1}^{n}(\Delta\beta_{exp,i})^2. \tag{5.22}$$

In practice, the actual value for the residual $\mathcal{R}$ is always larger than $\mathcal{R}_{perfect}$. Unfortunately the value of $\mathcal{R}_{perfect}$ is also unknown. However, its expectation value $\mu(\mathcal{R}_{perfect})$ can be calculated by taking the expectation value of Eq. (5.22), yielding:

$$\mu(\mathcal{R}_{perfect}) = \mu\left[\sum_{i=1}^{n}(\Delta\beta_{exp,i})^2\right] = \sum_{i=1}^{n}\mu\left(\Delta\beta_{exp,i}\right)^2 = \sum_{i=1}^{n}\sigma_{\beta_i}^2, \tag{5.23}$$

where σ_{β_i} is the standard deviation in the extinction coefficient β_i. Therefore, the expectation value $\mu(\mathcal{R}_{perfect})$ can be calculated if σ_β is known for each detector. Via equation (5.13), σ_β is related to σ_I, and this relation can then be re-written as:

$$\sigma_\beta = \frac{1}{lI}\sigma_I. \tag{5.24}$$

In this way, an estimate of the maximum achievable accuracy $\mu(\mathcal{R}_{perfect})$ is reconnected to an evaluation of the noise in the detectors, which can be obtained by means of a proper calibration, as explained in Appendix F. The time-averaged value of the actual residue $\mathcal{R}_{avg}$ is then compared with $\mu(\mathcal{R}_{perfect})$ to establish the quality of the fit.

Figure 5.7 shows this comparison ($\mathcal{R}_{avg}$, $\mu(\mathcal{R}_{perfect})$ versus S_0) for an experimental series, varying S_0. It is clearly seen that the difference between $\mathcal{R}_{avg}$ and $\mu(\mathcal{R}_{perfect})$ is small, so that the quality of the fit is not poor when compared to the time-averaged noise level in the detectors. Furthermore, the quality strongly depends on the initial conditions. This is due to the attenuation of the light beam being stronger at higher supersaturations, so that the relative importance of the noise in the measured irradiances increases with S_0. Despite the good agreement, the specific values of $\mathcal{R}_{avg}$ do not provide any indication of the signal-to-noise ratio, which is another important element in establishing the significance of the measurements. Obviously, for a given noise level, the signal-to-noise ratio is directly connected to the magnitude of the measured light attenuation. Figure 5.8 illustrates the typical time dependence of the extinction coefficients, corresponding to the following experimental conditions: $P_0 = 8.752 \cdot 10^4\,Pa$, $T_0 = 296.6\,K$, $S_0 = 1.188$.
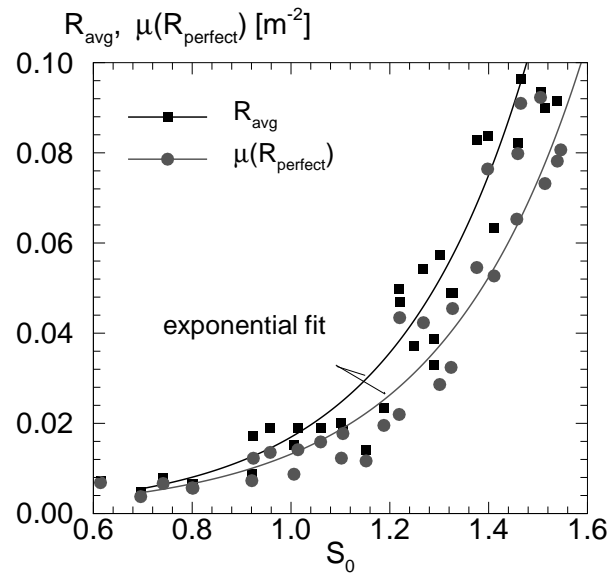
Figure 5.7: *Time-averaged residue $\mathcal{R}_{avg}$ and its expectation value $\mu(\mathcal{R}_{perfect})$ as function of the stagnation supersaturation S_0. The residual values are averaged over five periods. Nozzle: G2. Stagnation conditions: $P_0 = (8.69 \pm 0.015) \cdot 10^4\ Pa$, $T_0 = 296.8 \pm 0.4\ K$.*
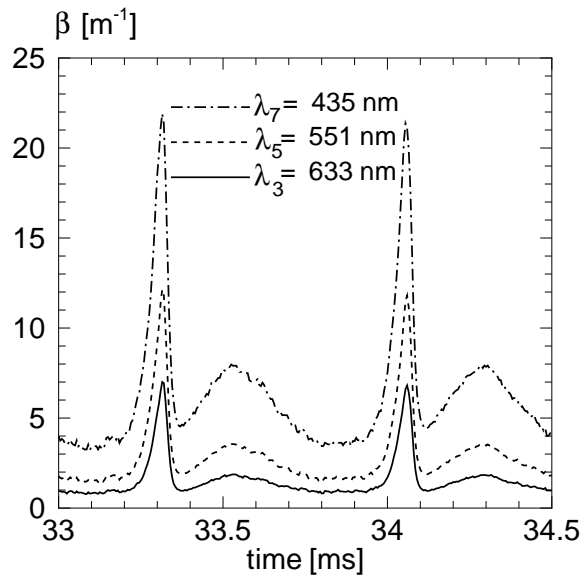
Figure 5.8: *Experimentally determined extinction coefficients. Nozzle: G2. Exp. 37 - Stagnation conditions: $P_0 = 8.752 \cdot 10^4\ Pa$, $T_0 = 296.6\ K$, $S_0 = 1.188$.*

The periodic character of the flow is immediately deducible from the plot. Further, it can be seen that, during one period of oscillation, the β's attain a distinct maximum and minimum value. The difference $[\beta(\lambda_7, t) - \beta(\lambda_1, t)]$ is often referred to as the dynamic

range in the extinction coefficients, at the time instant t. As a measure of the signal-to-noise level, the following ratios are defined:

$$SN_{1(max)} = \frac{\beta_{max}(\lambda_1)}{\mu(\mathcal{R}_{perfect})}; \qquad\qquad SN_{1(min)} = \frac{\beta_{min}(\lambda_1)}{\mu(\mathcal{R}_{perfect})};$$

$$SN_{7(max)} = \frac{\beta_{max}(\lambda_7)}{\mu(\mathcal{R}_{perfect})}; \qquad\qquad SN_{7(min)} = \frac{\beta_{min}(\lambda_7)}{\mu(\mathcal{R}_{perfect})};$$

which provide the dynamic range of the signal-to-noise ratio for a specific experiment. In other words, these ratios are a measure of the relative importance of the maximum and minimum level of signal (i.e. β_{max}, β_{min}) with respect to the noise level. Since these ratios are wavelength dependent, the shortest and longest one have been considered: all the other signals are contained within these bounds. Figure 5.9 shows the result of this evaluation for all the experiments performed.

(a) Lower Bound $SN_{i(min)}$ (b) Upper Bound $SN_{i(max)}$
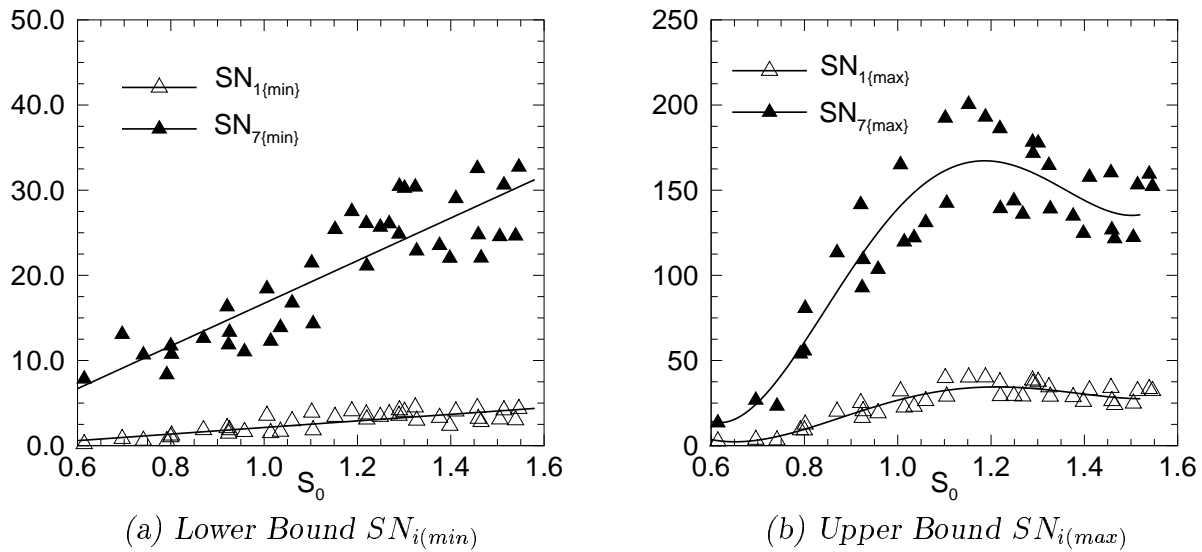
Figure 5.9: *Signal-to-noise ratios as function of the stagnation supersaturation S_0. Their values are calculated for the following wavelengths: $\lambda_1 = 772.3$, $\lambda_7 = 434.5$ nm. Nozzle: G2. Stagnation conditions: $P_0 = (8.69 \pm 0.015) \cdot 10^4$ Pa, $T_0 = 296.8 \pm 0.4$ K.*

For values of the supersaturation smaller than 1.0, the signal-to-noise ratios $SN_{i(min)}$ are quite low in the whole wavelength range. This indicates that, when the $\beta(\lambda_i)$ values approach their minimum value in time, the noise level in all signals is quite high: the droplets are so fine that no significant light attenuation is produced. For values of the supersaturation smaller than 0.8, the $SN_{i(max)}$ values are also small. This indicates that all experiments, conducted for $S_0 \leq 0.8$, do not yield reliable droplet size data. As a concluding remark, it is important to observe that the highest information content is to be found near the extinction peaks, where the largest droplets are expected.

5.3.2.2 Effect of the number of wavelengths used

As stressed in section 5.3.2, errors in the calculated solution for the droplet size distribution may be expected depending on the number of wavelengths used. In general, the higher the number of spectral data employed, the higher the reliability of the obtained solution. In this section, the sensitivity of the solution is checked by comparing the results obtained from the inversion technique using three, four, five, six, and seven wavelengths.
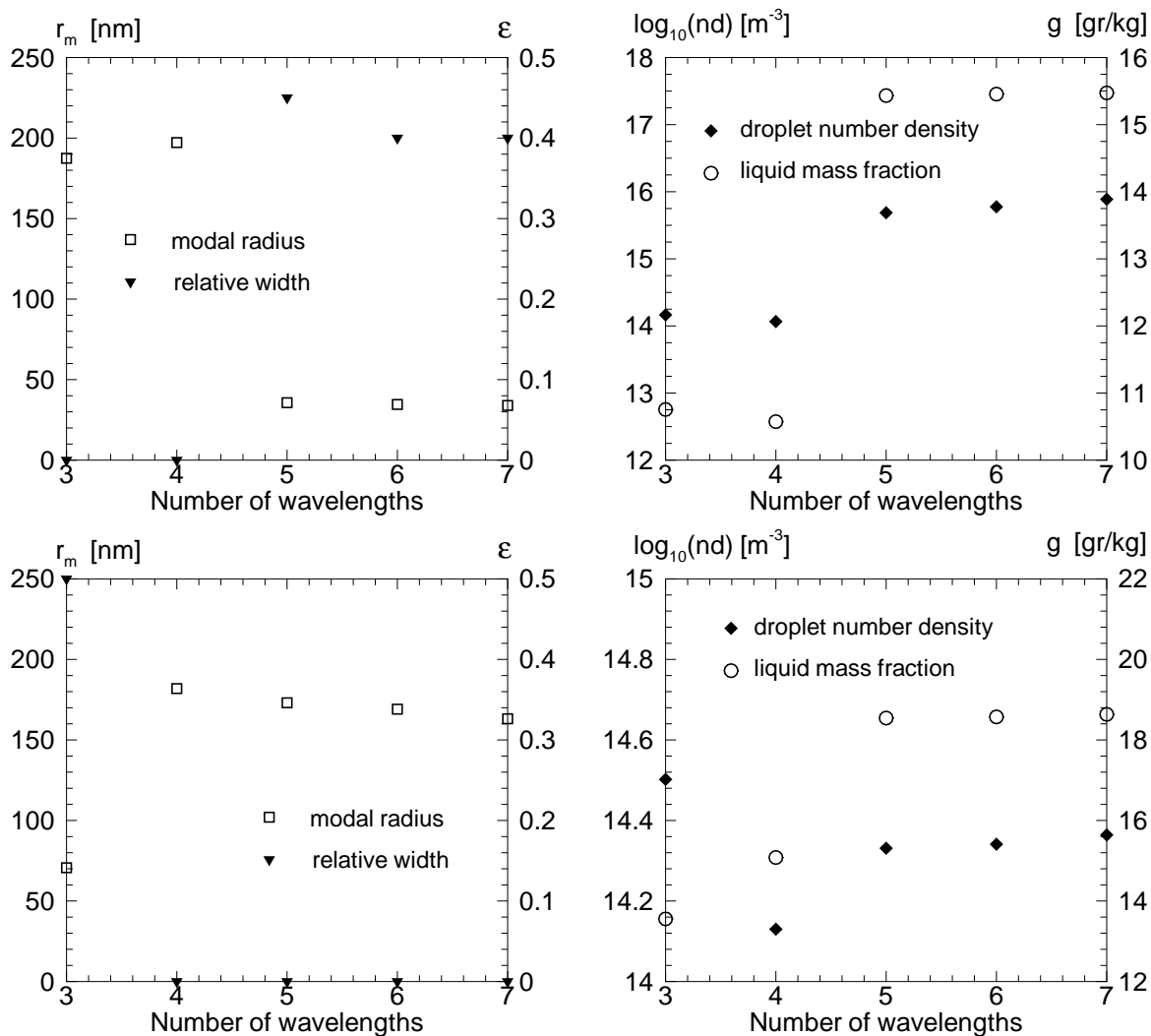
Figure 5.10: *Influence of the number of wavelengths used on the characteristics of the droplet size distribution. Nozzle: G2. Exp. 37 - Stagnation conditions: $P_0 = 8.75 \cdot 10^4 \, Pa$, $T_0 = 296.6 \, K$, $S_0 = 1.188$.*

top	:	Properties of the size distribution (r_d, n_d, ε) and estimated liquid mass fraction (g) at the time instant: $t_1 = 33.10 \, ms$. (near minimum β)
bottom	:	Properties of the size distribution (r_d, n_d, ε) and estimated liquid mass fraction (g) at the time instant: $t_2 = 33.31 \, ms$. (near maximum β)

Note that, for a given *trial function*, the minimum number of extinction data strongly depends on the size parameter α [106]. For Exp. 37 (whose extinction coefficients are shown in Fig. 5.8), the solution provided by the inversion method is inspected at two different instants of time: t_1 and t_2. They are representative of the two flow regimes normally encountered in the experiments, as discussed in section 5.3.3.1. All characteristic properties of the droplet size distribution are examined, namely: the modal radius r_m, droplet number density n_d, and relative width ε. As additional test, also the estimated liquid mass fraction g is calculated.

Figure 5.10 illustrates the results. It can be inferred immediately that the solution obtained from the least squares procedure depends, indeed, on the number of extinction signals used. With three or four attenuation signals, the analysis shows a considerable scatter. From 5 wavelengths on, instead, the solution converges to a limiting value. Noteworthy is also that, even in the near-Rayleigh regime (r_m of the order of 30 nm), the behaviour of the solution remains similar. This implies that this dependence on the number of wavelengths is, indeed, a peculiarity of the inversion method and not an effect due to the higher inaccuracies typical of the near-Rayleigh regime. Although the *trial function* method appears to have reached a correct solution already for five wavelengths, it is preferred to work always with seven signals, since this provides additional control variables.

5.3.3   Results: an example

As an example of the potential of the proposed method to follow the droplet size and number density in time, a typical solution, corresponding to Exp. 37, is discussed in detail. The occurrence of a periodic oscillating flow can already be inferred from the extinction signals, shown in Fig. 5.8. From these signals, at seven different wavelengths, the Rayleigh parameters R_{i1} have been calculated as functions of time for each wavelength. Two of them are shown in Fig. 5.11(c). It is clear that, during part of a period, the values of these parameters approach unity, which indicates that the particle sizes and wavelengths are near to the regime of Rayleigh scattering. However, in between, the R_{i1} become significantly smaller than unity, which points to droplet sizes beyond the Rayleigh regime.

By comparing Fig. 5.11(a) and (c), a very good correspondence can be observed between the values of the droplet radii and those of the parameters R_{i1}, namely: the maxima in droplet radii always correspond to the lowest values of the R_{i1}. For values of the Rayleigh parameters close to unity, droplet radii of the order of 35 nm (near-Rayleigh regime) are accordingly predicted by the inversion method. At these conditions, large errors inevitably occur, as indicated by the error bar given in Fig. 5.11(a). Nevertheless, the agreement between the calculated and measured droplet sizes is generally quite good, as shown in chapter 6. Figures 5.11(b) and (d) show the variation in time of the droplet number density n_d and relative variance ε. A first remark is that the droplet size maxima correspond to minimum values of the number densities (thus less droplets are produced), while the size distribution is almost monodispersed. A second remark is that, for most part of the period, extremely dense clouds are produced, which are characterised by very fine droplets and large dispersions ε around 0.40. Since the scattering of light by droplets of this size (35

nm) is quite small, the spectral curve shows very little identifying structure. Therefore, an accurate evaluation of the relative width ε cannot be accomplished at these conditions.
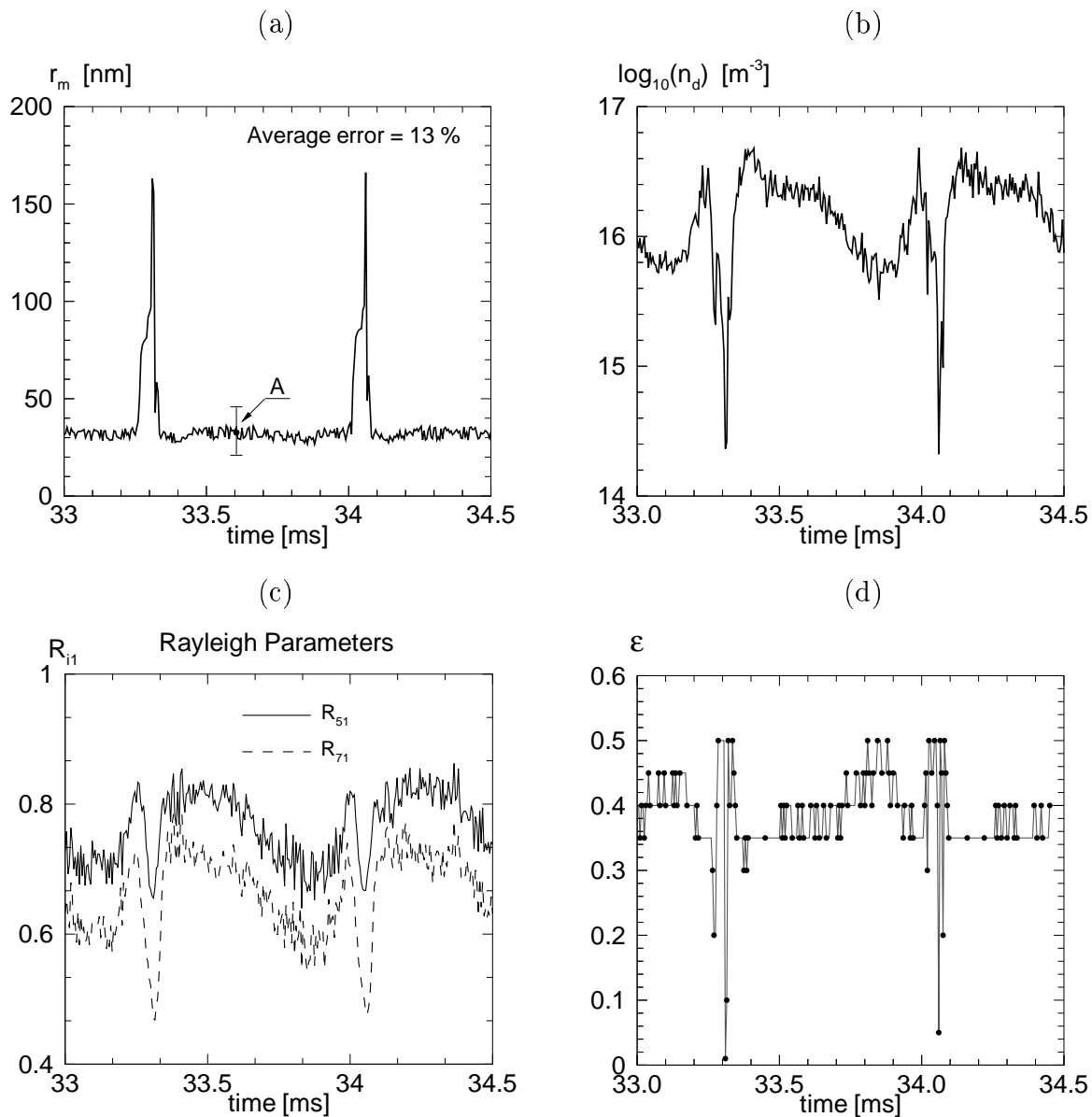
Figure 5.11: *Characteristic properties of the droplet size distribution and Rayleigh parameters as function of time, obtained from the inversion technique. Nozzle: G2. Exp. 37 - Stagnation conditions:* $P_0 = 8.752 \cdot 10^4\, Pa$, $T_0 = 296.6\, K$, $S_0 = 1.188$, $g_{max} = 25.20\, g/kg$.

top left	:	Modal radius (r_m).
top right	:	Droplet number density (n_d).
bottom left	:	Rayleigh parameters (R_{i1}), calculated directly form the extinction data at the following wavelengths: $\lambda_5 = 551.1$, $\lambda_7 = 434.5\ nm$.
bottom right	:	Relative variance (ε).

As an additional check, the condensed mass fraction is computed. The latter is proportional to the third moment of the size distribution and can be determined using the following expression:

$$g = \frac{4}{3}\pi \frac{\rho_l}{\rho} n_d r_m^3 e^{\frac{15}{2}\varepsilon^2},$$
(5.25)

where ρ_l and ρ have been estimated at $9.8 \cdot 10^3$ and $0.22 \, kg/m^3$, respectively. Both values are representative of the experimental conditions. If one calculates the ratio g/g_{max}, where g_{max} is the water vapour mass in the supply vessel, it follows that:

$$
\begin{array}{ll}
 & g/g_{max} \\
t_1 = 33.31 \, ms: & 0.93 \\
t_2 = 33.50 \, ms: & 1.92
\end{array}
$$

The unrealistic value obtained for the time instant t_2 (near-Rayleigh regime) confirms once again the high inaccuracy of the solution in this regime. Errors in the evaluation of the relative variance or droplet number density can readily explain this incongruity.

Despite these limitations, the results presented here are in line with the numerical predictions of White and Young [159]. They were the first to predict the characteristics of the droplet size spectrum for unsteady flows of condensing steam through a nozzle. Their findings can be summarised as follows:

1) due to the periodic quenching of nucleation larger droplets are produced. In their calculations the droplet Sauter mean radius varies in the range $[40 \div 150] \, nm$;

2) as a result of the unsteadiness, broader distributions are observed than those normally encountered in steady flows;

3) for a brief instant of time the droplet spectrum shows a bimodal character.

Except for finding (3), which lies beyond the limit of optical detection for the given droplet sizes, the results presented here constitute the first experimental validation of their findings.

5.3.3.1   Accuracy of the solution

In the previous sections, the accuracy of the solution has been checked in detail with respect to noise level and stability of the inversion method. Further, emphasis has been given to the theoretical and numerical constraints, which may hamper substantially the reliability of the inversion procedure in the near-Rayleigh regime. Nevertheless, no detailed check has been performed so far to validate the quality of the solution in its totality, that is with respect to its accuracy and realistic physical grounds.

This objective can be achieved by comparing the experimentally determined extinction spectrum $\beta(\lambda_i)$ with its theoretical counterpart $\overline{Q_{ext}}(\lambda_i, r_{char})$ averaged over all particle sizes. As characteristic size r_{char}, the Sauter Mean radius r_{32} is chosen:

$$r_{32} = \frac{\int f(r_d, \mathbf{p}) \, r_d^3 \, dr_d}{\int f(r_d, \mathbf{p}) \, r_d^2 \, dr_d},$$
(5.26)

where $f(r_d, \mathbf{p})$ is the postulated distribution function and the parameter vector $\mathbf{p}$ is given by the inversion method. Then, an averaged extinction efficiency $\overline{g}(\lambda_i, r_{32})$ can be assigned to r_{32}, on the basis of the experimentally determined extinction coefficients $\beta_{exp}(\lambda_i)$:

$$\overline{g}(\lambda_i, r_{32}) = \frac{\beta_{exp}(\lambda_i, r_{32})}{\int f(r_d, \mathbf{p}) \, r_d^2 \, dr_d}. \tag{5.27}$$

The quantity $\overline{g}(\lambda_i, r_{32})$ is often referred to as spectral turbidity. Its dependence on both wavelength and size can be combined in the size parameter α_{32}, calculated using the Sauter Mean radius ($\alpha_{32} = 2\pi r_{32}/\lambda$). In a similar fashion, an averaged theoretical extinction efficiency $\overline{Q_{ext}}(\alpha_{32})$ can be assigned to r_{32}:

$$\overline{Q_{ext}}(\lambda_i, r_{32}) = \frac{n_d \int \pi r_d^2 \, Q_{ext}(\lambda_i) \, f(r_d, \mathbf{p}) \, dr_d}{\int f(r_d, \mathbf{p}) \, r_d^2 \, dr_d}. \tag{5.28}$$

The theoretical values for the extinction coefficients $\beta_{theo}(\lambda_i)$ are derived from Mie theory and from the postulated size distribution $f(r_d, \mathbf{p})$, where $\mathbf{p}$ is obtained by the inversion method. In other words, $\overline{Q_{ext}}(\alpha_{32})$ represents the theoretical value of the averaged extinction efficiency that corresponds to the experimentally deduced characteristics of the droplet size distribution.

If the size distribution is monodispersed, then Eqs. (5.27) and (5.28) simplify considerably. Specifically, it follows that $r_{32} = r_d$, $\alpha_{32} = \alpha$, and $\overline{Q_{ext}}(\alpha_{32}) = Q_{ext}(\alpha)$. Furthermore, the spectral turbidity can be simply calculated as follows:

$$g(\alpha) = \frac{\beta_{exp}(\alpha)}{\pi \, n_d \, r_m^2}, \tag{5.29}$$

where r_d and n_d denote the droplet modal radius and number density, respectively, which are obtained directly from the inversion procedure.

With reference to Exp. 37 (whose time dependent solution in shown in Fig. 5.11), let us investigate its extinction spectrum at the following two instants of time: $t_1 = 33.10$ and $t_2 = 33.31$ ms. From Fig. 5.11, it is possible to infer the following:

	$t = t_1$	$t = t_2$
relative variance	≈ 0.40	≈ 0
scattering regime	near-Rayleigh	Mie

Since in the Rayleigh regime the relative variance ε can never be obtained accurately, Eq. (5.29) is employed for the time instant t_1, as well. Of course, discrepancies must be expected since the solution is, at this time, considerably polydispersed. The results are shown in Fig. 5.12 together with the theoretical curves corresponding to the regimes of Rayleigh and Mie scattering.

Figure 5.12(a) shows the result for the time instant t_1, where low extinction coefficients are detected ($\beta \approx \beta_{min}$). The discrepancy between theory and experiments is, as mentioned earlier, not surprising since Eqs. (5.27) and (5.28) should have been used. Despite this incongruity, each set of data points can still be associated with a specific part of the theoretical curve: thus indicating undoubtedly that one is, in fact, working in the near-Rayleigh regime. As direct consequence, it follows that, for large part of the period, only the modal radius can be obtained in a reliable way. Any deduced variation in the relative variance (ε) must be regarded simply as an indication of its *effective* time dependence, rather than as an accurate measure of the latter.

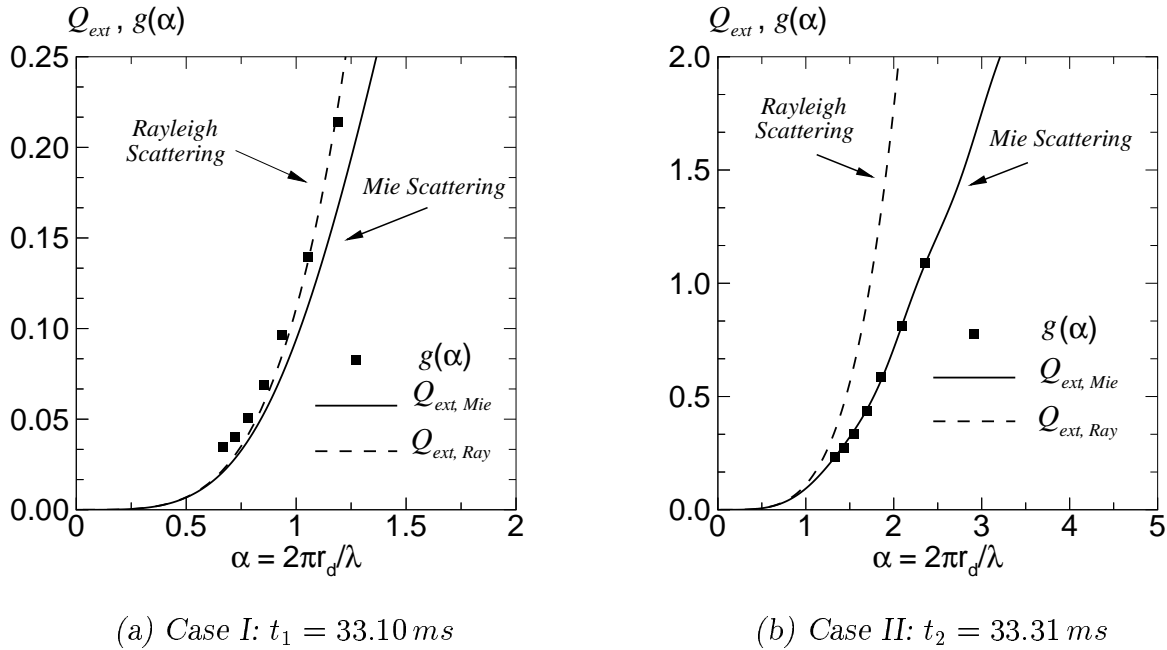(a) Case I: $t_1 = 33.10\,ms$ (b) Case II: $t_2 = 33.31\,ms$

Figure 5.12: *Theoretical extinction efficiency and spectral turbidity as function of the size parameter (α).*

Figure 5.12(b), instead, refers to the case where high extinction peaks are observed ($\beta = \beta_{max}$). The good agreement between the observed $g(\alpha)$ and corresponding $Q_{ext}(\alpha)$ has important implications, which are discussed next. First, it provides unquestionable proof that the measured spectrum is indeed beyond the Rayleigh regime. This is undoubtedly a major result, since no droplet sizing measurement can be considered trustworthy without such a proof. Second, it shows that the experimentally determined transmittances characterise accurately the extinction spectrum of the flowing mixture. In other words, experimental inaccuracies or forward scattered radiation do not hamper the quality of the extinction measurements. Third, the solution provided by the *trial function* method is very accurate and reliable in correspondence of the extinction peaks. As a direct consequence of this analysis, the validation of the different condensation models (see chapter 6) is based exclusively on those points where maximum droplet sizes are observed.

5.4 The influence of scattering on extinction measurements

In ideal extinction measurements only the attenuated light from the source is observed. In such situations, the transmitted light flux is accurately described by the Lambert-Beer law. This ideal situation, however, cannot be fully realised, because generally the light scattered in the forward direction cannot be eliminated completely. The influence of scattering on the extinction measurements is basically twofold. For optically dense media, multiple scattering effects are strong and no distinction can be made between forward scattered light, which has undergone several scattering events, and the attenuated light of the incident beam. Second, due to the finite size of any detector system, there is always a certain fraction of light, scattered in some small but finite range of angles around the forward direction, which may jeopardise the quality of the extinction measurements. In general the larger the particle, the greater the possible discrepancy between measured and calculated extinction.

To estimate and minimise the effects of forward scattered radiation on the extinction measurement the following approach is adopted. On one hand, the design of the optical set-up is optimised to keep forward scattering contributions small and easy to compute. This issue is tackled in sub-section 5.4.1. On the other hand, a Monte Carlo simulation, encompassing both single and multiple scattering effects, was applied by van Poppel [103] to ascertain quantitatively the effects of forward scattered radiation on the extinction measurements. The results from the Monte Carlo simulations are, then, compared with the theoretical case in which only single scattering occurs. This led to the formulation of design criteria for the optical set-up and the identification of limiting factors for the measured transmittances, so that the influence of forward scattering was kept within a few percent of the experimentally determined extinction signals.

5.4.1 Detection with a finite field of view

As pointed out in the introduction, scattered light in the forward direction cannot always be separated from the attenuated light of the original beam. In order to minimise this effect, it is necessary to increase the separation quality of the detection system. Depending upon the actual situation, there exist essentially two different approaches:

a)   the lens-pinhole detector system;
b)   the open detector system.

Both methods have been discussed by Deepak and Box [26, 27]. The second technique is particularly advantageous in measurements with very narrow beams (i.e. beam diameters of the order of 0.8 *mm* or smaller). For our application, the first method is preferred since it has an exact and constant angular field of view. In literature, the latter is often

referred to as the finite-field-of-view technique. The detection system consists of three elements, as sketched in Fig. 5.13: a positive lens with focal distance f, a pinhole with diameter d, positioned in the focal plane of the lens, and a conventional detector that accepts all incident light regardless of the direction of propagation.
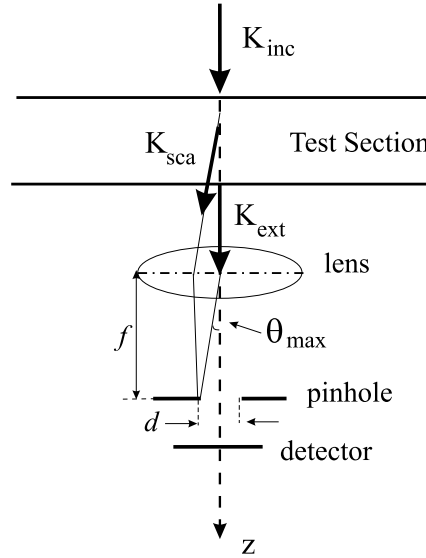
Figure 5.13: *Schematic illustration of the lens-pinhole detection system.*

Only the light that is incident on the lens with a direction of propagation that lies within a certain maximum angle θ_{max}, around the optical axis of the lens, is detected by the system, see Fig. 5.13. It is obvious that this maximum detection angle obeys the relation:

$$\theta_{max} = \frac{d}{2f}. \tag{5.30}$$

This detection system reduces drastically the effect of scattering when θ_{max} is chosen small enough, as explained in section 5.4.3 where the influence of the scattering process on the extinction measurements is simulated numerically.

5.4.2 Incoherent single scattering

Single scattering occurs if the major part of the light scattered by the droplet cloud does not undergo a second scattering event. Smolders [130] derived an equation for the contribution of single scattering to the extinction signal.

Consider an unpolarised light beam of cross-section A and irradiance I_0, incident perpendicularly to a slab of thickness l and filled with droplets, as shown in Fig. 5.14. The droplets have a radius r_d and a number density n_d. The attenuation of the light beam is measured with a detector having a half angle of detection θ_{max}.
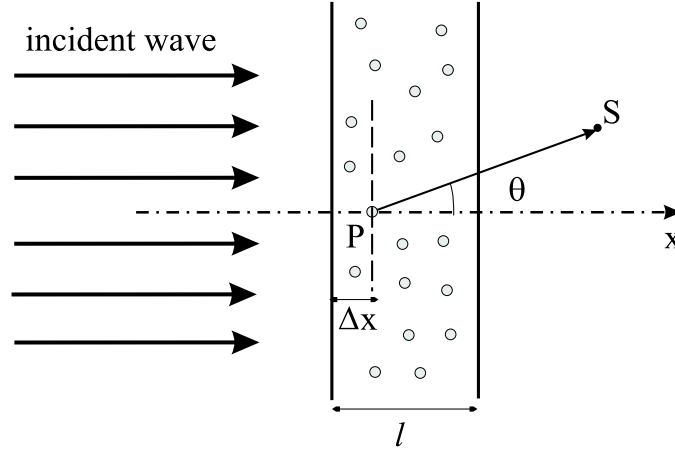
Figure 5.14: *Slab filled with particles.*

At a location (S) behind the slab, the irradiance of the scattered light due to a droplet at a depth Δx in the slab is (details can be found in Appendix G):

$$I_s = C_1 \, C_2, \tag{5.31}$$

with

$$C_1 \;=\; I_0 e^{-\beta \Delta x} \frac{1}{2k^2 r_d^2} \left[i_1(\alpha, m, \theta) + i_2(\alpha, m, \theta) \right], \qquad (\theta \ll 1) \tag{5.32}$$

$$C_2 \;=\; e^{-\beta(l - \Delta x)}. \tag{5.33}$$

In equations (5.32) and (5.33), β is the extinction coefficient of the droplet cloud, i_1 and i_2 are the irradiance components of the scattering matrix $\underline{\underline{S}}$. Term ($C_1$) represents the irradiance of the light scattered by the droplet at P, and term (C_2) indicates the attenuation due to the remaining part of the slab. In the hypothesis that the angle of detection is small, the power scattered by one droplet and received by the detector is:

$$P_s^1 = I_0 e^{-\beta l} \frac{\pi}{k^2} i_0(\alpha, m) \theta_{max}^2 = I_0 e^{-\beta l} \pi r_d^2 \frac{i_0(\alpha, m)}{\alpha^2} \theta_{max}^2, \tag{5.34}$$

where $i_0(\alpha, m) = i_1(\alpha, m, \theta = 0) = i_2(\alpha, m, \theta = 0)$. In this expression (Eq. 5.34), the scattered power does not depend on the position of the droplet. Therefore, the total received power, due solely to single scattering contributions, can simply be obtained by multiplying the power scattered by one droplet with the volume of the illuminated slab and the number density of the droplets:

$$P_s = n_d A l I_0 e^{-\beta l} \pi r_d^2 \frac{i_0(\alpha, m)}{\alpha^2} \theta_{max}^2. \tag{5.35}$$

The power of the attenuated light beam is given by the expression:

$$P_e = A I_0 e^{-\beta l}. \tag{5.36}$$

Then, the ratio between Eqs. (5.35) and (5.36) yields the final expression:

$$\frac{P_s}{P_e} = n_d l \pi r_d^2 \frac{i_0(\alpha, m)}{\alpha^2} \theta_{max}^2 = \beta l \frac{i_0(\alpha, m)}{Q_{ext}(\alpha, m)\alpha^2} \theta_{max}^2. \tag{5.37}$$

If the condition of single scattering is not satisfied, P_s will not equal the total scattered power that is detected; instead it will simply represent the single scattering contribution to the total detected power. In the next section, the multiple scattering process is simulated and the results compared with Eq. (5.37) in order to verify when deviations from single scattering become manifest.

5.4.3 Multiple scattering

The locution *multiple scattering* refers to situations in which each particle, acting as an isolated and randomly positioned scatterer, contributes to the radiant energy incident on the other scatterers. This circumstance may be encountered in the case of dilute media and large geometrical thickness (as in interstellar clouds), or in the case of large particle number density with small geometrical thickness (usual situation in industrial plants and laboratory experiments). In general, the extent of multiple scattering effects increases with turbidity and with the size of the illuminated volume. The extension of single scattering theory to an array of scatterers has been the subject of extensive experimental, computational, and theoretical studies since many years. Despite the extensive body of literature, few articles provided a practical guideline to quantify the effects of multiple scattering on the extinction measurements. More recently, Guidt *et al.* [47] performed particle diagnosis at large optical thickness, where multiple scattering phenomena occur. They proposed a new method for measuring particle sizes and number densities: the visible infrared double extinction technique (VIDE) at high optical thickness. A spin-off of this research is the study of the limitations of the Lambert-Beer law on which the technique relies. They concluded that measurements up to an optical thickness of 9 are still feasible with respect to the application of the Lambert-Beer law. Their conclusion seems, at first sight, quite surprising. However, a closer look to the experimental data reveals that such a high optical thickness is achieved at corresponding values of the size parameter α of 0.8. Under this condition, the particles are much smaller than the employed wavelengths, therefore their contribution to forward scattering is very small, thus permitting measurements at such high value of δ.

In this section, the results of Guidt *et al.* are generalised to encompass, in their totality, the effects of scattering on the extinction measurements. As shown in subsection 5.4.3.2, our results agree perfectly with those of Guidt. To this purpose, a Monte Carlo simulation of the scattering and extinction process in the test section is developed. The basic idea underlying the simulation is that the total detected power can be expressed as the sum of two contributions: the scattered power P_s and the attenuated power P_e. By independently evaluating these powers, one can obtain a quantitative information on the influence of scattering effects on the extinction measurements. Furthermore, by comparing the value obtained for the scattered power P_s with those obtained from Eq. (5.35), which

provides the single scattering contribution, one can also infer the relative importance of multiple scattering effects. The results are presented in subsection 5.4.3.2. In the following subsections, the mathematical model underlying the Monte Carlo simulation is described.

5.4.3.1   Mathematical model

The mathematical model of the scattering process is based on the work of Bucher [16, 17]. The simulation program assumes a homogeneous cloud within two plane-parallel boundaries, as sketched in Fig. 5.15. The cloud is assumed to have constant macroscopic properties and is modelled as an infinitely long slab of thickness l. In the simulation, photons leave from an identical location and have the same initial direction, therefore the effects of beam width and divergence are not taken into account. Each photon represents the same amount of energy. Typical ray paths are illustrated in Fig. 5.15 for all possible cases: singly/multiply scattered or undisturbed ray. Rays leaving the slab from the top boundary represent back scattered light and are not counted for. Rays exiting the slab from the bottom boundary indicate transmitted light and are, therefore, tracked. A scattered ray is detected only if its exit angle θ_{exit} is less than θ_{max}. These photons contribute to the scattered power P_s. If the photon leaves the tube undisturbed, it is also detected and contributes to the power P_e of the attenuated original beam. By tracing many paths,

A: *Singly scattered photon*
B: *Undisturbed photon*
C: *Multiply scattered photon*

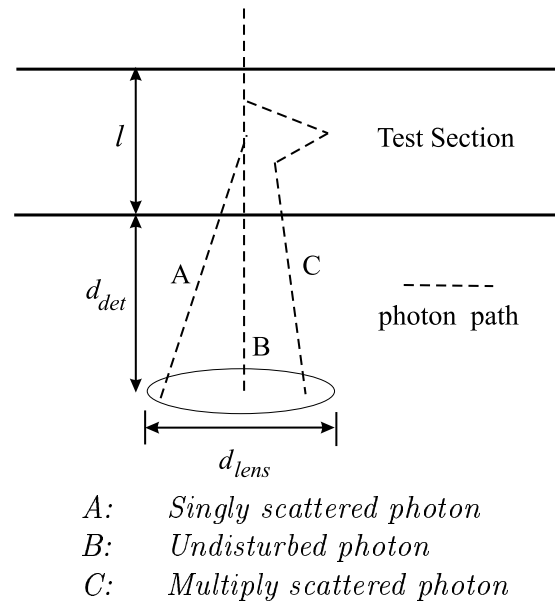**Figure 5.15:** *Schematic representation of possible photon paths in the test section.*

which are generated randomly in the simulation, one obtains a representative sample of the simulated scattering process in the medium. The distance d that a ray travels between two successive scattering events is randomly selected with a probability density function

$$p(d) = \beta\,e^{-\beta d}. \tag{5.38}$$

The choice of this probability density function is made plausible in Appendix H. Here, it is worth noting that the exponential distribution of path lengths is based on the hypothesis of a cloud of scatterers randomly distributed throughout the cloud volume and with a mean free path $<x>$ given by the inverse of the extinction coefficient. Recalling the definition of the non-dimensional parameter δ, it results:

$$\delta = \beta \, l = l/ <x>, \tag{5.39}$$

where l is the geometrical length of the test section. It is now clear why the condition $\delta \ll 1$ is the fundamental one for excluding multiple scattering effects. If the mean-free path between the scatterers is smaller or of the same order of magnitude than the geometrical path length, then proximity effects can no longer be neglected.

When a scattering event takes place, a scattering angle θ and an azimuthal angle φ are independently chosen. The angles θ and φ are defined as indicated in Fig. 5.2. The azimuthal angle φ is randomly selected with a constant probability between 0 and 2π. This uniform distribution is the direct consequence of the assumption of spherical scatterers. The θ-angle probability density function depends on the scattering mechanism. In this case, the correct expression for this function is given by equation:

$$p(\theta) = \frac{(i_1 + i_2) \sin \theta}{\int_0^\pi (i_1 + i_2) \sin \theta \, d\theta}, \tag{5.40}$$

where i_1 and i_2 follow from Mie theory (Appendix G). The detected scattered rays and the undisturbed rays are counted separately, so that the ratio between these numbers yields the power ratio P_s/P_e. In the experimental environment, this should be close to zero since one wants to measure only the attenuation of the incident light.

5.4.3.2   Monte Carlo simulation: results

In this subsection, some of the results from the Monte Carlo simulations are presented. In general, the magnitude of the powers P_s and P_e depends on a set of parameters characterising either the extinction process or the optical configuration of the set-up. These are namely: the extinction coefficients β, the size parameter α, the detector distance d_{det}, defined as the distance the attenuated light beam has to bridge between the test section and the lens, the lens diameter d_{lens}, the geometrical path length l, and the maximum detection angle θ_{max}. Some of these parameters are indicated in Fig. 5.15. Due to the geometrical configuration of the set-up, some of the parameters have a fixed value, specifically: $d_{det} = 5 \, cm$, $d_{lens} = 8 \, mm$, and $l = 10 \, cm$. A parametric study is performed to evaluate the dependency of the ratio P_s/P_e upon a specific parameter while keeping constant all others. The values of these constant parameters are taken as the exact or representative values for our experimental conditions.

First, the influence of the detector entrance angle θ_{max} is investigated and the results are shown in Fig. 5.16. As it can be inferred from Fig. 5.16, an increase of θ_{max} has a dramatic effect on the power ratio P_s/P_e. For this reason, the entrance angle of the set-up
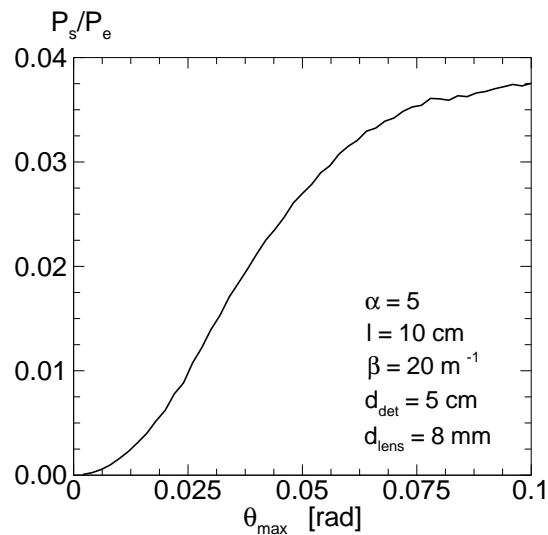
Figure 5.16: *The effect of the entrance angle θ_{max} on the power ratio P_s/P_e.*
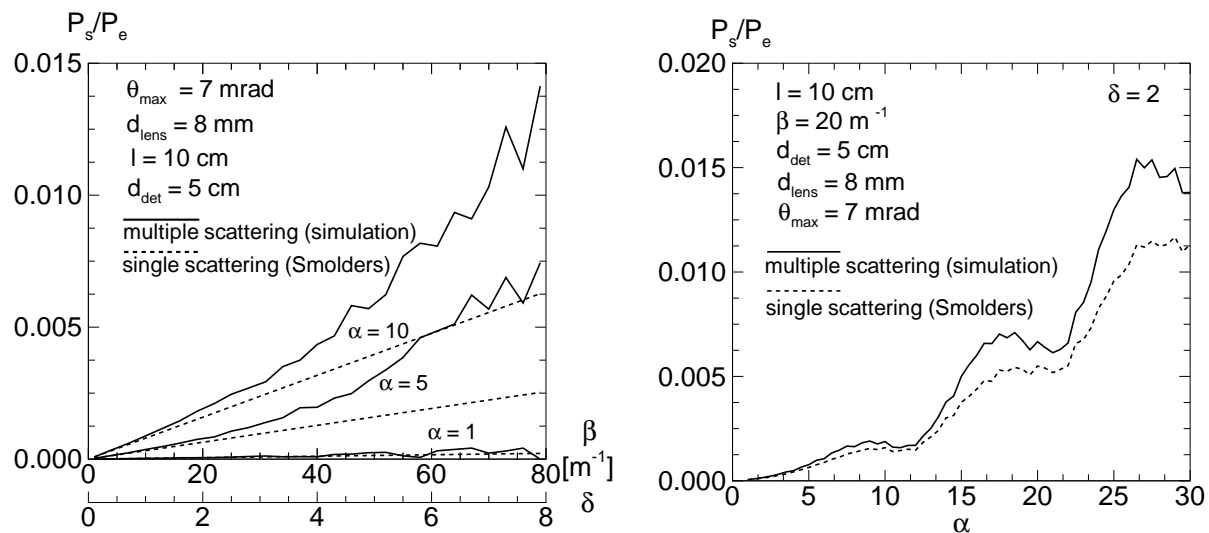
Figure 5.17: *The effect of the extinction coefficient β and size parameter α on the power ratio P_s/P_e.*

is chosen equal to 7 mrad, so that the influence of forward scattering is confined to values lower than 0.2 per cent. Figures 5.17 (a) and (b) illustrate the dependence of the ratio P_s/P_e on the extinction coefficient β and size parameter α, for both single and multiple scattering situations. It follows that the effect of forward scattered power can be neglected when $\alpha < 5$ and $\beta < 30$. At these conditions, the scattered power P_s will be less than 0.1% of the attenuated power of the original beam P_e. These requirements are satisfied in all experiments, since the size parameter α varies in the range $[0.4 \div 3]$ and the extinction coefficients do not exceed the value of 25 $[m^{-1}]$.

Figure 5.17 illustrates also the functional relationship between The optical depth δ and the extent of multiple scattering effects. From the observation of this plot, it follows that the notion of $\delta \ll 1$ is meaningful only when related to the size parameter α. For particles much smaller than the wavelength ($\alpha \leq 1$), the forward scattered contribution is so small that, even for extreme optical densities ($\delta \geq 9$), extinction measurements can still be performed in agreement with the results of Guidt $et\ al.$ [47]. For these situations, the limiting factor is represented by the phenomenon of $reddening$ of a white light beam on passing through a collection of very small particles: shorter wavelengths are extinguished sooner and more effectively than longer ones. It is, thus, this phenomenon rather than multiple scattering effects, which may hamper extinction measurements in condensing nozzle flows.

5.5   Conclusions

The preceding sections have presented an elaborate treatment of the technique of droplet sizing by light extinction. In particular, special care has been paid in assessing the quality of the method both with regard to experimental and theoretical issues. For the experimental side, a detailed study is performed to evaluate the influence of forward scattered radiation on the extinction measurements. Based on this study, the set-up has been designed in such a way as to contain this influence within few percent. An important pay-off of these simulations is the validation of the Lambert-Beer law on whose applicability the analysis fully relies. As for the numerical and theoretical counterpart, a detailed check is performed on the reliability of the inversion method. Result of this analysis is that the characteristics of the droplet size distribution can be, indeed, determined with great accuracy only in correspondence to the high extinction peaks. These are, in fact, the only instants in time where the droplet cloud is completely outside the Rayleigh regime. Despite these limitations, the derived time dependent variation in the droplet size agrees qualitatively with the theoretical predictions of Young. Due to the very small size of the droplets for supersaturation values lower than 0.9, the results are not reliable during the entire period of oscillation. Therefore, for the validation of the proposed condensation models, which is discussed in chapter 6, the comparison between experimental and theoretical results is restricted to experiments with stagnation supersaturations higher than 1.0 and limited to the extinction peaks.

Chapter 6

Results and discussion

6.1 Introduction

The aim of this chapter is to validate condensation models for water vapour/carrier gas mixtures, at nozzle stagnation pressures of about $1\,bar$. A thorough validation is, to the author's knowledge, for the first time possible for a water vapour/carrier gas mixture thanks to the availability of droplet size data. The accuracy of a given condensation model depends ultimately on the accuracy of the underlying theories of nucleation and droplet growth. As pointed out by Young [162], the quality of these theories can be tested to a sufficient extent independently only when both droplet sizes and pressure distributions (or alternatively frequency data) are available for a given experiment.

In order to accurately validate condensation models, a number of necessary steps have to be undertaken, which are, because of their importance, clearly outlined in the following. First, the reliability of droplet growth theory has to be established. This is achieved by comparing the predictions from different growth laws with droplet size experiments. In the course of this analysis, the equally important role of heat and mass transfer - for the correct quantitative evaluation of the droplet growth rate - is also experimentally confirmed. Then, by analysing the frequency data for a number of nozzles, the proper (and consistently applied) correction factor for the nucleation rate is individuated, which given the uncertainties in nucleation theory is a sensible course of action. It is explicitly **stressed** that this evaluation is performed in a range of temperatures in which **surface tension data** have been **experimentally determined**. Therefore, there is no arbitrariness in the surface tension values and the quality of the nucleation model can be ascertained independently of the extrapolation of surface tension values to low temperatures.

Once the proper nucleation and droplet growth model have been selected, the analysis proceeds with the examination of nozzle flows nucleating at increasingly larger subcoolings. A comparative study has been, then, undertaken to select a surface tension fit which best correlates all the collected experiments and satisfies the thermodynamic constraint given by the Nernst Postulate: $\partial\sigma/\partial T \rightarrow 0$ as $T \rightarrow 0$. Obviously, the accuracy of this extrapolation depends on the accuracy of the experimental data. Therefore, additional independent tests

are required to confirm the validity of the fit proposed by the present author.

A large number of the available published and well-documented data on condensing nozzle flows of water vapour/carrier gas mixtures have been collected and re-examined in light of the strategy just outlined. The results of this analysis are presented in the next sections and include steady/unsteady flow regimes, nearly one-dimensional till complex two-dimensional flow fields. To facilitate the understanding of the analysis, it is always clearly indicated which stage of the validation process is being considered. However, the implications and extent of this study can be fully assessed only when cast in a general perspective.

6.2 Condensation models

All condensation models analysed in this study are grouped in Table 6.1, with a clear indication of their constitutive elements. Note that the term "condensation model" refers to a specific combination of surface tension, nucleation, and droplet growth theory.

Author	Abbr.	Surface - Tension	Nucleation Model	Empirical Factor	Droplet Growth Model
Schnerr *et al.*	SD – HK	σ^{SD}	CNT	$\xi = 1$	HK ($T_d = T$)
CNT – wb	SD – HK^{wb}	σ^{SD}	CNT	$\xi = 1$	HK (wet-bulb)
Luijten – Prast	LP – gya82	σ^{LP}	ICCT	$\xi = 1$	gya82
ICCT – gya82	LP$^{\xi}$ – gya82	σ^{LP}	ICCT	$\xi = 0.01$	gya82
this author	LD – gya82	σ^{LD}	ICCT	$\xi = 0.01$	gya82
this author	LD – HK^{wb}	σ^{LD}	ICCT	$\xi = 0.01$	HK (wet-bulb)
this author	LD – gya63	σ^{LD}	ICCT	$\xi = 0.01$	gya63

Table 6.1: *A synoptic overview of the condensation models considered in this study. Abbreviations:*

CNT	=	Classical Nucleation Theory;	gya63	=	Gyarmathy growth model [48];
ICCT	=	Internally Consistent Classical Theory;	gya82	=	Gyarmathy growth model [49];
HK	=	Hertz-Knudsen growth formula [57, 68].			

6.3 Nozzle G2

The results and considerations presented in this section are central in the development and understanding of the present work. In fact, the validation of nucleation and droplet growth theories and the extrapolation of surface tension data to lower temperatures rely strongly on the analysis of droplet size experiments. Since these experiments are so crucial to our findings, a brief discussion on their accuracy and reliability is repeated in subsection 6.3.2. A more detailed survey can be found in section 5.4. This section is organised as follows: a phenomenological description on the interdependence of nucleation process, flow field, and properties of the droplet cloud is provided in subsection 6.3.1. Subsection 6.3.2 presents the analysis of droplet size experiments and the validation of condensation models. Subsection 6.3.3 discusses the results of the holographic experiments.

6.3.1 Phenomenology

The most important macroscopic product of condensing nozzle flows is the generation of a droplet cloud, whose characteristics strongly depend on the interaction between the transonic flow field and the nucleation process. To clarify this mutual interdependence, a simple heuristic explanation is offered in this section.

Intuitively, one can immediately realise the direct correlation between the features of the nucleation pulse and the attributes of the droplet size distribution: the nucleation rate is, for example, directly proportional to the droplet number density of the cloud. The width of the nucleation peak determines, to a certain extent, the relative variance of the droplet size distribution. The modality of the distribution function (e.g. monomodal or bimodal) is directly connected to the number of nucleation pulses occurring along the nozzle axis. In unsteady flow regimes, such as the ones considered in this section, this interdependence becomes somewhat more complicated due to the periodic quenching of the nucleation rate by upstream travelling disturbances. To illustrate this situation, the time evolution of the temperature and nucleation rate is plotted, along the nozzle axis, in Fig. 6.1. The calculation simulates Exp. J42 and is performed using the corrected Luijten-Prast model (LP^ξ-gya82).

Figure 6.2 illustrates the effects that these time dependent profiles have on the characteristics of the droplet size distribution. Although this figure is derived for Exp. J42, the trend is general, holds for all the experiments presented here, and has been experimentally confirmed, as shown in Fig. 5.11. As immediately inferable from Fig. 6.2, the droplet modal radius exhibits a clear maximum ($R_m \approx 150\,nm$) during one period of oscillation, to which corresponds an almost monodispersed distribution ($\varepsilon \approx 0$). For most part of the period, smaller droplets ($R_m \approx 70\,nm$) and wider distributions prevail. This variation in time is due to the interplay between the nucleation process and the flow field shown in Fig. 6.1: as the temperature perturbation propagates upstream, it quenches the nucleation at different positions along the nozzle axis (curves 6, 1, 2, 3, 4,). The lower the nucleation rate (i.e. less condensation nuclei are produced), the bigger the modal radius becomes, in that the total water vapour fraction is constant. As the disturbance moves away, the nucleation process

re-acquires again its maximum strength (curve 5). This corresponds to the smallest modal radius and the widest distribution ($\varepsilon \approx 0.41$ in Fig. 6.2).
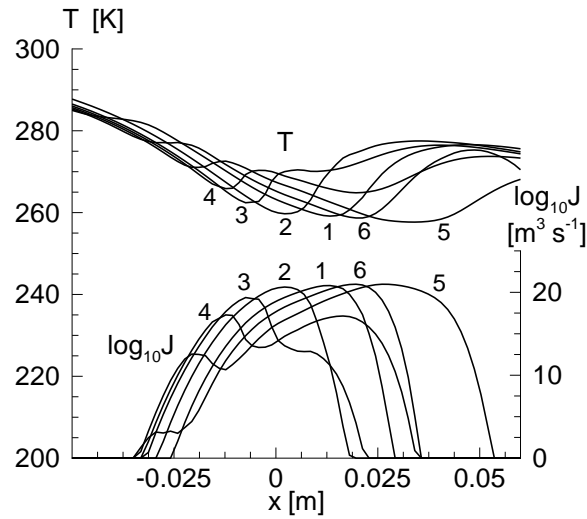

Figure 6.1: *Numerically derived profiles of nucleation rate and temperature along the nozzle axis, at 6 subsequent instants of time ($\Delta t = 0.86\,ms$). Nozzle: G2. Exp. J42 - Stagnation conditions: $P_0 = 8.63 \cdot 10^4\,Pa$, $T_0 = 296.9\,K$, $S_0 = 1.30$.*
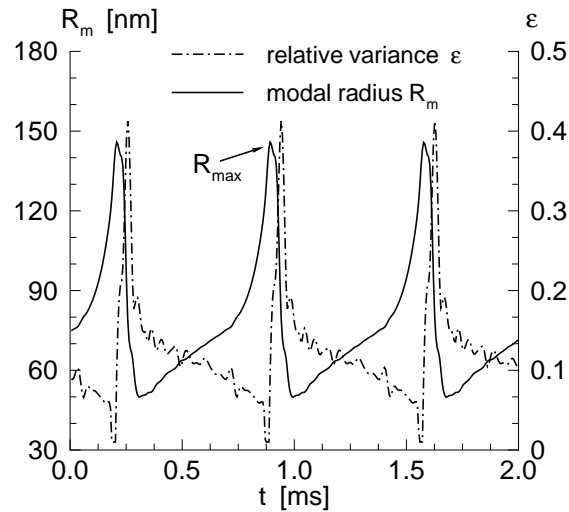
Figure 6.2: *Numerically derived properties of the size distribution as function of time. Point of observation: nozzle axis at $24\,cm$ downstream of the throat. Nozzle: G2. Exp. J42 - Stagnation conditions: $P_0 = 8.63 \cdot 10^4\,Pa$, $T_0 = 296.9\,K$, $S_0 = 1.30$.*

In this section, the comparison between experimental data and theoretical predictions is limited to the frequency of the oscillations and the maximum modal radius (R_{max}). As discussed in chapter 5, reliable droplet size information can be extracted from the extinction

measurements only if the size parameter $\alpha = 2\pi r_d/\lambda$ is bigger than one ($\alpha > 1$). In other words, the measuring point should correspond to a situation outside the regime of Rayleigh scattering. In the experiments analysed here, the size parameter α decreases to values of about 0.73 for modal radii of roughly $70 \, nm$, indicating that the measurements occur in the regime of near-Rayleigh scattering. For this reason, these points are excluded and the analysis concentrates solely on the maximum extinction values, for which reliable droplet size information can be derived. Specifically, the experimental inaccuracy varies between 5 and 10 %, depending on the stagnation supersaturation. This corresponds to an error in the maximum values of the modal radius between 10 and 20 nm.

6.3.2   Droplet size experiments

For all droplet size experiments, the stagnation pressure is approximately $0.865 \, bar$, while the stagnation supersaturation (relative humidity) varies in the range $[1 \div 1.6]$. The temperature, at which maximum nucleation occurs, can be inferred from Fig. 6.1. Although small differences might be observed in the predictions from the different models, the temperature range at which nucleation occurs remains essentially the same.

Due to the interaction between the nucleation process and the upstream moving disturbances, maximum nucleation rates take place at different temperatures in the range $[260 \div 270] \, K$. Within this range, as clearly shown in Fig. 2.1, surface tension data have been experimentally measured and, most important, there is a general agreement between the various fits proposed in literature. Having clarified that the results of the various condensation models only slightly depend on the choice of the surface tension fit, the experimental results can now be compared with the corresponding theoretical predictions. Figures 6.3 to 6.6 compare the predicted frequency of oscillations and the maximum modal radius with the experimental values, for each model listed in Table 6.1. The stagnation conditions for all experiments are: $P_0 = (8.69 \pm 0.015) \cdot 10^4 \, Pa$, $T_0 = 296.8 \pm 0.4 \, K$.

Two general remarks stem immediately from observing these plots. First, only when both nucleation and droplet growth theory are correctly evaluated, it is possible to match the entire sets of data with the corresponding experimental values, as deducible from a comparative study of the models' predictions. Second, the droplet sizes are correctly predicted every time the temperature difference $\Delta T = T_d - T$ is implemented in the droplet growth formula, either directly via the wet-bulb equation or indirectly as in the gya63 formulation. This fact corroborates the theoretical analysis presented in section 2.4.1.1, which can be summarised as follows: there exist two thermodynamic forces ΔP_v and ΔT which govern the irreversible process of droplet growth. Omission of ΔT as driving potential leads to an incorrect value of the droplet size by, approximately, a factor 3.

Having discussed these general aspects, the differences among the various condensation models are now examined in detail. Figure 6.3 compares results of the two versions of the Luijten-Prast model (original and corrected) with those of the LD-gya82 model. The droplet radius is correctly predicted by all models. Discrepancies, instead, appear in the frequency data. In the LP-gya82 model, the nucleation rate is too high and leads to an overestimation of the frequency value by roughly a factor 1.4. However, when the nucleation

rate is reduced by a factor[1] 100, the model is able to simulate properly all features of the condensation process.
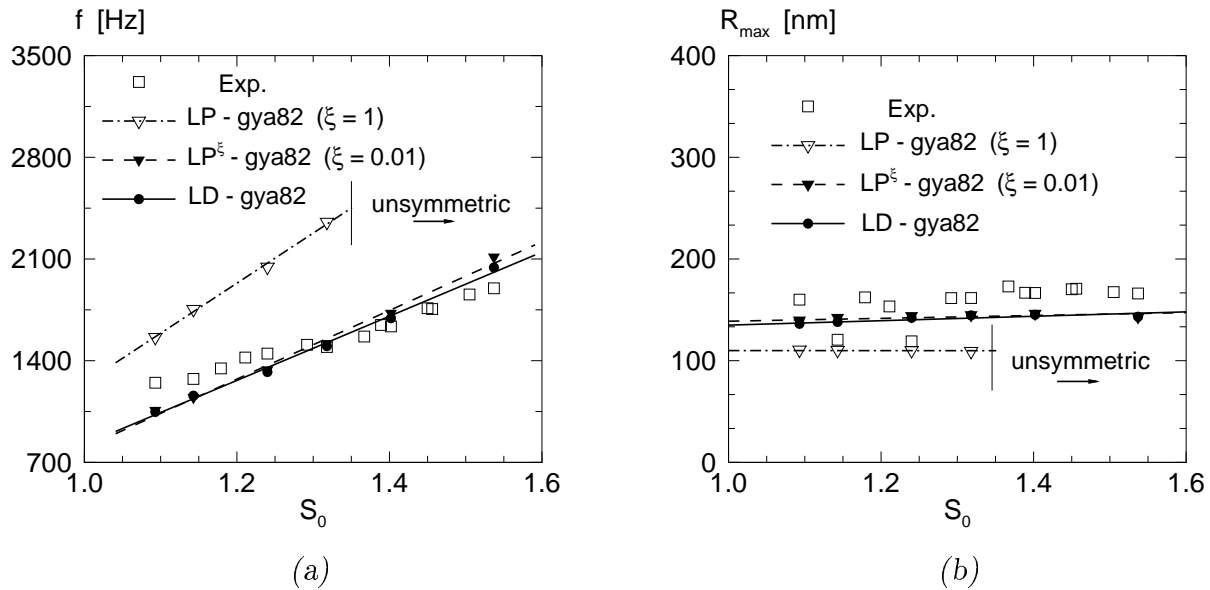

(a)   (b)

Figure 6.3: *Comparison of experimental data and theoretical predictions according to the following models: LP-gya82, LP$^\xi$-gya82, LD-gya82. Nozzle: G2. (a) Frequency of oscillations. (b) Maximum modal radius.*

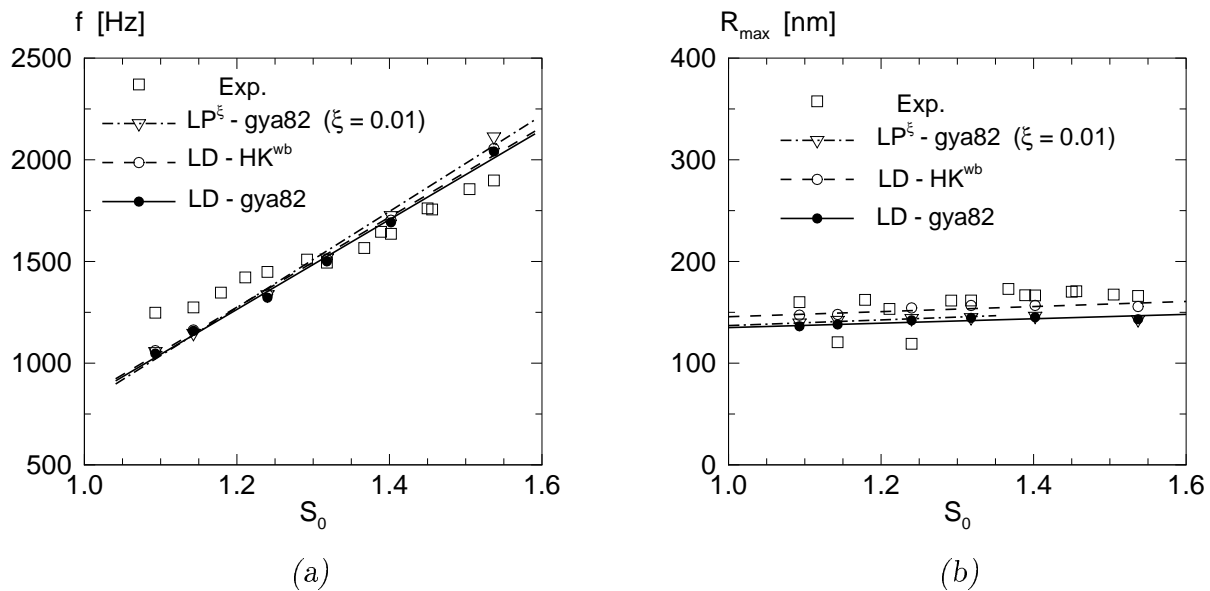(a)   (b)

Figure 6.4: *Comparison of experimental data and theoretical predictions according to the following models: LP$^\xi$-gya82, LD-gya82, LD-HK^{wb}. Nozzle: G2. (a) Frequency of oscillations. (b) Maximum modal radius.*

---

[1]in conformity with Luijten's measurements [77, 98].

Figure 6.4 juxtaposes the results from the following models: LD-gya82, LD-HK^{wb}, and the LP$^{\xi}$-gya82. As already discussed in section 2.4.2, for the experiments considered in this study, no substantial difference exists between the Hertz-Knudsen and the gya82 formulations. In the range of Knudsen numbers ($Kn \geq 2$), growth occurs in the near gas-kinetic flow regime and transitional effects play only a marginal role. In the same fashion, the LD-gya82 and LP$^{\xi}$-gya82 models do not differ much in their predictions. The different trend in frequency with supersaturation is due to the different surface tension fits. The Pruppacher-Klett [105] formula, employed in the LD-gya82 model, leads to a slightly better agreement with the experimental trend of the frequency versus supersaturation.
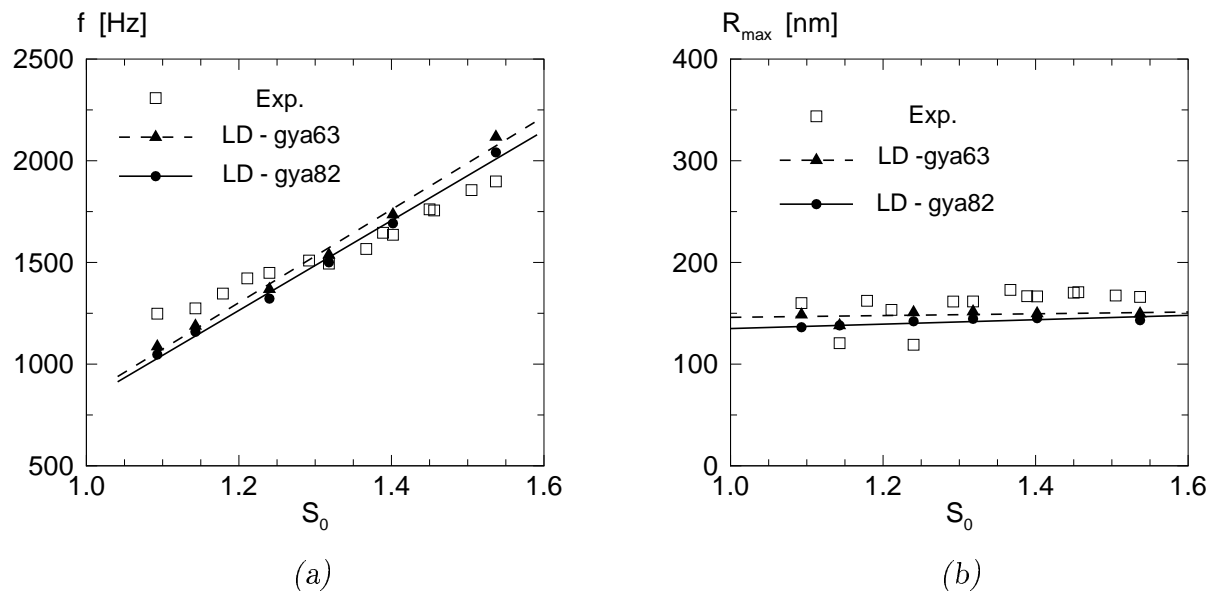

Figure 6.5: *Comparison of experimental data and theoretical predictions according to the following models: LD-gya82 and LD-gya63. Nozzle: G2. (a) Frequency of oscillations. (b) Maximum modal radius.*

In Fig. 6.5, two different droplet growth models are compared: gya82 and gya63. The nucleation rate is the same in both models: J_{ICCT} in combination with the σ^{LD} surface tension fit. Also in this case, no significant differences are observed and a satisfactory agreement between predictions and experiments is obtained.

Interesting conclusions can be derived by a closer examination of the Schnerr and Dohrmann model (see Fig. 6.6). This model predicts a fairly accurate frequency dependence with stagnation supersaturation, but clearly overestimates the droplet sizes by a factor $2.5 - 3$, as shown in Fig. 6.6(b). Moreover, when the wet-bulb equation is implemented in the Hertz-Knudsen formula (i.e. SD-HK^{wb} model), the results are reversed: now the droplet sizes are correct, but the frequency is wrong because the nucleation rate is too weak, as clearly deducible from Fig. 6.6(a). To understand this apparent incongruity in the model, let us consider, for a simple steady flow case, the interaction between nucleation and droplet growth and its impact on the final droplet size. Fig. 6.7 illustrates these effects for the two models SD-HK and SD-HK^{wb}.
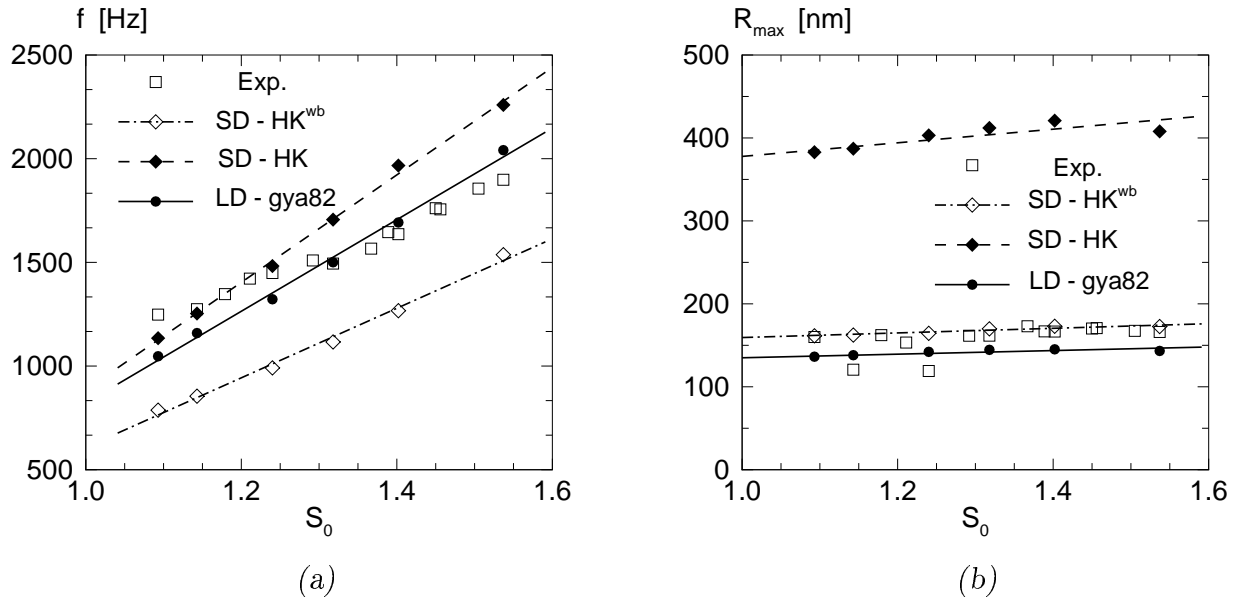
Figure 6.6: *Comparison of experimental data and theoretical predictions according to the following models: SD-HK, SD-HK^{wb}, LD-gya82. Nozzle: G2. (a) Frequency of oscillations. (b) Maximum modal radius.*
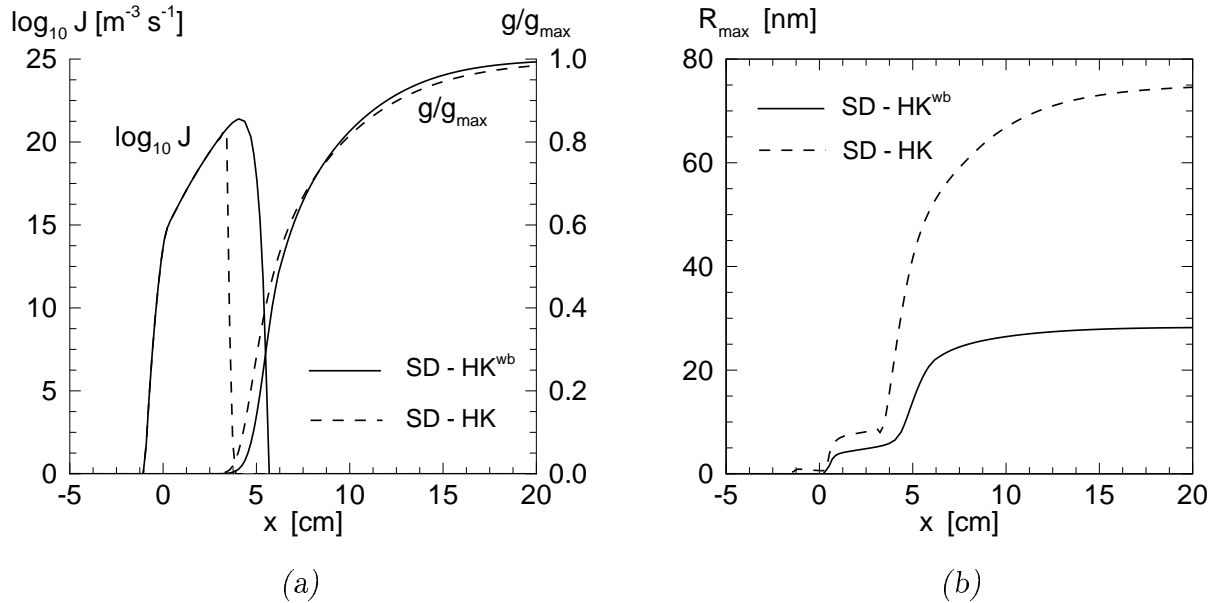
Figure 6.7: *Comparison of theoretical predictions from the SD-HK model, with and without wet-bulb. Nozzle: G2. (a) Axial distributions of nucleation rate J_{CNT} and condensate mass fraction g/g_{max}. (b) Axial distribution of modal radius. Stagnation conditions: $P_0 = 8.67 \cdot 10^4 \, Pa$, $T_0 = 296.6 \, K$, $S_0 = 0.50$.*

Having ascertained that the J_{CNT} is weaker than J_{exp}, this implies that the vapour starts nucleating at the wrong position along the nozzle axis. When the simplified HK formulation $(T_d = T)$ is used, the excessive release of latent heat, at the beginning of the growth process, shifts the quenching of the nucleation process upstream. In other words, it compensates for the delayed nucleation event. In this case, the shock location (or the frequency in an unsteady flow situation) will be correct. However, the nucleation is cut too early, too few condensation nuclei are produced, consequently the droplets grow too much. On the other hand, when the wet-bulb equation is implemented, the nucleation is quenched at the correct moment (i.e. the correct droplet size is obtained), but due to delayed start of the nucleation process, the axial position is wrong (i.e. the wrong frequency will result).

On the basis of this analysis, it becomes evident that the quality of a condensation model can be adequately and fully checked *only* when both droplet sizes and frequency (or pressure distributions) are available[2]. The Schnerr and Dohrmann model (SD-HK) has been thoroughly and carefully verified with respect to onset of condensation, shock position, frequencies, and modes of oscillations. From this point of view, their model provides very good results, as confirmed throughout this work as well, and their conclusions remain valid. However, their modelling requires improvements. As clarified in the preceding analysis, the good performance of the SD-HK model is due to a partial cancellation of effects rather than to an accurate model of the nucleation and droplet growth process. Specifically, the following elements should be modified:

(a) introduction of an empirical factor to compensate for the too low values of J_{CNT};
(b) inclusion of both energy and mass transfer in the determination of the growth rate;
(c) modification of the surface tension fit.

With reference to point (c), this is discussed in section 6.6, where the extrapolation of surface tension data to lower temperatures is analysed on the basis of the experimental results for nozzle G1 and on the basis of theoretical considerations.

The conclusions and arguments provided in this section rely on the accuracy of the droplet size measurements. A nontrivial question is how reliable and accurate are these results. In chapter 5, the answer to this question is discussed extensively from both a qualitative and quantitative perspective. Nevertheless, because of the extreme relevance of this issue, the main conclusions of chapter 5 are summarised here in a descriptive manner. Both theory and experiments (see Fig. 6.2 and 5.11) reveal a monodispersed size distribution in correspondence of the maximum modal radius. In this case, a simple and accurate correlation can be established between the theoretical extinction efficiency $Q_{ext,Mie}(\alpha)$, as provided by Mie theory, and the corresponding experimental quantity $Q_{ext,exp}(\alpha)$. Figure 6.8 illustrates graphically the results of this correlation. Hereafter, it is explained briefly how the experimental $Q_{ext,exp}$ is derived. More details can be found in section 5.3.3.1.

---

[2]Young [162] was amongst the first to insist on the necessity of droplet size measurements, already as early as 1982.
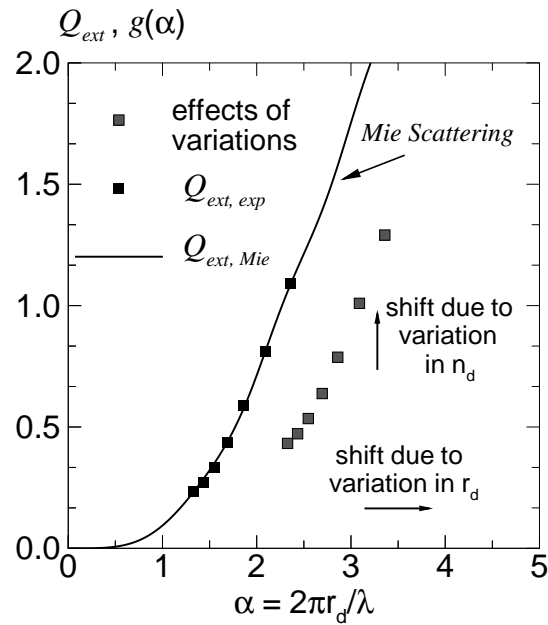
Figure 6.8: *Comparison of theoretical and experimental extinction efficiency as function of the size parameter (α). Nozzle: G2. Exp. 37 - Stagnation conditions: $P_0 = 8.752 \cdot 10^4\, Pa$, $T_0 = 296.6\,K$, $S_0 = 1.188$.*

The experimental extinction efficiency is defined as

$$Q_{ext,exp}(\alpha) = \frac{\beta_{exp}(\lambda_i)}{\pi\, n_d r_d^2}, \tag{6.1}$$

where

$$\alpha = \frac{2\pi r_d}{\lambda_i}. \tag{6.2}$$

Here, β_{exp} is the measured extinction coefficient, n_d and r_d are the droplet number density and modal radius, respectively, as derived from the extinction measurements. The size parameter α depends on the wavelength λ_i used and on the measured droplet size r_d. For each time instant, seven values of $Q_{ext,exp}$ can be calculated corresponding to one of the seven different wavelengths employed in the extinction measurement. These seven values are plotted in Fig. 6.8 as black dots.

The good agreement between theory (black line) and experimental values (black dots) gives the undeniable proof that the derived droplet size is quite accurate, at least in correspondence of its maximum value. Note that only when both droplet size r_d and number density n_d are correct, it is possible to match the theoretical curve following from Mie scattering theory. An error in one or the other parameter yields shifts in the horizontal and vertical directions. Particularly, the horizontal shift indicated in the picture would correspond to a droplet radius twice the measured one. Obviously, the difference in droplet sizes between the Schnerr & Dohrmann and the experiments ($\approx$ 3 times bigger than the experimental one) can not be attributed to experimental inaccuracies.

6.3.3   Holographic - interferometric experiments

This section illustrates a few examples of density fields, visualised by means of double exposure holographic interferometry. Unlike for nozzle G1, here a quantitative comparison between theory and holographic interferometric experiments could not be carried out, due to the difficulty of realising a steady-flow situation. Because of its very slender profile near the throat and its low cooling rate, the onset of condensation takes place, at low relative humidities, downstream of the test section window. As soon as the water vapour content is increased, the flow becomes immediately unsteady. Figure 6.9 presents three interferograms corresponding to snapshots of the flow field taken at different time instants.

$t_1 = 10.0 \, ms$

$t_2 = 10.2 \, ms$

$t_3 = 10.4 \, ms$
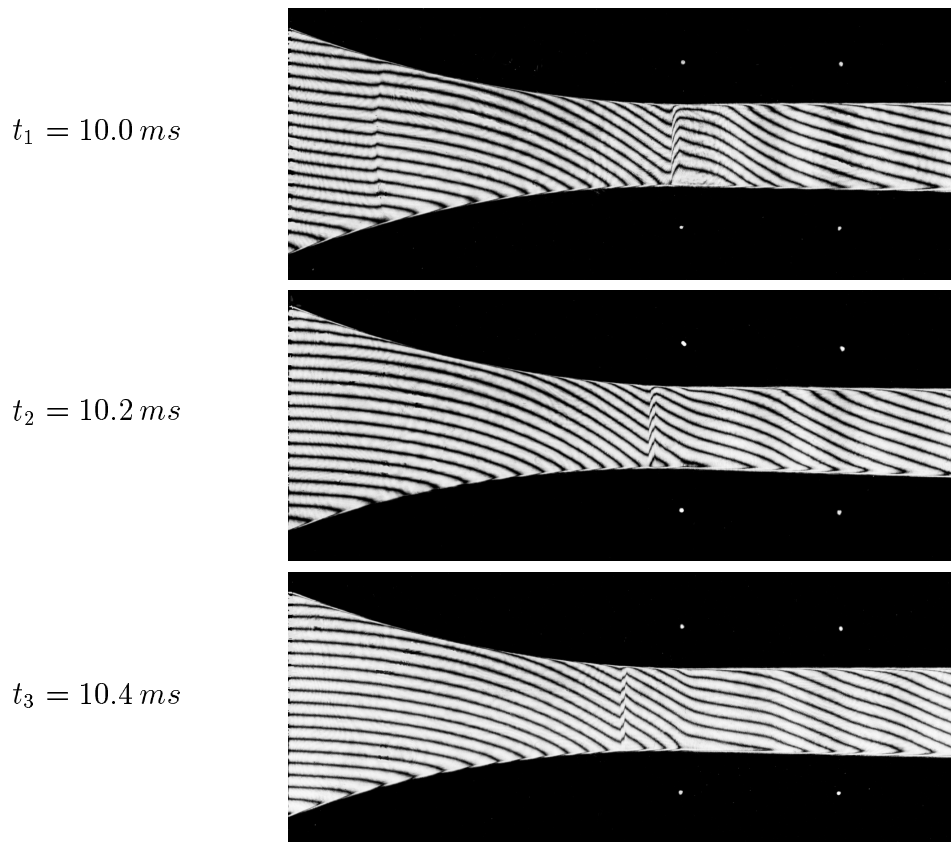
Figure 6.9: *Interferometric visualisation of Mode I. Snapshots taken at time intervals of $\Delta t = 0.2 \, ms$. Flow direction: from left to right. Nozzle: G2. Serie: I - Stagnation conditions: $P_0 = 8.83 \cdot 10^4 \, Pa$, $T_0 = 296.6 \, K$, $S_0 = 1.363$.*

Note that each interferogram is the result of a different experiment, since the interferometer is basically designed for the visualisation of steady flows. By a careful preparation of the mixture, it is possible to reproduce the stagnation supersaturation within 1%. The stagnation conditions for this "series" are: $T_0 = 282.6 \, K$; $P_0 = 8.83 \cdot 10^4 \, Pa$; $S_0 = 1.363$. Figure 6.10 compares the experimental density profiles, along the nozzle midline, with the

numerical results, obtained with the LD-gya82 model. Although only a qualitative comparison is possible, the simulation and the experiments show essentially the same trend.

(a)

(b)

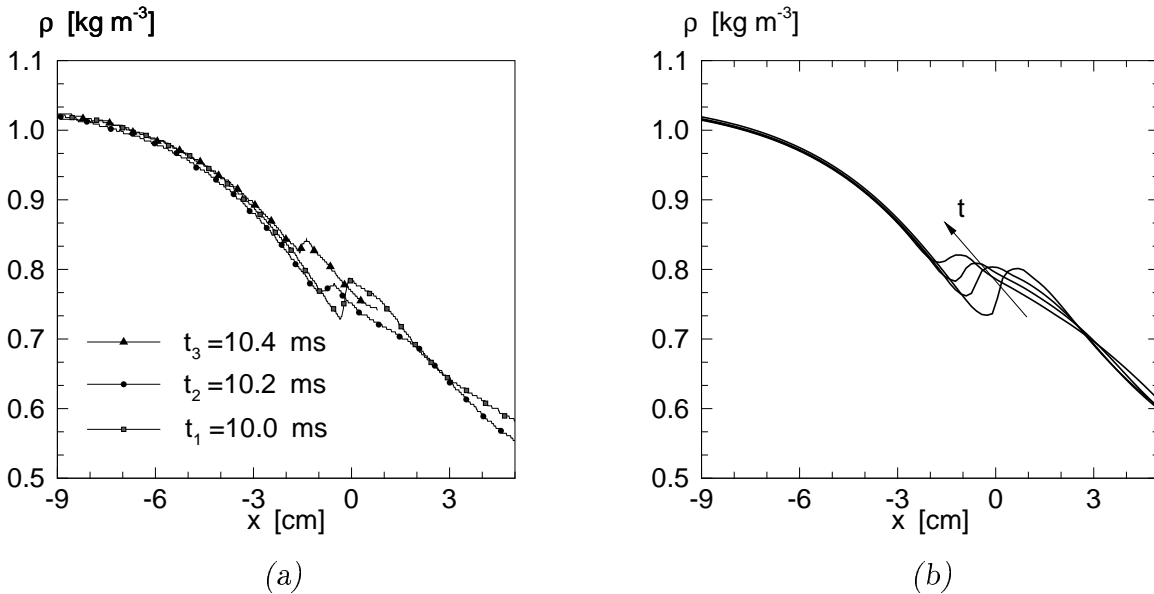**Figure 6.10:** *Experimental (a) and numerical (b) density profiles, along the nozzle midline. Nozzle: G2. Serie: I - Stagnation conditions:* $P_0 = 8.83 \cdot 10^4 \, Pa$, $T_0 = 296.6 \, K$, $S_0 = 1.363$.

6.4   Nozzle S2

As mentioned in section 1.2, different modes of oscillations may occur in a homogeneously condensing flow, depending on the supply relative humidity. Adam and Schnerr [3] performed a comprehensive experimental and numerical investigation of these modes, using several nozzles. In order to test the ability of the condensation models in capturing these features, nozzle S2 has been chosen essentially for two main reasons: the availability of reliable experimental data and the temperature range at which nucleation takes place. At a stagnation temperature of $295 \, K$, nozzle S2 nucleates between $[247 \div 240] \, K$. Within this range, very close to the limit of Hacker's measurements $(250 \, K)$, the surface tension trend will, most probably, still follow Hacker's experimentally based fit. For this reason, nozzle S2 enables the verification of the conclusion from nozzle G2, with no additional change in the modelling (surface tension fit). Figure 6.11 and 6.12 show the comparison of experimental and numerical frequency values, obtained from the various models.

Again the results from the LP-gya82 model confirm that the nucleation rate is too high, as clearly inferable from Fig. 6.11(b). When the correction $\xi = 0.01$ is implemented, then the model predictions agree fairly well with the experimental results. It should be noted that, for nozzle S2, the LD-gya82 and the LP$^\xi$-gya82 give exactly the same results, since, in this temperature range, they both follow Hacker's trend. The SD-HK also performs very

well and no substantial difference appears between the results of the SD-HK and those of the LD-gya82. Figure 6.12 compares the results of the gya63 and gya82 models. As for the G2 nozzle, no significant differences are observed. Note, in passing, that the predictions of the LD-gya63 almost coincide with those of the SD-HK formulation.
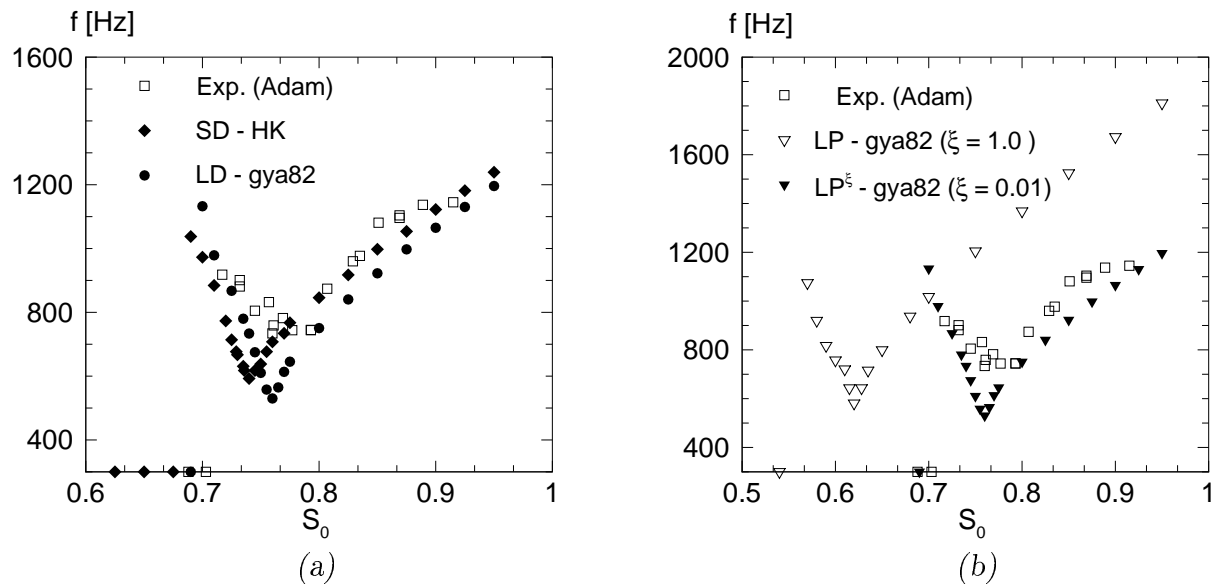
Figure 6.11: *Frequency of oscillations versus stagnation supersaturation. (a) Models: SD-HK, LD-gya82, Experiments. (b) Models: LP-gya82, LP$^\xi$-gya82, Experiments. Nozzle: S2. Stagnation conditions: $P_0 = 1.00 \cdot 10^5 \, Pa$, $T_0 = 295.0 \, K$.*
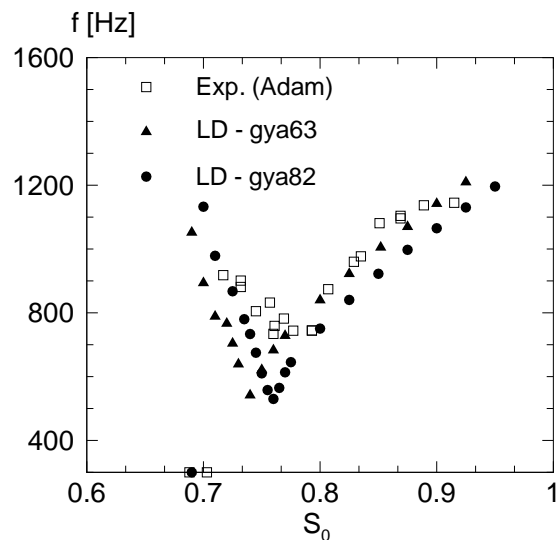
Figure 6.12: *Frequency of oscillations versus stagnation supersaturation. Models: LD-gya63, LD-gya82, Experiments. Nozzle: S2. Stagnation conditions: $P_0 = 1.00 \cdot 10^5 \, Pa$, $T_0 = 295.0 \, K$.*

6.5   Nozzle S1

Objective of this section is to verify the ability of the different condensation models in reproducing the main features of strong two-dimensional flow fields. For the S1 nozzle, such complicated 2-D structures have been experimentally visualised by Schnerr [114,116] by means of schlieren techniques. In this section, two examples are considered: one is the characteristic "X-shock", the other shows an interesting example of the interaction between the condensation front and the strongly two-dimensional flow field (hereafter denoted as case S71).

In Fig. 6.13, the experimental schlieren pictures [114] are compared with the corresponding numerical ones obtained with the LD-gya82 model. As immediately deducible from Fig. 6.13, the condensation model (LD-gya82) is able to capture the main characteristics of the flow field in both cases. The S71 case, however, needs some clarifications. For this case, maximum nucleation rates occur at about $T = 230\,K$. If the stagnation conditions indicated by the experimenter are used in the simulation, the results are in conflict with those from all other experiments considered here, including the X-shock.

Specifically, a much lower value of the surface tension is required at the same temperature ($T \approx 230\,K$) for the S71 case than for all other experiments. However, as indicated by Schnerr [114] in his work on "Homogene Kondensation in stationären transonischen Strömungen durch Lavaldüsen und um Profile" (pp. 128), the inaccuracy in the value of S_0 increases with increasing supply humidity. Particularly, the inaccuracy increases from about 1.8% at low humidities to almost 3.7% at high humidities. Furthermore, the inaccuracy in the stagnation temperature T_0 is about $0.5\,K$. It appears to be possible to reconcile the S71 experiment with the prediction from our model within the indicated error bounds. Therefore, the S71 case was run with values of $S_0 = 0.75$ and $T_0 = 287.3\,K$, in order to prove the ability of the model in capturing the main features of the complex 2-D structure[3]. Nevertheless, due to these uncertainties in the stagnation conditions, it is very difficult to evaluate the performances of the different models in the S71 case. Therefore, the comparison has been limited to the "X-shock" case.

Figure 6.14 compares the flow field obtained from the LD-gya63, SD-HK, and LP-gya82 models, for the X-shock case. The gya63 model agrees fairly well with the experimental results, shown in Fig. 6.13 (top left). The Schnerr and Dohrmann model provides reasonable results. However, the "X-shock" is already slightly cut, due to local excessive heat release. With reference to the LP-gya82 model, the nucleation rate is again too strong when the empirical factor $\xi = 1$ is used. The two condensation patches, propagating downstream, are interrupted by the presence of a strong normal shock, as clearly visible in Fig. 6.14. If the empirical factor is reduced to $\xi = 0.01$, then the results are very similar to those of the LD-gya82 model (Fig. 6.13, bottom left), since in this range of temperatures the surface tension fits basically coincide.

---

[3]In fact, the first numerical model employed by Schnerr and Dohrmann [117] showed perfect agreement with the experiments. The numerical results were based on the assumption of a solid condensate, using an empirical relation for the surface tension and a condensation coefficient equal to 0.2.
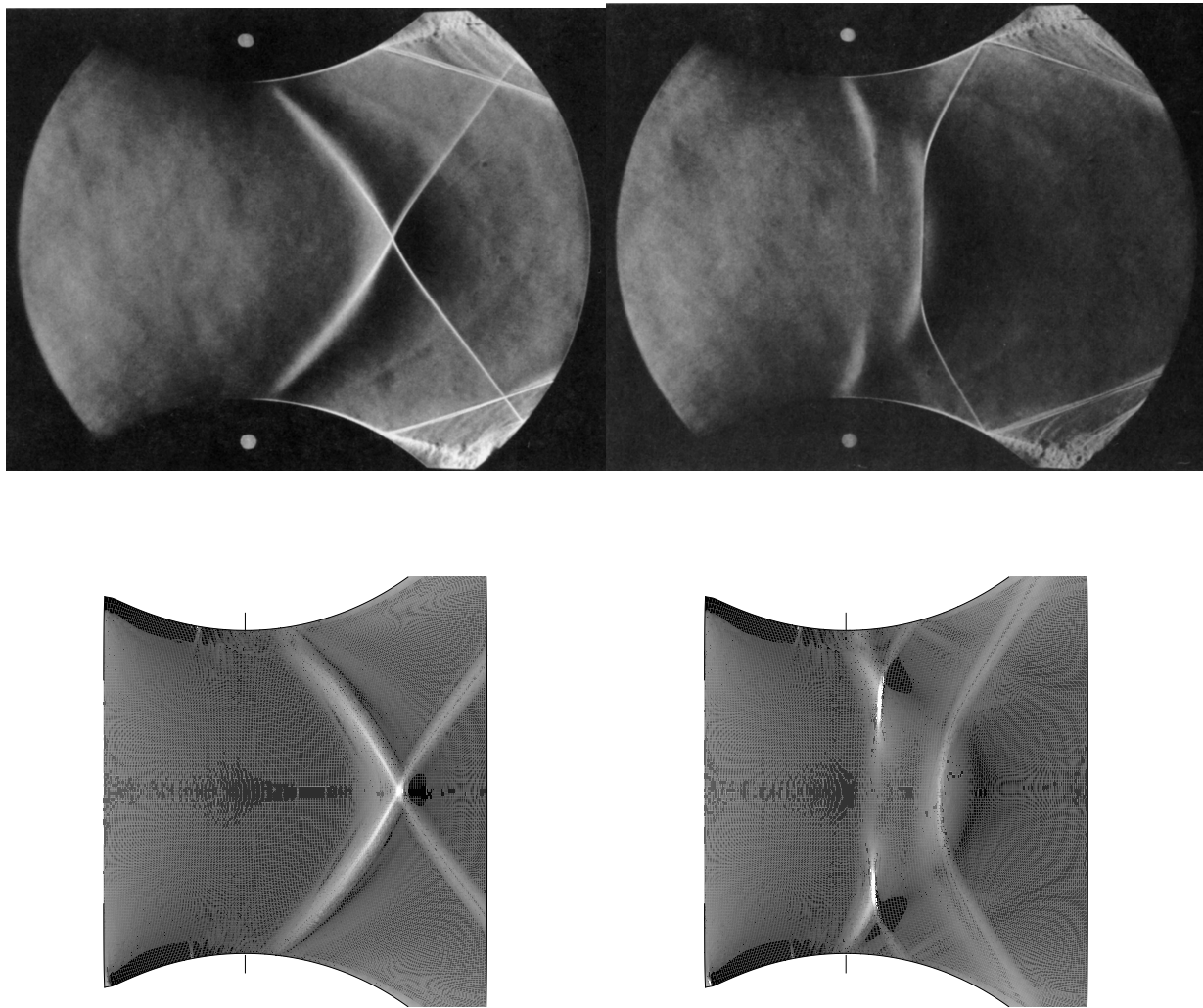
Figure 6.13: *Comparison of experimental [114] and numerical schlieren pictures. The numerical schlieren plots are obtained using the LD-gya82 condensation model.*

top left   : Experiment: X-shock.
              Stagnation conditions: $P_0 = 1.0 \cdot 10^5\, Pa$, $T_0 = 295.0\, K$, $S_0 = 0.372$.
top right   : Experiment: S71.
              Stagnation conditions: $P_0 = 1.0 \cdot 10^5\, Pa$, $T_0 = 286.8\, K$, $S_0 = 0.713$.
bottom left   : Numerical schlieren result for the X-shock.
              Stagnation conditions: $P_0 = 1.0 \cdot 10^5\, Pa$, $T_0 = 295.0\, K$, $S_0 = 0.372$.
bottom right : Numerical schlieren result for case S71.3.
              Stagnation conditions: $P_0 = 1.0 \cdot 10^5\, Pa$, $T_0 = 287.3\, K$, $S_0 = 0.750$.

LD-gya63   SD-HK   LP-gya82
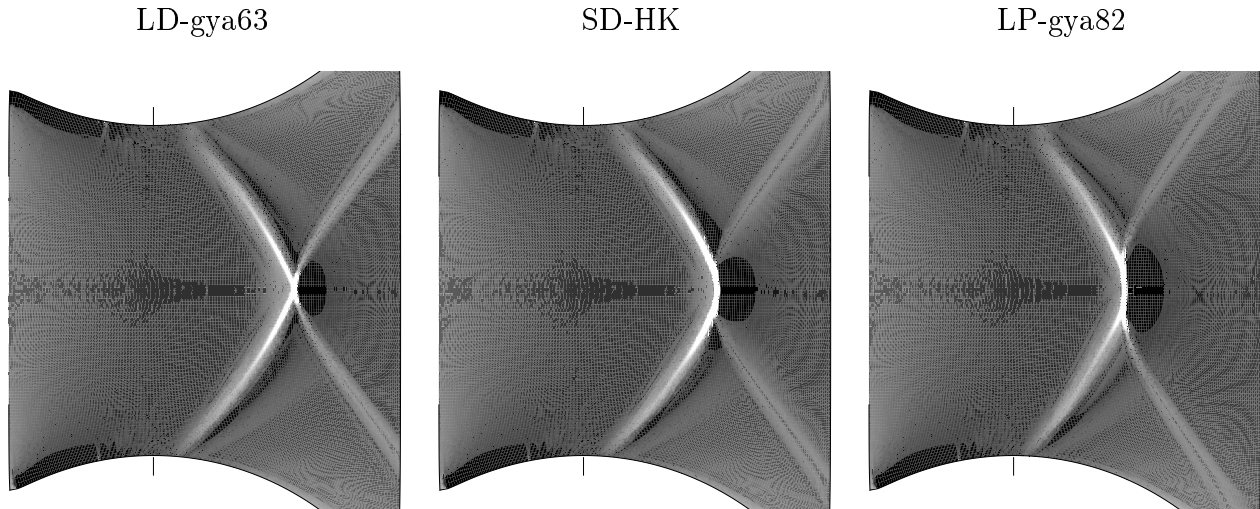
Figure 6.14: *Comparison of theoretical predictions according to different condensation models. Experiment: X-shock. Stagnation conditions:* $P_0 = 1.0 \cdot 10^5\,Pa$, $T_0 = 295.0\,K$, $S_0 = 0.372$.

6.6   Nozzle G1

In this section, two steady flow experiments are presented for nozzle G1, one corresponding to a subcritical and one to a supercritical flow regime. The experiments have been conducted in our laboratory using the holographic interferometer and unwrapping technique described in chapters 3 and 4. Despite their apparent simplicity, these experiments are extremely valuable for our analysis, since the maximum nucleation rate occurs at very large subcoolings: $T = 219\,K$ for experiment H14, and $T = 230\,K$ for experiment H19. They provide, thus, precious information on the extrapolation of surface tension data down to approximately $220\,K$. Figures 6.15 shows the density distributions along the nozzle axis, as predicted by the various condensations models of Table 6.1, for the subcritical case[4]. Note that in this case, the relevant part of the growth process occurs at Kn numbers in the range $[40 - 50]$.

As discussed already in section 2.4.3, the gya63 droplet growth formula is not expected to provide accurate results in the limit $Kn \gg 1$. As discussed by Fuchs and Sutugin in their review article [39], in this limit, the correction factor $f(Kn)$ should tend to the limit

$$\lim_{Kn \to \infty} f(Kn) = \frac{1}{1 + 2.66 Kn}, \tag{6.3}$$

---

[4] The experimental inaccuracy in the isentropic part of the density profile is ascribable to an erroneous localisation of the fringe skeleton, whose precise determination is strongly related to the local fringe spacing. At the condensation onset, the local concentration of the fringes assures a considerably higher accuracy in the determination of the density profile.

and not, as suggested by Gyarmathy, as

$$\lim_{Kn \to \infty} f(Kn) = \frac{1}{1 + 3.18 Kn}. \tag{6.4}$$

The good performance of the gya63 model, observed in the previous sections, can be explained in light of a possible cancellation of effects. The droplet temperature calculation is, in fact, not very accurate, when compared to Smolders' formulation [130], and leads to an overestimation of the actual growth rate. However, this effects is apparently partially compensated, in the Kn range $[2 \div 10]$, by the increased value of the factor λ ($\lambda = 3.18$). In the limit $Kn \to \infty$, this partial compensation of inaccuracies ceases to be valid, leading to the observed discrepancies.
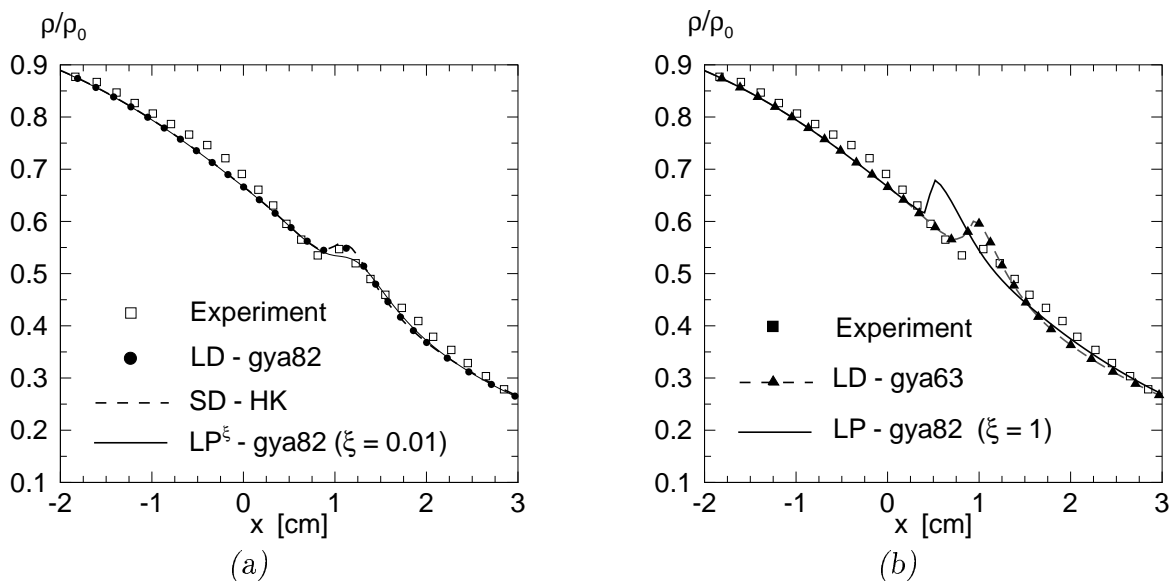
Figure 6.15: *Density distributions along the nozzle axis, as predicted by the various condensations models of Table 6.1. Nozzle: G1. Exp. H14 - Stagnation conditions: $P_0 = 8.60 \cdot 10^4 \, Pa$, $T_0 = 279.9 \, K$, $S_0 = 0.928$.*

With reference to the Luijten-Prast model, if the original version is implemented (i.e. $\xi = 1$), again a large difference is observed between prediction and the experimental results. Specifically, case H14 exhibits a clear shock at approximately $0.5 \, cm$ downstream of the nozzle throat, case H19 becomes, even, unsteady. When the empirical factor is reduced to $\xi = 0.01$, on the basis of Luijten's nucleation results [77, 98] and our own droplet size experiments (see section 6.5), the agreement between the theoretical predictions of the LP^ξ-gya82 model and the experimental values becomes excellent for experiment H19, as shown in Fig. 6.16. In the H14 case, instead, a substantial difference is still present, as can be inferred from Fig. 6.15(a), while the LD-gya82 model agrees very well with the experimental density distribution. Here, the only difference between the LP^ξ-gya82 and the LD-gya82 formulations is in the extrapolation of the surface data to lower temperatures (see Fig. 2.1).
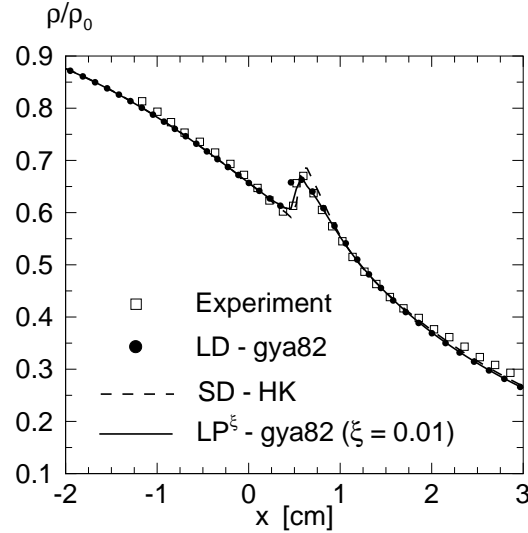
Figure 6.16: *Density distributions along the nozzle axis, as predicted by the following models: SD-HK, LD-gya82, LP^ξ-gya82. Nozzle: G1. Exp. H19 - Stagnation conditions:* $P_0 = 8.48 \cdot 10^4 \, Pa$, $T_0 = 279.8 \, K$, $S_0 = 1.240$.

As it can be see from Fig. 2.1, the σ^{LD} fit is, at $T = 219 \, K$ roughly $1.4 \, \%$ lower than the σ^{LP} one. Now, the thermodynamic constraint

$$\frac{\partial \sigma}{\partial T} \to 0 \qquad \text{as} \qquad T \to 0, \tag{6.5}$$

states that the surface tension cannot increase continuously with decreasing temperature, Exp. H14 provides the experimental confirmation of this trend. At this point, the strategy outlined in the introduction to this chapter (section 6.1) should not be forgotten. Recall that the σ^{LD} has not been derived such that the chosen nucleation and droplet growth models would nicely fit the experiments. In the present study, first the quality and relia-bility of nucleation and droplet growth theory has been assessed separately by analysing the droplet size experiments (nozzle G2). Then, these findings have been confirmed by the experiments of Adam [2] with nozzle S2. Recall, as well, that in both nozzles (G2 and S2), nucleation occurs at temperatures at which surface tension data are known, or very near to this range. Finally, this validated condensation model has been employed to derive the σ^{LD} extrapolation fit. Implicitly, it is assumed here that the nucleation model performs equally well independently of the temperature. There is some doubt about this hypothesis, as testified by the recent work on the scaling of nucleation rate (CNT theory) by McGraw [87]. Nevertheless, throughout this study, this assumption is maintained on the basis of the following arguments:

(a)   the temperature trend of the ICCT theory is confirmed by the experiments in nozzles G2 and S2 ;

(b)   the pressure is the same in all experiments (typically the stagnation pressure is roughly $1.0\,bar$);

(c)   the extrapolation is performed over a relatively small temperature range, of the order of $(20 - 25)$ degree.

Furthermore, as shown later in this section, the assumption that the ICCT has the correct behaviour allows to fulfil the existing thermodynamic constraint without additional modification to the modelling.

The Schnerr & Dohrmann model provides also excellent results in predicting the pressure/density distributions. In addition to the comments already made in section 6.3 on the accuracy of the nucleation and droplet growth formulations, a few remarks are also required on the surface tension fit used by the authors. The σ^{SD} fit has been derived under the assumption that the CNT theory is correct. The same approach was also adopted by Peters and Paikert [100], who independently obtained the same trend for the surface tension fit. In the same fashion, one could assume that the reduced ICCT is correct and obtain the σ^{LD} surface tension fit. To obtain more insights in this problem, the ratio $\log_{10} J_{ICCT}/J_{CNT}$ is plotted in Fig. 6.17, adopting the same surface tension fit for both models: the Pruppacher-Klett formula extrapolated down to $200\,K$.

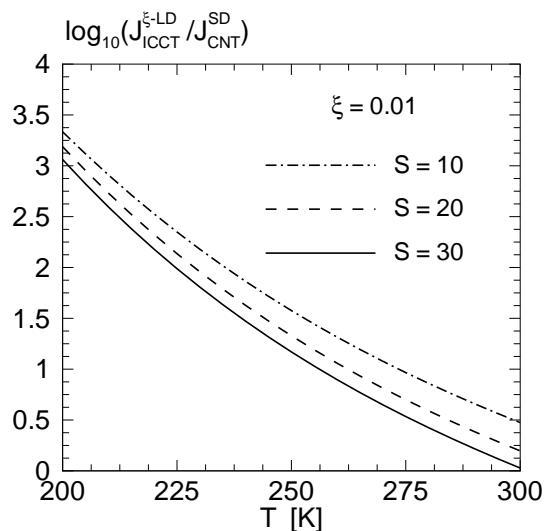**Figure 6.17:** *Comparison between J_{ICCT} and J_{CNT}, adopting for both the Pruppacher and Klett formula for the surface tension.*

From the plot, it is clear that the reduced J_{ICCT} is always stronger than J_{CNT} and becomes increasingly stronger with decreasing temperatures. Therefore, if one assumes J_{CNT} to be correct, then the increasing weakness of the nucleation rate must be compensated

by a decrease in surface tension, exactly as predicted by Schnerr and Peters. However, if one assumes J_{ICCT} to be correct, the "natural" increasing trend of the J_{ICCT} theory can be exploited and the surface tension does not need to be decreased so much. As a matter of fact, the assumption of correct J_{ICCT} theory, allows us, in a natural way, to follow the experimental trend measured by Hacker and to satisfy the thermodynamic constraint $\partial\sigma/\partial T \rightarrow 0$ as $T \rightarrow 0$. It is for these reasons that in the present study, the J_{ICCT} formulation has been preferred.

6.7   Conclusions

This chapter is centred on a review and validation of condensation models. Here, the terminology "condensation model" refers to a specific combination of nucleation, droplet growth, and surface tension formulations. The validation is performed in a stepwise manner, aimed at evaluating the quality and accuracy of each constitutive elements separately from each other. To pursue this objective, the well-documented experimental data on homogeneous condensation of water vapour/carrier gas mixtures have been collected and re-examined according to a well-defined strategy.

First, by analysing droplet size experiments, the accuracy of nucleation and droplet growth theories is tested independently in a range of temperatures, in which surface tension data are experimentally available. On the basis of this check, it can be concluded that both CNT and ICCT theory do not provide a correct quantitative description of the nucleation rate, at least in the pressure and temperature range considered in this thesis ($p \approx 1\,bar$, $220 < T < 270\,K$). As a matter of fact, both CNT and ICCT require the introduction of empirical factors to compensate for their erroneous predictions. Furthermore, it is ascertained that for an accurate prediction of the droplet number density and size, both the heat and mass transfer between the droplet and the surrounding vapour have to be simultaneously determined. Omission of one or the other leads to incorrect results. In fact, the rate of release of latent heat ultimately determines the axial position where nucleation is quenched.

Specifically, the gya82 droplet growth model, based on the assumption of an instantaneous balance between heat and mass transfer leads to good results for all experiments considered in the present study. In the numerical implementation of the gya82 model, an explicit growth formula is derived by performing a number of mathematical linearisations. Note, in passing, that these simplifications do not have a big influence in the range of supersaturations and Knudsen numbers considered in this thesis. The gya63 model performs reasonably well down to Kn numbers of approximately 10, while at higher Kn values the growth rate is overestimated. Higher Knudsen values, i.e. smaller droplets, correspond to high supersaturations and larger temperature differences ΔT between droplet and surrounding vapour. Since the correction factor, adopted by Gyarmathy ($\lambda = 3.18$), is too high in the entire Kn range - thus leading to a lower growth rate - the strong behaviour of the gya63 model must be attributed to an inaccurate droplet temperature calculation. Provided that the heat transfer is also taken into account, the Hertz-Knudsen formulation

provides also good results since, in all experiments considered here, growth occurs in the near free molecular regime. This proves that the droplet growth results, produced by the gya82 model, are only slightly affected by the quality of the Sherman interpolation formula.

Upon verifying these results for a variety of nozzle flows, for which surface tension is known, an optimised model has been derived. Its constitutive elements are: the reduced ICCT nucleation model and the explicit gya82 growth formula. In the course of this verification, it is found that the accurate predictions of the Schnerr and Dohrmann model with respect to shock position and frequency of oscillations, are imputable to a partial cancellation of effects. Specifically, the delayed nucleation event is compensated by a higher growth rate, which shifts forward the quenching of the nucleation rate. From this analysis, it emerges also clearly that a full validation of condensation models can only be achieved when both the predicted droplet sizes and pressure distributions are correlated with experimental data.

To gain more insight in the extrapolation of surface tension data to lower temperatures, nozzle flow experiments nucleating at increasingly lower temperatures have been considered. The Luijten-Prast fit does not provide good results at large subcoolings, down to temperatures of $220\,K$. This provides an indirect indication that surface tension cannot increase continuously with decreasing temperature, as required by the Nernst postulate. The Schnerr and Dohrmann fit is in agreement with the thermodynamic constraint and does provide good results, since it is derived in such a way as to guarantee the correct behaviour of CNT theory. By assuming the reduced ICCT behaviour to be correct, one derives the LD-fit which agrees with the experimental trend provided by Hacker, satisfies the limiting thermodynamic condition (i.e. Nernst Postulate), and provides good predictions. In light of the uncertainties of nucleation models in correctly predicting the temperature trend, modifications to the above mentioned extrapolations of surface tension might be expected as soon as new findings will become available.

Chapter 7

Conclusions and recommendations

The preceding chapters describe both experimental and theoretical aspects of homogeneously condensing nozzle flows. In such types of flow, the actual phase transition is preceded by homogeneous nucleation and then followed by droplet growth, which leads to the formation of a liquid droplet cloud. The associated release of latent heat produces a complex non-linear interaction between the flow field and the nucleation and droplet growth processes, which affects strongly the flow pattern and its stability. Therefore, the accurate modelling of homogeneous condensation relies essentially on the accuracy of its constitutive elements. By experimentally determining pressure/density profiles, droplet sizes, and frequencies of oscillations, it is possible to assess separately the accuracy of both nucleation and droplet growth theory.

The aim of the present work is to provide an experimental database for the validation of condensation models. To this purpose, the first part of this thesis is dedicated to a discussion of models proposed in the literature on nucleation and droplet growth processes. The second part of this thesis is dedicated to the development of experimental techniques for the accurate determination of density distributions, droplet sizes, and frequencies of oscillation. As test fluids, mixtures of water vapour in nitrogen or air are considered, at the following stagnation conditions : pressures of $1\ bar$, temperatures of the order of $290\ K$, and different degrees of supersaturations $(0 \div 1.6)$. Under such conditions, the inception of nucleation may occur at very large subcoolings (T of the order of $220\ K$) and droplet growth takes place mostly in the (near) free molecular regime. For nucleation theory, two variants of the classical nucleation theory have been considered: the CNT model in the version proposed by Volmer, Frenkel, and Zeldovich [36], and the ICCT model, ascribed to Girshick and Chiu [43]. The latter was chosen on the basis of Luijten's results [75, 77]. A simplifying assumption underlying all variants of classical nucleation theories is the "capillarity approximation", which implies the use of macroscopic thermodynamic equilibrium parameters to describe a non-equilibrium microscopic process. As a result, inaccurate models' predictions have to be surely expected. This has led to the introduction of an empirical factor to reconcile experiment and theory. In addition, by blending together thermodynamic considerations (i.e. the Nernst Postulate), measured surface tension data and results from nozzle flow experiments, a new extrapolation of surface tension to lower

temperatures is proposed.

Droplet growth is an intrinsically irreversible process involving the net transfer of mass and energy between the droplet and the surrounding vapour. As substantiated by linear irreversible thermodynamic theory, its correct description relies on the simultaneous solution of the interphase rate equations for the transport of mass and heat conduction. Directly connected to the evaluation of heat transfer, is the determination of the droplet temperature T_d. Here, an explicit formula is employed to determine T_d, based on the previous studies of Gyarmathy [48, 49] and Smolders [130]. This formulation relies on two main assumptions: the instantaneous balance between heat and mass transfer (i.e. wet-bulb approximation), and the equality of the vapour pressure at the droplet surface with the curvature corrected saturation pressure ($p_{vr} = p_{sr}$). A discussion on the applicability of these approximations to condensing nozzle flows is presented in chapter 2. For the droplet growth process, three models have been considered: the Hertz-Knudsen formulation and two transition models of Gyarmathy, denoted as gya63 and gya82, respectively. The gya63 model [48] is presented in a closed formulation. Here, a first-order accurate droplet temperature approximation, also based on the assumption $p_{vr} = p_{sr}$, is indirectly employed in the modelling. In the Hertz-Knudsen and gya82 model, the droplet temperature is treated as input variable. In both models, the droplet temperature is determined using the second-order approximation of Smolders [130]. The correct evaluation of the rate of heat addition is particularly important at the beginning of the growth process: it determines, in fact, the axial position at which nucleation is quenched and, therewith the final droplet number density and size.

Experimentally, the flow is visualised by means of double-exposure holographic interferometry. The design of the interferometer is based on the set-up of Takayama [135]. The optical configuration is such as to produce an image hologram with collimated beams. The main advantage of this optical configuration consist in the generation of sharp images of the test section and in the possibility of varying the OPL (optical path length) in such a way as to minimise the effects of refraction. Although the quality of the interferometric studies is rather good, a number of improvements are required for an optimal utilisation of the set-up. Specifically, the substitution of the polarising beam splitter with high-energy semi-transmitting mirrors should be considered, in order to prevent undesirable internal reflections which cause spurious fringes.

For droplet size measurements, a multi-wavelength light extinction technique is employed in combination with the trial function method. The set-up is similar to Walters' design [151]. However, for the present application, a number of modifications have been introduced in order to improve the spatial and temporal resolution. Due to the extreme relevance of droplet size measurements, special care has been taken in assessing the quality of the method with respect to both experimental and theoretical aspects. For the experimental part, the influence of forward scattered radiation on the extinction measurements is simulated numerically by means of a Monte Carlo method. Based on this study, the set-up has been designed in such a way as to contain this influence within a few percent. An important pay-off of these simulations is the validation of the Lambert-Beer law on which the analysis fully relies. As for the numerical and theoretical counterpart, a detailed check

is performed on the reliability of the inversion method. An important conclusion from this analysis is that the characteristics of the droplet size distribution can be determined with great accuracy only in correspondence to the high extinction peaks. These are, in fact, the only instants in time where the droplet cloud is completely outside the Rayleigh regime. In addition, all experiments, carried out at stagnation supersaturation lower than 0.9, are not reliable due to the small size of the detected droplets. In all these cases, the extinction of light is so weak that the measured transmitted intensities have a very low signal-to-noise ratio. For these reasons, in the validation of the proposed condensation models, the comparison between experimental and theoretical results is restricted to experiments with stagnation supersaturations higher than 1.0 and limited to the extinction peaks.

In the present study, the terminology "condensation model" refers to a specific combination of nucleation, droplet growth, and surface tension formulations. The validation is performed in a stepwise manner, aimed at evaluating the quality and accuracy of each constitutive element separately from each other. To pursue this objective, the well-documented experimental data on homogeneous condensation of water vapour/carrier gas mixtures have been collected and re-examined according to a well-defined strategy.

First, by analysing droplet size experiments, the accuracy of nucleation and droplet growth theories is tested independently in a range of temperatures, in which surface tension data are experimentally available. On the basis of this check, it can be concluded that CNT and ICCT theory both do not provide a correct quantitative description of the nucleation rate, in the pressure and temperature range considered in this thesis ($p \approx 1\,bar$, $220 < T < 270\,K$). On the basis of these results, the empirical correction factor ξ for the ICCT formulation is determined ($\xi = 0.01$), in agreement with Luijten's results [75,77]. For the droplet growth process, it is ascertained that the explicit droplet temperature calculation leads to the correct rate of heat transfer, regardless of the specific growth law to which it is applied, i.e. Hertz Knudsen or gya82. Both formulations provide very good results for all experiments considered in the present study. This indirectly proves that the growth process occurs mostly in the (near) free molecular regime and transitional effects play only a marginal role in the range of Kn numbers considered [$2 \div 50$]. The gya63 model performs reasonably well till Knudsen numbers of approximately 10, while at higher Kn values the actual growth rate is overestimated. Higher Knudsen values, i.e. smaller droplets, correspond to high supersaturations and larger temperature differences between droplets and surrounding vapour. On the basis of theoretical considerations [39], it is shown that the correction factor, adopted by Gyarmathy, is too large in the entire Kn range, thus leading to a reduction of the growth rate. Therefore, the good behaviour of the gya63 model must be attributed to an inaccurate droplet temperature calculation.

In literature, alternative formulations have been proposed on the transition correction as function of the Kn number, e.g. the work of Sahni [111] and Fuchs & Sutugin [39]. An interesting line of research would be to combine the explicit droplet calculation of Smolders, which on the basis of our droplet size experiments appears to be the most accurate, with these alternative formulations. However, it should be noted that the droplet growth experiments described in this thesis would represent only a partial check of this alternative formulation since in our experiments growth occurs mostly in the (near) free molecular

regime. Additional experiments for condensing nozzle flows with Kn numbers in the range $1 \div 0.01$ would be required for a complete validation. In this respect, droplet size measurements, for nozzle flows operating at a higher pressure, would be highly recommended.

Upon testing condensation models for a variety of nozzle flows in which surface tension is known, an optimised model is derived. Its constitutive elements are: the reduced ICCT nucleation model and the explicit gya82 growth formulation. The model is able to predict with satisfactory accuracy all features of condensing nozzle flows, namely: macroscopic gas dynamic properties, droplet sizes, and frequencies of oscillations. In the course of this validation, it is shown that the accurate predictions of the Schnerr and Dohrmann model with respect to shock position and frequency of oscillations, are attributable to a partial cancellation of effects. Specifically, the delayed nucleation event is compensated by a higher growth rate, which shifts forward the quenching of the nucleation rate. From this analysis, it emerges also clearly that a full validation of condensation models can only be achieved when both predicted droplet sizes and predicted pressure distributions are correlated with experimental data. To gain more insight in the extrapolation of surface tension data to lower temperatures, nozzle flow experiments, nucleating at increasingly lower temperatures, have been considered. By analysing these experiments, the following can be concluded: the Luijten-Prast extrapolation leads to inaccurate predictions at large subcoolings, down to temperatures of $220\,K$. This fact provides an indirect indication that surface tension cannot increase continuously with decreasing temperature, as required by the Nernst postulate. Both the (Schnerr and Dohrmann) σ^{SD} and (these authors) σ^{LD} extrapolations provide good results at such low subcoolings. In deriving these extrapolations, it is implicitly assumed, in both cases, that the nucleation model performs equally well independently of the temperature. Specifically, Schnerr and Dohrmann assumed CNT to be correct, while the present author preferred the ICCT variant. In the present study, the ICCT formulation is preferred since it predicts increasingly higher nucleation rates at low temperatures. This feature allows the derivation of a simple fit, which satisfies all existing thermodynamic constraints and provides, in combination with the ICCT model, good results also at large subcoolings. However, the proposed model can by no means be considered as a final result. From nucleation studies, in fact, it is well known that classical nucleation theory (and its variants) do not reproduce the temperature trend correctly. As an example, the reader is referred to the recent work of McGraw [87] on the scaling of nucleation rate (CNT theory), on the basis of thermodynamic considerations. It is, thus, to be expected that, in light of new findings in nucleation studies, modifications will have to be made to the extrapolations of surface tension data.

References

[1] F.F. ABRAHAM (1974), Homogeneous Nucleation Theory, Academic Press, New York.

[2] S. ADAM (1996), Numerische und experimentelle Untersuchung instationärer Düsenströmungen mit Energiezufuhr durch homogene Kondensation, *PhD thesis*, Fakultät für Maschinenbau, Universität Karlsruhe (TH).

[3] S. ADAM AND G.H. SCHNERR (1997), Instabilities and bifurcation of nonequilibrium two-phase flows, *J. Fluid Mechanics*, Vol. 348, pp. 1-28.

[4] W.K. ANDERSON, J.L. THOMAS AND B. VAN LEER (1986), Comparison of finite volume flux vector splittings for the Euler equations, *AIAA J.*, Vol. 24, pp. 1453-1460.

[5] H. BABINSKY AND K. TAKAYAMA (1995), Quantitative holographic interferometry of shock-wave flows using Fourier transform fringe analysis, in: *Proc. 20th Int. Symp. Shock Waves* Pasadena, pp. 1599-1604, World Scientific Press.

[6] J.C. BARRETT AND C.F. CLEMENT (1988), Growth rates for liquid droplets, *J. Aerosol Sci.*, Vol. 19, No. 2, pp. 223-242.

[7] D. BARSCHDORFF (1967), Kurzzeitfeuchtemessung und ihre Anwendung bei Kondensationserscheinungen in Lavaldüsen, *Strömungsmechanik und Strömungsmaschinen*, Vol. 6, pp. 18-39.

[8] D. BARSCHDORFF AND G.A. FILIPPOV (1970), Analysis of special conditions of the work of Laval nozzles with local heat supply, *Heat Transfer - Soviet Research*, Vol. 2, pp. 76-87.

[9] J.P.A.J. VAN BEECK (1997), Rainbow Phenomena: development of a laser-based, non-intrusive technique for measuring droplet size, temperature and velocity, *PhD thesis*, Eindhoven University of Technology.

[10] M. BERTERO, C. DE MOL AND E.R. PIKE (1988), Linear inverse problems with discrete data, in: *Optical Particle Sizing, Theory and Practice*, G. Gouesbet and G. Gréhan (editors), Plenum, London.

[11] P.A. BLYTHE AND C.J. SHIH (1976), Condensation shocks in nozzle flows, *J. Fluid Mech.* Vol. 76, pp. 593- 621.

[12] C.F. BOHREN AND D.R. HUFFMAN (1983), Absorption and Scattering of Light by Small Particles, John Wiley & Sons, New York.

[13] A. BÖLCS, T.H. FRANSSON AND M.F. PLATZER (1989), Numerical solution of inviscid transonic flow through nozzles with fluctuating back pressure, *Trans. ASME J. of Turbomachinery*, Vol. 11, pp. 169-180.

[14] D.J. BONE, H.A. BACHOR AND R.J. SANDEMAN (1986), Fringe pattern analysis using a 2-D Fourier transform, *Applied Optics*, Vol. 25, No. 10, pp. 1653-1660.

[15] D.J. BONE (1991), Fourier fringe analysis - the two-dimensional phase unwrapping problem, *Applied Optics*, Vol. 30, No. 25, pp. 3627-3632.

[16] E.A. BUCHER (1973), Computer simulation of light pulse propagation for communication through thick clouds, *Applied Optics*, Vol. 12, No. 10, pp. 2391-2400.

[17] E.A. BUCHER AND R.M. LERNER (1973), Experiments on light pulse communication and propagation through atmospheric clouds, *Applied Optics*, Vol. 12, No. 10, pp. 2401-2414.

[18] H.B. CALLEN (1960), Thermodynamics, John Wiley & Sons, New York.

[19] H.J. CAULFIELD (1979), Handbook of Optical Holography, Academic Press, New York, ISBN 0-12-165350-1.

[20] G. CINAR, B.S. YILBAS AND M. SUNAR (1997), Study into nucleation of steam during expansion through a nozzle, *Int. J. Multiphase Flow.*, Vol. 23, No. 6, pp. 1171-1188.

[21] R.J. COLLIER, C.B. BURCKHARDT AND L.H. LIN (1971), Optical Holography, Academic Press, New York.

[22] B. COLLIGNAN (1994), Contribution à l'Etude de la Condensation Instationnaire en Ecoulement Transsonique, *PhD thesis*, Université Pierre & Marie Curie, Paris.

[23] R. CONRAD (1977), Bildung und Wachstum von Kondensationskeimen in einer Düsenströmung, *PhD thesis*, RWTH Aachen.

[24] F.L. DAUM AND G. GYARMATHY (1968), Condensation of air and nitrogen in hypersonic wind tunnels, *AIAA J.*, Vol. 6, No. 3.

[25] H. DECONINCK AND R. STRUYS (1988), Consistent boundary conditions for cell centered upwind finite volume Euler solvers, in: *Numerical Methods for Fluid Dynamics III*, K.W. Morton and M.J. Baines (editors), Clarendon Press, Oxford.

[26] A. DEEPAK AND M.A. BOX (1978), *Applied Optics*, Vol. 17, pp. 2900-2908.

[27] A. DEEPAK AND M.A. BOX (1978), *Applied Optics*, Vol. 17, pp. 3169-3176.

[28] C.F. DELALE, G.H. SCHNERR AND J. ZIEREP (1993), Asymptotic solution of transonic nozzle flows with homogeneous condensation. I. Subcritical flows, *Phys. Fluids A*, Vol. 5, pp. 2969-2981.

[29] C.F. DELALE, G.H. SCHNERR AND J. ZIEREP (1993), Asymptotic solution of transonic nozzle flows with homogeneous condensation. II. Supercritical flows, *Phys. Fluids A*, Vol. 5, pp. 2982-2992.

[30] C.F. DELALE, G.H. SCHNERR AND J. ZIEREP (1993), The mathematical theory of thermal choking in nozzle flows, *ZAMP*, Vol. 44, pp. 943-976.

[31] C.F. DELALE, G. LAMANNA AND M.E.H. VAN DONGEN, On the stability of stationary shock waves in nozzle flows with homogeneous condensation, *Phys. Fluids A*, (to appear).

[32] M.E. DEYCH, A.V. KURSHAKOV, G.A. SALTANOV AND I.A. YATCHENI (1969), A study of the structure of two-phase flow behind a condensation shock in supersonic nozzles, *Heat Transfer - Soviet Research*, Vol. 1, pp. 95-105.

[33] U. DOHRMANN (1989), Ein numerisches Verfahren zur Berechnung stationärer transsonischer Strömungen mit Energiezufuhr durch homogene Kondensation, *PhD thesis*, Fakultät für Maschinenbau, Universität Karlsruhe (TH).

[34] M.E.H. VAN DONGEN, H.J. SMOLDERS, C.J.M. BRAUN, C.A.M. SNOEIJS AND J.F.H. WILLEMS (1994), Spectral light extinction to characterize fast fog formation, *Applied Optics*, Vol. 33, No. 10, pp. 1980-1988.

[35] K.K. ENKENHUS AND D.L. MERRITT (1971), *Technical Report 71-147*, (NOLTR) Naval Ordnance Laboratory, White Oak, Silver Spring, Md.

[36] J. FEDER, K.C. RUSSELL, J. LOTHE AND G.M. POUND (1966), Homogeneous nucleation and growth of droplets in vapors, *Adv. Phys. (Suppl. Phil. Mag.)*, Vol. 15, 111.

[37] W. FRANK (1978), Stationäre und instationäre Kondensationsvorgänge bei einer Prandtl-Meyer-Expansion, *Strömungsmechanik und Strömungsmaschinen*, Vol. 25, pp. 61-87.

[38] W. FRANK (1985), Condensation phenomena in supersonic nozzles, *Acta Mechanica*, Vol. 54, pp. 135-156.

[39] N.A. FUCHS AND A.G. SUTUGIN (1971), High-dispersed aerosols, in: *Topics in Current Aerosols Research*, G.M. Hidy and J.R. Brock (editors), Vol. 2, pp. 4-60, Pergamon Press, London.

[40] N. Fukuta and L.A. Walter (1956), Kinetics of hydrometeor growth from a vapor-spherical model, *J. Atmos. Sci.*, Vol. 27, No. 8, pp. 1160-1172.

[41] D. Gabor (1948), A new microscopic principle, *Nature*, Vol. 161, pp. 777-778.

[42] D. Gabor (1949), Microscopy by reconstructed wavefronts, *Proc. of the Royal Society A*, Vol. 197, pp. 454-487, Pergamon.

[43] S.L. Girshick and C.-P. Chiu (1990), Kinetic nucleation theory: A new expression for the rate of homogeneous nucleation from an ideal supersaturated vapor, *J. Chem. Phys.*, Vol. 93, pp. 1273-1277.

[44] J.W. Goodman (1996), Introduction to Fourier Optics, The McGraw-Hill Companies, ISBN 0-07-024254-2.

[45] G. Gousbet and G. Gréhan (1988), Optical Particle Sizing, Theory and Practice, Plenum, London.

[46] A. Guha and J.B. Young (1991), Time-marching prediction of unsteady condensation phenomena due to supercritical heat addition, *IMechE*, C423/057, pp. 167-177.

[47] J.B. Guidt, G. Gouesbet and J.N. Le Toulouzan (1990), Accurate validation of visible infrared double extinction simultaneous measurements of particle sizes and number densities by using densely laden standard media, *Applied Optics*, Vol. 29, No. 7, pp. 1011-1022.

[48] G. Gyarmathy (1963), Zur Wachstumsgeschwindigkeit kleiner Flüssigkeitstropfen in einer übersättigten Atmosphäre, *Z. für angew. Math. Physik*, Vol. 14, No. 3, pp. 280-293.

[49] G. Gyarmathy (1982), The spherical droplet in gaseous carrier streams: review and synthesis, in: *Multiphase Science and Technology*, Vol. 1, pp. 99-279, Springer, Berlin.

[50] P.T. Hacker (1951), Experimental values of the surface tension of supercooled water, *Technical Note 2510*, National Advisory Committee for Aeronautics.

[51] P. Hariharan (1996), Optical Holography: principles, techniques and applications, Cambridge University Press, ISBN 0-521-43965-5.

[52] R.M. Head (1949), Investigations of Spontaneous Condensation Phenomena, *PhD thesis*, Calif. Inst. of Technology, Pasadena, California.

[53] E. Hecht (1987), Optics, Addison-Wesley Publishing Comp., ISBN 0-201-11611-1.

[54] M. HEILER (1999), Instationäre Phänomeme in homogen/heterogen kondensierenden Düsen- und Turbinenströmungen, *PhD thesis*, Fakultät für Maschinenbau, Universität Karlsruhe (TH).

[55] M. HEILER, G. WINKLER AND G.H. SCHNERR (2000), Homogeneous/heterogeneous condensation in transonic nozzle flows, *ZAMM*, Vol. 80.

[56] R. HERMANN (1942), Der Kondensationsstoß in Überschall-Windkanäldüsen, *Luftfahrtforschung*, Vol. 19, 201.

[57] H. HERTZ (1882), *Ann. Phys.*, Vol. 17, 177.

[58] P.G. HILL (1966), Condensation of water vapor during supersonic expansion in nozzles, *J. Fluid Mech.*, Vol. 25, pp. 593-620.

[59] J. HILSENRATH *et al.* (1955), Tables of thermal properties of gases, *Technical Report*, Natl. Bur. std. (U.S.) Circ. 564.

[60] F. HOUWING AND K. TAKAYAMA (1999), Automated interactive analysis of finite fringe interferograms, including deconvolution of data from axisymmetric flows, *Technical Report*, Vol. 11, Rep. Inst. Fluid Sci., Tohoku University.

[61] W.L. HOWES AND D.R. BUCHELE (1966), Optical interferometry of inhomogeneous gases, *J. Opt. Soc. Am.*, Vol. 56, pp. 1517-1528.

[62] G.L. HUBBARD, V.E. DENNY AND A.F. MILLS (1975), Droplet evaporation: effects of transients and variable properties, *Int. J. Heat Mass Transfer*, Vol. 18, pp. 1003-1008.

[63] H.C. VAN DE HULST (1981), Light scattering by Small Particles, Dover, New York.

[64] J.A. JOHNSON III AND D.J. CAGLIOSTRO (1971), *AIAA J.*, Vol. 9, No. 1, pp. 101-105.

[65] S.W. KANG (1967), Analysis of droplet growth in rarefied and continuum environments, *AIAA J.*, Vol. 5, No. 7, pp. 1288-1295.

[66] R.A. KANTOLA (1982), Condensation in steam turbines, *Technical Report CS-2528*, RP 735-1, EPRI.

[67] M. KERKER (1969), The scattering of Light and other Electromagnetic Radiation, Academic Press, New York.

[68] M. KNUDSEN (1915), *Ann. Phys.*, Vol. 47, 697.

[69] P.M. KOLESNIKOV AND A.A. KARPOV (1989), Optical methods of analysis of two-phase flows, *Fluid Mechanics - Soviet Research*, Vol. 18, No. 3, pp. 1-21.

[70] E. KREYSZIG (1993), Advanced Engineering Mathematics, John Wiley & Sons, New York.

[71] LANDOLT-BÖRNSTEIN (1955), Stoffwerte und mechanisches Verhalten von Nichtmetallen, *Zahlenwerte und Funktionen aus Physik, Chemie, Astronomie, Geophysik und Technik*, Vol. 4, No. 1, Springer-Verlag, 6th edition.

[72] T.A.W.M. LANEN (1992), Digital Holographic Interferometry in Compressible Flow Research, *PhD thesis*, Delft University of Technology.

[73] H. LUDWIEG (1955), *Z. Flugwiss*, Vol. 3, pp. 206-216.

[74] H. LUDWIEG (1957), *Agard Report 143*, NATO Headquarters, Scheveningen, Holland.

[75] C.C.M. LUIJTEN (1998), Nucleation and Droplet Growth at High Pressure, *PhD thesis*, Eindhoven University of Technology, ISBN 90-386-0747-4.

[76] C.C.M. LUIJTEN AND M.E.H. VAN DONGEN (1999), Nucleation at high pressure. I. Theoretical considerations, *J. Chem. Phys.*, Vol. 111, No. 18, pp. 8524-8534.

[77] C.C.M. LUIJTEN, P. PEETERS AND M.E.H. VAN DONGEN (1999), Nucleation at high pressure. II. Wave tube data and analysis, *J. Chem. Phys.*, Vol. 111, No. 18, pp. 8535-8544.

[78] J. LUKASIEWICZ AND J.K. ROYLE (1953), Effects of air humidity in supersonic wind tunnels, *Technical Report 2563*, Aeronaut. Res. Council.

[79] F.E. MARBLE (1960), Some gasdynamic problems in the flow of condensing vapors, *Astronautica Acta*, Vol. 14, pp. 585-614.

[80] B.J. MASON (1953), The growth of ice crystals in a supercooled water cloud, *Quart. J. Roy. Meteor. Soc.*, Vol. 79, pp. 104-111.

[81] S. MATSUMURA, K. TAKAYAMA AND O. ONODERA (1998), Holographic interferometry visualization of very weak shock waves appearing in automobile exhaust pipes, in: *8th International Symposium on Flow Visualization*, G.M. Carlomagno and I. Grant (editors), Sorrento, September 1-4, CD ROM Proceedings - Paper 161, ISBN 0-9533991-09.

[82] K. MATSUO, S. KAWAGOE, K. SONODA AND T. SETOGUCHI (1983), Oscillations of Laval nozzle flow with condensation (Part 1), *Bulletin of JSME*, Vol. 26, pp. 1556-1562.

[83] K. MATSUO, S. KAWAGOE, K. SONODA AND T. SETOGUCHI (1985), Oscillations of Laval Nozzle flow with condensation (Part 2) *Bulletin of JSME*, Vol. 28, pp. 88-93.

[84] F. Mazoué, L. Walpot, M. Netterfield and L. Marraffa (1996), Development and validation of a nonequilibrium condensing flow solver, in: *31st AIAA Thermophysics Conference*, New Orleans, LA. Paper 96-1893.

[85] J.E. McDonald (1962), Homogeneous nucleation of vapor condensation I. Thermodynamic Aspects, *American J. of Phys.*, Vol. 30, pp. 870-877.

[86] R. McGraw, S. Nemesure and S.E. Schwartz (1998), Properties and evolution of aerosols with size distributions having identical moments, *J. Aerosol Sci.*, Vol. 29, No. 1, p. 1-12.

[87] R. McGraw (2000), Scaling properties of the critical nuclei and nucleation rate, in: *Nucleation and Atmospheric Aerosols 2000*, B.N. Hale and M. Kulmala (editors), Vol. 534, pp. 85-88, AIP Conference Proceedings 2000.

[88] C.A. Moses and G.D. Stein (1978), On the growth of steam droplets formed in a Laval nozzle using both static pressure and light scattering measurements, *J. Fluids Eng.*, Vol. 100, pp. 311-322.

[89] F.P. Mosnier (1976), Unsteady Supersonic Flow with Heat Addition due to Condensation, *PhD thesis*, Faculty of the Graduate School of Yale, Yale University.

[90] M. Mozurkewich (1986), Aerosol growth and the condensation coefficient for water: a review, *Aerosol Sci. Technol.*, Vol. 5, pp. 223-236.

[91] G. Mundinger (1994), Numerische Simulation instationärer Lavaldüsenströmungen mit Energiezufuhr durch homogene Kondensation, *PhD thesis*, Fakultät für Maschinenbau, Universität Karlsruhe (TH).

[92] Y. Onishi (1986), The spherical-droplet problem of evaporation and condensation in a vapour-gas mixture, *J. Fluid Mech.*, Vol. 163, pp. 171-194.

[93] E.S. Oran and J.P. Boris (1987), Numerical Simulation of Reactive Flow, Elsevier, Amsterdam.

[94] K. Oswatitsch (1941), Die Nebelbildung in Windkanälen und ihr Einfluß auf Modellversuche, *Jahrbuch der deutschen Luftfahrtforschung*, Vol. 1, pp. 692-703.

[95] K. Oswatitsch (1942), Kondensationserscheinungen in Überschalldüsen, *ZAMM.*, Vol. 22, pp. 1-14.

[96] K. Oswatitsch (1942), Kondensationsstöße in Lavaldüsen, *Z. Ver. deut. Ing.*, Vol. 86, 702.

[97] D.W. Oxtoby (1992), Homogeneous nucleation: theory and experiment, *J. Phys.: Condens. Matter*, Vol. 4, pp. 7627-7650.

[98] P. PEETERS (2000), Technische Universiteit Eindhoven, private communications.

[99] P. PEETERS, C.C.M. LUIJTEN AND M.E.H. VAN DONGEN (2001), Transitional
      droplet growth and diffusion coefficients, *Int. J. Heat Mass Transfer*, Vol. 44, No. 1,
      pp. 181-193.

[100] F. PETERS AND B. PAIKERT (1989), Nucleation and growth rates of homogeneously
      condensing water vapor in argon from shock tube experiments, *Exp. Fluids*, Vol. 7,
      pp. 521-530.

[101] F. PETERS AND K.A.J. MEYER (1995), Measurement and interpretation of growth
      of monodispersed water droplets suspended in a pure vapour, *Int. J. Heat Mass
      Transfer*, Vol. 38, No. 17, pp. 3285-3293.

[102] T.J POINSOT AND S.K. KELE (1992), *J. Comp. Physics* Vol. 101, p. 104.

[103] J. VAN POPPEL (1998), Droplet sizing by light extinction in a supersonic Laval
      nozzle flow with condensation, *Master thesis R-1475-A*, Eindhoven University of
      Technology.

[104] B. PRAST, Numerical Modelling of Condensation Processes in Laval Nozzle Flows,
      PhD thesis, Eindhoven University of Technology, (to appear).

[105] H.R. PRUPPACHER AND J.D. KLETT (1980), Microphysics of Clouds and Precipi-
      tation, Reidel, Dordrecht, Holland.

[106] G.M. QUIST AND P.J. WYATT (1985), Empirical solution to the inverse-scattering
      problem by the optical strip-map technique, *J. Opt. Soc. Am. A*, Vol. 2, No. 11, pp.
      1979-1985.

[107] K. RAŽNJEWIĆ (1977), Thermodynamische Tabellen, VDI-Verlag.

[108] R.C. REID, J.M. PRAUSNITZ AND B.E. POLING (1987), The Properties of Gases
      and Liquids, McGraw-Hill Book Company, New York.

[109] D.W. ROBINSON AND G.T. REID (1993), Interferogram analysis: digital fringe
      pattern measurement techniques, Institute of Physics Publishing, London, ISBN 0–
      7503–0197–X.

[110] G.A. SALTANOV AND R.A. TKALENKO (1975), Investigation of transonic un-
      steady state flow in the presence of phase transformations, *Zh. Prikl. Mek. i
      Tek. Fiz. (UdSSR)*, Vol. 6, pp. 42-48.

[111] D. SAHNI (1966), *J. Nucl. Energy.*, Vol. 20, 915.

[112] H. SCHLICHTING AND K. GERSTEN (1997), Grenzschicht-Theorie, 9th edition,
      Springer-Verlag.

[113] B. SCHMIDT (1962), Beobachtungen über das Verhalten der durch Wasserdampf-Kondensation ausgelösten Störungen in einer Überschall-Windkanaldüse, *PhD thesis*, Fakultät für Maschinenbau, Universität Karlsruhe (TH).

[114] G.H. SCHNERR (1986), Homogene Kondensation in stationären transsonischen Strömungen durch Lavaldüsen und um Profile, *Habilitation*, Fakultät für Maschinenbau, Universität Karlsruhe (TH).

[115] G.H. SCHNERR (1989), 2-D transonic flow with energy supply by homogeneous condensation: Onset condition and 2-D structure of steady Laval nozzle flow, *Exp. Fluids*, Vol. 7, pp. 145-156.

[116] G.H. SCHNERR, U. DOHRMANN, H.-A. JANTZEN AND R.R. HUBER (1989), Transsonische Strömungen mit Relaxation und Energiezufuhr durch Wasserdampf-kondensation, *Strömungsmechanik und Strömungsmaschinen*, Vol. 40, pp. 39-79.

[117] G.H. SCHNERR AND U. DOHRMANN (1990), Transonic flow around airfoils with relaxation and energy supply by homogeneous condensation, *AIAA J.*, Vol. 28, No. 7, pp. 1187-1193.

[118] G.H. SCHNERR (1993), Transonic aerodynamics including strong effects from heat addition, *Computers Fluids*, Vol. 22, No. 2/3, pp. 103-116.

[119] G.H. SCHNERR AND G. MUNDINGER (1993), Numerical visualization of self-excited shock oscillations in two-phase flows, in: *Proc. of the 5th Int. Symp. on Comp. Fluid Dynamics*, H. Daiguji (editor), Japan Society of CFD, Sendai.

[120] G.H. SCHNERR, S. ADAM AND G. MUNDINGER (1994), Frequency control of shock oscillations in high speed two-phase flow, in: *Proc. of the 4th Triennal Int. Symp. on Fluid Control, Measurement and Visualization*.

[121] G.H. SCHNERR, S. ADAM AND G. MUNDINGER (1995), New modes of periodic shock formation in compressible two-phase flows, in: *Proc. IUTAM Symposium Waves in Liquid/Gas and Liquid/Vapor Two-Phase Systems*, S. Morioka and L. van Wijngaarden (editors), Kluiwer Academic Publishers.

[122] G.H. SCHNERR (September 2000), Universität Karlsruhe (TH), private communications.

[123] W. SCHUMANN (1985), Holography and Deformation Analysis, Springer-Verlag, Berlin.

[124] P. SHERMAN (1963), in: *Rarefied Gas Dynamics, 3rd Symposium*, Vol. 2, 228, Academic Press, New York.

[125] J.S. SHUEN, M.S. LIOU AND B. VAN LEER (1990), Inviscid flux-splitting algorithms for real gases with non-equilibrium chemistry, *J. Comp. Phys.*, Vol. 90, pp. 371-395.

[126] M. SICHEL (1981), Unsteady transonic nozzle flow with heat addition, *AIAA J.*, Vol. 19, pp. 165-171.

[127] S.A. SKILLINGS AND R. JACKSON (1987), A robust time-marching solver for one-dimensional nucleating steam flows, *Heat and Fluid Flow*, Vol. 8, pp. 139-144.

[128] S.A. SKILLINGS, M.J. MOORE, P.T. WALTERS AND R. JACKSON (1988), A reconsideration of wetness loss in LP turbines, *British Nuclear Energy Society, Int. conf. "Technology of turbine plant operating with wet steam"*, Thomas Telford (editor), pp. 171-177, London.

[129] L.T. SMITH (1971), Experimental investigation of the expansion of moist air, *AIAA J.*, Vol. 9, No. 10, pp. 2035-2037.

[130] H.J. SMOLDERS (1992), Non-Linear Wave Phenomena in a Gas-Vapour Mixture with Phase Transition, *PhD thesis*, Eindhoven University of Technology.

[131] K. SNOEIJS (1992), De optische karakterisering van nevels, *Master thesis R-1170-A*, Eindhoven University of Technology,.

[132] D. SONNTAG AND D. HEINZE (1982), Sättigungsdampfdruck- und Sättigungsdampfdichtetafeln für Wasser und Eis, *Technical Report*, VEB Deutscher Verlag für Grundstoffindustrie.

[133] C.M. SORENSEN, J. CAI AND N. LU (1992), Light-scattering measurements of monomer size, monomers per aggregate, and fractal dimension for soot aggregates in flames, *Applied Optics*, Vol. 31, No. 30, pp. 6547-6556.

[134] R. STREY, P.E. WAGNER AND Y. VIISANEN (1994), The problem of measuring homogeneous nucleation rates and the molecular contents of nuclei: progress in the form of nucleation pulse experiments, *J. Phys. Chem.*, Vol. 98, No. 32, pp. 7748-7758.

[135] K. TAKAYAMA (1983), Application of holographic interferometry to shock wave research, in: *Proc. of the Society of Photo-Optical Instrumentation Engineers*, Vol. 398, pp. 174-180.

[136] K. TATSUNO AND S. NAGAO (1986), Water droplet size measurements in an experimental steam turbine using an optical fiber droplet sizer, *J. Heat Transfer*, Vol. 108, pp. 939-945.

[137] N.E. TAYALI AND C.J. BATES (1990), Particle sizing techniques in multiphase flow: a review, *Flow. Meas. Instrum.*, Vol. 1, No. 0, pp. 77-105.

[138] T. THEEUWES (1997), Development of a holographic interferometer for visualisation of compressible flow, *Technical Report R-1420-D*, Stan Ackermans Instituut, Technische Universiteit Eindhoven, ISBN 90-5282-752-4.

[139] I. THORMÄHLEN, J. STRAUB AND U. GRIGUL (1985), Refractive index of water and its dependence on wavelength, temperature, and density, *J. Phys. Chem. Ref. Data*, Vol. 14, No. 4, pp. 933-945.

[140] B.H. TIMMERMAN (1997), Holographic Interferometric Tomography for Unsteady Compressible Flows, *PhD thesis*, Delft University of Technology, ISBN 90-5651-044-4.

[141] Y.S. TOULOUKIAN (1970), Thermophysical Properties of Matter, Plenum, New York.

[142] S. TWOMEY (1963), On the numerical solution of Fredholm integral equations of the first kind by inversion of the linear system produce by quadrature, *J. Assoc. Comput. Mach.*, Vol. 10, pp. 97-101.

[143] S. TWOMEY (1975), Comparison of constrained linear inversion and an iterative nonlinear algorithm applied to the indirect estimation of particle size distribution, *J. Comp. Phys.*, Vol. 18, pp. 188-200.

[144] S. TWOMEY (1977), Introduction to the Mathematics of Inversion in Remote Sensing and Indirect Measurements, Elsevier, Amsterdam.

[145] N.B. VARGAFTIK (1975), Tables on the thermophysical properties of liquids and gases, 2nd edition, Wiley, New York.

[146] T. VERVOORT (1998), Droplet size measurements using the multi-wavelength light extinction method, *Technical Report R-1461-S*, Technische Universiteit Eindhoven.

[147] C.M. VEST (1979), Holographic Interferometry, John Wiley & Sons, New York.

[148] Le Alte Velocità in Aviazione (1935), in: *Atti del V Convegno Volta*, Roma, Sept.30 - Oct. 6, edited by Fondazione Alessandro Volta, Reale Accademia D'Italia, 1st ed. 1936 - XIV; 2nd ed. 1940 - XIX.

[149] P.E. WAGNER (1982), Aerosol growth by condensation, in: *Aerosol Microphysics*, W.H. Marlow (editor), Springer, Berlin.

[150] L. WALPOT, R. STEIJL, P. BAKKER AND L. MARRAFFA (1997), Development and validation of a two dimensional nonequilibrium condensing flow solver, in: *21st ISSW21, Int. Symposium on Shock Waves*, Great Keppel Island, Australia. Paper 6552.

[151] P.T. WALTERS (1973), Optical measurements of water droplets in wet steam, in: *Conf. Wet Steam 4, Warwick*, IMechE. Paper C32/73.

[152] P.T. WALTERS AND P.C. SKINGLEY (1979), An optical instrument for measuring the wetness fraction and droplet size of wet steam flows in LP turbines, in: *Conf. on Steam Turbines for the 1980's*, London, IMechE. Paper C141/79.

[153] P.T. WALTERS (1980), Practical applications of inverting spectral turbidity data to provide aerosol size distributions, *Applied Optics*, Vol. 19,No.14, pp. 2353-2365.

[154] P.T. WALTERS (1988), Improving the accuracy of wetness measurements in generating turbines by using a new procedure for analysing optical transmission data, in: *British Nuclear Energy Society, Int. conf. "Technology of turbine plant operating with wet steam"*, Thomas Telford (editor), pp. 207–215, London.

[155] P.P. WEGENER (1954), Water vapor condensation process in supersonic nozzles, *J. Appl. Phys.*, Vol. 25, pp. 1485-1491.

[156] P.P. WEGENER AND L.M. MACK (1958), Condensation in supersonic and hypersonic wind tunnels, in: *Advances in Appl. Mechanics*, H.L. Dryden and Th. von Kármán (eds.), Academic Press, New York.

[157] P.P. WEGENER AND D.J. CAGLIOSTRO (1973), Periodic nozzle flow with heat addition, *Combustion Science and Technology*, Vol. 6, pp. 269-277.

[158] P.P. WEGENER AND F. MOSNIER (1981), Periodic transonic nozzle flow with heat addition: new results, *Combustion Science and Technology*, Vol. 24, pp. 179-189.

[159] A.J. WHITE AND J.B. YOUNG (1993), Time-marching method for the prediction of two-dimensional unsteady flows of condensing steam, *J. Propulsion and Power*, Vol. 9, pp. 579-587.

[160] A.J. WHITE, J.B. YOUNG AND P.T. WALTERS (1996), Experimental validation of condensing flow theory for a stationary cascade of steam turbines blades, *Phil. Trans. R. Soc. London A*, Vol. 354, pp. 59-88.

[161] W.W. WILLMARTH AND H.T. NAGAMATSU (1952), Condensation of Nitrogen in a Hypersonic Nozzle, *J. Appl. Phys.*, Vol. 23.

[162] J.B. YOUNG (1982), The spontaneous condensation of steam in supersonic sozzles, *PhysicoChemical Hydrodynamics*, Vol. 3, No. 1, pp. 57-82.

[163] J.B. YOUNG AND A. GUHA (1991), Normal shock-wave structure in two-phase vapour-droplet flows, *J. Fluid Mech.*, Vol. 228, pp. 243-274.

[164] J.B. YOUNG (1991), The condensation and evaporation of liquid droplets in a pure vapour at arbitrary Knudsen number, *Int. J. Heat Mass Transfer*, Vol. 34, No.7, pp. 1649-1661.

[165] J.B. YOUNG (1993), The condensation and evaporation of liquid droplets at arbitrary Knudsen number in the presence of an inert gas, *Int. J. Heat Mass Transfer*, Vol. 36, pp. 2941-2956.

[166] J. ZIEREP AND S. LIN (1968), Ein Ähnlichkeitsgesetz für instationäre Konden-sationsvorgänge in Lavaldüsen, *Forschung im Ingenieurwesen*, Vol. 34, No. 4, pp. 97-132.

[167] J. ZIEREP (1974), Theory of flows in compressible media with heat addition, *Tech-nical Report 191*, AGARDograph.

[168] J. ZIEREP AND G.H. SCHNERR (1994), Fluiddynamische Instabilitäten und Oszil-lationen durch Kondensationsverzug und Phasenumwandlung im Nichtgleichgewicht, *Technical Report*, DFG-Zwischenbericht.

Appendix A

Physical properties

This appendix summarises the physical properties used in the numerical simulations. The reported formulas and values refer only to the condensation model proposed by the present author. In the present study, two inert carrier gases are considered: nitrogen and air. Their physical properties and constants are listed below, including their units and the source from which they are taken. Values are given for the mass of a molecule m, specific gas constants R, specific heat at constant volume c_v and at constant pressure c_p, thermal conductivity k, and dynamic viscosity μ.

Nitrogen

m	$=$	$4.651 \cdot 10^{-26}$	$[kg]$	[108]
R_a	$=$	296.81	$[J/(kg\,K)]$	[107]
c_{pa}	$=$	1041	$[J/(kg\,K)]$	[107]
c_{va}	$=$	743.57	$[J/(kg\,K)]$	[107]
k	$=$	$2.55 \cdot 10^{-2}\,(T/295)^{0.838}$	$[W\,m^{-1}\,K^{-1}]$	[141]
μ	$=$	$17.6 \cdot 10^{-6}\,(T/295)^{0.767}$	$[kg\,m^{-1}\,s^{-1}]$	[141]

Air

m	$=$	$4.810 \cdot 10^{-26}$	$[kg]$	[59]
R_a	$=$	287.04	$[J/(kg\,K)]$	[107]
c_{pa}	$=$	1004	$[J/(kg\,K)]$	[107]
c_{va}	$=$	717	$[J/(kg\,K)]$	[107]
k	$=$	$1.48 \cdot 10^{-2}\,(T/295)^{0.50}$	$[W\,m^{-1}\,K^{-1}]$	[108]
μ	$=$	$\mu_{ra}\,(T/T_r)^{3/2}\,(T_r+s)/(T+s)$	$[kg\,m^{-1}\,s^{-1}]$	[112]

In the last expression (Sutherland's formula), $\mu_{ra} = 19.1 \cdot 10^{-6}\,kg\,m^{-1}\,s^{-1}$ is a reference viscosity value, $T_r = 273.15\,K$ is a reference temperature and the constant s is, for dry air, equal to $s = 110$. The material properties of water vapour are reported next.

Water Vapour

m	$=$	$2.991 \cdot 10^{-26}$	$[kg]$	[59]
R_v	$=$	461.52	$[J/(kg\,K)]$	[107]
c_{pv}	$=$	1859	$[J/(kg\,K)]$	[107]
c_{vv}	$=$	1397.5	$[J/(kg\,K)]$	[107]
k	$=$	$D_0 + D_1\,T + D_2\,T^2 + D_3\,T^3$	$[W\,m^{-1}\,K^{-1}]$	[108]
μ	$=$	$(1.823 \cdot 10^{-6}\,\sqrt{T})/(1 + 673/T)$	$[kg\,m^{-1}\,s^{-1}]$	[71]

The values of the coefficients D_0, D_1, D_2, D_3, are:

D_0	$=$	$7.341 \cdot 10^{-3}$	$[W\,m^{-1}\,K^{-1}]$	[108]
D_1	$=$	$-1.013 \cdot 10^{-5}$	$[W\,m^{-1}\,K^{-2}]$	[108]
D_2	$=$	$1.801 \cdot 10^{-7}$	$[W\,m^{-1}\,K^{-3}]$	[108]
D_3	$=$	$-9.100 \cdot 10^{-11}$	$[W\,m^{-1}\,K^{-4}]$	[108]

Note that the dynamic viscosity and thermal conductivity of the gas-vapour mixture are defined as follows:

$$\mu \;=\; \frac{(1 - g_{max})\,\mu_a + (g_{max} - g)\,\mu_v}{1 - g}, \tag{A.1}$$

$$k \;=\; \frac{(1 - g_{max})\,k_a + (g_{max} - g)\,k_v}{1 - g}, \tag{A.2}$$

where the subscripts "a, v" denote the carrier gas and the water vapour component, respectively.

Latent heat

From the Clausius-Clapeyron relation, the following relation can be derived for the latent heat of condensation:

$$L(T) = \; R_v\,(A_{10}\,T^2 + 2A_{11}\,T^3 + B_1\,T - C_0) \qquad [J/kg] \qquad [132]$$

The values of the coefficients A_{10}, A_{11}, B_1, C_0, are:

A_{10}	$=$	$-2.7246 \cdot 10^{-2}$	$[1/K]$	[132]
A_{11}	$=$	$1.6853 \cdot 10^{-5}$	$[1/K^2]$	[132]
B_1	$=$	2.4576	$[-]$	[132]
C_0	$=$	-6094.4642	$[K]$	[132]

Saturation pressure

Following Vargaftik [145], the saturation pressure is expressed as:

$$p_{s\infty} = 610.8 \exp\left[-5.1421 \ln\left(\frac{T}{273.15} \right) - 6828.77 \left(\frac{1}{T} - \frac{1}{273.15} \right) \right] \quad [Pa] \qquad (A.3)$$

Binary diffusion coefficients

water-nitrogen: $\quad \mathcal{D} = 24.5 \cdot 10^{-6} \, (T/295)^{2.085}/p(bar) \qquad [m^2 \, s^{-1}] \qquad$ [145]

water-air: $\qquad\quad \mathcal{D} = 24.9 \cdot 10^{-6} \, (T/295)^{1.75}/p(bar) \qquad [m^2 \, s^{-1}] \qquad$ [108]

Density of liquid water

The density of liquid water is expressed, following Pruppacher and Klett [105], as:

$$\varrho_l(t) = \begin{cases} \dfrac{A_0 + A_1 \, t + A_2 \, t^2 + A_3 \, t^3 + A_4 \, t^4 + A_5 \, t^5}{1 + B_0 \, t} & [kg/m^3] \qquad \text{for} \quad t \geq 0°C \\ A_6 + A_7 \, t + A_8 \, t^2 \quad [kg/m^3] & \text{for} \quad t < 0°C \end{cases} \qquad (A.4)$$

with t in $°C$ and the constants:

A_0	$=$	999.84	$[kg/m^3]$	[105]
A_1	$=$	18.224944	$[kg\,°C/m^3]$	[105]
A_2	$=$	$-7.92221 \cdot 10^{-3}$	$[kg\,°C^2/m^3]$	[105]
A_3	$=$	$-55.44846 \cdot 10^{-6}$	$[kg\,°C^3/m^3]$	[105]
A_4	$=$	$149.7562 \cdot 10^{-9}$	$[kg\,°C^4/m^3]$	[105]
A_5	$=$	$-393.2952 \cdot 10^{-12}$	$[kg\,°C^5/m^3]$	[105]
A_6	$=$	999.84	$[kg/m^3]$	[105]
A_7	$=$	0.086	$[kg\,°C/m^3]$	[105]
A_8	$=$	-0.0108	$[kg\,°C^2/m^3]$	[105]
B_0	$=$	$18.159725 \cdot 10^{-3}$	$[°C]$	[105]

Surface tension of liquid water

During the supersonic expansion of water vapour/carrier gas mixtures in Laval nozzles large subcoolings are achieved and the temperature drops well below the triple point ($T_{tr} = 273.15 \, K$). In these circumstances, it is not sure whether the condensate remains in the liquid phase. Dohrmann [33], Mundinger [91], and Adam [2] obtained a good agreement between theory and experiments by assuming the condensate to remain liquid.

More recently, Strey *et al.* [134] obtained the experimental confirmation of this, by observing the Mie peaks from scattered light. Therefore, the assumption of liquid condensate is retained throughout this work.

The surface tension dependence on temperature follows the empirical formula derived by Pruppacher and Klett [105] for $T \geq 250\,K$. For the extrapolation of σ to low temperatures, the reader is referred to sections 2.3.2 and 6.6.

$$\sigma^{LD}(T) = \begin{cases} 8.52000 \cdot 10^{-2} - 3.54236 \cdot 10^{-4}\,T + 3.50835 \cdot 10^{-6}\,T^2 \\ -8.71691 \cdot 10^{-9}\,T^3 \quad [N/m] \qquad \text{for} \quad T < 250.0\,K \\ (76.1 + 0.155\,(273.15 - T)) \cdot 10^{-3} \qquad [N/m] \\ \qquad \text{for} \quad T \geq 250.0\,K \end{cases} \tag{A.5}$$

Appendix B

Droplet temperature calculation

This appendix describes the derivation of Smolders' explicit, second-order accurate, droplet temperature relation. A more detailed treatment can be found in the thesis of Smolders [130] and Prast [104]. Here, the most relevant passages and simplifying assumptions are summarised. As a starting point, the expressions for the mass and energy transfers are substituted in the definitions of the Nusselt numbers (Eq. 2.44), for both the free molecular and continuum limit. As mentioned already in section 2.4.1, in the determination of the droplet temperature only the energy transfer due to heat conduction is considered. In the free molecular limit, this simplification consists in neglecting the term $\dot{M}^{fm}T_d R_v/2$ with respect to $\dot{M}^{fm}L$. Due to the high value of the latent heat of water, an error smaller than 5 % is committed. In this approximation, the expressions of the Nusselt numbers become:

Free molecular limit

$$Nu_{\dot{M}}^{fm} = \sqrt{\frac{2}{\pi}\frac{R_v}{\overline{R}}}\left[1 + \left(1 - \sqrt{\frac{T_\infty}{T_d}}\right)\frac{p_{vr}}{p_{v\infty} - p_{vr}}\right]\frac{Sc}{Kn}, \tag{B.1}$$

$$Nu_{\dot{H}}^{fm} = \sqrt{\frac{2}{\pi}\frac{\overline{\gamma}+1}{2\,\overline{\gamma}}\frac{Pr}{Kn}}, \tag{B.2}$$

where $\gamma = c_{p0}/c_{v0}$, the Schmidt number Sc is defined by Eq. (2.65), and the Prandlt number Pr by Eq. (2.62). Both the Sc and Pr numbers should be evaluated at the intermediate temperature T_m, defined following Hubbard et al. [62] as $T_m = 1/3\,(2\,T_d + T_\infty)$. A bar over a group of variables indicates averaged properties of the gas/vapour mixture. In deriving Eqs. (B.1)-(B.2), it is implicitly assumed that the gas mixture behaves as a calorically perfect gas. In the continuum limit, the expressions of the Nu numbers read as follows:

Continuum limit

$$Nu_{\dot{M}}^{ct} = 2\,\frac{\ln\left[1 + \left(\frac{p_{v\infty} - p_{vr}}{p_{g\infty}}\right)\right]}{\left(\frac{p_{v\infty} - p_{vr}}{p_{g\infty}}\right)}, \tag{B.3}$$

153

$$Nu_{\dot{H}}^{ct} = 2 \frac{\ln\left[1 + \left(\frac{c_{pv}(T_\infty - T_d)}{L}\right)\right]}{\left(\frac{c_{pv}(T_\infty - T_d)}{L}\right)}. \tag{B.4}$$

In the hypothesis that $c_{pv}(T - T_d)/L$ and $(p_v - p_{vr})/p_{g\infty}$ are much smaller than unity, both expressions of the Nusselt numbers (Nu_M^{ct}, Nu_H^{ct}) tend to the limiting value of two. This assumption is retained throughout the present work.

The droplet temperature T_d is then calculated from the approximated wet-bulb equation ($\dot{H} = -L\,\dot{M}$), expressed in terms of Nusselt numbers:

$$\left(\frac{T_d}{T_\infty} - 1\right) = \frac{\theta}{T_\infty}\frac{p_{v\infty} - p_{vr}}{p_{g\infty}}, \tag{B.5}$$

where p_{vr} is equal to the curvature corrected saturation pressure $p_{vr} = p_{sr}(T_d, r_d)$ and θ is defined by Eq. (2.52). For clarity, the definition of θ is repeated below:

$$\theta = \frac{\mathcal{D}_{mod}L}{k}\frac{Nu_M^{tr}}{Nu_{\dot{E}}^{tr}}. \tag{B.6}$$

Equation (B.5) provides an implicit relation for the droplet temperature. However, by introducing some simplifying assumptions, it is possible to derive an explicit relation which relates the droplet temperature to the droplet size and the environmental conditions. A first simplification is to assume that the latent heat L and all transport coefficients are basically constant within the range (T_d, T_∞) and may, therefore, be calculated in the far field (i.e. at T_∞). The wet-bulb relation (Eq. B.5) can now be re-written as:

$$\frac{T_\infty}{\theta_\infty S_\infty}\left(\frac{p_\infty}{p_{s\infty}} - S_\infty\right)\left(\frac{T_d}{T_\infty} - 1\right) = -\left(\frac{p_{vr}}{p_{v\infty}} - 1\right). \tag{B.7}$$

Implicitly, in Eq. (B.7), it is assumed that the parameter θ (i.e. the Nu numbers) is also evaluated in the far field. This is a necessary approximation in order to make the wet-bulb equation explicit. Essentially, this approximation reduces to the surmise that the square-bracketed term in Eq. (B.1) is approximately equal to one. Equation (B.7) is still not explicit due to the presence of $p_{vr} = p_{sr}(T_d, r_d)$. To eliminate p_{vr}, two additional simplifications are introduced. First, the vapour pressure at the droplet surface p_{vr} is approximated as:

$$p_{vr} = p_{s\infty}(T_d)\exp Ke_\infty, \tag{B.8}$$

that is, the Ke is not evaluated at the droplet surface but in the far field. The term $p_{s\infty}(T_d)$ can be obtained from the integrated Clausius-Clapeyron equation, which yields:

$$\ln\left[\frac{p_{s\infty}(T_d)}{p_{s\infty}(T_\infty)}\right] = \frac{L_\infty}{R_v T_\infty}\frac{T_\infty}{T_d}\left(\frac{T_d}{T_\infty} - 1\right). \tag{B.9}$$

Second, a Taylor series expansion of p_{vr} around $p_{v\infty}$ is performed with truncation after the first-order term, yielding:

$$\ln\left(\frac{p_{vr}}{p_{v\infty}}\right) = \xi_{ln}\left(\frac{p_{vr}}{p_{v\infty}} - 1\right), \tag{B.10}$$

where the factor ξ_{ln} can be estimated using relation (B.7):

$$\xi_{ln} \approx 1 + \frac{1}{2}\frac{T_\infty}{\theta_\infty S_\infty}\left(\frac{p_\infty}{p_{s\infty}} - S_\infty\right)\left(\frac{T_d}{T_\infty} - 1\right). \tag{B.11}$$

By combining Eqs. (B.7), (B.8), (B.9), and (B.10), the following relation is obtained:

$$\left(\frac{T_d}{T_\infty} - 1\right) = f(S_\infty, Ke_\infty)\left[\frac{T_\infty}{\theta_\infty S_\infty}\left(\frac{p_\infty}{p_{s\infty}} - S_\infty\right)\xi_{ln} + \frac{L_\infty}{R_v T_\infty}\frac{T_\infty}{T_d}\right]^{-1}. \tag{B.12}$$

Finally, to obtain an explicit equation, Smolders [130] further assumes $T_\infty \approx T_d$ and $\xi_{ln} \approx 1$, which yields the desired expression:

$$\left(\frac{T_d}{T_\infty} - 1\right) = f(S_\infty, Ke_\infty)\left[\frac{T_\infty}{\theta_\infty S_\infty}\left(\frac{p_\infty}{p_{s\infty}} - S_\infty\right) + \frac{L_\infty}{R_v T_\infty}\right]^{-1}. \tag{B.13}$$

The accuracy of Eq. (B.13) with respect to the implicit solution (Eq. B.12) has been studied in detail by Prast [104]. He showed that, at low temperatures ($T \approx 230\,K$), significant errors (up to 50 %) are introduced by using Eq. (B.13). To improve the quality of the solution, Smolders [130] formulated a second-order correction to Eq. (B.13). This correction was obtained by comparing Eqs. (B.12) with (B.13) and by using Eq. (B.11) for the expression of ξ_{ln}:

$$\delta_1 \approx \frac{\frac{1}{2}C_1^2 - C_2}{(C_1 + C_2)^2}\left(\ln S_\infty - Ke_\infty\right), \tag{B.14}$$

where C_1 and C_2 are defined in Eqs. (2.52). Finally, the second-order, explicit relation becomes:

$$\left(\frac{T_d}{T_\infty} - 1\right) = f(S_\infty, Ke_\infty)[C_1 + C_2]^{-1}(1 - \delta_1). \tag{B.15}$$

Prast [104] evaluated also the quality of Eq. (B.15) with respect to Eq. (B.12), for condensing nozzle flow applications. A significant improvement is obtained by using Smolders' correction, which leads to an inaccuracy of $\pm 5\,\%$ in the phase of relevant growth.

Once the droplet temperature has been calculated, the droplet growth rate can be computed via the mass conservation law:

$$\frac{dr_d^2}{dt} = -\frac{Nu_M^{tr}(T_\infty)\mathcal{D}_{mod}}{\rho_l}\frac{p_{v\infty} - p_{sr}(T_d)}{p_{g\infty}}. \tag{B.16}$$

Note that Eq. (B.16) is a simplified version of Eq. (2.55), in that the transition Nu number is evaluated at T_∞ and not at T_d. However, assuming a temperature difference $(T_d - T_\infty)$ of approximately $20\,°C$, this simplification corresponds to an error smaller than $4\,\%$ in the expression of Nu_M^{fm}.

Appendix C

Hill's method

To integrate the integro-differential equation (Eq. 2.23), expressing the formation of the condensate mass, Hill's method is used. This method consists in tracking the time evolution of the lower moments of the size distribution function. In the first place, let us define the n-th moment of the droplet size distribution $f(r)$ as:

$$\varrho \mathcal{Q}_n = \int\limits_0^\infty r^n f(r) dr. \tag{C.1}$$

This integral can also be evaluated in terms of the nucleation rate and subsequent droplet growth. Assume the droplet, formed at a time τ, has a size $R(t, \tau)$ at the current instant t. Then, it results:

$$\varrho \mathcal{Q}_n = \int\limits_{-\infty}^t \frac{\varrho(t)}{\varrho(\tau)} J(\tau) r^n(t, \tau) d\tau. \tag{C.2}$$

In fact, $J(\tau) d\tau / \varrho(\tau)$ is the number of droplets formed in between τ and $\tau + d\tau$, per unit mass of mixture. If there is no velocity slip between droplets and gas, the same number of droplets is still present in the same mass element at time t. Since $\varrho \mathcal{Q}_n$ is defined per unit volume, the integral in Eq. (C.2) has to be multiplied by $\varrho(t)$.

The moment equations are obtained by taking the total (material) derivative of $\mathcal{Q}_n$:

$$\frac{D\mathcal{Q}_n}{Dt} = \frac{1}{\varrho(t)} J(t) r^{*n} + \int\limits_{-\infty}^t \frac{J(t)}{\varrho(\tau)} n r^{n-1} \frac{Dr}{Dt} d\tau. \tag{C.3}$$

If the growth rate of the droplet formed is independent of size and, therefore, independent of τ, the equation becomes:

$$\frac{D\mathcal{Q}_n}{Dt} = \frac{1}{\varrho(t)} J(t) r^{*n} + \frac{Dr}{Dt} n \mathcal{Q}_{n-1}. \tag{C.4}$$

Note that the material derivative of Eq. (C.2) yields:

$$\frac{\partial \varrho \mathcal{Q}_n}{\partial t} + \nabla \cdot (\varrho \mathcal{Q}_n \underline{v}) = \mathcal{Q}_n \left(\frac{\partial \varrho}{\partial t} + \nabla \cdot (\varrho \underline{v}) \right) + \varrho \left(\frac{\partial \mathcal{Q}_n}{\partial t} + \underline{v} \cdot \nabla \mathcal{Q}_n \right). \qquad (C.5)$$

The first term on the right-hand-side (RHS) of Eq. (C.5) is zero due to the continuity equation (i.e. mass conservation). Therefore, the substantial derivative of $\varrho \mathcal{Q}_n$ becomes simply:

$$\frac{\partial \varrho \mathcal{Q}_n}{\partial t} + \nabla \cdot (\varrho \mathcal{Q}_n \underline{v}) = \varrho \frac{D \mathcal{Q}_n}{D t} \qquad (C.6)$$

The parameters of the size distribution $(n_d,\ r_m,\ \varepsilon)$ are related to the lowest four moments as follows:

$$
\begin{aligned}
n_d &= \varrho \mathcal{Q}_0, \\[2mm]
r_m &= \frac{\mathcal{Q}_1^4}{\mathcal{Q}_0^2 \mathcal{Q}_2 \sqrt{\mathcal{Q}_0 \mathcal{Q}_2}}, \\[2mm]
\varepsilon &= \sqrt{\ln \left(\frac{\mathcal{Q}_0 \mathcal{Q}_2}{\mathcal{Q}_1^2} \right)}.
\end{aligned}
\qquad (C.7)
$$

Appendix D

Nozzles and computational grids.

An example of a typical mesh, employed in the numerical simulations for Nozzle G1, is shown in Fig. D.1. In Table D.1, the typical mesh densities, used for all the investigated nozzles, are given. These values have been selected on the basis of the results from Mundinger [91] and Adam [2], who studied in detail the influence of grid density on the numerical solution.
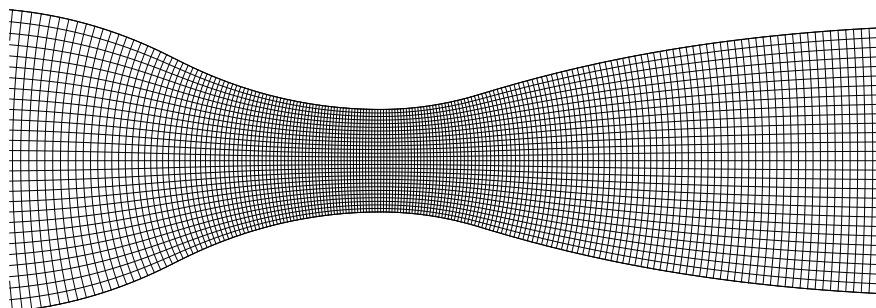

Figure D.1: *Example of the computational grid. Nozzle: G1.*

Nozzle	Type	l $[cm]$	h^* $[cm]$	R_{0-}^* $[cm]$	R_{0+}^* $[cm]$	$(-dT/dt)_{1-D}^*$ $[K/\mu s]$	Mesh Resolution
G1	Parallel outflow	20	2	8	6	0.820	200×30
G2	Parallel outflow	50	2	30	400	0.100	200×30
S1	Circular arc	-	12	10	10	0.237	240×130
S2	Circular arc	-	3	40	40	0.237	200×30

Table D.1: *Standard data and mesh resolution employed in the numerical simulations of the investigated nozzles.*

The contour of nozzles G1 and G2 is given in Table C.2.

Nozzle G1					Nozzle G2			
x [cm]	y [cm]	x [cm]	y [cm]		x [cm]	y [cm]	x [cm]	y [cm]
-7.746	3.000	2.165	1.391		-21.541	5.000	2.950	1.011
-7.454	2.995	2.456	1.478		-20.820	4.991	3.670	1.017
-7.163	2.979	2.748	1.562		-20.100	4.965	4.391	1.024
-6.871	2.952	3.039	1.643		-19.380	4.922	5.111	1.033
-6.580	2.915	3.331	1.719		-18.659	4.861	5.831	1.042
-6.288	2.866	3.622	1.792		-17.939	4.783	6.551	1.054
-5.997	2.806	3.914	1.862		-17.219	4.687	7.272	1.066
-5.706	2.735	4.205	1.928		-16.498	4.573	7.992	1.080
-5.414	2.653	4.496	1.990		-15.778	4.441	8.712	1.099
-5.123	2.558	4.788	2.049		-15.058	4.291	9.433	1.111
-4.831	2.450	5.079	2.104		-14.337	4.122	10.153	1.129
-4.540	2.329	5.371	2.157		-13.617	3.935	10.873	1.148
-4.248	2.195	5.662	2.206		-12.897	3.728	11.594	1.168
-3.957	2.046	5.954	2.253		-12.177	3.501	12.314	1.186
-3.665	1.889	6.245	2.296		-11.456	3.254	13.034	1.212
-3.374	1.746	6.537	2.337		-10.736	2.987	13.755	1.237
-3.082	1.618	6.828	2.374		-10.016	2.721	14.475	1.262
-2.791	1.502	7.120	2.409		-9.295	2.476	15.195	1.289
-2.499	1.400	7.411	2.442		-8.575	2.252	15.916	1.317
-2.208	1.311	7.703	2.472		-7.855	2.047	16.636	1.346
-1.916	1.233	7.994	2.499		-7.134	1.861	17.356	1.377
-1.625	1.167	8.286	2.524		-6.414	1.694	18.076	1.409
-1.333	1.112	8.577	2.546		-5.694	1.545	18.797	1.442
-1.042	1.068	8.869	2.567		-4.973	1.41	19.517	1.476
-0.750	1.035	9.160	2.585		-4.253	1.303	20.237	1.512
-0.459	1.013	9.452	2.601		-3.533	1.209	20.958	1.549
-0.167	1.002	9.743	2.615		-2.812	1.132	21.678	1.583
0.124	1.001	10.035	2.626		-2.092	1.073	22.398	1.613
0.416	1.014	10.326	2.636		-1.372	1.031	23.119	1.638
0.707	1.042	10.618	2.644		-0.652	1.007	23.840	1.657
0.999	1.084	10.909	2.649		0.069	1.000	24.559	1.673
1.290	1.140	11.201	2.653		0.789	1.001	25.280	1.683
1.582	1.212	11.492	2.655		1.509	1.003	25.000	1.688
1.873	1.300				2.230	1.006		

Table C.2: *Set of data points describing the top contour of nozzles G1 and G2.*

Appendix E

The holographic experiment

Here, a brief outline is presented of a typical holographic interferometric experiment. Before carrying out an experiment, the optical alignment of the set-up has to be checked, by means of the CW-HeNe laser. The alignment presents no serious difficulties: the only strict requirement is the projection of a sharp image of the test section on the holographic plate. The ratio between the intensities of the scene and reference beam has to be also checked. Optimal results are obtained with a ratio of $6 \div 5$. The alignment of the optical system is checked for the pulsed laser as well. In practice, this is a very fast check, since the system is tuned in such a way that the path for the HeNe and Ruby pulse laser basically coincide. Once the alignment has been verified, the experiment can start.

Upon preparing the test mixture, as explained in section 3.1.2, a first exposure is made with the mixture at rest in the test section. Then, the mirror (TM) (see Fig. 3.4) is tilted and the experiment is started by breaking the diaphragm. A delay trigger unit assures that the laser is triggered at the desired moment, typically $30 - 35\,ms$ after the breaking of the membrane. The delay unit has an accuracy of $1\,\mu s$, thus enabling a precise determination of the time instant the laser is fired. This feature has been successfully exploited to obtain snapshots at different time steps Δt of the order of $0.2\ ms$, for the visualisation of periodically oscillating flows. These snapshots are made during different experiments. Thus, in order to obtain acceptable results, it is essential to reproduce exactly the same initial conditions. For the pressure and temperature values, this can be achieved very accurately. For the initial relative humidity, whose reproducibility is of $1.6 - 4\,\%$, this condition can only be reached after several runs for which the same supply conditions are repetitively applied. The good agreement between numerically and experimentally determined density fields confirms the validity of this approach.

As photographic material, the AGFA 8E75 HD emulsion has been used, on the basis of a selection performed by Theeuwes [138]. For phase holograms, a large number of chemical processing procedures can be found in the literature. Here, the one suggested by the manufacturer (AGFA) is adopted. First, the emulsion is developed with GP61 ($20°C$) for $2\,min$. After rinsing it in flowing water ($2\,min$, at $20 \pm 2°C$), the emulsion is fixed for $5\,min$ in a dilute bath (1 part fixer + 4 parts distilled water) of either G321 or G334. After rinsing the hologram in water, as described above, the hologram is bleached. For

bleaching, a dilute bath of GP431 (1 part) and distilled water (4 parts) is employed. The bleaching process lasts until the hologram becomes completely transparent. The composition of the developer and bleach can be found in the technical information from AGFA. For completeness, the recipes of the GP61 and G321 are reported below.

Distilled water	$700\,ml$
Metol	$6\,g$
Hydrochinon	$7\,g$
Phenidone	$0.8\,g$
Na_2SO_3	$30\,g$
Na_2CO_3	$60\,g$
KBr	$2\,g$
Na_4EDTA	$1\,g$

Table E.1: *Ingredients for the preparation of the developer GP61. Add distilled water till $1\,ltr$.*

Distilled water	$600\,ml$
Ferri nitrate nonahydrate	$150\,g$
KBr	$30\,g$
Fenosafranine	$300\,mg$
Ethanol	$200\,ml$

Table E.2: *Ingredients for the preparation of the bleach GP431. Add distilled water till $1\,ltr$.*

E.1   Determination of the stagnation conditions

As explained in section 3.1.2, the stagnation conditions for a given experiment are not directly measured, but have to be derived from the conditions in the supply vessel. Prior to each experimental run, the supply pressure P_{ini}, temperature T_{ini}, and supersaturation S_{ini} are measured. Furthermore, by means of the pressure transducer Pk_1, the pressure P_{inlet} at the nozzle inlet is dynamically determined following the passage of the expansion fan.

This section illustrates the relation among stagnation, supply, and inlet conditions, derived from standard shock-tube, gas dynamic relations and subject to the assumption of isentropic flow and calorically perfect gas. Specifically, it holds:

$$
\begin{aligned}
M_{inlet} &= \frac{2}{\gamma - 1} \left[\left(\frac{P_{ini}}{P_{inlet}} \right)^{\frac{\gamma-1}{2\gamma}} - 1 \right], \\
T_{inlet} &= T_{ini} \left[1 + \frac{\gamma - 1}{2} M_{inlet} \right]^{-2},
\end{aligned}
\tag{E.1}
$$

$$
\begin{aligned}
P_0 &= P_{inlet} \left[1 + \frac{\gamma - 1}{2} M_{inlet}^2 \right]^{\frac{\gamma}{\gamma-1}}, \\
T_0 &= T_{inlet} \left[1 + \frac{\gamma - 1}{2} M_{inlet}^2 \right].
\end{aligned}
\tag{E.2}
$$

To determine the stagnation supersaturation S_0, first the water vapour partial pressure p_v is obtained from the supply conditions:

$$
p_v = S_{ini} \, p_{s\infty}(T_{ini}),
\tag{E.3}
$$

where $p_{s\infty}(T_{ini})$ is the saturation pressure. Then, it follows immediately

$$
S_0 = \frac{p_v}{p_{s\infty}(T_0)}.
\tag{E.4}
$$

Appendix F

MWLS set-up

This appendix describes two important aspects of the multi-wavelength light extinction set-up, which are both relevant for a correct execution and evaluation of the experimental results. Specifically, the calibration of the detection system and the evaluation of detector noise.

F.1   Calibration of the detection system

Objective of the calibration procedure is to express the direct correspondence between the micrometer reading and the spectrum location in a simple analytical form. The calibration was performed by Vervoort [146] according to the following procedure: 1) a laser beam is aligned at the entrance diaphragm (D3) of the Spectrograph (see Fig. 3.7); 2) the micrometer is positioned in such a way that a maximum signal is detected at each of the seven detector; 3) this procedure is repeated for four different lasers, emitting at the wavelengths (λ = 543.5, 632.5, 670.0, and 780.0 nm); 4) from these data, a linear relation between wavelength and micrometer position can be established for each detector:

$$
\begin{array}{lll}
\text{Detector 1:} & \lambda_1 = 285.9\,p + 189.5 & \text{(F.1)} \\
\text{Detector 2:} & \lambda_2 = 281.2\,p + 141.9 & \text{(F.2)} \\
\text{Detector 3:} & \lambda_3 = 285.1\,p + 81.50 & \text{(F.3)} \\
\text{Detector 4:} & \lambda_4 = 290.3\,p + 13.20 & \text{(F.4)} \\
\text{Detector 5:} & \lambda_5 = 284.5\,p - 28.80 & \text{(F.5)} \\
\text{Detector 6:} & \lambda_6 = 293.7\,p - 108.1 & \text{(F.6)} \\
\text{Detector 7:} & \lambda_7 = 290.4\,p - 157.3 & \text{(F.7)}
\end{array}
$$

In the above relations, λ represents the central wavelength, expressed in [nm] and the parameter p indicates the position of the spectrograph micrometer. Once the micrometer position is chosen, the central wavelength, detected at each slit, can be also computed, using

165

equations (F.1) - (F.7). For all experimental runs considered in this work, the micrometer reading was 2.038, corresponding to the following central wavelengths:

Detector Number	Central wavelength $[nm]$ ± 1 nm
1	772.3
2	715.0
3	662.6
4	604.8
5	551.1
6	490.6
7	434.5

Table F.1: *Central wavelengths detected at the different slits. Micrometer reading: 2.038.*

F.2   Detector noise evaluation

In section 5.3.2.1, it is shown that the maximum achievable accuracy in the determination of droplet sizes is directly connected to the noise level in the detectors. In this section, the procedure to evaluate the detectors' physical noise is elucidated. First, the transmitted intensities $[I_i'(t); \quad i = 1, \ldots 7]$ are corrected for their offset values. Second, the intensity fluctuations due to energy fluctuations of the light source have also to be taken into account. This is accomplished by measuring, during one experimental run, the light intensity $I_r(t)$ of the Xenon lamp by means of a reference detector placed just before the test section, as shown in Fig. 3.6. Then, the measured intensities can be corrected for these fluctuations via the following relation:

$$I_i(t) = \frac{I_{r0}}{I_r(t)} \frac{I_i'(t)}{I_{i0}'} = e^{-\beta_i l}, \qquad i = 1, \ldots 7, \tag{F.8}$$

where l is the width of the test section, β is the extinction coefficient, and I_{r0} is the time-averaged value of $I_r(t)$. Similarly, $I_i'(t)$ is the directly transmitted signal at each wavelength and I_{i0} is the corresponding time-averaged value, calculated before condensation occurs. To evaluate the standard deviation σ_I/I,[1] the following procedure is adopted. For different intensity levels, obtained by varying the light source power, the intensity I is measured for a short time interval, while there is no flow activated in the test section. Therefore, it results $\beta = 0$ and $e^{-\beta l} = 1$.

The relative standard deviation σ_I/I can be, now, calculated from the left hand side of equation (F.8). The calculated σ_I/I values and the measured detector signals have been correlated with a hyperbolic fit for each detector. These relations are listed below for all

---

[1]The subscript i has been dropped for simplicity.

detectors:

$$\text{Detector 1:} \qquad \frac{\sigma_I}{I} = \frac{1.43}{v - v_d} - 2.23 \cdot 10^{-4}, \qquad\qquad \text{(F.9)}$$

$$\text{Detector 2:} \qquad \frac{\sigma_I}{I} = \frac{1.12}{v - v_d} + 7.12 \cdot 10^{-4}, \qquad\qquad \text{(F.10)}$$

$$\text{Detector 3:} \qquad \frac{\sigma_I}{I} = \frac{1.33}{v - v_d} + 2.74 \cdot 10^{-4}, \qquad\qquad \text{(F.11)}$$

$$\text{Detector 4:} \qquad \frac{\sigma_I}{I} = \frac{1.66}{v - v_d} - 5.05 \cdot 10^{-5}, \qquad\qquad \text{(F.12)}$$

$$\text{Detector 5:} \qquad \frac{\sigma_I}{I} = \frac{1.48}{v - v_d} + 1.33 \cdot 10^{-4}, \qquad\qquad \text{(F.13)}$$

$$\text{Detector 6:} \qquad \frac{\sigma_I}{I} = \frac{1.72}{v - v_d} - 5.21 \cdot 10^{-4}, \qquad\qquad \text{(F.14)}$$

$$\text{Detector 7:} \qquad \frac{\sigma_I}{I} = \frac{1.90}{v - v_d} - 2.88 \cdot 10^{-3}, \qquad\qquad \text{(F.15)}$$

where v represents the measured light intensity at each detector and v_d the corresponding voltage in the absence of incident light (dark value). Both v and v_d are expressed in mV. To conclude this subsection, the response diagram of the detectors is plotted in Fig. F.1.
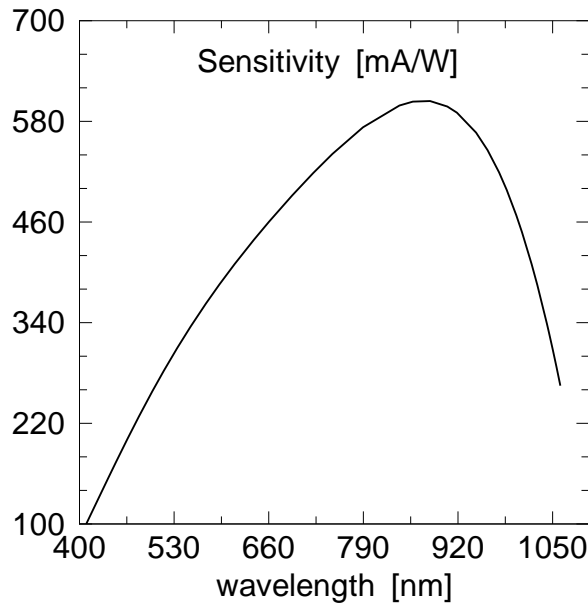
Figure F.1: *Response of the detectors (Siemens BPW 34).*

Appendix G

Mie theory

This appendix contains the analytical expressions for the amplitude scattering matrix and the efficiency factors, which are introduced in chapter 5, in the hypothesis of a homogeneous sphere and incident plane wave. As explained in section 5.2.1, the relation between incident and scattered field amplitudes is:

$$
\begin{pmatrix} E_{ls} \\ E_{rs} \end{pmatrix} = \frac{e^{ik(r-z)}}{-ikr} \begin{pmatrix} S_2 & 0 \\ 0 & S_1 \end{pmatrix} \begin{pmatrix} E_{li} \\ E_{ri} \end{pmatrix}.
\tag{G.1}
$$

The complex amplitude functions are given by

$$
\begin{aligned}
S_1(\alpha, m, \theta) &= \sum_{n=1}^{\infty} \frac{2n+1}{n(n+1)} \left[a_n(\alpha, m)\pi_n(\cos\theta) + b_n(\alpha, m)\tau_n(\cos\theta) \right], \\
S_2(\alpha, m, \theta) &= \sum_{n=1}^{\infty} \frac{2n+1}{n(n+1)} \left[a_n(\alpha, m)\tau_n(\cos\theta) + b_n(\alpha, m)\pi_n(\cos\theta) \right].
\end{aligned}
\tag{G.2}
$$

In the above equations, π_n and τ_n are defined as

$$
\begin{aligned}
\pi_n(z) &= \frac{1}{\sin\theta} P_n^1(z) \\
\tau_n(z) &= \frac{dP_n^1(z)}{d\theta},
\end{aligned}
\tag{G.3}
$$

with P_n^1 being the associated Legendre functions. The coefficients a_n and b_n, in equations (G.3), are given by:

$$
\begin{aligned}
a_n(\alpha, m) &= \frac{\psi_n'(m\alpha)\psi_n(\alpha) - m\psi_n(m\alpha)\psi_n'(\alpha)}{\psi_n'(m\alpha)\zeta_n(\alpha) - m\psi_n(m\alpha)\zeta_n'(\alpha)}, \\
b_n(\alpha, m) &= \frac{m\psi_n'(m\alpha)\psi_n(\alpha) - \psi_n(m\alpha)\psi_n'(\alpha)}{m\psi_n'(m\alpha)\zeta_n(\alpha) - \psi_n(m\alpha)\zeta_n'(\alpha)},
\end{aligned}
\tag{G.4}
$$

with

$$\psi_n(z) = \sqrt{\frac{\pi z}{2}} J_{n+1/2}(z),$$

$$\zeta_n(z) = \sqrt{\frac{\pi z}{2}} H^2_{n+1/2}(z). \tag{G.5}$$

In these equations, J_n and H_n represent the Bessel functions of the first kind and the second Hankel functions, respectively. The expressions for the Bessel, Hankel, and Legendre functions can be found in [70].

The corresponding expressions for the efficiency factors are:

$$Q_{ext}(\alpha, m) = \frac{2}{\alpha^2} \sum_{n=1}^{\infty} (2n+1) \text{Re}\left[a_n(\alpha, m) + b_n(\alpha, m)\right],$$

$$Q_{sca}(\alpha, m) = \frac{2}{\alpha^2} \sum_{n=1}^{\infty} (2n+1) \left[|a_n(\alpha, m)|^2 + |b_n(\alpha, m)|^2\right], \tag{G.6}$$

$$Q_{abs}(\alpha, m) = Q_{ext}(\alpha, m) - Q_{sca}(\alpha, m).$$

Finally, in the hypothesis of unpolarised incident light, the irradiance of the scattered wave is

$$I_s = \frac{I_0}{k^2 \, r^2} \mathcal{F}(\theta, \varphi),$$

$$= \frac{I_0}{2} \left(\frac{1}{k \, r}\right)^2 [i_1(\alpha, m, \theta) + i_2(\alpha, m, \theta)], \tag{G.7}$$

where i_1 and i_2 are the scattered irradiances per unit incident irradiance and are polarised parallel and perpendicular to the scattering plane, respectively. Their expressions, as function of the *amplitude scattering matrix* coefficients are:

$$i_1(\alpha, m, \theta) = |S_1(\alpha, m, \theta)|^2,$$

$$i_2(\alpha, m, \theta) = |S_2(\alpha, m, \theta)|^2. \tag{G.8}$$

Appendix H

Probability density function for distance

In chapter 5, an exponential distribution of path lengths (Eq. 5.38) is assumed in order to express the probability density between two successive scattering events. Hereafter, the reasoning for such a choice is elucidated.

Indicating with x the distance covered by the photon while traversing the test section, let $q\,dx$ be the probability that the photon is scattered within x and $x + dx$, assuming it reached the position x without being scattered. Indicating with $P(x)$ the probability that the photon is scattered before it has reached station x, the probability that a photon is, then, scattered within x and $x + dx$ is $[1 - P(x)]\,q\,dx$. For $P(x)$ the following equation holds:

$$P(x) = \int_0^x [1 - P(x')]\,q\,dx',$$ (H.1)

which can be cast in differential form as:

$$\frac{dP(x)}{dx} = [1 - P(x)]\,q.$$ (H.2)

The solution to this equation is:

$$P(x) = 1 - e^{-qx}.$$ (H.3)

The probability density function $p(x)$ corresponding with $P(x)$ is:

$$p(x) = \frac{dP(x)}{dx} = q\,e^{-qx}.$$ (H.4)

The mean free path $<x>$ of a photon between two successive scattering events can now be expressed in terms of q:

$$<x> = \int_0^x x\,p(x)\,dx = \frac{1}{q};$$ (H.5)

therefore it results

$$p(x) = \frac{1}{<x>}\,e^{-\frac{x}{<x>}}.$$ (H.6)

171

The mean free path $<x>$ can be estimated by dividing the total distance covered by the photon l for the total number of droplets present in the testing volume N_v. Indicated with n_d the droplet concentration, it results $N_v = l\, C_{ext}\, n_d$. In this expression, it was taken into account that the ray does not "see" the geometrical cross section $\pi\, r_d^2$, but the extinction cross section $C_{ext} = Q_{ext}\, \pi\, r_d^2$, which equals the scattering cross section in the absence of absorption. The average distance between two successive scattering events is, then:

$$< x >= \frac{1}{Q_{ext}\, l\, \pi\, r^2\, n_d} = \frac{1}{\beta}. \tag{H.7}$$

Substitution of this expression into Eq. (H.6) yields:

$$p(x) = \beta\, e^{-\beta x}. \tag{H.8}$$

Appendix I

Droplet size experimental data

This appendix summarizes the results of droplet size experiments, conducted for a mixture of water vapour in nitrogen, at different degree of stagnation supersaturation. In Table I.1, the following items are listed: experimental run, stagnation pressure P_0, temperature T_0, and supersaturation S_0, maximum modal radius R_{max}, and frequency of oscillations $\mathcal{F}req$.

Run	$P_0 \times 10^4$ $[Pa]$	T_0 $[K]$	S_0	R_{max} $[nm]$	$\mathcal{F}req$ $[Hz]$
37	8.75	296.6	1.19	162	1347
38	8.77	296.9	1.51	167	1856
41	8.63	296.8	1.10	160	1248
42	8.63	296.9	1.30	161	1509
43	8.65	296.9	1.29	160	1489
44	8.65	297.0	1.46	165	1814
46	8.65	296.9	1.55	166	1898
47	8.64	296.9	1.15	121	1274
50	8.57	296.5	1.29	163	1492
52	8.68	296.9	1.22	164	1417
53	8.67	296.8	1.41	167	1636
55	12.8	297.2	1.25	119	1449
56	8.67	296.7	1.22	153	1422
57	8.68	296.8	1.54	160	1849
58	8.69	296.8	1.33	162	1494
59	8.69	296.8	1.38	173	1566
63	8.67	296.6	1.10	159	1232
70	8.70	296.9	1.51	170	1873
71	8.70	296.8	1.46	170	1761
72	8.69	296.9	1.47	171	1756
73	8.69	296.9	1.40	167	1646

Table I.1: *Experimental droplet size and frequency of oscillations data.*

Summary

Dropwise condensation from the gaseous supersaturated state plays an important role in numerous problems of interest in science and technology, such as the formation of aerosols or condensed matter in astrophysical applications, expansion flows in steam turbines, humid air flows around aircraft wings or in phase separation devices. The present investigation comprises a systematic study of condensing supersonic nozzle flows of water vapour in nitrogen (or air) and encompasses both a theoretical and experimental analysis.

In nozzle flows, the nonequilibrium condensation process is initiated by homogeneous nucleation, that is the spontaneous formation of metastable clusters from the vapour phase, and then followed by droplet growth. The subsequent release of latent heat affects strongly the flow pattern and leads, depending on the amount of heat released and the location, to either steady or periodically oscillating flow regimes. As a consequence of this coupling, the characteristics of the droplet cloud will depend on the coupling between the supersonic flow, nucleation and droplet growth rates. It is immediately clear that an accurate modelling of the entire nonequilibrium process relies on the quality of both nucleation and droplet growth models.

In the literature, many different models have been proposed and verified thoroughly. However, no definitive conclusions could be derived due to the scarcity of reliable experimental data on droplet sizes. Measured droplet sizes constitute a sensitive test for assessing the quality of the proposed condensation models, in that only when both frequency data (or pressure distributions) and droplet sizes are available, it is possible to evaluate to a certain extent separately the quality of nucleation and growth theories. Our first objective is, therefore, to provide this set of data by developing a facility capable of following the time evolution of the droplet size distribution. Our second objective is to validate condensation models and to gain more insights into the physical background. To this aim, this research has developed along three parallel lines: an experimental, a theoretical, and a numerical study.

Experimentally, the flow field has been visualised by means of double exposure holographic interferometry. As hologram type, the image hologram has been chosen since this optical configuration, combined with the use of collimated beams, offers many advantages in the visualisation of phase distortions in optically transparent media. The time dependent droplet size distribution is determined by means of a multi-wavelength white light extinction set-up, characterised by a high spatial and temporal resolution. Due to the importance of droplet size measurements, attention has been paid in assessing the reliabil-

ity and accuracy of these data. The quality of the measurements has been checked with respect to noise level, number of signals recorded, scattering effects, and distance from the regime of Rayleigh scattering. A by-product of this analysis is the assessment of the validity of single scattering approximations (Lambert-Beer law) for a variety of experimental conditions. The experiments have been carried out in two different nozzles: one with a high cooling rate (G1) and one with a low cooling rate (G2).

Theoretically, literature data on nucleation and droplet growth theories have been revised. The "Internally Consistent Classical Nucleation Theory" (ICCT) is chosen to describe the nucleation process. The "Classical Nucleation Theory" (CNT) is kept only for reference. Due to the experimental unavailability of surface tension data for subcooled water ($220 < T < 250\,K$), extrapolation from the known data is necessary. In deriving a possible extrapolation, use is made of the Nernst Postulate, which implies that the partial derivative of surface tension with respect to temperature approaches zero as $T \rightarrow 0$. The so-called Gyarmathy transitional droplet growth model has been adopted. An important feature of the model is the inclusion of a temperature difference between the droplet and surrounding vapour, as a consequence of the released latent heat. This temperature difference is very important, particularly in the initial phase of the droplet growth process, and determines the maximum supersaturation and maximum nucleation rate.

For the numerical simulations, a two-dimensional, time accurate unsteady Euler solver, developed by Prast, is used. A comparative study has been conducted for different nucleation and droplet growth models. By comparing the numerical and experimental results, the quality of the different condensation models could be ascertained. As experimental database, both our own measurements and the measurements published by Schnerr and co-workers (nozzles S1 and S2) have been employed.

In performing this comparison, a precise strategy is adopted. First, the droplet size experiments from nozzle G2 are employed to evaluate the quality of nucleation and droplet growth theories. The evaluation occurred in a temperature range where no uncertainty exists on surface tension values and led to the following conclusions. In the temperature range $(260 \div 270\,K)$, both ICCT and CNT do not predict correctly the actual nucleation rate. This led to the introduction of an empirical factor ($\xi = 0.01$) to compensate for the erroneous ICCT predictions. Accurate droplet sizes are predicted only when the temperature difference between droplet and surrounding vapour is taken into account. Subsequently, the study proceeds with analysing nozzle experiments nucleating at increasingly larger subcoolings. Agreement between theory and experiment could be obtained with a new extrapolation of surface tension fit to low temperatures, in compliance with the thermodynamic constraint derived from the Nernst postulate. The entire set of experimental data can be best correlated with a numerical model based on the following combination: reduced ICCT for the nucleation rate, the transitional Gyarmathy model for the droplet growth process and, the newly proposed surface tension fit.

Samenvatting

Druppelvorming vanuit een oververzadigde gasvormige toestand is van belang voor tal van wetenschappelijke en technologische problemen. Voorbeelden zijn: de vorming van aerosolen in astrofysische toepassingen, expansiestromingen in stoomturbines, luchtstromingen rond vleugelprofielen of de scheiding van zuiver gasvormige en condenseerbare componenten. Het in dit proefschrift beschreven onderzoek heeft betrekking op een systematische studie van condenserende nozzle stromingen van waterdamp in stikstof en lucht en omvat zowel theoretisch als experimenteel werk.

In nozzle stromingen wordt het niet-evenwichts condensatieproces geïnitieerd door homogene nucleatie, de spontane vorming van metastabiele clusters vanuit de dampfase, gevolgd door druppelgroei. De daarbij vrijkomende latente warmte heeft een sterke invloed op de stroming en kan, afhankelijk van de lokatie en de sterkte van de vrijkomende warmte, leiden tot stationaire of oscillerende stromingen. Als gevolg daarvan zullen de eigenschappen van de gevormde druppelwolk afhangen van de koppeling tussen supersone stroming, nucleatie en druppelgroei. Het is duidelijk dat een nauwkeurige modellering van het gehele niet-evenwichtsproces berust op de kwaliteit van de nucleatie- en druppelgroeimodellen.

In eerder werk zijn veel verschillende modellen toegepast en grondig geverifieerd. Echter, definitieve conclusies waren niet goed mogelijk als gevolg van het ontbreken van experimentele data met betrekking tot druppelgroottes. Gemeten druppelafmetingen vormen een gevoelige test voor de kwaliteit van de condensatiemodellen in die zin dat wanneer zowel druppelgrootte als oscillatiefrequentie beschikbaar zijn het in zekere zin mogelijk is nucleatie en druppelgroei separaat te valideren. Het eerste doel was dan ook om een meetmethode te ontwikkelen voor de bepaling van de temporele ontwikkeling van de druppelgrootteverdeling. Het tweede doel was om condensatiemodellen te valideren en inzicht te verwerven in de fysische achtergrond ervan. Het onderzoek bevatte een experimentele, een theoretische en een numerieke studie.

Het stromingsveld is experimenteel bestudeerd door middel van "dubbel puls holografische interferometrie". Als hologramtype is gekozen voor het afbeeldingshologram omdat deze optische configuratie, gecombineerd met toepassing van parallelle bundels, zeer geschikt is voor het vastleggen van faseveranderingen in optisch transparante media. De tijdsafhankelijke druppelgrootteverdeling is vastgelegd door middel van spectraal opgeloste lichtextinctie, gekenmerkt door een hoge ruimtelijke en temporele resolutie. Vanwege het belang van de druppelgroottemetingen is veel aandacht besteed aan de betrouwbaarheid en nauwkeurigheid van de experimentele gegevens. De kwaliteit van de metingen is onder-

zocht met betrekking tot ruisniveau, aantal gekozen golflengtes, meervoudige verstrooiing en voldoende "afstand" in de parameter ruimte tot het regiem van Rayleigh verstrooiing. Een nevenproduct van het onderzoek is het vastleggen van criteria voor enkelvoudige verstrooiing voor een reeks van experimentele condities. Experimenten zijn uitgevoerd met twee verschillende nozzles, een met hoge koelsnelheid (G1) en een met lage koelsnelheid (G2).

Wat betreft de theorie zijn nucleatie- en druppelgroeimodellen vergeleken en geëvalueerd. De "Internally Consistent Classical Nucleation Theory" (ICCT) is gekozen om het nucleatieproces te beschrijven. De "Classical Nucleation Theory" (CNT) is gebruikt als referentie. Omdat voor de oppervlaktespanning van onderkoeld water tussen 220 en 250 K geen experimentele gegevens beschikbaar zijn, is extrapolatie noodzakelijk. Daarbij is gebruik gemaakt van het "Nerst postulaat", dat leert dat de temperatuur afgeleide van de oppervlaktespanning tot nul nadert voor $T \rightarrow 0$. Het z.g. transitiemodel van Gyarmathy is gebruikt om de druppelgroei te beschrijven. Een belangrijk aspect daarvan is dat rekening gehouden wordt met het temperatuurverschil tussen druppel en omgeving als gevolg van het vrijkomen van latente warmte. Dit temperatuurverschil is erg belangrijk in het begin van druppelgroei en is in sterke mate bepalend voor de waarde van de maximale oververzadiging en van de maximale nucleatiesnelheid.

Wat betreft de numerieke analyse is gebruik gemaakt van een twee-dimensionale, tijd opgeloste Euler code, ontwikkeld door Prast. Een vergelijkende numerieke studie is uitgevoerd voor verschillende nucleatie- en druppelgroeimodellen. Voorts zijn numerieke en experimentele uitkomsten met elkaar vergeleken, zodat de kwaliteit van de verschillende condensatiemodellen kon worden vastgesteld. Wat betreft de experimentele data is zowel gebruik gemaakt van eigen metingen als van metingen gepubliceerd door Schnerr en medewerkers (de nozzles S1 en S2).

De uitvoering van deze vergelijkende studie is gedaan als volgt. Eerst zijn de druppelgroottemetingen, verkregen voor nozzle G2, gebruikt om de kwaliteit van nucleatiemodel en druppelgroeimodel vast te stellen. In eerste instantie werden alleen die experimenten geëvalueerd, waarbij geen onzekerheid bestond over de waarde van de oppervlaktespanning. Dit leidde tot de volgende conclusies. In het temperatuurbereik (260-270 K) wordt de nucleatiesnelheid noch door ICCT, noch door CNT correct voorspeld. De ICCT voorspelling moet met een factor $\xi = 0.01$ gecorrigeerd worden. Correcte druppelgroottes worden alleen verkregen als het temperatuurverschil tussen druppel en omgeving in rekening wordt gebracht. Vervolgens is de analyse uitgebreid tot experimenten waarbij nucleatie plaatsvindt bij een lagere temperatuur. Overeenkomst tussen theorie en experiment kon worden verkregen op basis van een nieuwe extrapolatie van de oppervlaktespanning naar lagere temperatuur, rekening houdend met de beperking gegeven door het Nernst postulaat. De volledige set van experimentele gegevens correleerde goed met het numerieke model gebaseerd op de volgende combinatie: gereduceerd ICCT voor de nucleatiesnelheid, het model van Gyarmathy voor de druppelgroei, en een enigszins aangepaste extrapolatie voor de temperatuurafhankelijkheid van de oppervlaktespanning.

Acknowledgements

ferometry is very much appreciated. Dr. Dominic Doyle and Dr. Brenda Timmermann are gratefully acknowledged for their valuable suggestions on the holographic set-up. Also, the critical remarks of prof.dr. Takayama are highly appreciated since they led to substantial improvements in the implementation of holographic techniques to transparent media.

Thank you Anita, Brigitte, Marjan, Giovanna, Corinne, Saskia, Luc, Luis, Gert, Paul, Carlo, Roel for the pleasant time together. Special thanks also to all my friends and particularly to Judith, Patricia and Tjaart for putting up with me also in times when I was a bit down. The social contacts and interactions within the department would not have been so effective without the "regular" parties of Mico Hirschberg and GertJan van Heijst. Their continuous efforts in promoting a friendly and enjoyable atmosphere have certainly made my stay in the department more pleasant.

I owe a tremendous debt to my family who supported and cheered me up throughout all this time. And to you, Michael, many thanks for our long discussions, help and patience during the final rush.

Grazia Lamanna
Eindhoven, October 2000

Curriculum Vitae

25 March 1970   : born in Napoli (I)

1983 - 1989   : Diploma, Liceo Scientifico Statale "F. Brunelleschi",
Afragola (Napoli)

1989 - 1994   : Master degree (*cum laude*) in Aerospace Engineering,
University of Napoli Federico II (I)

1994 - 1995   : Research project on Marangoni convection,
Dept. of Chemical Engineering
University of Groningen (NL)

Summer 1995   : Summer Session Programme in Stockholm (S),
International Space University (ISU)

1996 - 2000   : PhD reserach at the Gas Dynamics Group,
Eindhoven University of Technology (NL)